In the Beginning There was Light:
Blue Emissive Perovskite Nanocrystals

Synthesis, Post-Synthetic Modifications, and Their Optoelectronic Properties

Dissertation

der Mathematisch-Naturwissenschaftlichen Fakultät
der Eberhard Karls Universität Tübingen
zur Erlangung des Grades eines
Doktors der Naturwissenschaften
(Dr. rer. nat.)

vorgelegt von
Christopher Kirsch
aus Neumarkt i.d.OPf.

Tübingen
2023

Gedruckt mit Genehmigung der Mathematisch-Naturwissenschaftlichen Fakultät der Eberhard Karls Universität Tübingen.

Tag der mündlichen Qualifikation:	01.02.2024
Dekan:	Prof. Dr. Thilo Stehle
1. Berichterstatter/-in:	Prof. Dr. Marcus Scheele
2. Berichterstatter/-in:	Prof. Dr. Reinhold Fink

This dissertation was prepared in the time from February 2019 to June 2023 in the group of Prof. Dr. Marcus Scheele at the Institute for Physical and Theoretical Chemistry at the Eberhard Karls University Tübingen.

Abstract

Recently, lead halide perovskites (LHPs) have become a focus of research due to their promising properties for innovative applications in the field of electroluminescent light-emitting diodes (LEDs). In particular, their nanoparticles have attracted considerable interest because they combine the characteristic properties of bulk materials, such as defect tolerance, with the advantages of colloidal quantum dots, such as tunable band gaps and high photoluminescence quantum yields.

However, a major challenge for electroluminescent nanoparticles is the inability to simultaneously achieve high quantum yields and effective charge transport. Although similar issues may arise with lead halide perovskite nanocrystals (NC), a detailed investigation of this aspect is still lacking. In addition to efficiency concerns, perovskite nanoparticles face several instability issues that limit their potential use in optoelectronic devices.

Therefore, this cumulative thesis is dedicated to the development of innovative approaches for the optimization of perovskite nanoparticles and their use in electroluminescent light-emitting diodes (ELQLEDs). The aim of the work is to modify cesium lead halide perovskite nanoparticles to increase their stability while at the same time satisfying the balancing act of being bright emitters and good electrical conductors. This work is expected to help improve the efficiency and quality of ELQLEDs and make a significant contribution to the development of lighting technology.

Initially, the work focuses on the study of self-assembled caesium lead halide perovskite nanocrystal superlattices (SL) and their optical properties. Spatially resolved fluorescence and X-ray nanodiffraction measurements were used to identify surface defects that lead to blue shift and reduced fluorescence lifetime. Loss of structural coherence, increasing atomic misalignment between adjacent nanocrystals, and increasing compressive strain near the surface of the superlattice were found to be responsible for the

observed optical effects. The results emphasize the importance of fabricating structurally high-quality emitter films for the application of perovskites in diodes.

Subsequently, using a custom-synthesized zwitterionic ligand, research efforts were directed toward targeted modifications of the ligand shell surrounding the nanocrystals. A comprehensive characterization of this ligand was performed using nuclear magnetic resonance spectroscopy and mass spectrometry, allowing a thorough understanding of its effect on the electronic properties of the nanocrystals. Following the successful exchange of the ligand, the modified particles were seamlessly integrated into an electroluminescent device, resulting in a significant improvement in both the efficiency and the stability of the device. This important result demonstrated that exchange with suitable ligands can effectively improve the performance of LEDs, paving the way for further advances in the field.

In the following, the optical and electronic effects of doping nanoparticles in LEDs with an organic lithium salt, LiTFSI, were investigated. Photoluminescence spectroscopy, including time-resolved and parallel-polarized angle-dependent measurements, demonstrated that doping improves the quantum yield and light extraction compared to undoped nanoparticles. X-ray photoelectron spectroscopy revealed a reduction in the energy barrier for hole injection and thus an improved balance of charge carriers. This improved the efficiency of blue LEDs compared to untreated nanoparticles.

Finally, the decomposition mechanism of cesium lead halide perovskite nanocrystals was studied using X-ray photoelectron spectroscopy, with particular emphasis on the influence of surface ligands. The aim was to understand how ligand exchange affects the decomposition process. The results showed that the surface ligand plays a crucial role in the decomposition of the nanocrystals. Specifically, it was shown that the decomposition mechanism can be effectively slowed down by exchanging the ligand. This finding highlights the potential for ligand engineering as a means of enhancing the sta-

bility and lifetime of cesium-lead halide perovskite nanocrystals, opening the way for improved applications in a variety of optoelectronic devices.

In summary, this dissertation, with a special focus on blue-emitting perovskite nanocrystals, has experimentally validated the effectiveness of targeted ligand exchange as a practical approach to improve stability, electrical conductivity, and optical properties. The research is an important contribution to ongoing efforts to develop more efficient and reliable LEDs. In particular, it addresses the efficiency limitations of blue LEDs compared to their red and green counterparts. The results obtained thus represent promising approaches for the application of these nanocrystals in optimized light-emitting diodes.

Deutsche Zusammenfassung

Bleihalogenidperowskite stehen seit kurzer Zeit im Fokus der Forschung, weil sie vielversprechende Eigenschaften für neuartige Anwendungen im Bereich von elektrolumineszenten Leuchtdioden aufweisen. Besonders interessant sind dabei deren Nanopartikel, die typische Eigenschaften des Bulk-Materials wie Defekttoleranz mit den Vorteilen kolloidaler Quantenpunkte wie der Anpassungsmöglichkeit der Bandlücke und hohe Photolumineszenz Quantenausbeuten vereinen.

Bislang zeigen elektrolumineszierende Nanopartikeln das Problem, dass hohe Quantenausbeuten und effektiver Ladungstransport nicht gleichzeitig gegeben ist. Bei LHP-Nanokristallen können ähnliche Probleme auftreten, was jedoch noch nicht im Detail erforscht wurde. Neben den Effizienzproblemen leiden Perovskit Nanopartikel unter verschiedenen Instabilitätsproblemen, was ihre Verwendung in optoelektrischen Geräten einschränkt.

Die vorliegende kumulative Dissertation widmet sich daher der Entwicklung innovativer Ansätze zur Optimierung von Perovskit-Nanopartikeln und deren

Verwendung in elektrolumineszenten Leuchtdioden (ELQLED). Das Ziel der Arbeit besteht darin, Cäsium-Bleihalogenid- Perovskit-Nanopartikel so zu modifizieren, dass ihre Stabilität erhöht wird, während sie gleichzeitig den balanceact erfüllen helle Emitter und gute elektrische Leiter zu sein. Diese Arbeit soll dazu beitragen, die Effizienz und Qualität von ELQLEDs zu verbessern und somit einen wichtigen Beitrag zur Weiterentwicklung der Beleuchtungstechnologie zu leisten.

Zunächst konzentriert die Arbeit sich auf die Untersuchung von selbstorganisierten Cäsium-Bleihalogenid-Perowskit-Nanokristall-Superkristallen und ihre optischen Eigenschaften. Durch ortsaufgelöste Fluoreszenz- und Röntgen-Nanodiffraktionsmessungen konnten Oberflächendefekte aufgedeckt werden, die zu einer Blauverschiebung und einer verringerten Fluoreszenzlebensdauer führten. Es wurde gezeigt, dass ein Verlust an struktureller Kohärenz, ein zunehmender atomarer Versatz zwischen benachbarten Nanokristallen und eine zunehmende Druckbelastung nahe der Oberfläche des Superkristalls für die beobachteten optischen Effekte verantwortlich sind. Die Ergebnisse betonen die Wichtigkeit einer Herstellung von strukturell hochwertigen Emitterfilmen für die Anwendung von Perowskiten in Dioden.

Anschließend lag der Fokus darauf, die Ligandenhülle der Nanokristalle gezielt durch einen eigens synthetisierten zwitterionischen Liganden zu modifizieren. Dieser Ligand wurde vollständig durch Kernspinresonanzspektroskopie und Massenspektrometrie charakterisiert und seine Auswirkungen auf die elektronischen Eigenschaften der Nanokristalle untersucht. Die erfolgreich ausgetauschten Partikel konnten anschließend in einem elektrolumineszenten Bauteil mit erhöhter Effizienz und Stabilität integriert werden. Es konnte gezeigt werden, dass durch Austausch mit geeigneten Liganden die Effizienz und Stabilität in LEDs erhöht werden kann.

Im Folgenden wurden die optischen und elektronischen Effekte der Dotierung von Nanopartikeln in LEDs mit einem organischen Lithiumsalz, LiTFSI, untersucht. Durch

Photolumineszenzspektroskopie, einschließlich zeitaufgelöster und parallelpolarisierter winkelabhängiger Messungen, konnte gezeigt werden, dass die Dotierung die Quantenausbeute und die Lichtauskopplung im Vergleich zu undotierten Nanopartikeln verbessert. Röntgen-Photoelektronenspektroskopie offenbarte eine Verringerung der Energiebarriere für die Injektion von Löchern und damit eine verbesserte Balance der Ladungsträger. Dadurch konnte die Effizienz der blauen LEDs im Vergleich zu unbehandelten Nanopartikeln verbessert werden.

Zuletzt wurde mittels Röntgenphotoelektronenspektroskopie der Zersetzungsmechanismus von Cäsium-Bleihalogenid-Perowskit-Nanokristallen untersucht, wobei die Abhängigkeit vom Oberflächenliganden im Fokus stand. Es konnte gezeigt werden, dass durch Ligandenaustausch der Zerfallsmechanismus verlangsamt werden konnte.

Zusammenfassend lässt sich sagen, dass in dieser Dissertation mit besonderem Schwerpunkt auf blau emittierenden Perowskit-Nanokristallen die Wirksamkeit eines gezielten Ligandenaustauschs als praktischer Ansatz zur Verbesserung der Stabilität, der elektrischen Leitfähigkeit und der optischen Eigenschaften experimentell validiert wurde. Die Forschungsarbeit ist ein wichtiger Beitrag zu den laufenden Bemühungen, effizientere und zuverlässigere LEDs zu entwickeln. Sie befasst sich insbesondere mit den Effizienzbeschränkungen von blauen LEDs im Vergleich zu ihren roten und grünen Gegenstücken. Die erzielten Ergebnisse stellen somit vielversprechende Ansätze für die Anwendung dieser Nanokristalle in optimierten Leuchtdioden dar.

This page was intentionally
left blank.

Table of Contents

1. Introduction

“Let there be light, and there was light” - this phrase from the Book of Genesis highlights the importance of light for the universe since the beginning of all being.[1] Even today, light has a significant impact on our daily lives and an immense importance for our modern technology. Through historical developments, we have the privilege of generating light in a very different way than our ancestors, who had to make do with the glow of a torch or candle.

For example, the invention of the incandescent light bulb in 1879 was an important step toward today's lighting methods.[2] For a long time, the incandescent bulb was considered the dominant light source, in which a wire (usually made of tungsten) is made to glow by electricity, producing light.

Just as the development of the incandescent light bulb triggered a revolution in living habits, expectations were high for the light-emitting diode (LED), which promised far greater efficiency in converting electricity into light. With "more" light, there should be less loss in the form of heat. This property and its robust design made it possible to use LEDs for tasks that the incandescent bulb could not perform. LEDs are semiconductor-based electronic components that can emit light when electrically excited. The first commercially available LED was a red LED invented by Nick Holonyak in 1962.[3] Initially, its use was limited to applications where little light was needed. One example is the display of digital watches and calculators.

In the following two decades, the focus of LED development was primarily on increasing efficiency to make LEDs suitable for more power-intensive lighting applications. However, one major issue was the color of the light. With the help of materials such as gallium nitride (GaN), almost all colors of the visible spectrum could be produced. However, there was a lack of a practical solution for short-wave light, especially for the range from blue to ultraviolet. The development of blue LEDs has been chal-

lenging because blue light requires higher energy and is more difficult to produce than other colors. The work of Japanese scientists Isamu Akasaki, Hiroshi Amano, and Shuji Nakamura was awarded the 2014 Nobel Prize in Physics.[4] Their work on the development to produce efficient blue LEDs inaugurated the long-awaited triumph of LEDs. With blue light, it was finally possible to produce white light through additive color mixing, replacing the more inefficient and environmentally harmful incandescent and halogen lamps.

LEDs have now taken an indispensable place and are used in numerous applications, including smartphones, televisions, cars, and household lighting. In order to meet the demands of novel and more efficient technologies, LEDs have been further developed accordingly. In recent years, organic light-emitting diodes (OLEDs) have achieved a breakthrough primarily in display applications. Unlike LEDs, OLEDs use organic materials that are applied in thin layers and can emit light themselves when electrically stimulated. As a result, OLEDs can be extremely thin, flexible, and energy-efficient. However, there is a new class of materials that is considered a promising alternative for television screens: Quantum Dots in so-called QLEDs.

1.1 Motivation

QLEDs are a further development of conventional LEDs and OLEDs. They use semiconductor nanocrystals that emit extremely pure colored light and produce an exceptionally high-contrast and brilliant image. Unlike OLEDs, where each pixel is self-emitting, QLEDs require a backlight, similar to traditional liquid crystal displays (LCDs). The light from the backlight passes through a layer of quantum dots before reaching the display. In the process, the nanoparticles are excited and emit light within a very narrow range of colors due to their material properties. This results in higher color accuracy and a wider color gamut compared to conventional LCDs. To maximize the benefits of both technologies, one approach is to combine the material properties of

nanoparticles with the layer structure of an OLED - electroluminescent quantum dot LEDs (ELQLEDs). Such a device structure would no longer require a backlight to excite the quantum dots. Instead, the injection of carriers would be shifted to the nanoparticle layer itself, potentially leading to higher efficiencies and thinner screens. The use of nanoparticles offers the advantage that the emission spectrum can be tailored to the size of the particles, rather than being limited to specific materials with suitable band gaps.

This approach is already being extensively investigated in research on various semiconductor nanoparticles. For such a structure to work, the respective charge carriers (electrons and holes) transported via the electrodes into the emitting layer, i.e. the nanoparticle layer, must recombine radiatively. For this to work efficiently, the nanoparticles must be both bright emitters (high quantum yield) and good electrical conductors (efficient charge injection). However, for electroluminescent quantum dots, there is often the dilemma that high photoluminescence quantum yield and efficient charge injection and transport, which are prerequisites for electroluminescence, counteract each other. Indium phosphide nanoparticles (InP), which have already been studied in such an application, have the problem of low quantum yields due to their high surface-to-volume ratio and the associated trap-states. This problem can usually be solved with so-called core-shell nanoparticles, which in turn can inhibit efficient charge carrier injection.[5]

A possible solution to this dilemma can be provided by lead halide perovskites (LHP), which have recently gained significant attention in optoelectronics. In particular, perovskite nanoparticles are attractive as luminescent materials for LEDs. They offer high defect tolerance and thus quantum yields close to 100%, with narrow emission widths for perfect color brilliance. Furthermore, they can emit light in all colors within the visible spectrum.

Current external quantum efficiencies (EQE) of red and green perovskite light-emitting diodes (PeLEDs) can already compete with state-of-the-art organic LEDs and have reached a remarkable value of over 20 %.[6,7] In comparison, the efficiency of blue PeLEDs is far behind, showing values of about 12 %.[8]

1.2 Aim and outlook of this work

In this work, perovskite nanostructures are investigated and optimized for use in ELQLEDs. Since the efficiency of blue LEDs is still far behind that of green and red LEDs, a special focus is put on the fabrication of high-quality blue emitters. This cumulative thesis is structured as follows.

Chapter 2 deals with the relevant fundamentals of perovskites and their nanoparticles. First, the class of perovskites is introduced, and their atomic and optoelectronic properties are discussed. The chapter then briefly discusses nanostructures and their fabrication and ordering in superlattices (SL). It then introduces surface enhancement or modulation and its effect on the optoelectronic nature of the particles. The chapter outlines the concept of ELQLEDs and addresses the stability of nanoparticles.

Chapter 3 discusses the influence of superstructure on the optical properties of perovskite nanocrystals in the solid state. It is shown that increasing atomic misalignment between adjacent nanocrystals and increasing compressive strain near the surface of the supercrystal leads to a change in the emission properties. This change is investigated and discussed.

In Chapter 4, the native ligand shell on perovskite nanoparticles is replaced by an appropriately functionalized organic semiconductor. This new carbazole ligand, specifically designed for this purpose, and its effects on the optoelectronic properties of the nanoparticles are investigated. Finally, both native and exchanged systems are used in ELQLEDs and their effects on the devices are discussed.

Chapter 5 deals with the doping of perovskite nanoparticles with an organic lithium salt. The effects of the doping on the efficiency and stability of the LEDs are investigated and analyzed in more detail.

Perovskite nanoparticle films are known to have low resistance to external influences and low intrinsic stability. This property has a negative impact on the lifetime of LEDs. Chapter 6 is therefore dedicated to the study of native and exchanged nanoparticle films under continuous X-ray irradiation. The different effects on the degradation mechanism are demonstrated and analyzed.

2. Theoretical Background and Methodology

2.1 Physicochemical Properties of Lead Halide Perovskites

Initially, the name "Perovskite" originated from the discovery of the mineral calcium titanate by Gustav Rose in 1839 with the composition $CaTiO_3$. He named this particular mineral after a befriended russian mineralogist Lev Perovski.[9,10] By utilizing X-ray diffraction experiments for structural analysis and the subsequent discovery of several minerals with the same crystal structure, the term "perovskite" was established for an entire class of substances with the same basic crystal structure as $CaTiO_3$.

Besides metal oxide perovskites, there are also metal halide perovskites (MHP), which are generally classified by their cations. Their cations can either be organic or inorganic, in hybrid and all-inorganic perovskites, respectively. Initial research showed the outstanding properties of this material class for the usage in optoelectronic devices like solar cells or light emitting diodes (LED). Especially methylammonium lead iodide ($MAPbI_3$), which has become very popular due to its discovery as an excellent photovoltaic (PV) material in mid-2012, is a very interesting example.[11] State of the

art silicon-based solar cells reach efficiencies of ~ 26 %, after being optimized for almost 50 years.[12] $MAPbI_3$, on the other hand, achieves comparable values within a short time, with efficiencies of over 25 %.[13,14] This highlights the potential that lies within this material class upon further optimization.

In contrast to the aforementioned $MAPbI_3$, which represents organic-inorganic perovskites, caesium lead halides ($CsPbX_3$) are among the most investigated all-inorganic perovskites. In the following subsections, the structural, electronic, and optical properties of lead halide perovskites (LHP) are described in more detail.

2.1.1 Atomic Structure of Perovskites

The ideal perovskite structure can be considered a simple cubic crystal structure[15] and their general chemical formula can be expressed as ABX_3 (A = large cation, B = medium-sized cation and X = anion). A typical representative of this idealized crystal structure is $SrTiO_3$, in which the Ti^{4+} ions are coordinated octahedrally by 6 O^{2-} ions, and the Sr^{2+} ions are coordinated by 12 O^{2-} ions in the form of a cuboctahedron (**Figure 2.1**). In the cubic unit cell, where A represents the central atom, the lattice constant a can be expressed as twice the bond length of B and X (B—X).

$$2\ \mathrm{B}\text{—}\mathrm{X}\ = \mathrm{a} \tag{2.1}$$

Furthermore, twice the bond length between Atoms A and X (A—X) is equal to $\sqrt{2a}$, which is the width of the cuboctahedral cage side.

$$2\ \mathrm{A}\text{—}\mathrm{X}\ = \sqrt{2a} \tag{2.2}$$

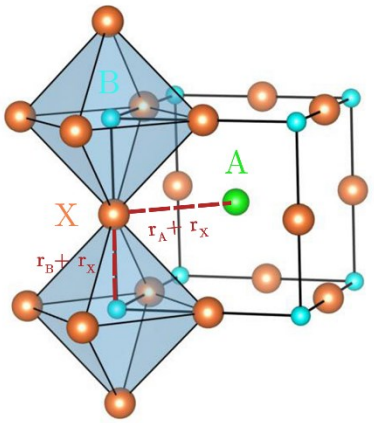

Figure 2.1: The perovskite crystal structure ABX_3 consists of cornersharing BX_6 octahedra. Therein a B-cation (cyan) is coordinated by six X-anions (orange). The void in between is occupied by an A-cation (green).

From these rather simple geometrical considerations, one can estimate the ideal structure from the ratio of the bond lengths:

$$\frac{\mathrm{A}-\mathrm{X}}{\sqrt{2}\ \mathrm{B}-\mathrm{X}} = 1 \tag{2.3}$$

This relationship was first discovered in 1926 by Victor M. Goldschmidt,[16] who introduced a tolerance factor t to predict whether the perovskite simple cubic structure would form. It was assumed that said phase will form if the value of the tolerance factor t is close to 1. When Goldschmidt discovered this, very few crystal structures existed, so they used ionic radii of the atoms involved (r_A, r_B, r_X), instead of bond lengths.

$$t = \frac{\mathrm{r_A} + \mathrm{r_X}}{\sqrt{2}\ \mathrm{r_B} + \ \mathrm{r_X}} = 1 \tag{2.4}$$

To date, almost all perovskites known have t values ranging between 0.75 and 1.00.[15] In simple terms, there are three cases that lead to a deviation from the ideal structure or to a reduction of the tolerance factor.[17] If the cations of the octahedral gap become too small, they can be displaced, which, depending on the strength and direction of the distortion, can lead to a tetragonal, trigonal, or orthorhombic structure.

On the other hand, octahedral tilts or rotations are other structural responses of the perovskite structure. They are caused by A cations that are too small for the cubocta-

hedral cage site, therefore the BX_6 octahedra twist in order to reduce cavity dimensions, allowing the structure to accommodate values of t less than 1.[17] Lastly, the BX_6 octahedra itself can be distorted, leading to an elongated or flattened octahedron. It is possible for these three modifications to occur independently or in combination. A change in temperature or pressure may modify the degree or type of distortion. This can lead to structural changes, usually resulting in orthorhombic structures at lower temperatures (*i.e.*, ambient conditions), as well as pseudocubic or cubic structures at higher temperatures and pressures.[18]

For example, bulk caesium lead bromide ($CsPbBr_3$), which occurs in a orthorhombic structure (γ, space group Pmna) at room temperature, changes as the temperature increases (**Figure 2.2**). As $CsPbBr_3$ is heated above $T_{\gamma-\beta} = 88$ °C, a tetragonal β-perovskite structure (P4/mbm) forms, and at even higher temperatures ($T_{\beta-\alpha} =$ 130 °C) the cubic (Pm-3m) α-structure is formed.[19] However, the absolute temperatures are dependent on the material morphology. Notably, upon utilizing nanoscaled perovskites (at least one spatial dimension < 100 nm) the phase transition temperatures are altered.[20]

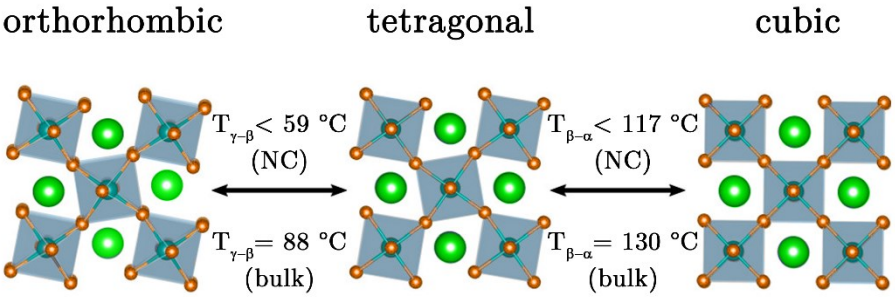

Figure 2.2: Phase transitions of $CsPbBr_3$ bulk and nanocrystals from orthorhombic to tetragonal to cubic phases at corresponding temperatures. The green spheres represent Cs atoms, while the purple polyhedra represent the octahedral perovskite cage formed by the bonding of Pb (cyan) and Br (orange) atoms. Reprinted with permission from Cottingham *et al.*.[19] Copyright 2018 American Chemical Society. Partly edited.

Therefore, when compared to bulk materials, nanomaterials often have substantially lower phase transition temperatures.[19,21–23] Experimentally, this phenomenon is important for the distinction of the crystal structure *via* diffraction methods. Due to their small size and the resulting Scherrer broadening of the Bragg peaks, it gets hard to distinguish between the orthorhombic and cubic structures. When the cubic structure is mentioned in the following to describe $CsPbX_3$ nanoparticles, it actually refers to a pseudocubic structure.[23]

But as Li *et al.* pointed out, the tolerance factor t by itself is not sufficient to distinguish the perovskite structure, since systems exist that do not exhibit the characteristic structure, even though t lies within the most favorable range (0.8 – 0.9).[24]

2.1.2 Optoelectronic Properties of Perovskites

One of the reasons for LHPs' success in optoelectronic devices, such as LEDs and photovoltaics, are their electronic structure. The band structure is mainly determined by the BX_6 octahedra, the A-side cations play a subordinate role.[25–27] The p-orbital of the halide (X) and the s-orbital of the metal cation (B) mainly contribute to the valence band maximum (VBM). The conduction band minimum (CBM), on the other hand, is mainly determined by the p-orbital of the metal cation (B) (**Figure 2.3a**).

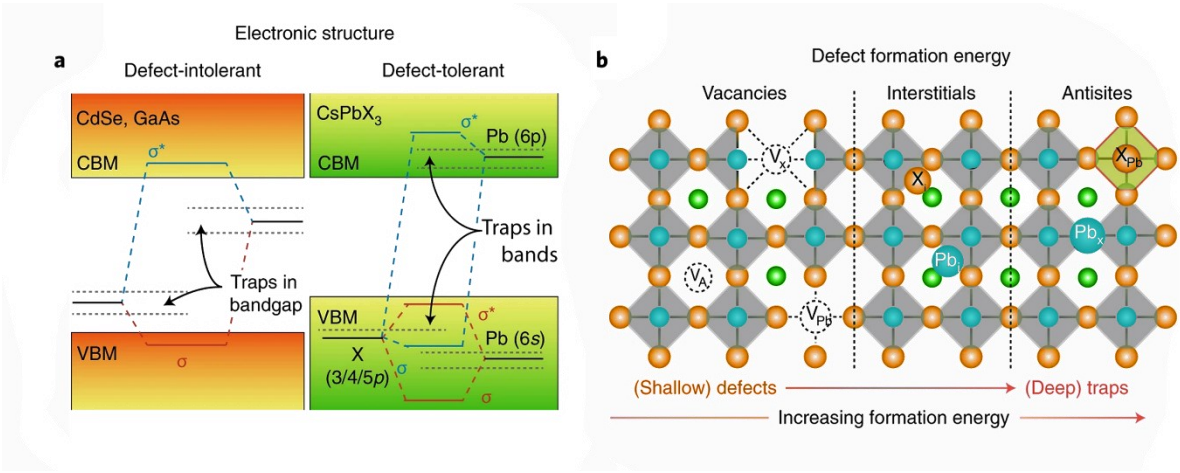

Figure 2.3: a) MO Scheme of the electronic band structure of classical (left) and LHP semiconductors (right). **b**) Typical point defects in LHPs, including vacancies, interstitial and anti-site atoms, arranged in order of increasing formation energy, and their respective depths in the bandgap. Reprinted by permission from Akkerman *et al.*: Springer Nature, Nature Materials, Genesis, challenges and opportunities for colloidal lead halide perovskite nanocrystals, Akkerman *et al.*,[28] Nature materials (2018). partly edited.

The actual electronic structure can therefore be affected by a variety of influences, for example the halide composition, lattice constant, and electronic nature of the A-site cation.[28] Firstly, by exchanging the halides, the band structure in MHPs can be altered considerably. For example, if one changes the halide composition from chloride over bromide to iodide, the bandgap (E_g) decreases gradually due to the initial electronegativity difference between the atomic orbitals.[29] Secondly, although the A-site cations have no direct influence on the band structure (**chapter 2.7.1**), they influence the band gap indirectly. When comparing lead perovskites with the same BX_6 structure but with

different cations in the A-site, significant differences in band gap can be observed. For lead iodide perovskites, a decrease in the band gap of the material with increasing size of the monovalent cations is observed in both theoretical and experimental studies.[30–33] A clear trend can be observed for cesium (Cs), methylammonium (MA) and formamidinium (FA), where the effective ionic radii increase in the order mentioned. Consequently, the band gap decreases from 1.73 eV for $CsPbI_3$ NCs to 1.48 eV for $FAPbI_3$ NCs. Changing the size affects the bandgap either by changing the lattice structure or by tilting the BX_6 octahedron.

In typical semiconductors, such as cadmium chalcogenides, the bandgap is formed between bonding (σ) and antibonding (σ^*) orbitals (MO theory). However, every crystal contains defects which result in the formation of trap states. Due to point defects or dangling bonds, weak binding (shallow) or non-bonding (deep) states within the bandgap can emerge and negatively affect the performance of optoelectronic devices. An important advantage of LHPs is that the energy location of potential defects is either in or very near the conduction or valence band (shallow traps, see **Figure 2.3a**). This feature of the electronic structure of LHPs is usually referred to as defect tolerance, as these defects have little effect on radiative recombination and other optoelectronic properties.[34–36] In perovskites, interstitial and anti-site defects, which would create deep trap states in the electronic structure, are almost absent since the ions are energetically difficult to relocate (**Figure 2.3b**). This fact becomes more important when considering nanocrystals, as the surface to volume ratio increases and therefore usually more defects are created (see **chapter 2.6**). The defect tolerance of LHPs is reflected in the large charge carrier diffusion lengths, which ranges from ~ 1 µm[37] (polycrystalline film) to over 100 µm[38] (single crystal) in $MAPbI_3$ perovskites. This high mobility of charge carriers indicates a highly effective charge carrier screening, which can be explained with a lower scattering rate between optical phonons and charge carriers. More precisely this originates in the formation of large polarons (charge carrier –

phonon quasiparticle), which have a reduced scattering rate compared to isolated charge carriers or small polarons.[39] Another outstanding feature of LHPs for use in optoelectronic devices is their exceptionally large absorption coefficient. LHPs have an even higher band edge absorption than conventional direct band gap materials such as GaAs, mainly due to the band edge degeneracy of the conduction band and the comparatively low effective mass of the holes (flat valence band).[40,41]

From the phenomena explained above, one can already see that LHPs offer a wide range of options for modification in order to improve their performance. Even more so upon utilizing nanomaterials, which offer the ideal basis for extending and improving these technologies. Therefore, the following chapters will primarily focus on the special properties of perovskite nanoparticles.

2.2 Nanoparticle Synthesis

Generally, the term nanoparticle refers to a composite of a few to several thousand atoms or molecules with a size typically in the range of 1 to 100 nanometers.[42] Due to their size and the associated larger surface area-to-volume ratio, nanoparticles differ significantly in their physical and chemical properties compared to their respective bulk materials. The increasing interest in these materials in industry and research during recent decades has led to outstanding developments in the fabrication of nanomaterials, especially in terms of size, shape, and functionalization.[43] The first logical step is the synthesis of such materials, which is drastically different from their bulk counterparts. The synthesis of nanoparticles can be roughly divided into two main approaches, as shown in **Figure 2.4**, namely the "top-down" and "bottom-up" methods. The first refers to the more physical approach of starting from bulk materials and gradually decreasing the size until the desired particle is created, *e.g.*, the Scotch-tape method, or mechanical processes like milling and etching.[44] A major limitation of this method is the

imperfections of the surface structure and size, which leads to application-limiting defects.[45]

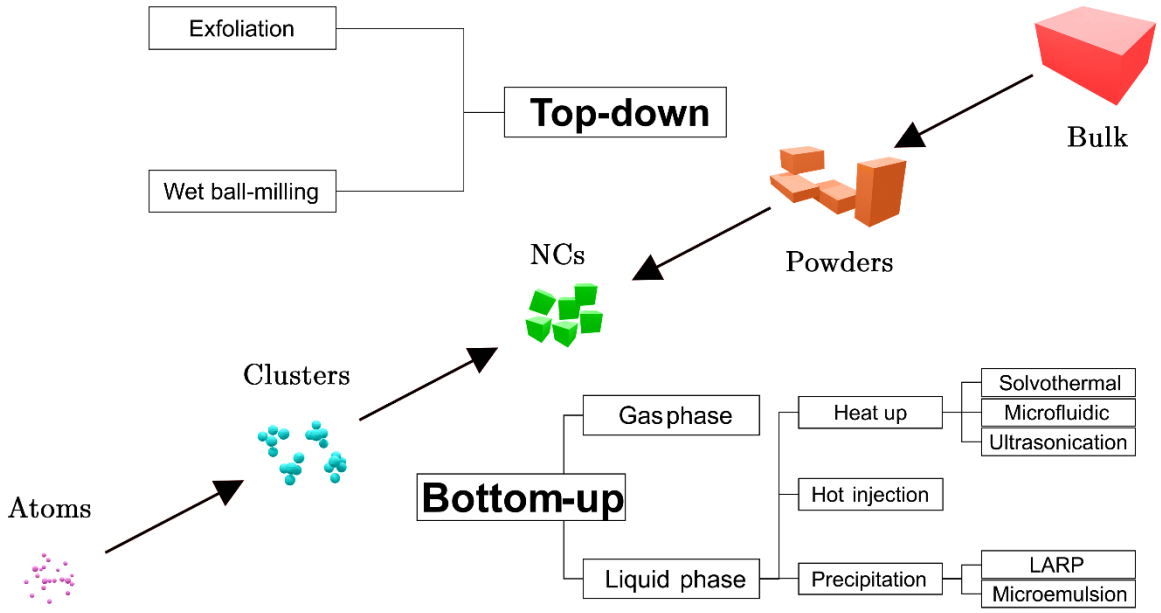

Figure 2.4: Schematic representation of a bottom-up and top-down nanoparticle synthesis from atomic precursors (purple) via clusters (cyan) and from bulk (red) via powder (orange) to nanoparticles (green), respectively. Overview of various nanoparticle fabrication techniques, specifically for the synthesis of LHP nanocrystals.

In contrast, during a "bottom-up" method, nanoparticles are synthesized mostly through wet synthesis from molecular precursors. Wet chemical methods, such as microemulsions, sol–gel, hot-solution decomposition, sonic waves, microwaves, and electrochemistry, rely heavily on three parameters: precursors, organic surfactants, and solvents. An effective method for synthesizing monodisperse high quality nanoparticles is the hot-injection method, pioneered by Bawendi[46] and Alivisatos[47] *et al.* These papers describe the chemical synthesis of semiconductor nanocrystals made from cadmium chalcogenides using organometallic Cd and Se precursors in a coordinating solvent at high temperatures. The underlying physical processes responsible for the formation of nanoparticles in the hot-injection method, namely nucleation and growth, are described in more detail in the next sections.

2.2.1 General Model

In 1950, LaMer and Dinegar[48] developed the first quantitative theory for the nucleation and growth of colloidally stable nanoparticles. Known as “LaMer growth”, the LaMer–Dinegar theory is a three-stage model of particle growth based on classical nucleation theory (CNT).[47,48] The concept has been proven useful for the synthesis of many colloidal materials, including semiconductor nanoparticle quantum dots. A core success of the LaMer model is describing conditions to control polydispersity. Particle growth is described as three distinct steps: (I) building up of active monomer, (II) supersaturation and nucleation, and (III) diffusion-limited growth (

Figure 2.5).

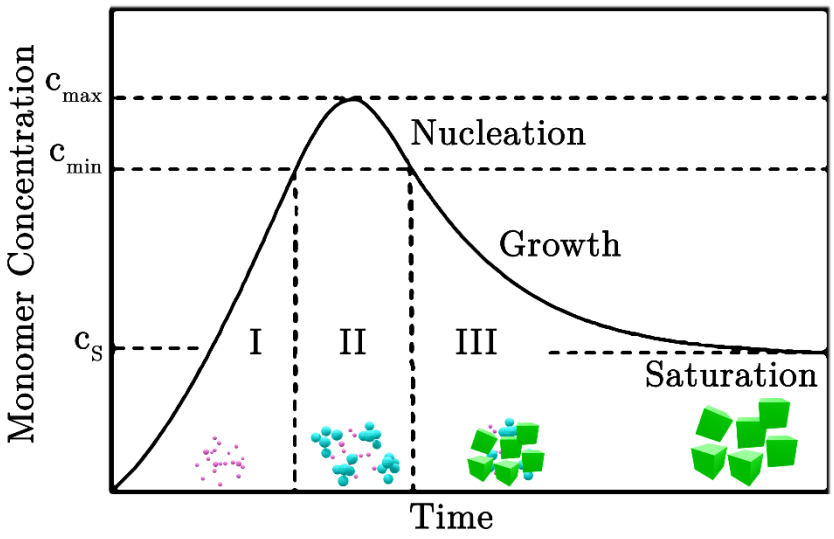

Figure 2.5: Schematic representation of the monomer concentration during the nucleation and growth of Nanoparticles from the solution in a classical LaMer mechanism.

Stage I involves the buildup of active precursors and monomers due to the nucleation-associated free energy barrier. Although the bulk solid phase may have a lower free energy than the solution-phase precursor, the interfacial free energy is usually larger.[49] Because of this, small nuclei with a high surface area to volume ratio are thermodynamically unfavorable and statistically likely to dissociate. Growth on the respective

critical nucleus becomes thermodynamically favorable at sufficiently high concentrations, which is referred to as critical supersaturation. This is equivalent to an increase in solution chemical potential, which defines stage II. During the final stage III, the particles grow until an equilibrium between the adsorption of monomers on their surface and the monomer in solution is reached.

Therefore, control of the nucleation and growth phases is crucial in order to influence size, morphology, and monodispersity. Monodisperse nanoparticles can be obtained by keeping the nucleation phase as short as possible. Once sufficiently rapid nucleation has occurred, monomer concentration drops dramatically, making nucleation during subsequent stages unfavorable.

2.2.2 Perovskite Synthesis

The ideal case of synthetic routes is to produce phase pure, purifiable, monodisperse nanocrystals with a good yield. Through the appropriate changes of synthetic parameters, for example, temperature and precursor concentration, their size, shape, and composition should be adjustable systematically.

As with classical nanoparticle synthesis, there are several ways to synthesize perovskite nanoparticles. The most common methods are the ligand-assisted reprecipitation (LARP) method, often used for $MAPbI_3$ nanoparticles,[50] and the hot-injection (HI) method. An extension of the HI approach for the colloidal synthesis of caesium LHP NCs was carried out in 2015 by Protesescu *et al.*[29] This synthesis can be described as an arrested co-precipitation of ions in apolar media in the presence of long-chain capping ligands.[51] Cs-oleate was injected into a hot solution of PbX_2 salts, which served as Pb^{2+} and X^- sources dissolved in octadecene (ODE), carboxylic acids, and primary amines to obtain $CsPbX_3$ NCs. Perovskites with mixed halides could also be readily synthesized by simply adjusting the ratio of the lead halide salts used as precursors. By

tuning the NC size or varying the halide composition, the PL emission could be modulated over the entire visible spectrum (410–700 nm).

Compared to classical II – VI semiconductor nanoparticles, the study of the formation mechanism of perovskite nanoparticles is challenging due to their rapid nucleation and growth, which occur in less than 5 seconds.[52] Therefore, multiple groups have studied the formation of $CsPbX_3$ using various methods to optimize and monitor the reaction in real-time. De Mello and Kovalenko[52] employed a microfluidic synthesis, while Li *et al.* developed a slowed-down microwave-assisted synthesis to gain insights into the fast formation mechanism.[53] Their TEM study showed that the filling of the lead halide octahedra $[PbX_6]^{4-}$ with caesium ions is the rate-limiting step in the growth kinetics. Considering the elements responsible for the formation of the perovskite structure individually, one would expect that the formation of the strongest bond, the lead-halide bond, determines the rate limiting step of both nucleation and growth. Since lead halogen salts are typically used as precursors for the synthesis, the $[PbX_6]^{4-}$ octahedra are already formed before the caesium precursor is injected. Therefore, Sun *et al.* advanced the idea by employing individual halide, lead, and caesium precursors instead of using a conventional PbX_2 source.[54] Their results indicated that the halide precursor determines the nucleation process.

The reaction rate for the formation of nuclei according to the LaMer theory, can be written in the Arrhenius form (**Equation (2.5)**), where A is the pre-exponential factor, γ is the surface energy, V_M is its molar volume, T is the temperature, k_B is Boltzmann's constant, N_A is the Avogadro constant and S is the supersaturation of the solution.[55]

$$\frac{dN}{dt} = A \cdot \exp\left(-\frac{16\pi\gamma^3 V_M^2}{k_B^3 T^3 N_A^2 \ln S^{\ 2}} \right) \tag{2.5}$$

In **Equation (2.5)**, there are three parameters, γ, T, and S, that can be experimentally controlled. The surface energy γ is largely influenced by the type and amount of

ligands at the particle surface. The temperature and supersaturation can be directly manipulated by altering the injection temperature or adjusting the concentration of the precursors, respectively. For instance, Sun *et al.* demonstrated that increasing the ratio of halide precursors leads to the formation of smaller NCs. It was assumed that a higher concentration of halide precursor would result in a greater number of $[PbX_6]^{4-}$ octahedra, or nuclei, which would consume both Pb and Cs monomers during the nucleation process. This would result in a shortage of Pb and Cs monomers, hindering the continued growth of the nuclei and leading to smaller NCs.

Besides variation in size and monodispersity of LHP NCs, different compositions and morphologies can also result from changing the synthesis parameters.[56–59] Thus, high concentrations of caesium and halide precursors allows for the formation of low-dimensional (0D) perovskite-related structures, such as Cs_4PbX_6. The term "low dimensionality" refers to the arrangement of the lead halide octahedra. In particular, in the structure of Cs_4PbX_6, the $[PbX_6]^{4-}$ octahedra are completely isolated from each other.

Variations of the concentration and/or chain length of oleic acid (OA) and oleylamin (OLA) in combination with reaction temperature have direct influence of the shape and morphology of the resulting NCs (**Figure 2.6**). Generally, the application of OLA and OA at low temperatures (between 90 – 130 °C) results in the growth of NCs in an anisotropic manner, resulting in quasi-2D structures commonly known as "nanoplatelets" (NPLs). Conversely, high reaction temperatures (170 – 200 °C) and extended reaction times result in the formation of nanowires.[60]

2.3 Self-Assembly into Superlattices

When using colloidal nanoparticles for optoelectronic applications, it becomes more important to consider that it is not the individual nanoparticle but their macroscopic arrangements that will be crucial for efficient devices.[61] Nanocrystals or nanoclusters

can serve as so-called building blocks, which in turn can serve as starting materials for a bottom-up construction to create larger, more complex ensembles. The spontaneous arrangement of these individual building blocks into highly ordered structures is called "self-assembly".[62] The Self-assembly process is driven by the desire to minimize the Gibbs free energy ΔG, and a negative difference between the initial (colloidal solution) and assembled states ($\Delta G < 0$) is necessary for an ordered assembly. This can be achieved through a decrease in enthalpy ΔH, an increase in entropy ΔS, or a combination of both while maintaining a constant temperature (T).[62]

$$\Delta G = \Delta H - T\Delta S \tag{2.6}$$

In this case, the contribution of ΔH is equivalent to interparticle interactions, such as van der Waals forces, steric repulsions, and capillary forces. This contribution is usually small for semiconductor nanoparticles and is on the order of magnitude of the thermal energy $k_B T$.[63] In classical thermodynamics, entropy can be seen as a measure of disorder. The fact that an increase in order leads to an increase in entropy is, in a sense, a contradiction in terms. However, this seemingly paradoxical concept was explained by studying the free volume of colloidal units in both a disordered dense dispersion and an ordered superlattice.[64,65] As a result of more efficient packing in the ordered state, each particle has more space to move around compared to concentrated colloidal solutions, leading to an increase in the total number of possible configurations and resulting in $\Delta S > 0$. In addition, it is important to consider that the particles in a solution are surrounded by numerous solvent molecules. These solvent molecules, in turn, exhibit considerable freedom of movement and disorder after the process of self-assembly.

If the arrangement consists of a regular crystal-like arrangement of the NCs in the respective dimensions, it is called a superlattice (SL). As early as 1995, Murray *et al.* demonstrated that CdSe nanoparticles can be used as building blocks to form three-

dimensional (3D) superlattices.[66] With their discovery and further research, the interest in such structures increased and a separate research topic developed.

Lead halide perovskites (LHP) are different from traditional chalcogenide NCs because of unique features like highly dynamic surface ligands,[67] fast anion exchange,[68] and easy ion migration.[69] This poses challenges for forming SLs, whether they are 1D superlattice chains,[70] 2D layered superlattices,[71] or 3D superlattices, as the unstable equilibrium of surface ligands can cause them to merge into large bulky crystals.

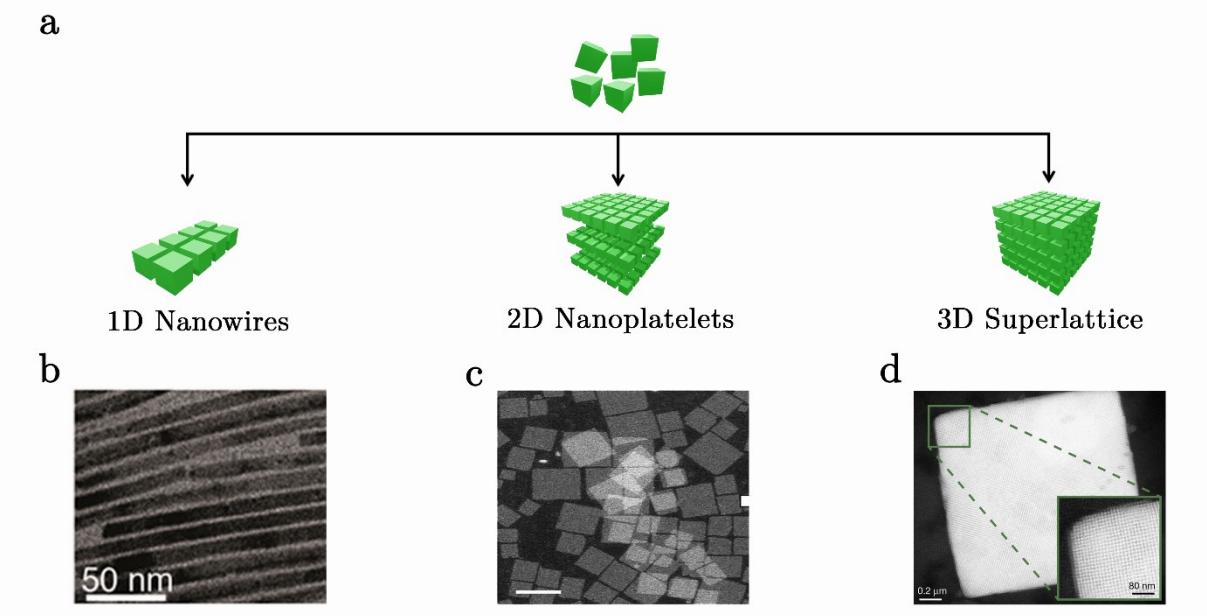

Figure 2.6: a) schematic representation of the self-assembly of monodispersed NCs into different Superlattices. TEM or STEM micrographs of $CsPbBr_3$ NCs assembled into 1D Superlattices (**b**), reprinted with permission from Zhang *et al.*[72] Copyright 2016 American Chemical Society. 2D Superlattices (**c**) reproduced from ref.[73] with permission from Nature Publishing Group (2020). 3D Superlattices (**d**), reprinted by permission from Rainò *et al.*: Springer Nature, Nature Superfluorescence from lead halide perovskite quantum dot superlattices, Rainò *et al.*,[74] Nature (2018). Partly edited.

The self-assembly of NCs is typically induced by either evaporating the solvent or by altering the polarity of the reaction system to destabilize the NC capping ligands.[75] The most commonly used method for producing metal-halide perovskite superlattices is the evaporation technique. The usual procedure, as depicted in **Figure 2.7**, involves spreading multiple droplets of purified nanocrystals in a nonpolar solvent on a sub-

strate, followed by a slow evaporation process. Multiple factors, such as concentration, solvent, and substrate, influence the quality and size of the resulting SLs. High monodispersity and shape uniformity are essential for long-range ordering in the resulting superlattices. This can be achieved by using a starting colloid of LHP-NCs with a standard deviation of size of less than 10 %.[51]

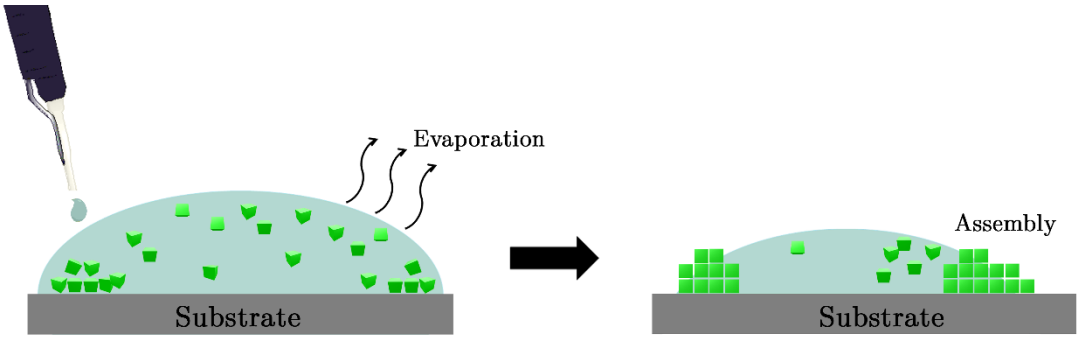

Figure 2.7: Schematic illustration of evaporation-based self-assembly of perovskite nanocrystals into superlattices.

This chapter contributes to a better understanding of chapter 3.

2.4 Ligand Exchange

Nanomaterials have a distinctive characteristic of possessing a large surface-to-volume ratio, which means that their surfaces have a significant impact on numerous physical and chemical processes. It is therefore not surprising that molecules that bind to the surface of nanoparticles – so-called surface ligands – play a decisive role in their synthesis, optoelectronic properties, processability, and application.

The binding of ligands to the surface of NCs is determined by both the type of ligand and the NC surface, with three main categories of ligand binding: L-type, Z-type, and X-type.[76] These interactions can be explained by the classification of covalent bonds, which was originally proposed for metal coordination complexes and later adapted to NCs by Owen and colleagues to describe the interaction between the NC core and the

head group of the ligand.[77,78] The classification of ligands is based on their neutral form, where the L-type ligands (2-electron donors) are known as Lewis bases, X-type ligands (1-electron donors) are referred to as radicals (or ionic species), and Z-type ligands (0-electron donors) are designated as Lewis acids(**Figure 2.8**).[79] Thus, this classification is based solely on the binding type at the surface. For instance, the binding of two carboxylate ligands ($RCOO^-$) to a metal ion (such as Pb) could be described as two X-type ligands or one Z-type ligand. However, if it is demonstrated that $Pb(OOCR)_2$ dissociates from the nanoparticle surface, the ligand classification could be more accurately determined, and it would be considered a Z-type ligand in this scenario.[77]

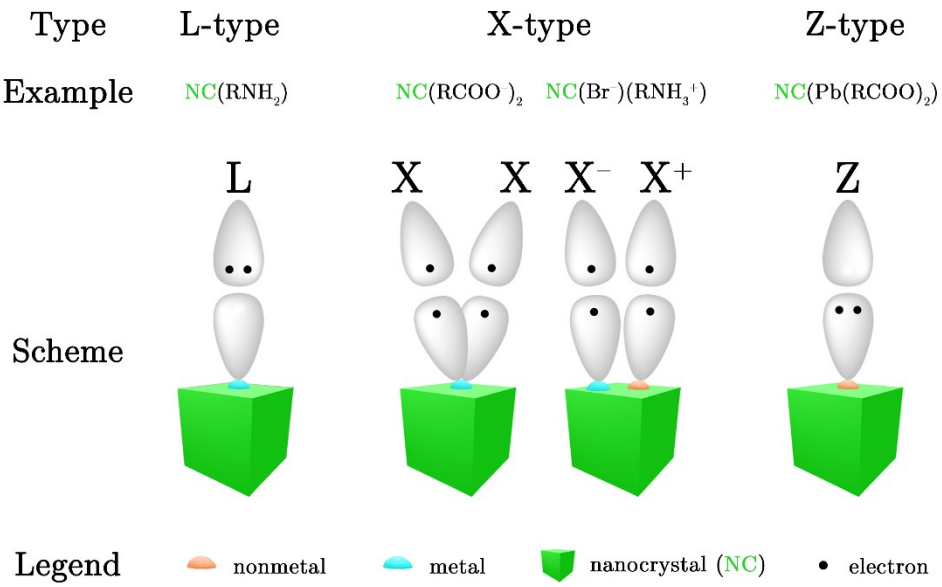

Figure 2.8: Schematic illustration of L, X, and Z-type ligands binding to the surface of NCs with typical ligands categorized according to the functional group and covalent bond classification.

In the case of the perovskite nanoparticles, the binding situation of the native ligands on the surface of the NC has not yet been fully clarified, so the following binding possibilities arise as shown in **Figure 2.9a**.

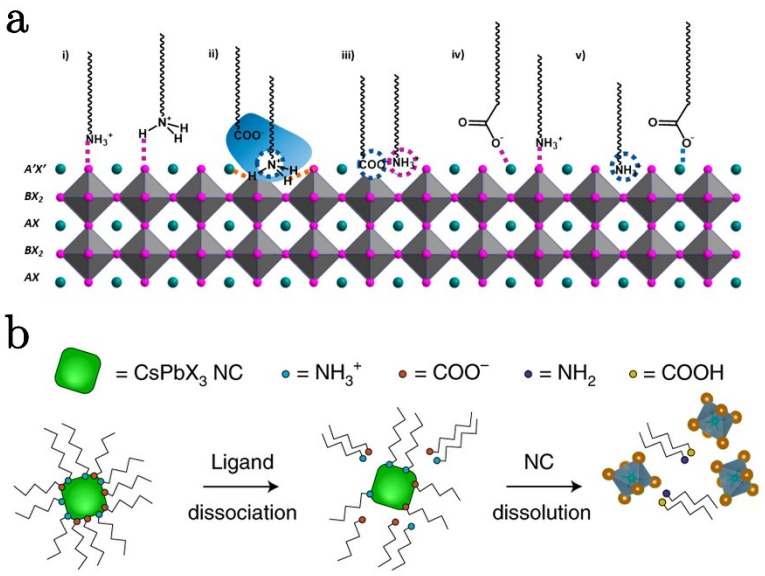

Figure 2.9: a) Schematic illustration of the different binding modes of oleylamine and oleic acid to a LHP NC surface, reprinted with permission from Fiuza-Maneiro[80] Copyright 2023 American Chemical Society. Partly edited. **b)** Schematic illustration of the structural lability of LHP NCs due to the desorption of weakly bound ligands. Reprinted by permission from Akkerman *et al.*: Springer Nature, Nature Materials, Genesis, challenges and opportunities for colloidal lead halide perovskite nanocrystals, Akkerman *et al.*,[28] Nature materials (2018). partly edited.

The understanding of how ligands bind to the surface of nanoparticles is crucial as these ligands play multiple roles throughout the lifespan of the nanoparticle. Starting with the formation of the nanoparticles, particularly in the synthesis of perovskite nanoparticles as discussed in **chapter 2.2.2**, ligands can significantly affect the structural, stability, and optoelectronic properties.[60,81,82] It is important, for example, that the binding of ligands to surface atoms cannot surpass the inter-atomic binding strength, as it would impede the processes of nucleation and growth. Consequently, the use of ligands containing sulfur-centered functional groups, such as thiols, is often precluded due to their strong binding affinity towards metal atoms. Moreover, the ligands function to stabilize the as-synthesized nanoparticles as stable colloidal solutions, primarily by using their long steric alkyl residues to repel adjacent nanoparticles and avoid agglomeration. This is, unfortunately, where the main problem lies with the required lig-

ands for the synthesis, oleic acid and oleylamine, as they form a dynamic equilibrium at the surface of the LHP NCs.[67,83,84]

One of the most significant outcomes of loose ligand binding is the challenge of isolating and purifying NCs through conventional methods, such as repeated precipitation using anti-solvents followed by redispersion in a pure solvent. Frequently, this procedure leads to either the dissolution of LHP NCs into their initial components or the promotion of their aggregation (**Figure 2.9b**), as the native ligand shell is removed within the washing steps.

One of the final stages in the life cycle of a nanoparticle, beyond its synthesis and storage, is its final application in end-use devices. As a result, distinct ligand systems are necessary for various applications. The control of charge injection into and transport between nanocrystals is pivotal for successful optoelectronic device applications, such as LEDs (c**hapter 2.8**). Therefore, it is essential to replace the existing ligand system with a more optimized one, which is described in **chapter 2.5**.

2.5 Ligand Synthesis

As previously discussed in **chapter 2.4**, the optoelectronic properties of nanoparticles are greatly influenced by the choice of ligands. Hence, the selection of ligands can be customized for specific applications such as facilitating aqueous dispersion,[85] or adding complementary optoelectronic functionality.[80,86,87]

Replacing ligands on the surface of nanoparticles can generally be achieved by either utilizing alternative ligands during the initial formation of the nanoparticle or by substituting the ligands post-synthetically (**Figure 2.10a**). Although the former approach has some benefits, it also has a significant disadvantage. When new ligands are introduced during synthesis, they may not only bring about the desired changes but also interfere with the nucleation and growth phase of the nanoparticles. Consequently, this

may result in alterations to the morphology, size, and overall reaction profile.[88–92] In turn, this often requires a considerable synthetic effort to achieve the same level of synthetic control as an already established pathway. Consequently, post-synthetic exchange of surface ligands typically proves to be a simpler and more effective way to alter the desired properties of the particles.

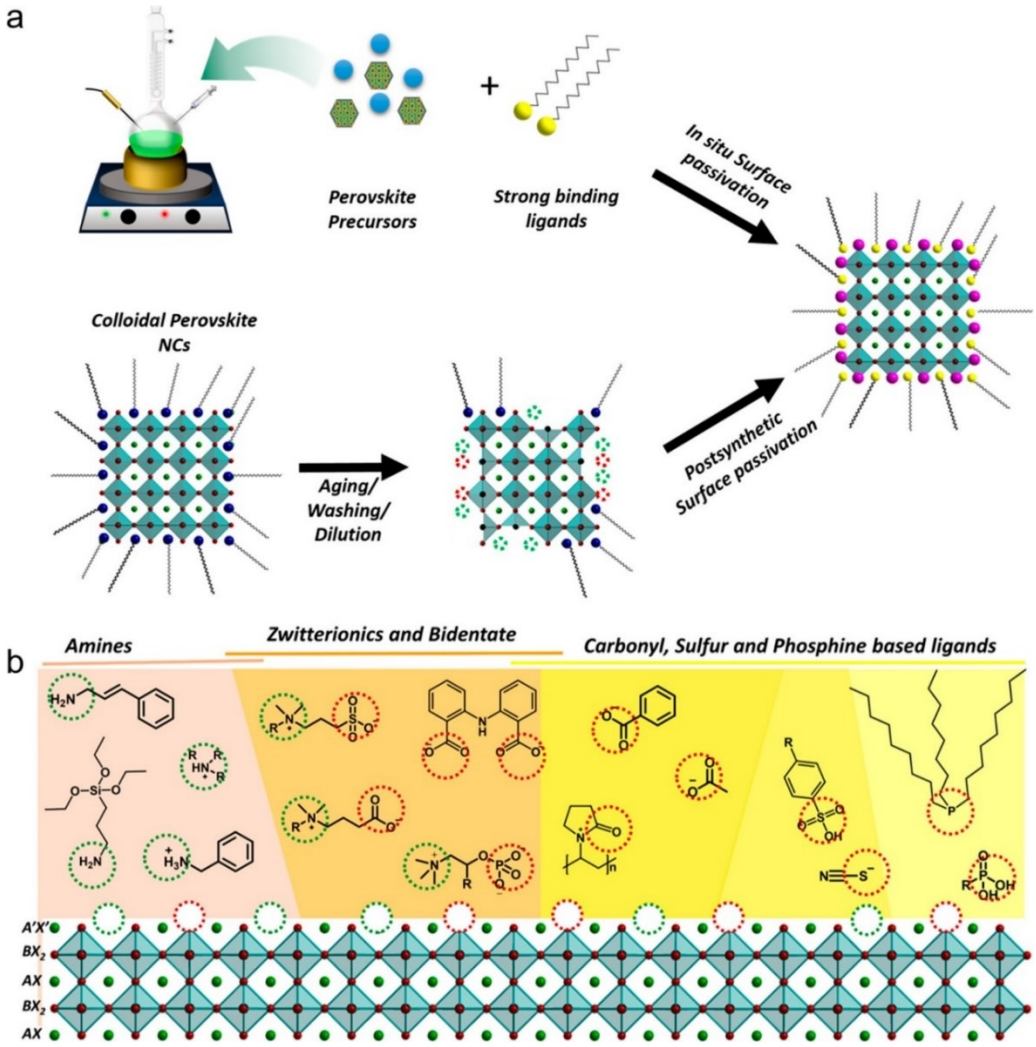

Figure 2.10: a) Schematic illustration of the synthesis of trap-free LHP-NCs by either in situ passivation or postsynthetic surface passivation with strong binding ligands. b) Summary of ligands used for surface passivation, where binding occurs either at A-cation sites or halide vacancies. The functional groups of the ligands are categorized based on their binding site and are represented by green or red dotted circles. In this diagram, different entities are labeled with different colors for easy identification. The A-cations, A-cation vacancies, halides, halide vacancies, and lead atoms are highlighted with solid green, dotted green, solid red, dotted red, and black, respectively. Reprinted with permission from Fiuza-Maneiro[80] Copyright 2023 American Chemical Society.

The replacement of ligands on NCs can typically be initiated through differences in binding energy, mass action, or surface reactions.[93] Ligand exchange is commonly driven by the difference in binding energy between the native and new ligands. To enable the exchange process, the cleaned solution of nanocrystals (NCs) is typically mixed with the new ligand and stirred until complete exchange occurs.[86] After the exchange process, the nanoparticles are precipitated with an antisolvent to remove impurities and then carefully resuspended in a solvent that is free of impurities. This ensures that the nanoparticles are purified and ready for further use in end devices.

The functional groups of the ligands that bind to the NC surface, as depicted in **Figure** 2.10**b**, can be used as a basis for their classification. Up to now a wide range of ligands, e.g. ammonium salts,[94,95] carboxylates,[96] phosphonates[97] and sulfonates[81] have been tested to improve the stability of perovskite nanocrystals, by removing the native ligands for ligands with a stronger binding motif. The most promising approach is to use zwitterionic or bidentate ligands as shown by Krieg *et al.*[98] Zwitterionic systems, such as the naturally occurring lecithin, bind to the surface of the NC in a bidentate manner, resulting in a kinetic stabilization through the chelating effect that cannot be achieved by monodentate systems.[87] Unfortunately, most naturally occurring or commercially available phosphatidylcholines, such as soy lecithin, contain long insulating alkyl groups as their tails. While these alkyl groups provide stability to particle solutions through steric repulsion, they also hinder charge carrier injection in optoelectronic devices.[99] The ideal ligand for perovskite NCs should have strong binding affinity with the nanocrystal surface and provide sufficient repulsion to avoid agglomeration. In addition, the ligand should have suitable energy levels to enable efficient charge transport in devices. To fulfill these requirements, Yamaguchi esterification offers a straightforward method for producing the desired ligand. This chemical reaction involves the reaction of a carboxylic acid or carboxylic acid anhydride with an alcohol in the presence

of a catalyst, resulting in the formation of an ester composed of the alcohol and the carboxylic acid derivative.

In this context, L-α-glycerophosphorylcholine (GPC) can be used as an alcohol component in the reaction to provide a cost-effective way of preparing a zwitterionic bidentate ligand, which is readily available. As for the acid component, an organic semiconductor specialized for the respective application of the NCs in optoelectronic devices can be used.

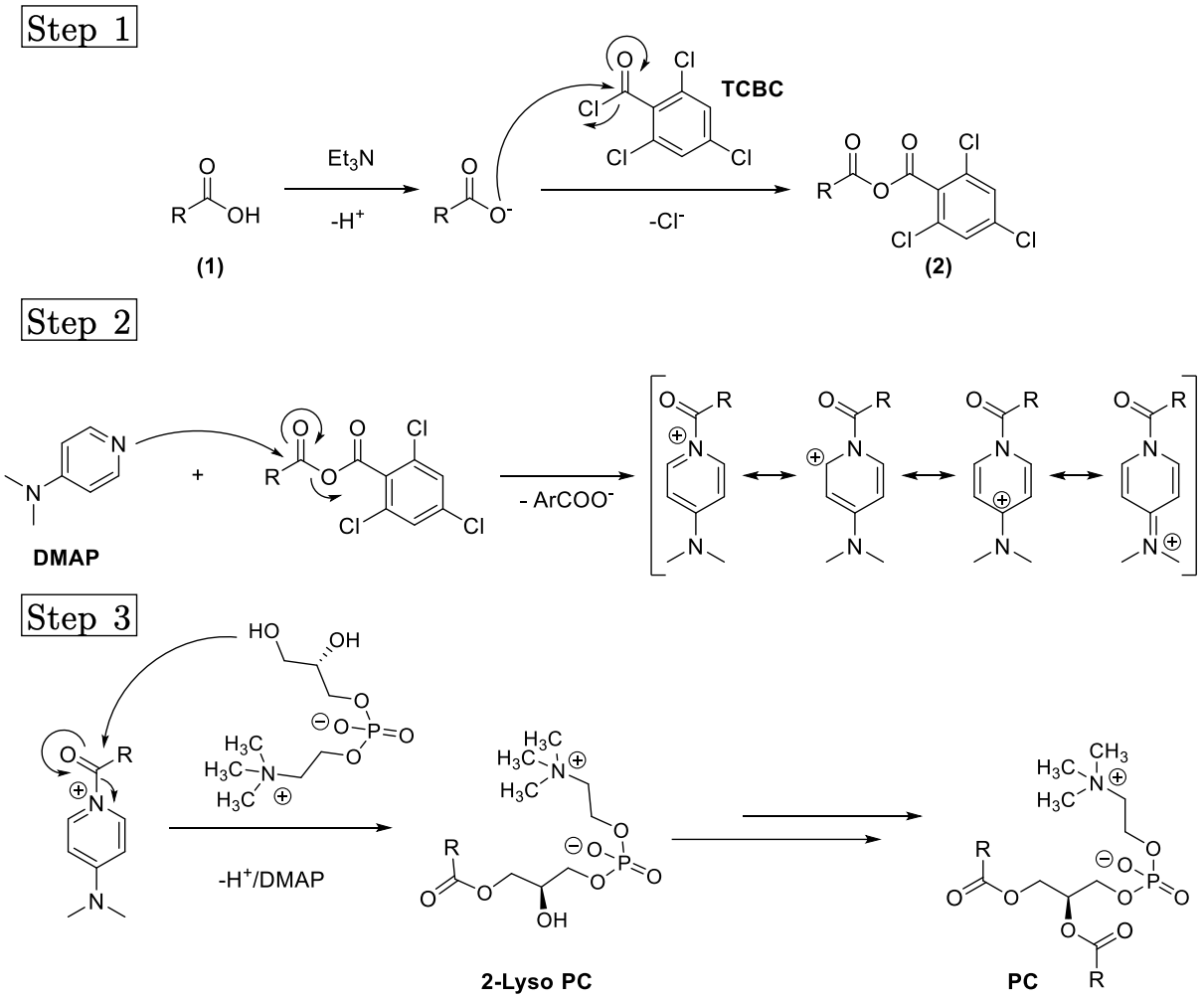

Figure 2.11: Detailed illustration of the Yamaguchi esterification process using 2,4,6-trichlorobenzoyl chloride (TCBC) and 4-(dimethylamino)pyridine (DMAP) for the synthesis of phosphorylcholine (PC) from a carboxylic acid (1) and sn-glycero-3-phosphocholine (GPC).

The first step in this reaction involves the activation of the carboxylic acid **(1)** by reaction with a coupling reagent such as 2,4,6-Trichlorbenzoylchlorid (TCBC) to form

a mixed anhydride **(2)** (**Figure 2.11**). Then, 4-(dimethylamino)pyridine (DMAP) acts as an acetyl transfer reagent and reacts with the sterically unhindered carboxyl group. This results in the formation of a less hindered intermediate, in which the acyl group is polarized and DMAP serves as a good leaving group, enabling a rapid reaction with the alcohol. If the alcohol is used as the stoichiometric limiting factor, the main product is diacetylated phosphorylcholine. However, this method is not very effective for the preparation of lysophosphocholines (lyso PCs) or mixed fatty acid PCs,[100,101] and alternative approaches should be considered. One possible alternative is sn-1 tritylation of GPC, which can provide access to mixed fatty acid PCs.[102,103]

The issue of ligand synthesis of perovskite NCs is particularly relevant to Chapter 4.

2.6 Optical Properties of LHP Nanocrystals

Distinct behaviors from their bulk counterparts occur when physical properties reach critical dimensions in the nanoscale regime. The following section discusses the nano-effects observed in caesium lead halide perovskite nanocrystals. Lead halide perovskite nanocrystals exhibit similar phases and phase transitions (**chapter 2.1**) as their solid counterparts. Although the temperatures of the phase transitions are usually lower, the phases do not change at room temperature. The energetic structure is also retained to a large extent, with the exception of the effects of quantum confinement.

In nanometer-sized semiconductor particles, a gradual transition from bulk to molecule takes place as the particle size decreases. Energy bands thereby become discrete, quantized energy levels as shown in **Figure 2.12**. NCs have both bulk density of states (DOS) with quasi-continuous (VB and CB) molecular orbitals (MOs) and single-molecule DOS with well-defined individual states at the band edges. A decrease in the NC size results in an increase in the band gap and an discretization of energy levels

near the band edges[104] The effect associated with the increase in band gap is called the "quantum confinement effect".

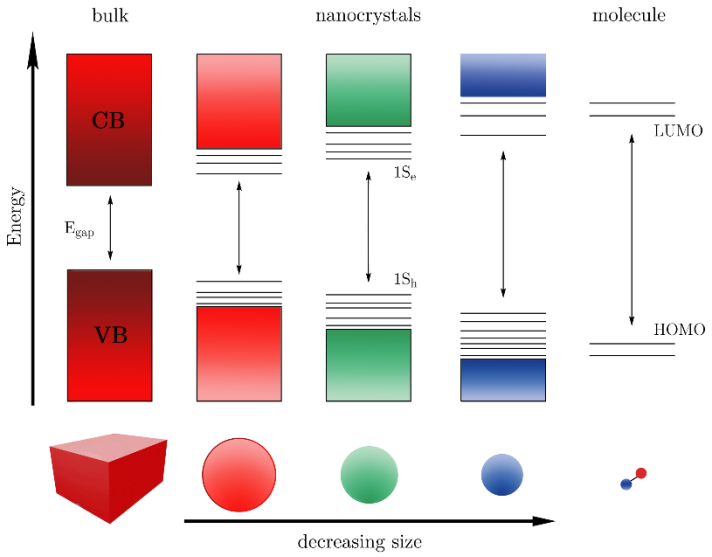

Figure 2.12: Schematic illustration of the quantum confinement effect in nanocrystals. As the size of the nanocrystal decreases, the band gap increases and discrete energy levels appear at the band edges. $1S_e$ and $1S_h$ correspond to the conduction band (CB) and valence band (VB) edges, respectively.

A more physical approach to understanding the quantum confinement effect is to consider the electron-hole pair that results from the excitation of an electron from the ground state to an excited state. Due to the Coulomb interaction, an excited electron in the CB can be bound to the corresponding hole in the VB, if the energy associated with the Coulomb interaction is larger than k_BT. This electron-hole pair, called an exciton, occupies a defined "space". This volume, or more simplified its radius, can be described by the exciton Bohr radius (a_0), as shown in **Equation (2.7)**.

$$a_0 = \frac{\hbar^2 \varepsilon}{e^2} \left(\frac{1}{m_e^*} + \frac{1}{m_h^*} \right) \tag{2.7}$$

The exciton´s whole radius depends on the effective masses of the electron and the hole. These in turn depend on the material in which they are located. For $CsPbCl_3$, $CsPbBr_3$, and $CsPbI_3$, exciton Bohr radii of 5, 7, and 12 nm, respectively, have been

determined.[29] If the semiconductor is significantly larger than a_0, the electron and hole can move freely around the equilibrium distance a_0. If the semiconductor is about as large as a_0, the charge carriers can no longer move freely around the equilibrium distance a_0 and are therefore spatially confined. If the size of the NC continues to decrease until it is smaller than a_0, the exciton is not only confined, but its energy also increases because the equilibrium distance cannot be obtained, similar to how the energy of a particle in a box increases as the "box" gets smaller. The band gap of a spherical NC E_{NC} can be described by the Brus equation:[105]

$$E_{NC} = E_{Gap} + \frac{h^2}{8r^2}\left(\frac{1}{m_e^*} + \frac{1}{m_h^*}\right) - \frac{1.8\ e^2}{4\pi\varepsilon_r\varepsilon_0 r} \tag{2.8}$$

As elucidated by Brus *et al.*, the energy gap of a NC can be predicted by taking the bulk gap E_{Gap} and reducing it by the excitons binding energy (third term on the right side) and adding the confinement energy arising from a particle-in-a-box consideration (second term on the right side). As the Bohr radius depends on the semiconductor composition, as shown in **Equation (2.8)**, the extent of quantum confinement depends on the composition. For example, 10 nm lead sulfide nanoparticles with a Bohr radius of 18 nm exhibit strong quantum confinement, while $CsPbBr_3$ with a size of 10 nm and a Bohr radius of 7 nm only experience weak confinement and thus will have similar optical properties to its bulk equivalent.

Previous discussion of quantum confinement effects has focused on nanoparticles whose three dimensions are all confined. In fact, it is possible to synthesize nanoparticles of different sizes and shapes (**chapter 2.5**). In general, nanoparticles with different shapes can be classified according to their dimensionality.

In further detail, three-dimensional (3D) nanoparticles, in which none of the dimensions are quantum confined, have properties similar to their bulk counterparts, while a two-dimensional (2D) nanoparticle is defined as a nanoplatelet or quantum well if it exhibits quantum confinement in only one dimension. Other examples are nanowires or

quantum wires, which are one-dimensional (1D) nanoparticles with two dimensions that exhibit quantum confinement. Zero-dimensional (0D) nanoparticles, so-called quantum dots, exhibit quantum confinement in all three dimensions.

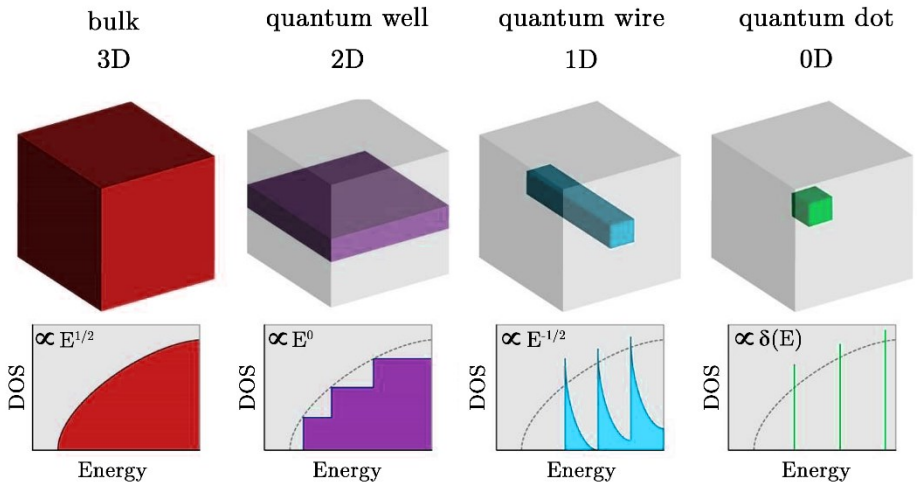

Figure 2.13: Schematic representation of structure and density of states (DOS) of bulk semiconductors (3D) and semiconductor nanostructures (2D–0D) with reduced dimensionality.

These changes in dimensionality strongly affect the DOS, which is the number of energy states available to electrons in a material per volume in k-space (**Figure 2.13**). Bulk semiconductors have a square root dependence on energy, while 2D quantum wells have a stepwise DOS with a constant dependence, and quantum wires have an inverse square energy dependence. Quantum dots exhibit a DOS where states are allowed only at discrete energy levels.

This section, which discusses the optoelectronic properties of perovskite NCs, will enhance the understanding of chapters 3, 4, and 5.

2.6.1 Recombination of Excitons and their PLQY

Electron-hole pairs can be created in semiconductor materials by irradiation with light. The prerequisite for this is a sufficiently large energy of the incident photons to

lift electrons from the valence band to the conduction band (**Figure 2.14a**). The minimum energy required for this is the band gap E_{Gap} of the semiconductor crystal. After excitation, the electron and hole each undergo a cascade of inelastic scattering processes, e.g. by phonons or crystal defects, whereby they release their kinetic energy. On a time scale of typically a few nanosseconds up to 400 ns for perovskites,[106] a bound state (exciton) can now form due to the attractive Coulomb interaction between electron and hole. In semiconductors, so-called Mott-Wannier excitons occur predominantly, which have Bohr radii of typically $a_0 \sim 10$ nm due to the comparatively weak bonding between electron and hole and thus span several unit cells of the crystal lattice.[107,108] This contrasts with the limiting case of strongly bound excitons, so-called Frenkel excitons.[109] Frenkel excitons are essentially to be considered as an excited state of an atom at which they are localized. Excitons in LHP are weakly bound and there is agreement that they are Wannier-Mott type excitons.[110,111]

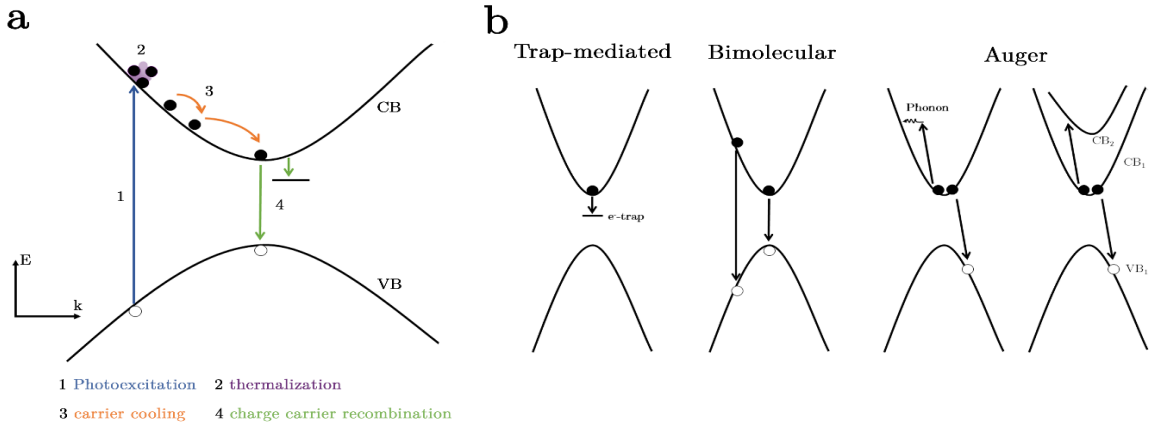

Figure 2.14: a) Schematic illustration of relaxation dynamics of charge carriers after photoexcitation. b) Trap-mediated recombination is a monomolecular process. It involves the capture of either an electron (as shown) or a hole in a specific trap state (e.g. defect). Bimolecular recombination can occur between electrons and holes, either from the relaxed state or from states higher in the band. Auger recombination is a higher-order process in which at least three particles are involved. Energy from one electron (or hole) is transferred to another electron (or hole) to enable nonradiative recombination with a hole (or electron). All processes must satisfy energy and momentum conservation. Reprinted with permission from the Annual Review of Physical Chemistry. Volume 67:65-89, copyright 2016 Annual Reviews.[111] Partly edited.

There are two types of processes, radiative and non-radiative, that can help to return a system to its ground state. **Figure 2.14b** demonstrates the various recombination processes involved. In lead halide perovskites in bulk form, the low concentration of multiple charge carriers results in low efficiency at low excitation energies. However, in nanocrystals, even with the same number of charge carriers, the charge carrier concentration is much higher due to their smaller size. Consequently, processes with multiple charge carriers become more important in these nanocrystals.

To measure the efficiency of emission, we can use a performance index obtained by comparing the rates of radiative and non-radiative recombination. The rate of radiative recombination (i.e., the decay rate of excited electrons, represented by γ_{rad}) can be compared to the rate of non-radiative recombination (represented by γ_{nrad}). The ratio of γ_{rad} to γ_{nrad}, shown in **Equation (2.9)**, gives the quantum efficiency (η) or photoluminescence quantum yield (PLQY) of a material.

$$\eta = \frac{\gamma_{\mathrm{rad}}}{\gamma_{\mathrm{rad}} + \gamma_{\mathrm{nrad}}} \tag{2.9}$$

The photoluminescence quantum yield (PLQY) of a material is not an inherent property of the material, but rather depends on its quality, type, and environment as well as how it is processed or synthesized. Perovskite nanoparticles, for instance, have higher quantum yields than their bulk counterparts, making them promising candidates for use in LEDs, as outlined in **chapter 2.8**.

2.7 Doping of NCs (LiTFSI)

Since the beginnings of semiconductor research, controlling the type and density of charge carriers (electrons and holes) through doping has been crucial in transforming semiconductors into relevant technologies. Doping refers to intentionally adding small concentrations of "impurities" to a pure material (host) to enhance its electronic prop-

erties, such as electron or hole transport, without altering the crystal structure of the host material.[112] An example are inorganic semiconductors like silicon (Si), where a small percentage (usually less than 1%) of aliovalent impurity atoms like boron or phosphorus can be used to create an excess or deficiency of electrons in the crystal lattice. This excess or deficiency of electrons results in donor or acceptor states near the conduction and valence bands, thereby increasing the charge carrier concentration. For example, native (undoped) Si is a poor conductor due to its low intrinsic electron concentration of about 10^{10} cm^{-3} at room temperature.[113] However, intentional introduction of impurities reduces the specific resistance by many orders of magnitude, resulting in Si having either p-type or n-type conductivity. While p-type doping refers to the addition of impurities with fewer valence electrons than the host material, n-type doping refers to the addition of impurities with more valence electrons than the host material.

In addition to the ligand exchange discussed in **chapter 2.4**, doping offers an additional way to modulate the optoelectronic properties of LHP NCs. Numerous examples can be found in the literature of doping or alloying perovskite nanoparticles.[114–118] Dopants are often used in high concentrations and should be better described as alloyed NCs.[119,119,120] The crucial difference between the two terms is that alloying creates new materials, while doping alters the properties of the host material.[121] Unfortunately, these terms are often used synonymously, leading to confusion. To avoid this, this section will not distinguish between alloys and doped NCs.

Due to their pronounced ionic crystal structure, doping of LHP-NCs (in the form of ABX_3) is more versatile and easier than in conventional semiconductors or their bulk counterparts. The doping or alloying process can be classified into three types based on the position of the substituted ions: A-site, B-site, and X-site, which will be further discussed below. Regardless of the site of doping – whether at the A-, B-, or X-site –

dopants can be introduced as precursors during synthesis[120] or post-synthetically by blending the finished nanoparticles with dopants.[122]

Doping and its influence on the optoelectronic properties of perovskite nanoparticles is of particular interest for chapter 5.

2.7.1 A-Site Doping

The choice of A-site dopants is generally based on previous research on perovskite solar cells, where perovskite films were doped with different monovalent cations (Rb^+, Na^+, K^+, Li^+ and Ag^+) to improve their energy conversion efficiency and stability.[123–125]

In general, doping the A-site of a material can result in a slight increase or decrease of the bandgap, depending on the size of the cations introduced. For example, if $CsPbX_3$ is used as the host material, adding larger impurities (like FA^+ or MA^+) will decrease the bandgap, whereas smaller dopants (such as Rb^+ or K^+) will increase it.[126]

Chen and colleagues conducted a study using X-ray diffraction (XRD) and high-resolution transmission electron microscopy (HRTEM) measurements to investigate the impact of gradually replacing FA^+ with Cs^+ ions in $CsPbBr_3$ NCs. They found that this replacement did not alter the cubic phase of the material or cause any significant changes in its size. However, they discovered that increasing the concentration of FA^+ allowed for precise tuning of the emission wavelength of LHP NCs within the range of 519 – 533 nm. Conversely, incorporating smaller cations like Rb^+ resulted in an opposite effect, as observed by Amgar *et al.*.[127] The effect of A-site cation substitution on the band gap is caused by the modified Pb – Br bond lengths and angles in $[PbX_6]^{4-}$ (**chapter 2.1**) induced by larger FA^+ or smaller Rb^+ ions. Consequently, the band gap is indirectly influenced by structural distortions. As the size of the A-site cation decreases, as is the case with Rb^+, the Pb–X–Pb angle becomes more distorted (regardless of whether it is larger or smaller than the ideal 180° angle), leading to a greater octa-

hedral tilt. This results in a deformation of the overlap of the anti-bonding orbitals of the Pb^{2+} metal cation and halide anion, compared to the ideal cubic perovskite structure, which explains the increased band gap.[128]

2.7.2 B-Site Doping

Compared to A-site substitution, B-site doping offers additional freedom in designing the properties of LHP NCs, as the replacement of Pb^{2+} with a foreign atom directly affects the band gap. A variety of metal ions have been used for B-site doping of perovskite NCs. These metal ions can be divided into two categories depending on the valence electrons of the extrinsic ions and the Pb^{2+} host, namely the isovalent (Sn^{2+}, Cd^{2+}, Zn^{2+}, Sr^{2+}, Mn^{2+}, Mg^{2+}, Ni^{2+})[120,129–132] and heterovalent (with Bi^{3+}, Ln^{3+} (lanthanide ions), and Al^{3+})[133–135] dopants.

Except for Ni^{2+}, perovskites doped with homovalent ions exhibit a wider optical band gap (blue shift of absorption) than undoped perovskites. Since all these ions have a smaller radius compared to Pb^{2+}, they lead to a stronger lattice contraction with shorter B – X bonds and an enhanced interaction between Pb and X orbitals, which is responsible for the broader band gap.[122] However, Ni^{2+} exhibited a different trend (red shift), as it was assumed that Ni doping leads to improved lattice order.[132]

The heterovalent doping of trivalent ions, particularly Ln^{3+} (Ce^{3+}, Sm^{3+}, Eu^{3+}, Yb^{3+}, Er^{3+}, Dy^{3+}, Tb^{3+}, Tm^{3+}), results in interesting intermediate energy levels inside the bandgap of LHP NCs, which provide new transfer channels for excited electrons and enable energy transfer between the host and dopants.[126] Recently, Milstein *et al.* and Zhou *et al.* showed that inorganic lead halide perovskite nanocrystals $CsPbX_3$ (X = Cl or Cl/Br) doped with Yb^{3+} enable near-infrared photoluminescence with PLQYs of nearly 170 %, making quantum cutting with PLQYs of over 100 % possible.[136,137] Quantum cutting is an interesting optical phenomenon in which a high-energy photon

is converted into two low-energy photons, leading to photoluminescence quantum yields (PLQYs) of over 100 %.[138] Therefore, Yb-doped perovskites are a promising material for solar down conversion, which can increase the efficiency of commercial solar cells.

2.7.3 X-Site Doping

The process known as "X-site doping", which in this case should more accurately referred to as "alloying", provides a direct means of manipulating the emission band gap of LHP-NCs through the halide composition.[27,29] As mentioned in **chapter 2.1.2**, the tuning of the emission bandgap of LHP-NCs differs from that of conventional II-VI, III-V, and IV-VI semiconductor quantum dots, where the emission bandgap is mainly controlled by the size of the nanoparticles through quantum confinement effects.[139]

One way to produce mixed halides ($CsPb(Br/Cl)_3$ or $CsPb(Br/I)_3$) is through either a direct synthesis strategy, where precursor materials for the mixed anions are used directly during the synthesis[29] of the nanocrystals, or through a post-synthetic strategy, where excess amounts of Cl^-- or I^--halide precursors can be introduced into pre-existing colloidal nanocrystals based on $CsPbBr_3$. Some of the possible choices for Cl^-- or I^--halide precursor materials are inorganic halogen-containing salts (PbX_2),[140] organic ammonium halides (Oleylammonium halides (OLAM-X)), and aryl-based hydrohalides (Ar-HX).[7]

In comparison to cation exchange, anion exchange is relatively fast and simple in perovskite systems due to its low defect formation energy, the rigid nature of its cationic sublattice, and the high ion mobility in the lattice caused by the presence of vacancies.[141,142] This makes it possible to perform an anion exchange between two different colloidal halide perovskite nanocrystal suspensions by simply mixing them in a flask.[68] However, there is a limitation: the exchange of halides between Cl and I in perovskite nanocrystals is difficult due to the large difference in their ionic radii, which leads to

the destruction of the lattice. Only Cl^-–Br^- and Br^-–I^- pairs can be successfully exchanged. Attempts to directly obtain $CsPbCl_3$ from $CsPbI_3$ nanocrystals or intermediate $CsPb(Cl/I)_3$ nanocrystals have so far been unsuccessful, as the complete disappearance of photoluminescence indicates the dissolution of particles.[68]

However, the simple exchange of halogens also results in disadvantages in particle storage. Caution is advised when storing LHP NCs in halogenated solvents such as dichloromethane (DCM), as it has been observed that $CsPbX_3$ nanocrystals excited by light transfer electrons to solvent molecules and in situ generate halide anions through reductive dissociation. The extent of the anion exchange reaction can be precisely controlled by adjusting the photon dose or the wavelength of the excitation light.[143]

2.8 Electroluminescent Quantum Dot Light-Emitting Devices

One of the potential commercial applications for LHP NCs is in the display industry. Currently, quantum dot light-emitting diodes (QDLEDs) require external light sources to excite them, typically located behind the actual display. A more advanced technology in this area are electroluminescent quantum dot light-emitting devices (ELQLEDs). These are electrically driven devices that emit light when excited by an electric current. Unlike QDLEDs, the energy source for ELQLEDs does not come from optical stimulation, but from an external source.

ELQLEDs are thin-film structures (**Figure 2.15a**) consisting of organic functional layers deposited on various substrates by methods such as spin coating or vapor deposition. Typically, glass substrates are used, coated with a transparent conductive oxide such as indium tin oxide (ITO) as the electrode (anode). A highly reflective metal layer, such as aluminum, is typically used as the second electrode (cathode). In perovskite

LEDs, light is generated by the radiative recombination of the injected charge carriers, which form bound electron-hole pairs, called excitons, in the emission layer (EML).

A perovskite LED (PeLED) composed of five different layers is shown in **Figure 2.15b**. The goal of this design is to generate excitons in the emission layer (i.e., LHP NCs) that can radiatively decay and emit photons. The required charge carriers, electrons, and holes are injected from the respective electrodes into the adjacent charge transport layer (CTL). After being injected into the CTL, the charge carriers drift towards the interface of the CTL and the EML, driven by the interaction of the external and internal electric fields. Both CTL layers are usually made of different materials adapted to the respective carrier transport. Therefore, they are typically referred to as the hole transport layer (HTL) and the electron transport layer (ETL). Charges can migrate into the EML where they can form excitons under ideal conditions if there are no additional potential barriers between the CTLs and the EML.

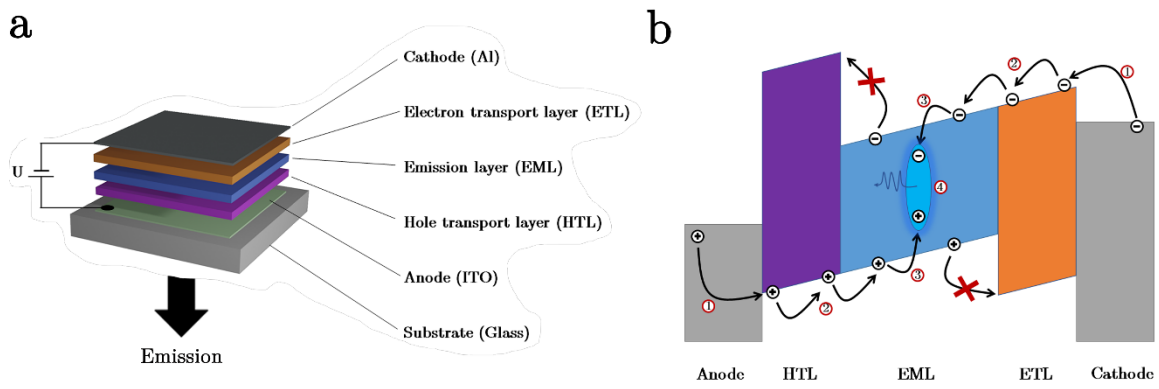

Figure 2.15: **a)** Typical layer structure of a light-emitting diode with light-transmitting anode made of indium tin oxide for the injection of positive charge carriers and a metallic cathode for electron injection. The emission zone consists of LHP NCs **b**) Schematic representation of the main processes in LED operation: 1) Injection of carriers. 2) Carrier transport. 3) Formation of excitons 4) Radiative recombination.

2.8.1 Maximizing Efficiency

The efficiency of converting electrical energy into visible light, in addition to the cost and lifetime of such LEDs, is critical to the success of this technology. In particular, the extraction of light from the device is a limiting factor. Two quantities are used to measure the efficiency of a device: either the light output per electrical power input in lumens per watt, or the external quantum efficiency (EQE), which is the number of photons emitted divided by the number of charge carriers injected, expressed as a percentage (η_{EQE}). Typically, the total EQE (**Equation (2.10)**) is separated into various subfactors that affect the overall emission.[144,145]

$$\eta_{EQE} = \gamma \cdot q_{eff} \cdot \eta_{out} \tag{2.10}$$

Herein, γ represents the balance of charge carriers, specifically the ratio of electrons to holes in the EML that recombine with each other. This parameter is critical, especially for blue emitting perovskites, and is typically controlled through the device architecture.[145] Additional factors affecting the EQE are thus the effective radiative quantum yield (q_{eff}) and the light outcoupling efficiency (η_{out}). Any improvement in the QY of the LHP layer improves the EQE, since q_{eff} depends mainly on the quantum efficiency of the emitting layer. The light outcoupling efficiency η_{out} is determined by the stack configuration and the transition dipole moment of the NC.

The topic of maximizing efficiency plays an important role, especially in chapter 5.

2.9 Environmental Stability

Despite their excellent optoelectronic properties and variability, one of the major concerns regarding LHP NCs is their long-term stability. Their unstable nature and sensitivity to environmental factors hinder their industrial relevance and long-term ap-

plication. The following chapter will discuss the stability of perovskite nanoparticles in relation to environmental factors and their application in optoelectronic devices.

The term "stability" is often used superficially in the literature concerning LHP NCs and encompasses various aspects of stability. Generally, instability can be divided into two categories, namely intrinsic and extrinsic instability.[89]

In addition to the intrinsic instability of the crystal structure or the dynamic binding of surface ligands, which were already mentioned in **chapters 2.1.1** and **2.4**, there are also extrinsic factors that can affect the stability of LHP NCs. Extrinsic instability refers to the instability of LHP NCs caused by external factors such as heat, oxygen, water (or polar solvents), or light. It should be added that these external factors also significantly affect the intrinsic stability of perovskites, e.g., moisture can accelerate phase transitions in $CsPbI_3$ nanowires.[146] Due to the generally ionic structure[147] of LHP NCs combined with relatively weakly binding surface ligands,[67] polar solvents, especially water, tend to decompose the NCs into their corresponding salts.[148] This instability against water and polar solvents not only reduces the application in end devices but also complicates the classical purification of nanoparticles by precipitation. Therefore, anhydrous solvents should be used for purification and the exposure time to such solvents should be reduced to a minimum.

Another form of extrinsic instability is observed with prolonged exposure to UV or X-ray radiation,[149–152] resulting in light degradation manifested by the formation of Pb^0 clusters, ultimately leading to a reduction in emission intensity. The energy levels of the Pb^0 cluster defects are located within the bandgap of the perovskite as deep trap states that act as charge carrier traps, resulting in a reduced PL intensity.[153]

Another challenge for the stability of perovskite NCs is posed by temperature and oxygen. Apart from the influence of temperature on the individual crystal phases (**chapter 2.1.1**), some studies have shown that an increase in temperature in the range

of 320-400 K results in an irreversible loss of PL intensity.[150,154] This loss is attributed to the increasing detachment of ligands due to the rise in temperature, leading to agglomeration of nanoparticles and increased surface defects.[89]

The presence of oxygen alone does not have a significant effect on the stability of LHP NCs. Li *et al.* demonstrated that there is a negligible difference in the optical properties of $CsPbBr_3$ NCs observed in either nitrogen or oxygen atmospheres in the dark.[150] However, a synergistic effect between oxygen and moisture occurs when the perovskites are exposed to continuous light irradiation. This oxygen-induced quenching of the fluorescence accelerates the agglomeration and regrowth of LHP NCs into large crystals with low PLQYs.[155,156] Minimizing the factors described in this chapter through techniques such as ligand exchange (**chapter 2.4**) or doping (**chapter 2.7**) is essential for fabricating efficient end devices such as LEDs (**chapter 2.8**). The issue of the environmental stability of perovskite NCs is particularly relevant to chapter 6 because here the instabilities of these NCs have been studied in more detail.

3. Spatially Resolved Fluorescence of Caesium Lead Halide Perovskite Supercrystals Reveals Quasi-Atomic Behavior of Nanocrystals

Dmitry Lapkin[1,], **Christopher Kirsch**[2,*], Jonas Hiller[2,*], Denis Andrienko[3], Dameli Assalauova[1], Kai Braun[2], Jerome Carnis[1], Young Yong Kim[1], Mukunda Mandal[3], Andre Maier[2,4], Alfred J. Meixner[2,4], Nastasia Mukharamova[1], Marcus Scheele[2,4,+], Frank Schreiber[4,5], Michael Sprung[1], Jan Wahl[2], Sophia Westendorf[2], Ivan A. Zaluzhnyy[5], Ivan A. Vartanyants[1,6,+]*

1. *Deutsches Elektronen-Synchrotron DESY, Notkestraße 85, 22607 Hamburg, Germany*
2. *Institut für Physikalische und Theoretische Chemie, Universität Tübingen, Auf der Morgenstelle 18, 72076 Tübingen, Germany*
3. *Max Planck Institute for Polymer Research, Ackermannweg 10, 55128 Mainz, Germany*
4. *Center for Light-Matter Interaction, Sensors & Analytics LISA+, Universität Tübingen, Auf der Morgenstelle 15, D-72076 Tübingen, Germany*
5. *Institut für Angewandte Physik, Universität Tübingen, Auf der Morgenstelle 10, 72076 Tübingen, Germany*
6. *National Research Nuclear University MEPhI (Moscow Engineering Physics Institute), Kashirskoe shosse 31, 115409 Moscow, Russia*

* These authors contributed equally

+To whom correspondence should be addressed

This chapter is based on the publication published in Nature Communications: Nat. Commun. **13,** 892 (2022), DOI: 10.1038/s41467-022-28486-3.

3.1 Abstract

We correlate spatially resolved fluorescence (-lifetime) measurements with X-ray nanodiffraction to reveal surface defects in supercrystals of self-assembled caesium lead halide perovskite nanocrystals and study their effect on the fluorescence properties. Upon comparison with density functional modeling, we show that a loss in structural coherence, an increasing atomic misalignment between adjacent nanocrystals, and growing compressive strain near the surface of the supercrystal are responsible for the observed fluorescence blueshift and decreased fluorescence lifetimes. Such surface defect-related optical properties extend the frequently assumed analogy between atoms and nanocrystals as so-called quasi-atoms. Our results emphasize the importance of minimizing strain during the self-assembly of perovskite nanocrystals into supercrystals for lighting application such as superfluorescent emitters.

3.2 Introduction

Advances in the self-assembly of colloidal nanocrystals (NCs) from solution into three-dimensional arrays with long-range order have enabled the design of microscopic "supercrystals" that approach the structural precision of atomic single crystals.[157] The individual NCs, which are the building blocks of a supercrystal, are often regarded as "artificial atoms", and hence analogies between atomic crystals and such supercrystals have been made.[158,159] NC supercrystals are susceptible to doping,[160] and they can exhibit exceptional mechanical properties,[161] quasicrystal formation,[158] enhanced electronic coupling,[162] and engineered phonon modes.[163] In view of the recent progress in exploiting the massive structural coherence in NC supercrystals to generate collective optoelectronic properties,[74,164,165] a critical question remains whether this artificial atom analogy can be extended towards the optical properties of NC supercrystals. Due to surface dangling bonds and surface reconstruction, even the purest and most carefully prepared atomic crystals are not structurally perfect.[166,167]

For atomic crystals, such surface defects strongly affect the fluorescence spectra, lifetime, and quantum yield.[168–172] For supercrystals, this is much less understood.

In this work, we show that in close analogy to atomic crystals,[173,174] $CsPbBr_2Cl$ and $CsPbBr_3$ NC supercrystals exhibit structural distortions near their surfaces which significantly alter their fluorescence properties. This finding is of high relevance for the application of these materials as tunable, bright emitters with superfluorescent behavior.[74,164,165] Superfluorescence is a key property for the design of spectrally ultra-pure laser sources[175] or highly efficient light-harvesting systems.[176] Recent quantum chemical simulations have suggested that structural disorder in $CsPbBr_3$ supercrystals and its effect on the thermal decoherence plays a pivotal role in the efficiency of the superfluorescence.[177] Previous structural investigations of ensembles of $CsPbBr_3$ supercrystals by grazing-incidence small angle X-ray scattering (SAXS) indicated a primitive unit cell with slight tetragonal distortion,[178] and wide-angle X-ray scattering (WAXS) showed a high degree of structural coherence.[179] Electron microscopy of individual supercrystals revealed a frequent occurrence of local defects in the supercrystals, such as isolated NC vacancies.[180] Confocal fluorescence microscopy of individual $CsPbBr_3$ supercrystals displayed spatial variations in the fluorescence peak wavelength and intensity, indicating that local structural inhomogeneities may substantially affect the fluorescence properties of the entire supercrystal.[152] Our approach is based on simultaneous WAXS and SAXS measurements with a nano-focused beam to probe the structural defects and crystallographic orientation of the supercrystal and the constituting NCs on a local level with dimensions of ~3 µm and 7–9 nm, respectively.[181–183] By correlation with diffraction-limited confocal fluorescence microscopy and modeling with density functional theory (DFT) we present proof that compressive strain, a loss of structural coherence and an increasing atomic misalignment between adjacent nanocrystals at the edges of $CsPbBr_2Cl$ NC supercrystals are responsible for a blueshifted emission and decrease of the fluorescence lifetimes.

3.3 Results

We study self-assembled $CsPbBr_2Cl$ and $CsPbBr_3$ NC supercrystals on glass substrates (see "Methods" for details on synthesis and self-assembly of NCs). Spatially resolved photoluminescence spectra of the NC supercrystals under 405 nm excitation in a confocal laser scanning microscope with a step size of 250 nm and 100 nm, respectively, are shown in Figure **3.1**. When approaching an edge of the supercrystal, we find a continuous blueshift of the emission peak wavelength. This blueshift is strongest for relatively small (few µm edge length) and highly faceted supercrystals, where it reaches up to 20 meV for $CsPbBr_2Cl$. We observe the same blueshifting behavior for supercrystals composed of $CsPbBr_3$ NCs, although to a lesser extent (up to 12 meV).

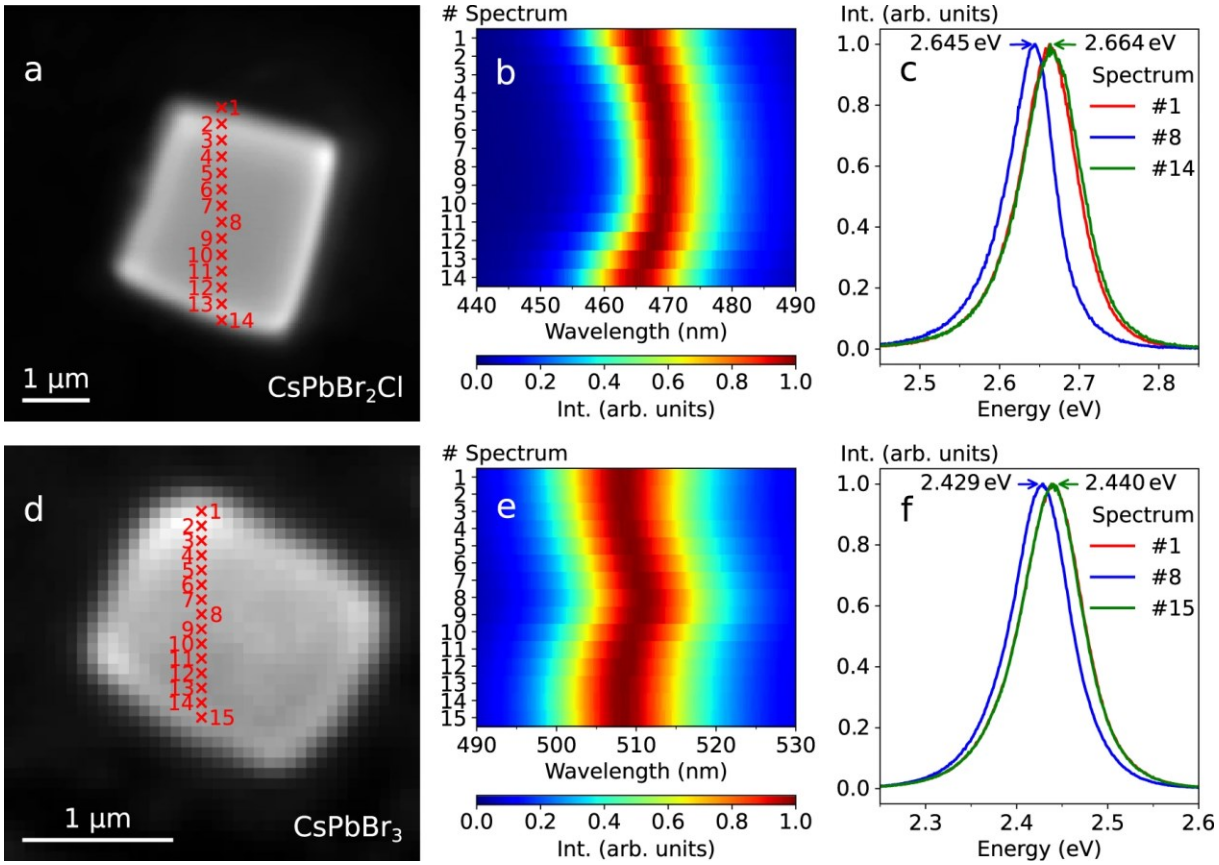

Figure 3.1: a) Optical micrograph of a $CsPbBr_2Cl$ NC supercrystal. Positions of the measured photoluminescence spectra are indicated. b) The corresponding normalized spectra. c) Selected normalized spectra, acquired at the edges and the center of the supercrystal. d-f) Corresponding data for a $CsPbBr_3$ supercrystal.

In **Figure 3.2**, we display fluorescence lifetime images of self-assembled $CsPbBr_2Cl$ and $CsPbBr_3$ supercrystals measured on glass substrates with a lateral resolution of 200 nm under 405 nm excitation. For both supercrystal compositions, we obtain good fits of the experimental time-resolved fluorescence by pixel-by-pixel monoexponential reconvolution using an instrument response function acquired on a clean glass coverslip (**Figure S3.2, Figure S3.3**). In the case of supercrystals composed of $CsPbBr_2Cl$ NCs, we measure typical fluorescence lifetimes (τ) around 2.1 ns in the center which decrease by approximately 20% when scanning from the center of a supercrystal towards its edges. Supercrystals composed of $CsPbBr_3$ NCs exhibit typical lifetime values around 1.5 ns in the center, which shorten by approximately 30% when approaching the edges. We note that this holds true only for freshly prepared NC supercrystals. After several days of exposure to air, the trend in the spatially resolved τ-values is reversed in that

such aged supercrystals exhibit longer lifetimes at the edges. However, the overall blueshift of the fluorescence peak wavelength towards the edges is preserved.

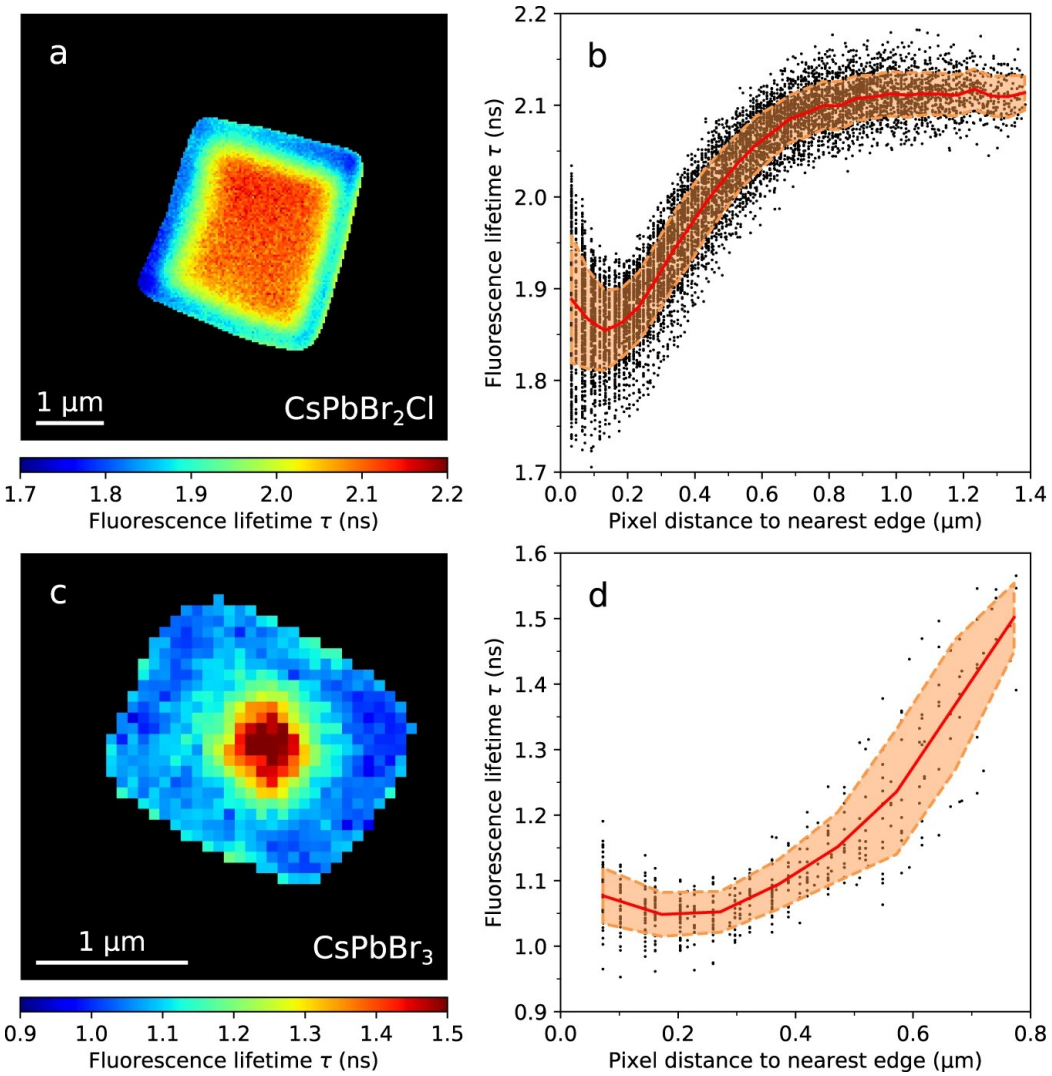

Figure 3.2: a) Fluorescence lifetime image of a $CsPbBr_2Cl$ NC supercrystal obtained by fitting the experimental time-resolved fluorescence with a monoexponential decay function. **b**) Fluorescence lifetime values obtained at each pixel inside the supercrystal as a function of the distance to the nearest edge, where the red line shows the mean value, and the dashed lines indicate the confidence interval of $\pm\sigma$. **c-d)** Analogous results for a $CsPbBr_3$ NC supercrystal.

To correlate the fluorescence data with the structure of the supercrystals, we carry out X-ray synchrotron measurements by SAXS and WAXS at PETRA III facility (Hamburg, Germany) (see **Figure 3.3 a** and "Methods" for details). Using a 400 × 400 nm^2 X-ray beam, we perform a spatially resolved scan of a typical $CsPbBr_2Cl$ NC supercrystal on a Kapton substrate. While the results presented here are for one typical supercrystal, examples of more supercrystals are provided in the Supplementary

information (**Section S3.7**). First, all individual patterns are integrated to obtain the average structure. The averaged background-corrected WAXS and SAXS diffraction patterns are shown in **Figure 3.3 b and 3.3 c**, correspondingly. The signal in the WAXS region contains three orders of Bragg peaks from the atomic lattice (**Figure 3.3 b**), and the SAXS region (shown enlarged in **Figure 3.3 c**) displays several orders of Bragg peak from the supercrystal. A real-space map of the scan based on the integrated SAXS intensity at $q < 2\,\mathrm{nm}^{-1}$ is shown in **Figure 3.3 d**. The map represents a square area of high intensity corresponding to a single supercrystal. For comparison, we display a scanning electron micrograph of a similar supercrystal (see the inset in **Figure 3.3 a** and **Figure S3.8**) from which we determine an average NC diameter of $7.3 \pm 0.4\,\mathrm{nm}$ and an interparticle distance of $2.5 \pm 0.5\,\mathrm{nm}$. For strongly faceted supercrystals, the NC diameter is rather uniform over the whole crystal. For less faceted supercrystals, occasional ensembles of smaller NCs are found in the vicinity of the edges. However, the spatial extent of such smaller NC populations is always limited to ~200 nm (see **Section S3.3**).

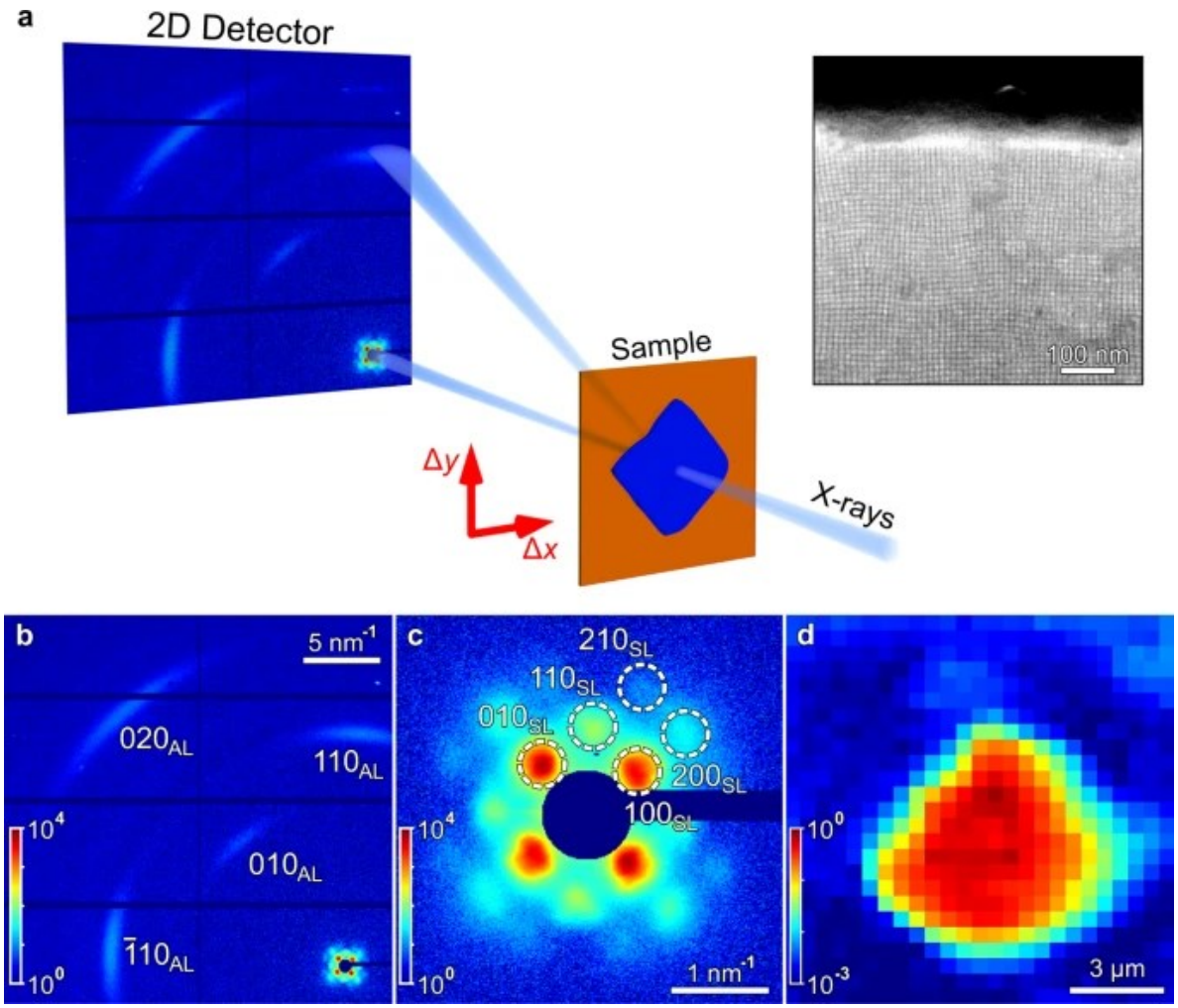

Figure 3.3: a) Scheme of the X-ray experiment. EIGER X 4M 2D detector is positioned downstream from the sample. The arrows show the directions Δx and Δy of spatial scanning. Inset (top right): a SEM micrograph of the $CsPbBr_2Cl$ NC supercrystal. **b)** Average diffraction pattern for a supercrystal. Several orders of WAXS and SAXS Bragg peaks from the atomic and supercrystal structure, respectively, are well visible. The WAXS Bragg peaks are indexed using pseudo-cubic notation. **c)** Enlarged SAXS region of the averaged diffraction pattern. The Bragg peaks are indexed according to a simple cubic structure. **d)** Diffraction map for a scan based on the integrated intensity of the SAXS diffraction patterns at $q < 2$ nm^{-1}. The pixel size (the step size) is 500 nm.

The average diffraction pattern in the WAXS region (see **Figure 3.3** b) contains four prominent Bragg peaks, originating from the atomic lattice (AL) of the NCs. Their radial positions at $q = 10.93\,\mathrm{nm}^{-1}$, $15.44\,\mathrm{nm}^{-1}$, and $21.90\,\mathrm{nm}^{-1}$ (see **Figure S3.10**) can be attributed to a cubic AL. We note that although a cubic phase for $CsPbBr_2Cl$ has been reported,[184,185] the most stable phase at room temperature is expected to be orthorhombic. Due to the small NC size and the resulting broadening of the Bragg peaks, it is impossible to distinguish between these two very similar structures. Thus, we use a

pseudocubic notation to index the WAXS peaks: 110 and 002 orthorhombic peaks correspond to 100_{AL} pseudocubic peak, 112 and 200 – to 110_{AL}, and 220, 004 – to 200_{AL} peaks. The present peaks and their azimuthal positions indicate a primary orientation of the NCs along the $[001]_{AL}$ axis with respect to the incident beam. We find the unit cell parameter to be $a_{AL} = 0.575 \pm 0.003$ nm, which is in good agreement with previously reported values for $CsPbBr_2Cl$.[186] From the peak broadening, we extract the NC size (d) and lattice distortion (g) using the Williamson–Hall method with $d = 6.8 \pm 0.1$ nm and $g = 2.3 \pm 0.1\%$ (see **Section S4**). The obtained NC size is in good agreement with the scanning electron microscopy (SEM) results.

The SAXS pattern in **Figure 3.3 c** represents the typical 4-fold pattern of a simple cubic lattice oriented along the $[001]_{SC}$ axis with four visible orders of Bragg peaks that can be attributed to 100_{SC}, 110_{SC}, 200_{SC}, and 210_{SC} reflections of the supercrystal of NCs. We determine an average unit cell parameter of $a_{SC} = 9.9 \pm 0.4$ nm. Considering the NC size obtained by SEM, we obtain an interparticle distance of 2.6 ± 0.4 nm, which is in good agreement with the SEM result (2.5 ± 0.5 nm). All crystallographic axes of the NCs are aligned with the corresponding axes of the supercrystal (e.g. $[100]_{AL}||[100]_{SC}$ and $[010]_{AL}||[010]_{SC}$), which is consistent with ref. [180].

Analyzing individual SAXS patterns from different locations on the supercrystal, we find substantial local deviations from the average structure (see **Figure S3.12** for examples of single diffraction patterns). To illustrate this, from the Bragg peak positions, we extract the basis vectors a_1 and a_2, the angle γ between them, and the average azimuthal position φ, which are defined in **Figure 3.4 a** (see the "Methods" section for details). As depicted in **Figure 3.4 b**, the mean unit cell parameter is largest in the center of the supercrystal with 10.7 nm and smallest at the edges with 7.8 nm. Although both unit cell parameters a_1 and a_2 decrease at the edges (see **Figure S3.16**, for separate maps of a_1 and a_2 values), we observe that this lattice contraction is anisotropic. The ratio of the in-plane unit cell parameters a_2/a_1 differs from unity by ±20%

in such a way that the NC spacing in the directions along the nearest supercrystal boundary is smaller than normal to it, as shown in **Figure 3.4 c**. We note that the mean value $\langle a \rangle = 9.4 \pm 0.7\,\mathrm{nm}$ is slightly smaller than the unit cell parameters extracted from the average diffraction pattern. We attribute this to the low intensity of scattering from the supercrystal edges, which reduces their contribution to the average pattern. We do not observe a clear trend in the size of the SAXS Bragg peaks (see **Figure S3.15**, for the maps). The instrumental peak broadening, determined by the incident X-ray beam size is about $0.015\,\mathrm{nm}^{-1}$ (full width at half maximum, FWHM). The observed peak sizes are much larger and vary in the range from $0.05\,\mathrm{nm}^{-1}$ to $0.2\,\mathrm{nm}^{-1}$ and, as such, they depend mainly on the superlattice distortion. The characteristic length scale on which this distortion evolves is, most probably, smaller than the incident beam. Thus, the areas with different lattice parameters simultaneously illuminated by the incident beam lead to the peak broadening.

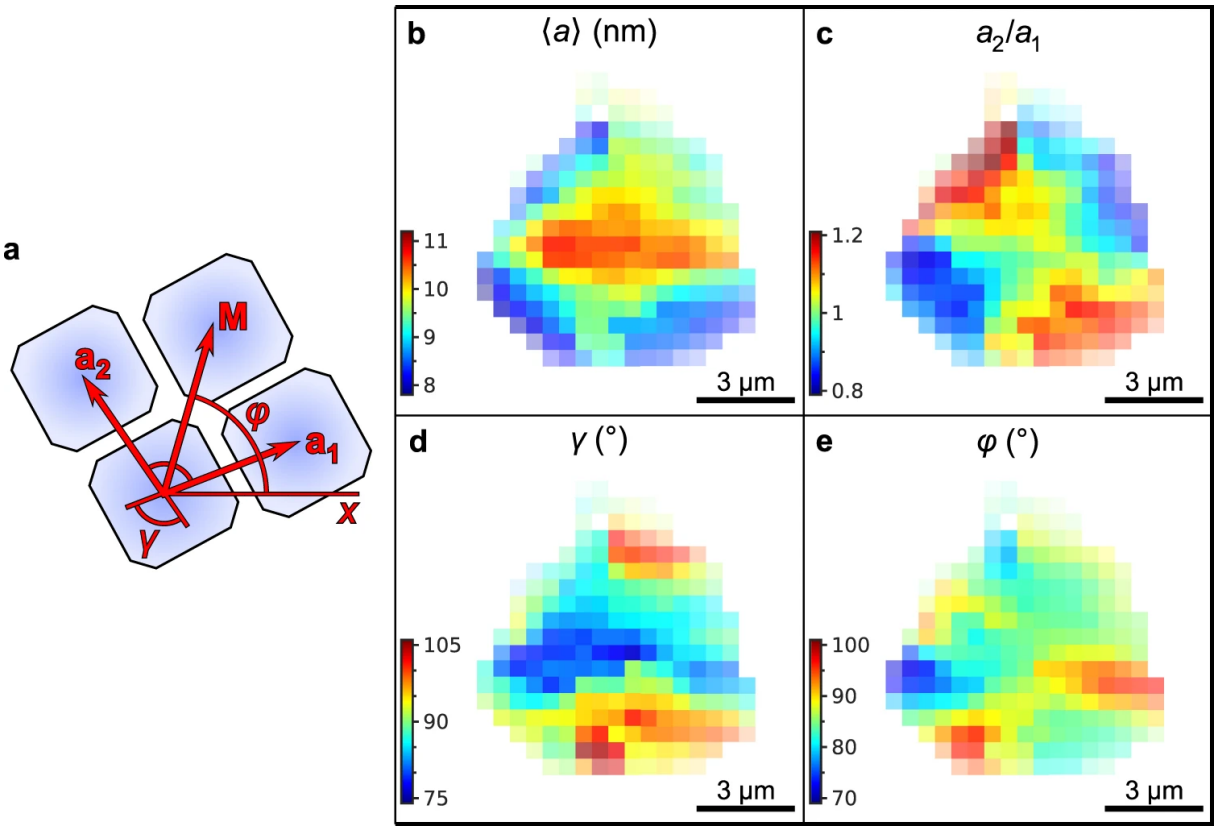

Figure 3.4: **a)** Definition of the geometrical parameters of a superlattice unit cell: the basis vectors a_1 and a_2 with the angle γ between them, and the mean line M between the basis vectors at the angle φ; **b)** average unit cell parameter $\langle a \rangle = (a_1+a_2)/2$; **c)** ratio a_2/a_1 of the unit cell parameters along the basis vectors a_2 and a_1; **d)** angle γ between the basis vectors a_1 and a_2; **e)** azimuthal position φ of the mean line M between the basis vectors a_1 and a_2. The pixel size in **b-e)** is 500 nm.

The angle γ between the $[100]_{SC}$ and $[010]_{SC}$ axes differs from its average value of $\langle \gamma \rangle = 90 \pm 6°$ in a range of 76° to 105° over the whole supercrystal as shown in **Figure 3.4 d**. Specifically, we find $\gamma > 90°$ close to the top and bottom corners of the supercrystal and $\gamma < 90°$ close to the left and right corners. Thus, the angle pointing towards the corner of the supercrystal is always obtuse. We further calculate the azimuthal position φ of the mean line **M** between the $[100]_{SC}$ and $[010]_{SC}$ axes. This angle can be interpreted as the azimuthal orientation of the unit cell of the supercrystal. The orientation changes inhomogeneously throughout the superlattice in the range from 72° to 97° as shown in **Figure 3.4 e**. There is no obvious correlation between the lattice orientation and the spatial position within the sample. Overall, these results suggest that

the supercrystal is simple cubic on average, but it exhibits substantial local monoclinic distortions.

We analyze the Bragg peaks in the WAXS region of individual diffraction patterns at different locations to study the angular orientation of the NCs inside the superlattice. From the WAXS Bragg peak analysis, we extract the average WAXS intensity $\langle I_{AL} \rangle$ and the azimuthal position Ψ of the $[010]_{AL}$ axis defined in **Figure 3.5 a** (see "Methods" section and **Section S3.6**). In contrast to the intensity of the SAXS Bragg peaks, the WAXS intensity $\langle I_{AL} \rangle$ decreases towards the edges, as shown in **Figure 3.5 b**, indicating an out-of-plane rotation of the NCs that shifts the Bragg peaks slightly out of the Ewald sphere[182]. We find that Ψ changes in a wide range from 120° to 142° as shown in **Figure 3.5 c** The map of Ψ resembles that of the azimuthal orientation φ of the mean line **M**, shown in **Figure 3.4 e**. The 45° offset between the $[010]_{AL}$ axis and the mean line **M** indicates the alignment of the $[110]_{AL}$ axis with the mean line **M** between the $[100]_{SC}$ and $[010]_{SC}$ axes (see **Figure S3.23**).

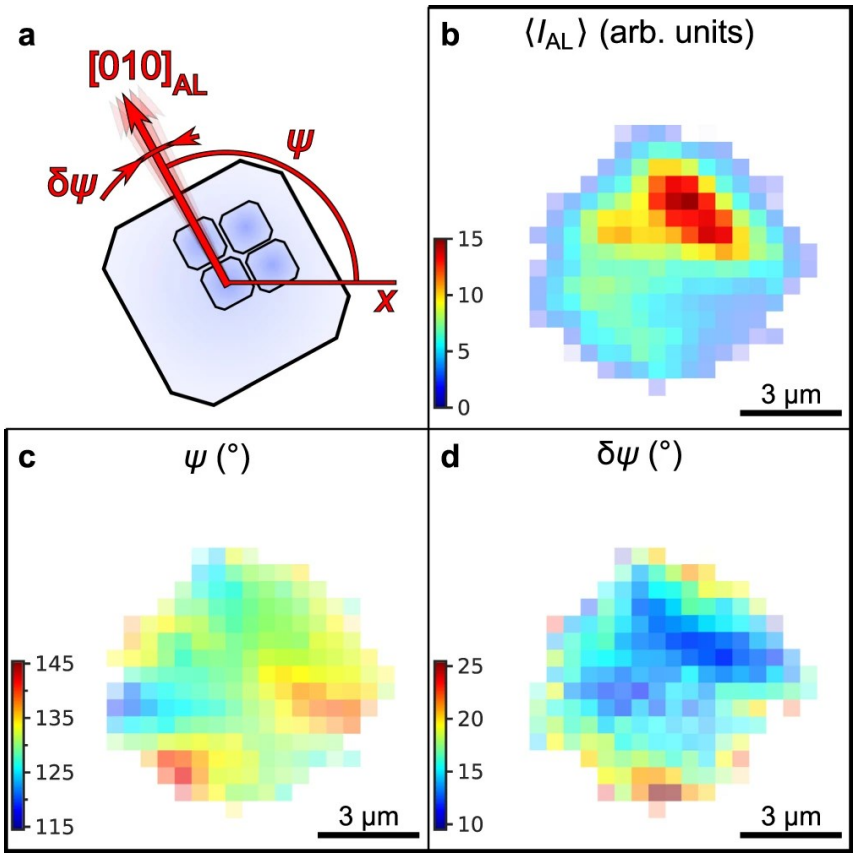

Figure 3.5: a) Definition of the geometrical parameters of the atomic lattice extracted by fitting of the Bragg peaks; **b)** mean intensity of the WAXS Bragg peaks $\langle I_{AL} \rangle$ **c)** azimuthal position Ψ of the 100_{AL} crystallographic axis of the NCs **d)** FWHM $\delta\Psi$ of the angular disorder of the NCs around the mean azimuthal position Ψ extracted from the azimuthal FWHMs of the Bragg peaks by the Williamson-Hall method. The pixel size in **b-d)** is 500 nm.

From the azimuthal FWHMs of the WAXS Bragg peaks, we extract the angular disorder $\delta\Psi$ of the individual nanocrystals at each spatial point by the Williamson–Hall method as shown in **Figure 3.5 d** (see "Methods" for details). The disorder is smallest in the center of a supercrystal (9.9°) and increases to a maximum of 24.0° at the edges. The mean value of the angular disorder is $\langle \delta\Psi \rangle = 16.1 \pm 2.8°$, which is consistent with previously observed values for similar superstructures.[180–183]

Despite the fact that the atomic lattice parameter a_{AL} is constant within the error bars throughout the whole supercrystal (see **Figure S3.20**, for the map of a_{AL}), we find a difference in the radial width of the Bragg peaks at different locations. By the Williamson–Hall method, we extract the lattice distortion g_q (the ratio $\delta a_{AL}/a_{AL}$,

where δa_{AL} is the FWHM of the unit cell parameter distribution around the mean value a_{AL}) at each spatial point (see "Methods" section for details). We find a clear trend of increasing atomic lattice distortion towards the edges of the supercrystal with a maximum of 2% at the edge, while it is about 1% at a distance 3 µm into the center, as shown in **Figure 3.6**. The trend is even more evident for another supercrystal with particularly good signal-to-noise ratio of the WAXS intensity (see **Figure S3.29**).

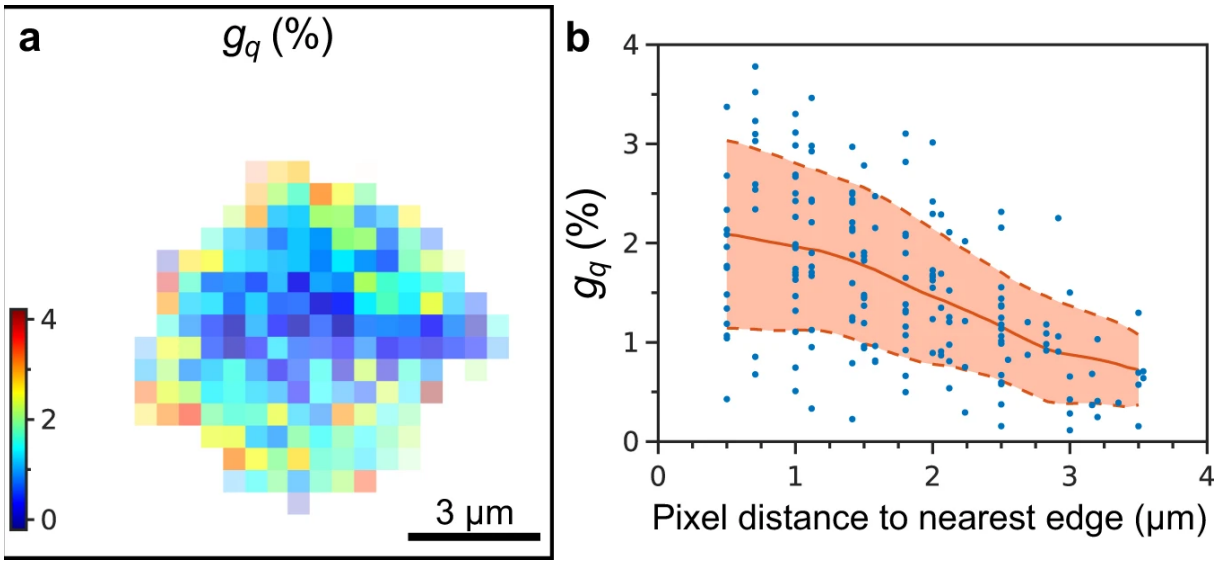

Figure 3.6: a) Atomic lattice distortion g_q extracted from the radial FWHMs of the WAXS Bragg peaks by the Williamson-Hall method. The pixel size is 500 nm. **b)** The same value g_q for each pixel plotted against the distance from this pixel to the nearest edge of the supercrystal. The red line shows the mean value, the dashed lines indicate the confidence interval of $\pm\sigma$.

To rationalize the experimental trend of increased fluorescence energies at the edges of the supercrystal as compared to its center, we carry out density functional modeling of the system. We consider three individual contributions in this regard. First, we recognize that the number of nearest neighbors at the surface of the supercrystal is lower than that in the center, leading to stronger exciton confinement and hence increased fluorescence energies at the edges. Indeed, our DFT calculations confirm this trend in **Figure 3.7 a**, which is consistent with the blueshift of the fluorescence spectra observed experimentally for the NCs at the edges. "Nearest neighbors" refers here to adjacent NCs with near-perfect orientational order, that is, a low value of $\delta\Psi$ (**Figure 3.5 d**). A large orientational misalignment ($\delta\Psi$) is likely to have a similar effect on

nearest-neighbor coupling as a reduced number of nearest neighbors. Second, we anticipate that the shorter interparticle spacing (**Figure 3.4 b**) should facilitate better electronic coupling between the nanocrystals at the edges and, therefore, a decrease in the optical gap at the edges is anticipated. While this expectation is confirmed computationally in **Figure 3.7 b**, we note that it is exactly opposite to what is observed experimentally in Figure **3.1 b, c** (see Discussion section for details). Third, the supercrystal is compressed at the edges, as evident from **Figure 3.4 b**. While it is reasonable to assume that the compressive strain will mostly manifest in a denser packing of the soft oleylamine/oleic acid ligand sphere of the NCs, we also consider a partial compression of the hard-inorganic lattice-core. In **Figure 3.7 c** we calculate the effect of such compression on the HOMO–LUMO gap (E_{gap}) of the NC. While axial stress applied to the CsCl-terminated surface of the $CsPbBr_2Cl$ particle results in a steady increase of the optical gap consistent with the experiment, similar stress on the CsBr-terminated surfaces of both particles are found to both increase or decrease E_{gap}, depending on the magnitude of the applied stress.

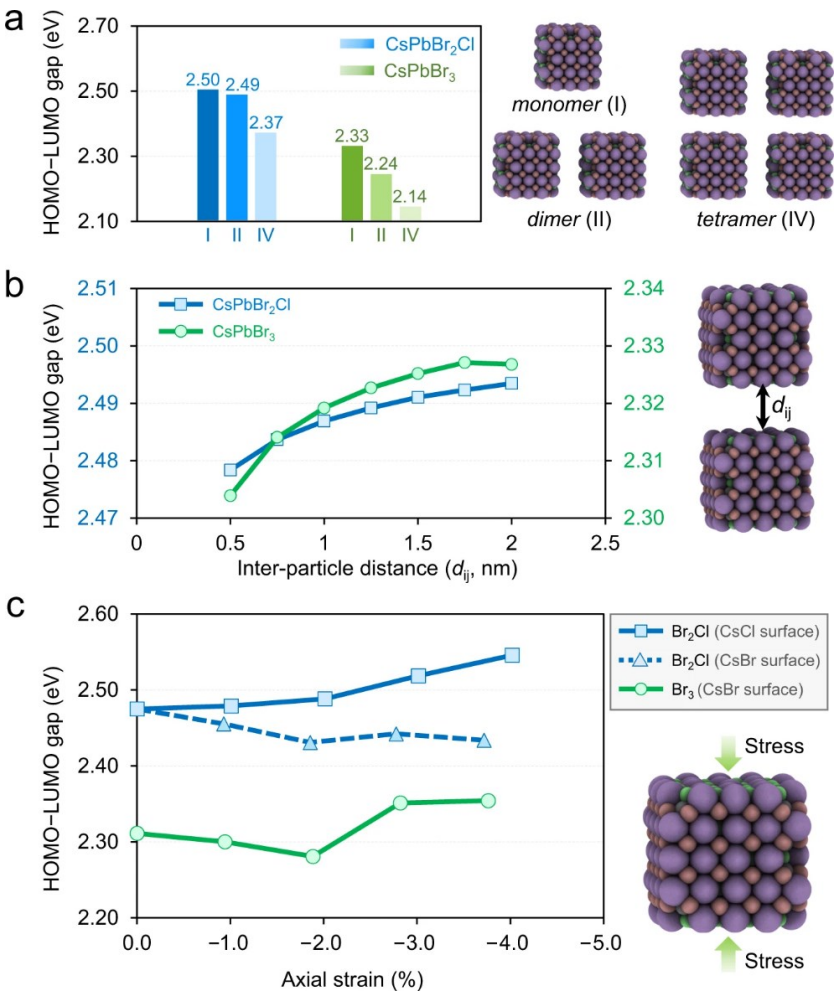

Figure 3.7: Computed HOMO–LUMO gaps as a function of **a)** number of neighboring particles considered (dimers and tetramers are 0.5 nm apart), **b)** distance between two adjacent particles, and **c)** applied axial strain, for both $CsPbBr_2Cl$ and $CsPbBr_3$ particles. All energies are in eV computed at PBE/DZVP level of theory.

Overall, our computational modeling suggests that the spectral blueshift of the fluorescence from the edges of the supercrystal can be caused mainly due to a reduced NC coordination number at the edges as well as the compressive atomic lattice strain in some cases, knowing that the third factor—the shorter interparticle distance—works in the opposite direction, facilitating electronic coupling between adjacent nanocrystals and decreasing the optical gap. However, since the experimentally measured spectral shift is seemingly a combination of all three effects discussed above, a fully quantitative prediction would require more detailed knowledge on their relative contributions as well as the relative orientation and positions of individual nanocrystals, which are currently not available.

3.4 Discussion

When NCs are self-assembled into supercrystals from colloidal solution via slow drying, the increasing curvature and surface tension of the evaporating solvent invokes compressive strain on the supercrystal.[187,188] We hold such a strain responsible for the observed compression of the unit cell parameter by over 20% of the $CsPbBr_2Cl$ NC supercrystals in **Figure 3.4 b**. This compression is possible due to the softness of the oleylamine/oleic acid ligand shell of the NCs, enabling a large decrease of the interparticle distance by growing interdigitation of adjacent ligand spheres. We note that the compression occurs gradually over a length scale of many lattice planes (>1 µm), meaning that it is not a localized surface reconstruction as commonly observed in atomic crystals.[167] The accompanying loss in the angular correlation of the constituting NCs with the superlattice fits a scenario where strain in the supercrystal is partially relieved by forming local structural defects. The comparison of the average (**Figure 3.3 c**) *vs.* the local (**Figure 3.4**) structure of the supercrystal shows that such distortions are indeed frequently present. We note that recent work on $CsPbBr_3$ NC supercrystals reported perfect structural coherence exclusively in the out-of-plane direction.[179] Since our experiment is only sensitive to in-plane structural features, the findings here are not contradictive to that report.

Our results in **Figure 3.4 c** support the view of Kapuscinsky *et al.* that strain during the self-assembly is initially isotropic but later becomes increasingly anisotropic.[187] In a simple cubic supercrystal, the preferred direction for anisotropic structural changes to manifest is the $\langle 111 \rangle_{SC}$, which will result in a shear deformation of the ligand spheres.[189] The expected structure of the supercrystal after this shear deformation is reasonably resembled by the local structure depicted in **Figure 3.4**.

The compression in the supercrystals is not exclusively limited to the soft ligand sphere. With an interparticle distance of <1 nm close to the edges of a supercrystal, the space for the two ligand spheres of adjacent NCs is so constrained, that the inorganic cores of the NCs become compressed as well (**Figure 3.6**). Strain in lead halide perovskite thin films plays an important role for their optoelectronic properties and application in photovoltaic devices.[190] Our fluorescence and fluorescence lifetime data in Figure **3.1** and **Figure 3.2** suggest that this is also the case for lead halide NC supercrystals. A comparison of Figure **3.1** with **Figure 3.4 b** reveals a strong correlation between the gradual blueshift of the fluorescence peak wavelength and the progressive compression of the supercrystal. We suggest that the shift by up to 20 meV is the result of three, partially competing phenomena: (1) a loss in structural coherence as well as isoorientation of NCs (**Figure 3.5 c,d**), (2) a decrease of the interparticle distance (**Figure 3.4 b**), and (3) the distortion of the atomic lattices of the NCs (**Figure 3.6**). Our DFT calculations in **Figure 3.7 a** suggest that the first effect should be associated with a significant blueshift of the fluorescence due to reduced coupling, consistent with a previous report about the importance of structural coherence for electric transport in supercrystals.[162] While the second effect can only lead to a redshift (**Figure 3.7 b**), the third effect is also shown to invoke a blueshift for specific facets or magnitudes of strain (**Figure 3.7 c**).

With reference to several studies on $CsPbBr_3$ NCs which reported a redshifted fluorescence after assembly into supercrystals, we note that the resultant peak wavelength may further be affected by the concomitant changes in the dielectric environment, aging, miniband formation as well as cooperative emission.[74,164,191–193] However, most of these observations were made under markedly different conditions, such as low temperature, prolonged exposure to air, or self-assembly at the liquid/gas interface, which may be the reason that they are not a dominating factor in our study.

We note a previous report on the spatially resolved fluorescence of $CsPb(I_{0.28}Br_{0.72})_3$ NC supercrystals with a similar fluorescence blueshift between the center and the edge.[152] As a main conclusion, gradual release of I_2 gas under intense laser illumination led to the blueshift since lead bromide perovskites exhibit a larger bandgap than the corresponding lead iodide perovskites. The authors argued that the I_2 loss commenced from the edges towards the center, which would explain the spatial fluorescence variations. In $CsPbBr_2Cl$ however, this mechanism is not easily applicable since the reduction potential of Br^- is much lower than that of I^-. In line with this, $CsPbBr_3$ NC supercrystals without a halide mixture show a similar blueshift, indicating that a change in the mixed halide composition is not required to observe the effects reported here.

The decrease of the fluorescence lifetime in **Figure 3.2** is also strongly correlated with the gradual compression of the supercrystal towards the edges. Moreover, many supercrystals exhibit particularly decreased lifetime values at the corners, which bears similarities with the anisotropic changes in the lattice spacings in **Figure 3.4 c**, highlighting again the correlation between structural and optical properties. We speculate that the increased atomic lattice distortion and loss of structural coherence near the edges of the supercrystals result in a reduced stability of the excited state of the emitting NCs. This view is supported by the decreased radiative lifetime values from these locations as well as previous reports on the fluorescence lifetime at grain boundaries of large organic-inorganic pervoskites.[194,195] In view of the currently pursued application of lead halide NC supercrystals as superfluorescent emitters,[74,165] this would imply that bright and coherent emission originates from the center of the supercrystals as long as they are freshly prepared. Conversely, for aged $CsPbBr_2Cl$ NC supercrystals, the lifetimes are longest at the edges, which points to an increased stability of the excited state, potentially due to the formation of a protective oxide shell.[196]

As an alternative explanation for the spatial differences in the fluorescence (-lifetime) in the supercrystals, we also consider a photon propagation effect, that is, multiple

emission and (re-)absorption events, which become more likely with increasing thickness of the emitter material.[191] Therefore, reabsorption should occur predominantly in the center of the supercrystals but not at the edges. This effect results in an overall redshift of the fluorescence and an increase of the fluorescence lifetime, which would be in line with the observations in this work.[197,198] Moreover, we would expect the absolute fluorescence intensity per emitter to be lower for an area with frequent reabsorption events and the time-resolved fluorescence decay to be increasingly multiexponential due to the non-radiative losses and multi-step nature of the photon propagation effect. However, we find the fluorescence decay to be monoexponential (**Figure S3.2 c** and**Figure** S3.3 **c**) and the fluorescence intensity to be highest in the center, from where it gradually decreases toward the edges (**Figure S3.6 b and****Figure** S3.7 **b**). This decrease extends over a much larger distance than the flattening of the edges which we occasionally observe on less facetted supercrystals (**Figure S3.9 c**), such that the high fluorescence intensity in the center cannot be a mere thickness effect. We note that we would expect a negative correlation between the fluorescence intensity with its corresponding lifetime if reabsorption was dominant in the supercrystals, but we do not find such a correlation in our data (**Figure S3.6 f and****Figure** S3.7 **f**). In summary, given the relatively high fluorescence quantum yield of lead halide perovskite NCs, reabsorption is likely to partially contribute to the spatially varying optical properties of supercrystals thereof,[199] but our data is inconsistent with it as the dominant cause.

In conclusion, supercrystals of lead halide perovskite NCs self-assembled from solution exhibit a loss in structural coherence, an increasing atomic misalignment between adjacent NCs, and compressive strain near their surfaces. These structural distortions are strongly correlated with a blueshifted fluorescence and decreased radiative lifetimes. We note that structural distortion and surface defects have been shown to strongly affect the fluorescence properties in atomic crystals, such as transition metal dichalco-

genides.[168–172] The structure-fluorescence correlations in supercrystals revealed here are thus another example for the analogy between atoms and NCs as so-called quasi-atoms.

Acknowledgement

We acknowledge DESY (Hamburg, Germany) for the provision of experimental facilities. Parts of this research were carried out at PETRA III synchrotron facility and we would like to thank the beamline staff for assistance in using the Coherence Application P10 beamline. This work was supported by the Helmholtz Associations Initiative Networking Fund (grant No. HRSF-0002), the Russian Science Foundation (grant No. 18-41-06001) and the DFG under grants SCHE1905/8-1, SCHE1905/9-1, AN680/6-1 and SCHR700/38-1. D.L., N.M., D.As., Y.Y.K., M.Sp., and I.A.V. acknowledge support of the project by Edgar Weckert.

Authors contribution

D.L., C.K., and J.H. contributed equally to this work. D.L., D.As., J.C., Y.Y.K., N.M., I.Z. and M.Sp. performed the X-ray scattering experiments. C.K., S.W. and J.W. synthesized the NCs, conducted optical absorption and fluorescence measurements in solution and prepared all samples. J.H. carried out the confocal fluorescence (-lifetime) measurements. M.M. performed DFT calculations and A.M. undertook the SEM and AFM measurements. F.S., A.J.M., K.B., D.A., I.A.V. and M.S. conceived and supervised the project. D.L., J.H., M.M., I.A.V. and M.S. wrote the manuscript with input from all authors. All authors have given approval to the final version of the manuscript.

Competing interests

The authors declare no competing interests.

Data availability

The X-ray and optical data that support the findings of this study are available in Zenodo.org at https://zenodo.org/deposit/5607366.[200]

3.5 Methods

Chemicals

1-Octadecene (ODE), technical grade, 90%, Sigma Aldrich; Oleic acid (OA), 97%, Acros Organics; Oleylamine (OAm), 80 - 90%, Acros Organics; Caesium carbonate (Cs2CO3), 99.99% (trace metal basis), Acros Organics; Lead(II)chloride (PbCl2), 99.999% (trace metal basis), Sigma Aldrich; Lead(II)bromide (PbBr2), ≥98%, Sigma Aldrich; Toluene, 99.8%, extra dry, AcroSeal, Acros; Tetrachloroethylene (TCE), ≥99%, Acros Organics; Kapton® polyimide membranes (125 µm thickness) were purchased from DuPont; Si/SiOx wafers (200 nm SiOx thickness) were purchased from Siegert Wafer GmbH. All chemicals were used as purchased.

Preparation of Cs-oleate

203.5 mg Cs_2CO_3 (0.625 mmol) was loaded into a 25 mL three-neck flask along with 10 mL 1-octadecene and 0.625 mL oleic acid, dried for 1 h at 120 °C and then heated to 150 °C under nitrogen atmosphere until all Cs_2CO_3 reacted with oleic acid. The mixture was kept in a glovebox and heated to 110 °C before injection.

Synthesis of $CsPbX_3$ nanocrystals

$CsPbX_3$ NCs were made by a hot-Injection synthesis using a modified literature method.[29] To synthesize 9 nm $CsPbBr_3$ or 7 nm $CsPbBr_2Cl$ NCs, 138 mg (0.38 mmol) $PbBr_2$ or 92 mg (0.25 mmol) PbBr2 and 35 mg (0.125 mmol) $PbCl_2$ were degassed in 10 mL ODE in a 25 mL three- neck flask under reduced pressure at 120 °C for 2 h.

Then, 1 mL of dried oleylamine (OAm) and 0.5 mL of dried oleic acid (OA) were injected at 120 °C under nitrogen atmosphere with continuous stirring and the reaction mixture was heated to 160 °C. After the solubilization was completed, 0.8 mL of a previously prepared solution of Cs-oleate in ODE (0.125 M) was swiftly injected, and the reaction mixture was cooled to room temperature using an ice-bath.

Isolation and purification of $CsPbX_3$ nanocrystals

$CsPbX_3$ NCs were collected by centrifuging the suspension (7000 rpm, 10 min), decanting the supernatant, and collecting the precipitate. The precipitate was centrifuged again without addition of a solvent (7000 rpm, 5 min), and the resulting supernatant was removed with a syringe, to separate the traces of residual supernatant. The precipitate was dissolved in 2 mL hexane and centrifuged again (2500 rpm, 5 min) to remove aggregates and larger particles. The resulting supernatant was filtered through a 0.2 µm PTFE syringe filter and stored as stock solution inside of a glovebox with a typically concentration of 16 mM following Maes *et al.*[201]

Self-assembly of NC superlattices

For the growth of supercrystals, different substrates (Si wafer, Kapton, glass) were used, depending on the desired experiment. The self-assembly experiment was set up in a glass Petri dish (with a 60 mm diameter), for this purpose three substrates each were placed in such a Petri dish together with a PTFE-lid filled with 1 mL tetrachloroethylene. To each of these substrates, 40 µL of a 1 – 3 mM solution of the perovskites in TCE was added. The lid of the Petri dish was closed, covered with aluminum foil, and allowed to stand for 24 h. After that, the lid was opened and left for another 5 h to dry completely. All self-assembly preparations were performed under inert atmosphere. The more monodisperse the size distribution of the perovskites, the better the resulting superlattices

Spatially resolved optical measurements

All spatially resolved optical measurements were performed using a home-built inverted confocal laser scanning microscope. The measurements were performed on glass substrates utilizing a high numerical aperture oil immersion objective (NA = 1.4) and a 405 nm pulsed diode laser (Picoquant LDH P-C-405) with variable repetition rates (Picoquant PDL 800-D laser driver) as the excitation source. Under these conditions the lateral resolution of the instrument is approximately 200 nm. A single photon avalanche diode (MPD PDM Series) was used in conjunction with the Picoquant HydraHarp 400 as a time-correlated single photon counting system to detect time-resolved fluorescence. Time-resolved data acquisition and analysis was performed using Picoquants SymPhoTime 64 software package. The spectral data was recorded using an Acton Spectra Pro 2300i spectrometer with a 300 grooves/mm grating. The detector temperature (Princeton PIXIS CCD) was kept steady at –45 °C.

X-ray diffraction experiment

The nano-diffraction experiment was performed at the Coherence Applications beamline P10 of the PETRA III synchrotron source at DESY. An X-ray beam with the wavelength $\lambda = 0.0898$ nm ($E = 13.8$ keV) was focused down to a spot size of approximately 400 × 400 nm^2 (FWHM) with a focal depth of about 0.5 mm at the GINIX nano-diffraction endstation.[202] The two-dimensional detector EIGER X 4M (Dectris) with 2070 × 2167 pixels and a pixel size of 75 × 75 µm^2 was positioned 412 mm downstream from the sample. The detector was aligned ~6 cm off-center in both directions normal to the incident beam to allow simultaneous detection of SAXS and WAXS. We performed a spatially resolved scan of the sample on a Kapton substrate by 25 × 25 spatial points with 500 nm step size and collected 625 diffraction patterns in transmission geometry. The exposure time was set to 0.5 s to prevent radiation damage of the

sample. The background scattering pattern from a pure Kapton film was subtracted from every collected pattern.

Bragg peak analysis

Each diffraction pattern was interpolated onto a polar coordinate grid with the origin at the direct beam position. The radial profiles were obtained by averaging along the azimuthal coordinate. To extract parameters of the WAXS and SAXS Bragg peaks separately, we fitted each of them by the 2D Gaussian function

$$I\ q,\varphi\ = \frac{I_0}{2\pi\sigma_q\sigma_\varphi}\exp\left[-\frac{q-q_0\ ^2}{2\sigma_q^2}-\frac{\varphi-\varphi_0\ ^2}{2\sigma_\varphi^2}\right],$$

where I_0 is the integrated intensity, q_0 and φ_0 are the radial and azimuthal central positions, and σ_q and σ_φ are the corresponding root mean square (rms) values. The FWHMs of the Bragg peaks were evaluated according to relations: $w_q = 2\sqrt{2ln2}\ \sigma_q$ and $w_\varphi = 2\sqrt{2ln2}\ \sigma_\varphi$. The fitting was done in the appropriate region of the polar coordinates with a single isolated Bragg peak.

For the SAXS peaks, the parameters were pairwise averaged for the corresponding Friedel pairs of the Bragg peaks to improve statistics. The resulting momentum transfer values and angles were used to calculate the real-space parameters of the unit cell: the length of the basis vectors a_1 and a_2, the angle γ between them and the average azimuthal position φ counted counterclockwise from an arbitrary horizontal axis (see Supplementary Materials for details).

For the WAXS peaks, we calculated an average Bragg peak intensity IAL and the azimuthal position Ψ of the $[010]_{AL}$ axis. To obtain the average azimuthal position Ψ, we averaged all four azimuthal positions for 010_{AL}, 020_{AL}, 110_{AL}, and 100_{AL} Bragg peaks, but corrected the last two values by $+45°$ and $-45°$, respectively. We used the Williamson–Hall method[203] to analyze the size of the WAXS Bragg peaks at each spatial

point of the supercrystal. The FWHM of the Bragg peak is determined by the NC size and the lattice distortion as follows:

$$w_{q,\varphi}^2\ q\ = \left(\frac{2\pi K}{L}\right)^2 + (g_{q,\varphi} q)^2, \tag{3.1}$$

where $w_{q,\varphi}$ is the FWHM of the Bragg peak at q in radial or azimuthal direction, respectively, L is the NC size, $g_{q,\varphi}$ is the radial or angular lattice distortion of the atomic lattice, respectively, K is a dimensionless shape parameter that is about 0.86 for cubic NCs.[204] The radial lattice distortion g_q calculated from the radial FWHM wq is equal to the ratio $\delta a_{AL}/a_{AL}$, where δa_{AL} is the FWHM of the unit cell parameter distribution around the mean value a_{AL}. The angular lattice distortion g_φ calculated from the azimuthal FWHM w_φ is equal to the FWHM $\delta\Psi$ of the angular distribution of the NCs around their average azimuthal position Ψ. For the spatially resolved analysis of the FWHMs, the NC size L was fixed at the value, obtained from the average radial profiles. For details of the analysis, see Supplementary materials.

Scanning electron and atomic force microscopy

SEM imaging of supercrystals on Si/SiOx devices was performed with a HITACHI model SU8030 at 30 kV. To estimate the thickness of micro-crystals, samples were tilted by 45° with respect to the incoming electron beam. AFM investigations were conducted with a Bruker MultiMode 8 HR in contact mode.

Density functional theory calculations

All computations are performed using the CP2K 5.1 program suite using the Quickstep module.[205] The PBE exchange correlation functional,[206] a dual basis of localized Gaussians and plane waves (GPW)[207] with a 350 Ry plane-wave cutoff, double-ζ basis-set

augmented with polarization functions (MOLOPT variant)[208], and GTH pseudopotentials[209] for core electrons are used for all calculations. The van der Waals (VDW) interaction was accounted for by employing Grimme's DFT-D3 method.[210] SCF convergence criterion was set at 10^{-6} for all calculations.

Initial geometries of $CsPbX_3$ (X = Cl, Br) nanocrystals were obtained by cutting small cubes (~2.4 nm) from the bulk, exposing the CsX layer at the surface and maintaining overall charge neutrality of the particle.[211] All structures were then optimized in vacuum using the BFGS optimizer imposing non-periodic boundary conditions with a wavelet Poisson solver,[212] setting a maximum force of $5\,\mathrm{meV}\cdot\mathrm{Å}^{-1}$ (10^{-4} hartree/bohr) as convergence criteria. For these non-periodic systems, axial strain was simulated by fixing the length of one side of the cube. If the relaxed cubic nanocrystal has side length $a \times b \times c$, and stress is to be applied along the z-direction, "c" is fixed at some c' by constraining the z coordinates of both the top and bottom surface-atoms along the z-direction, with all other coordinates of all atoms relaxed. % Strain is reported as $(c' - c)/c \times 100\%$. For calculations involving dimers and tetramers, 2/4 monomers were explicitly considered, but periodic boundary condition was imposed with at least 10 Å vacuum above the surface of the nanocluster to avoid spurious interaction with its periodic image.

3.6 Supplementary Information

Spatially resolved fluorescence of caesium lead halide perovskite supercrystals reveals quasi-atomic behavior of nanocrystals

Dmitry Lapkin[1,*], **Christopher Kirsch**[2,*], Jonas Hiller[2,*], Denis Andrienko[3], Dameli Assalauova[1], Kai Braun[2], Jerome Carnis[1], Young Yong Kim[1], Mukunda Mandal[3], Andre Maier[2,4], Alfred J. Meixner[2,4], Nastasia Mukharamova[1], Marcus Scheele[2,4,+], Frank Schreiber[4,5], Michael Sprung[1], Jan Wahl[2], Sophia Westendorf[2], Ivan A. Zaluzhnyy[5], Ivan A. Vartanyants[1,6,+]

1. *Deutsches Elektronen-Synchrotron DESY, Notkestraße 85, D-22607 Hamburg, Germany*

2. *Institut für Physikalische und Theoretische Chemie, Universität Tübingen, Auf der Morgenstelle 18, D-72076 Tübingen, Germany*

3. *Max Planck Institute for Polymer Research, Ackermannweg 10, D-55128 Mainz, Germany*

4. *Center for Light-Matter Interaction, Sensors & Analytics LISA⁺, Universität Tübingen, Auf der Morgenstelle 15, D-72076 Tübingen, Germany*

5. *Institut für Angewandte Physik, Universität Tübingen, Auf der Morgenstelle 10, D-72076 Tübingen, Germany*

6. *National Research Nuclear University MEPhI (Moscow Engineering Physics Institute), Kashirskoe shosse 31, 115409 Moscow, Russia*

* These authors contributed equally

+To whom correspondence should be addressed

Section S3.1 Optical absorption and fluorescence of $CsPbBr_2Cl$ and $CsPbBr_3$ nanocrystals in solution

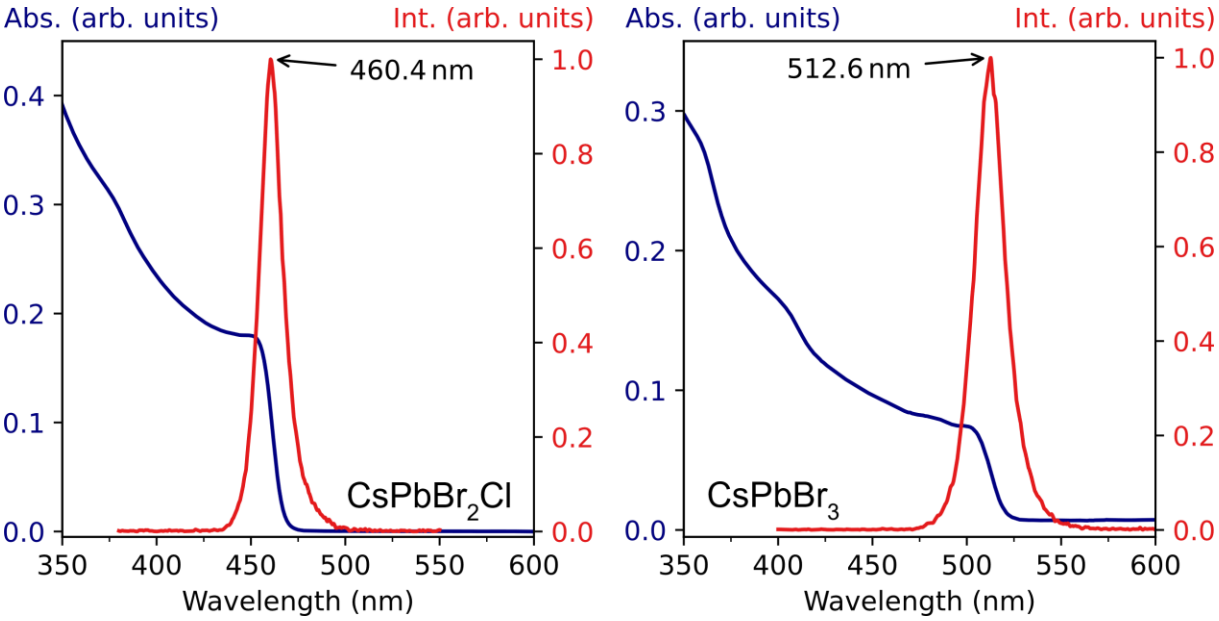

Figure S3.1: a) Absorption and emission spectrum of $CsPbBr_2Cl$ NPs dispersed in Toluene. **b)** Absorption and emission spectrum of $CsPbBr_3$ NPs dispersed in Hexane.

Optical measurements were performed on a UV-vis-NIR spectrometer (Agilent Technologies, Cary 5000) and a fluorescence spectrometer (PerkinElmer FL8500). All spectra were acquired under ambient conditions in Toluol at room temperature (25 °C) in a cuvette of 1 cm pathlength.

Section S3.2 Fluorescence lifetime imaging

A fast fluorescence lifetime imaging microscopy (fast FLIM) image is recorded by scanning the excitation laser over an area of interest while recording the time-resolved fluorescence in the form of a time-correlated single photon counting (TCSPC) histogram at each pixel. The fast lifetime hereby obtained for each pixel is to be understood as the mean photon arrival time after the excitation laser pulse and therefore includes the time the light takes to travel through the instrument. The histogram of the excitation pulse is called the instrument response function (IRF) and was directly measured by the means of scattered light from a clean glass substrate. The physical decay of the sample is obtained by fitting the experimental decay curves recorded at each pixel by

employing the IRF in an n-exponential reconvolution with a maximum likelihood estimation method employed for fit optimization.

For both compositions of the investigated self-assembled supercrystals, good results were obtained by fitting a monoexponential reconvolution to the experimental decay curves. Exemplary fits for the center pixels in the FLIM images of the self-assembled supercrystals composed of $CsPbBr_2Cl$ NCs and $CsPbBr_3$ NCs are depicted in **Figure S3.2** and **Figure S3.3,** respectively.

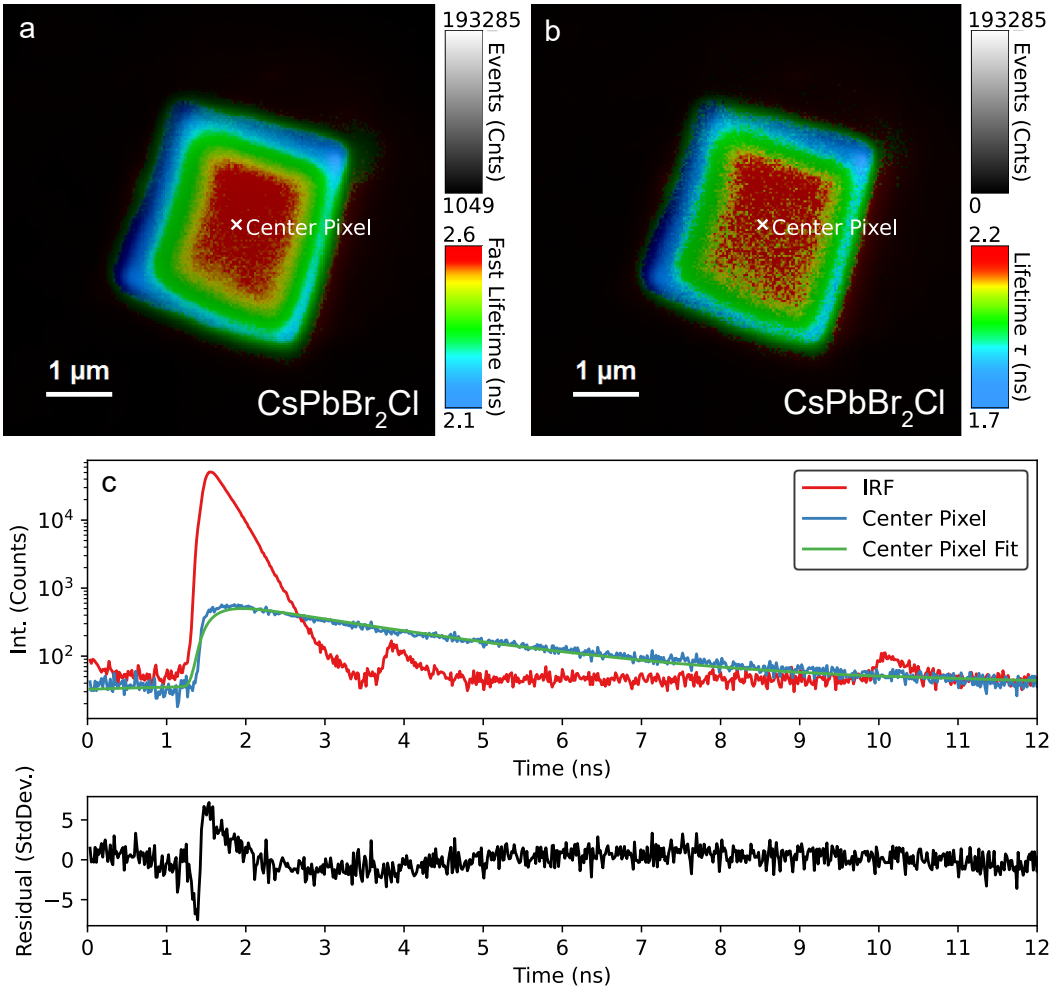

Figure S3.2: For each pixel of the FLIM images the fluorescence intensity is encoded on a brightness scale while fast lifetimes and fluorescence lifetimes are displayed in RGB false color. **a)** Fast FLIM image of a self-assembled $CsPbBr_2Cl$ supercrystal and **b)** the corresponding fitted FLIM image obtained through a pixel-by-pixel monoexponential reconvolution. **c)** The experimentally acquired IRF as well as an exemplary decay curve of a pixel in the center of the supercrystal and its corresponding monoexponential fit.

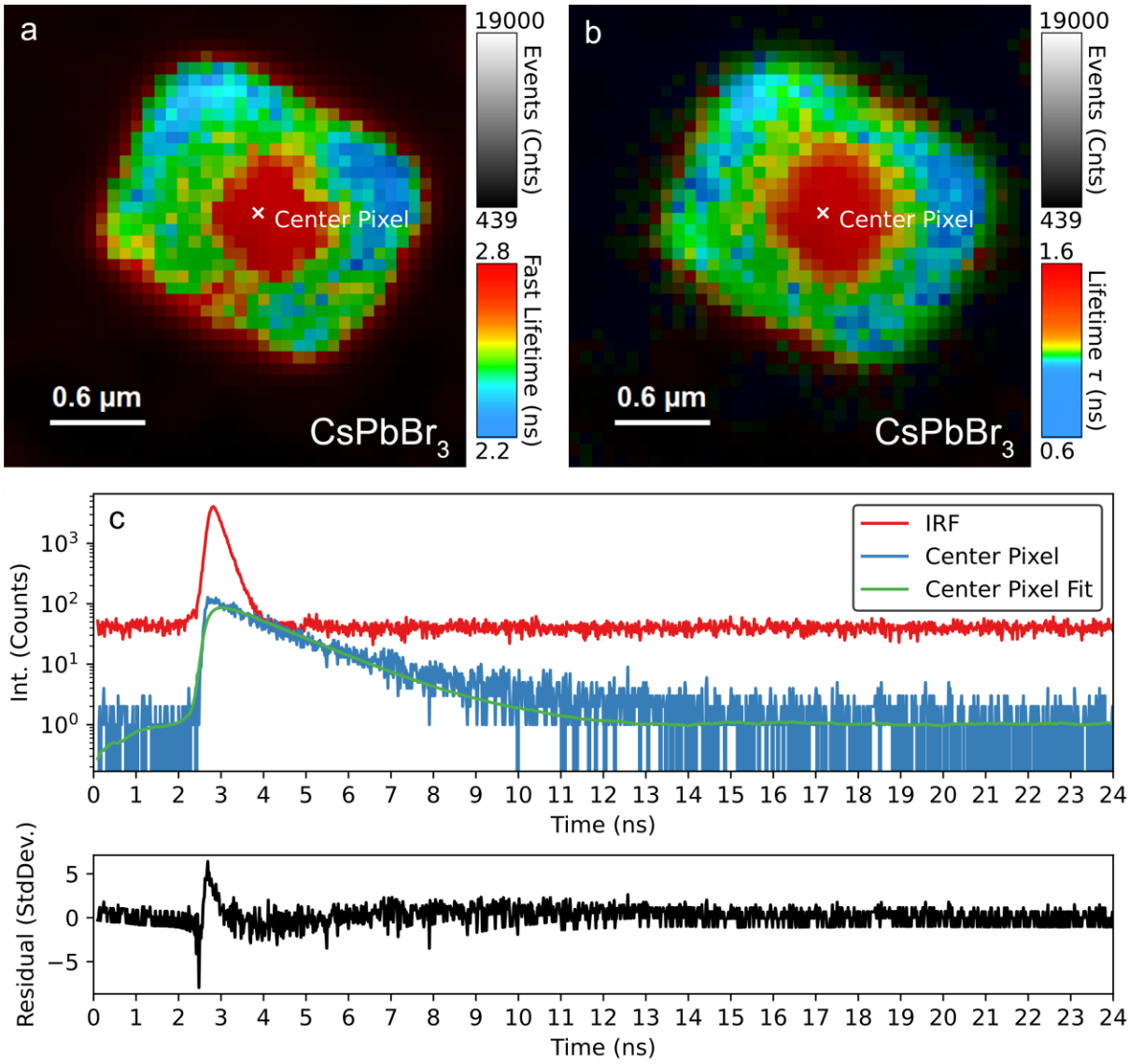

Figure S3.3: For each pixel of the FLIM images the fluorescence intensity is encoded on a brightness scale while fast lifetimes and fluorescence lifetimes are displayed in RGB false color. **a)** Fast FLIM image of a self-assembled $CsPbBr_3$ supercrystal and **b)** the corresponding fitted FLIM image obtained through a pixel-by-pixel monoexponential reconvolution. **c)** The experimentally acquired IRF as well as an exemplary decay curve of a pixel in the center of the supercrystal and its corresponding monoexponential fit.

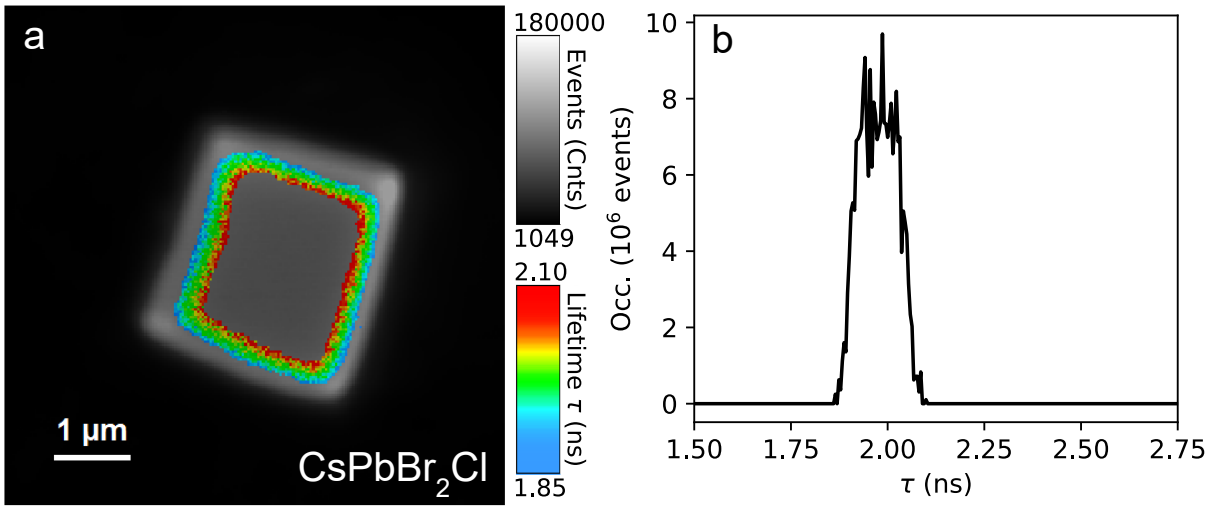

Figure S3.4: a) Region of interest (ROI) FLIM image of the intermediate area of the CsPbBr$_2$Cl supercrystal depicted in Fig. S2. **b)** The occurrence of the τ-values associated with the monoexponential decay throughout the ROI FLIM image. This ROI FLIM image demonstrates that the decrease of the τ-values when scanning from the center of the supercrystal towards its edges is rather gradual. The "step-like" decrease that **Figure S3.2** seems to imply is due to the chosen RGB color- scaling.

Section S3.2.1 Determining the shortest euclidean distance to the supercrystal edge for each pixel

The first step in the analysis is differentiating between the pixels located inside and those located outside of the supercrystal. This was achieved by assigning the lifetime value 0 to each pixel for which the measured fluorescence intensity is less than half the maximum recorded fluorescence intensity. Because the transition between the inside and the outside of the supercrystal is characterized by a steep drop in the recorded fluorescence intensity, all pixels inside the supercrystal are unaffected and keep their non-zero lifetime value, while all pixels outside of the supercrystal are assigned the lifetime value 0. The masking process for the CsPbBr$_2$Cl supercrystal is depicted in **Figure S3.5**. The pixel-to-edge distance for all pixels inside the supercrystal is then the shortest distance between a pixel with a non-zero lifetime value and a pixel with the associated lifetime value 0. The free Python machine learning library Scikit-learn was employed for the actual calculations.

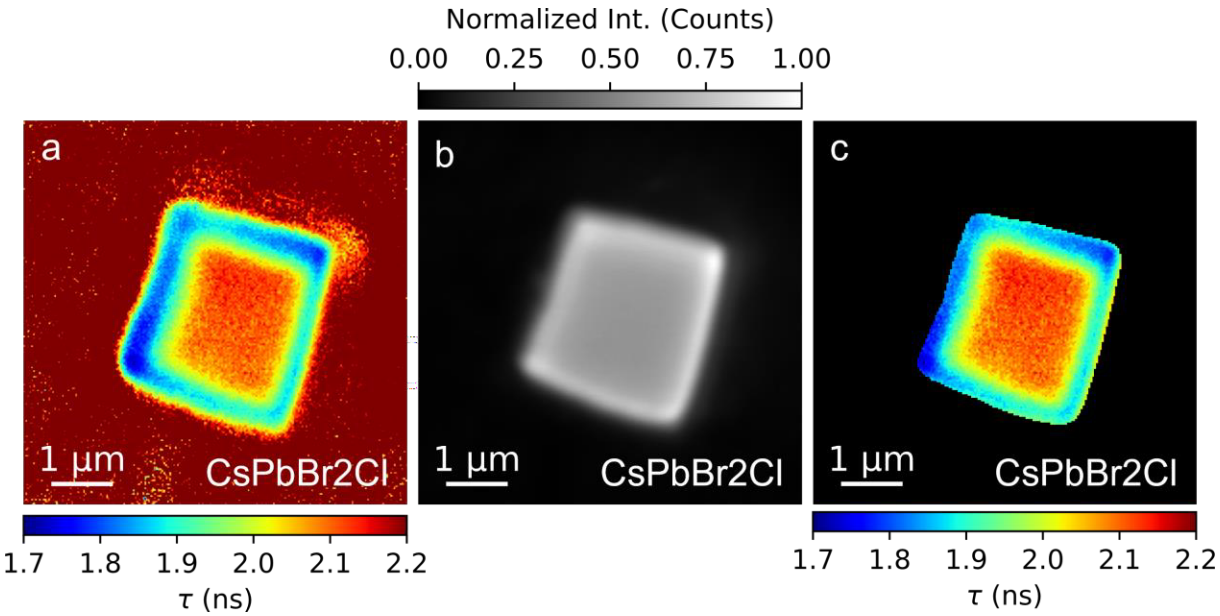

Figure S3.5: For each of the 200x200 pixels the fluorescence lifetime **a)** as well as the fluorescence intensity **b**) are recorded. **c)** Result of assigning the lifetime value 0 to all pixels for which the recorded fluorescence intensity is less than half the maximum recorded fluorescence intensity. All pixels inside the supercrystal remain unaffected and keep their non-zero lifetime value as determined by the measurement.

Section S3.2.2 Concerning the influence of reabsorption / photon recycling

The reabsorption and subsequent reemission of photons is discussed as a factor contributing to the commonly observed redshifting of the photoluminescence of perovskite nanocrystals when assembled into supercrystals.[191,198] One could reasonably speculate that the effect of such a material geometry dependent photon recycling process is not constant throughout the supercrystal, but that the thinning toward the edges of a not entirely homogenous supercrystal results in an outwardly decreasing influence of reabsorption. It stands to reason that areas with higher rates of reabsorption exhibit lower emission intensity, red-shifted photoluminescence, and an increased PL lifetime.

If the spatially resolved optical response of the investigated supercrystals were dominated by changes in the photon propagation due to the supercrystal geometry, we would expect an increase of the PL intensity towards the edges, which would be anticorrelated with a decreasing PL lifetime. The non-normalized single spectra depicted in **Figure S3.6 a, b** and **Figure S3.7 a, b** for a $CsPbBr_3$ and a $CsPbBr_2Cl$ supercrystal respectively, show that for a typical supercrystal the PL decreases when

scanning towards its edges. Furthermore, **Figure S3.6 f** and **Figure S3.7 f** show that there is no clear correlation between the PL intensity and lifetime measured at each pixel for both superlattice compositions. While likely playing an important role in the photophysics of supercrystals, the spatially resolved optical data presented here does not show effects that we would associate with changes in the overall reabsorption.

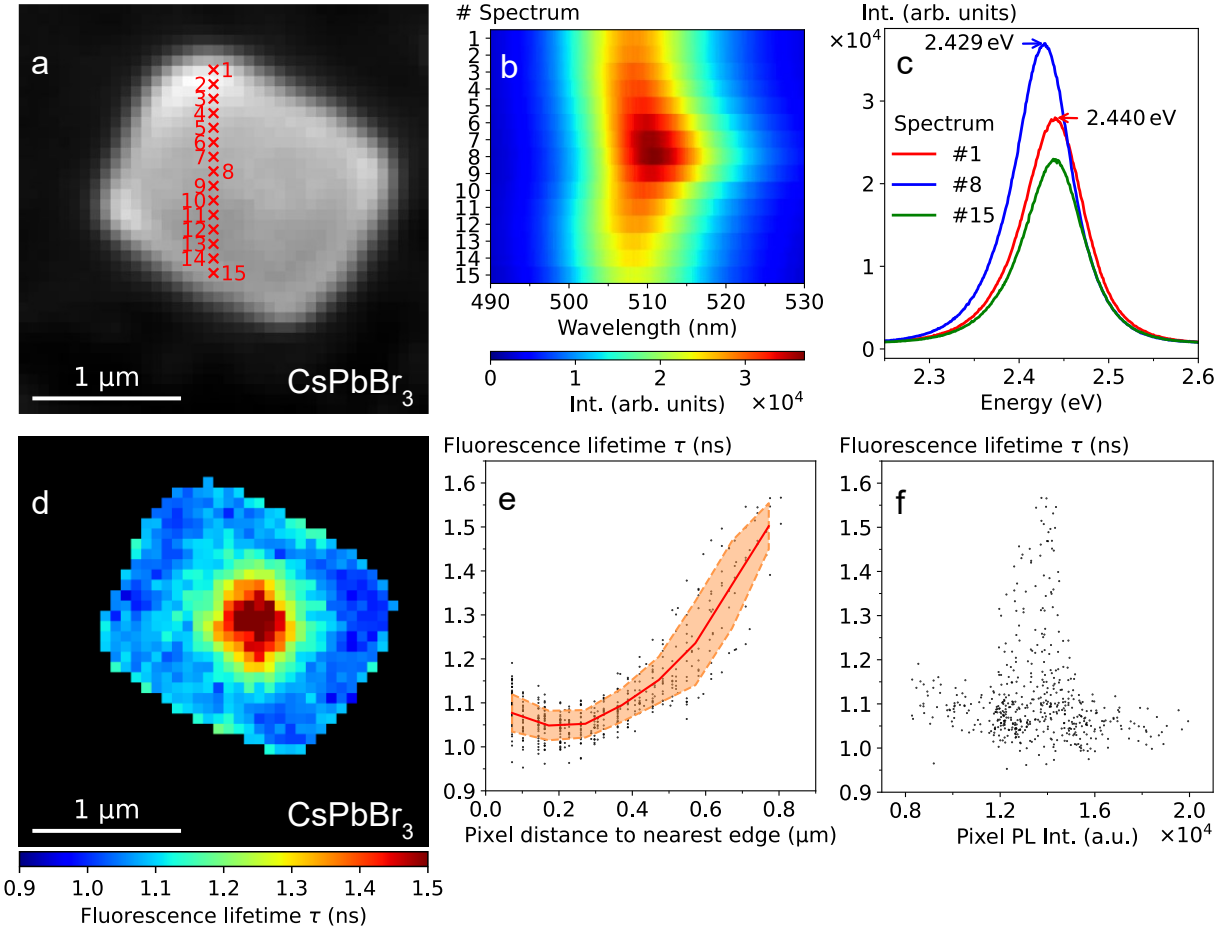

Figure S3.6: a) Positions of photoluminescence single spectra, acquired on a $CsPbBr_3$ supercrystal. **b)** The corresponding spectra. **c)** Selected spectra, acquired at the edges and the center of the supercrystal. **d)** Fluorescence lifetime image of a $CsPbBr_3$ NC supercrystal obtained by fitting the experimental time-resolved fluorescence with a monoexponential decay function. **e)** Fluorescence lifetime values obtained at each pixel inside the supercrystal as a function of the distance to the nearest edge, where the red line shows the mean value, and the dashed lines indicate the confidence interval of $\pm\sigma$. **f)** Fluorescence lifetime values obtained at each pixel inside the supercrystal as a function of the corresponding pixels PL intensity.

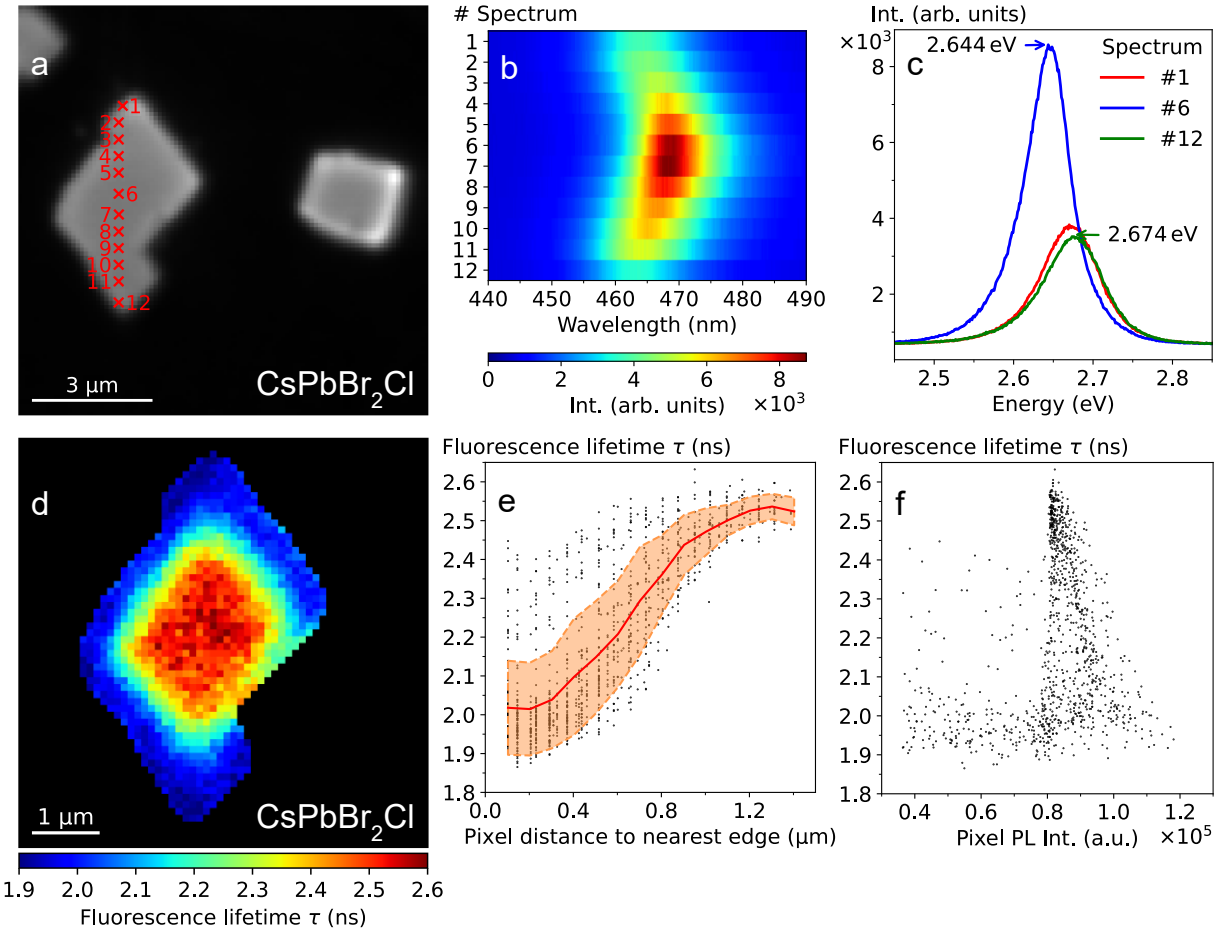

Figure S3.7: **a**) Positions of photoluminescence single spectra, acquired on a $CsPbBr_2Cl$ supercrystal. **b**) The corresponding spectra. **c**) Selected spectra, acquired at the edges and the center of the supercrystal. **d**) Fluorescence lifetime image of a $CsPbBr_2Cl$ NC supercrystal obtained by fitting the experimental time-resolved fluorescence with a monoexponential decay function. **e**) Fluorescence lifetime values obtained at each pixel inside the supercrystal as a function of the distance to the nearest edge, where the red line shows the mean value, and the dashed lines indicate the confidence interval of $\pm\sigma$. **f**) Fluorescence lifetime values obtained at each pixel inside the supercrystal as a function of the corresponding pixels PL intensity.

Section S3.3 Electron microscopy of $CsPbBr_2Cl$ supercrystals

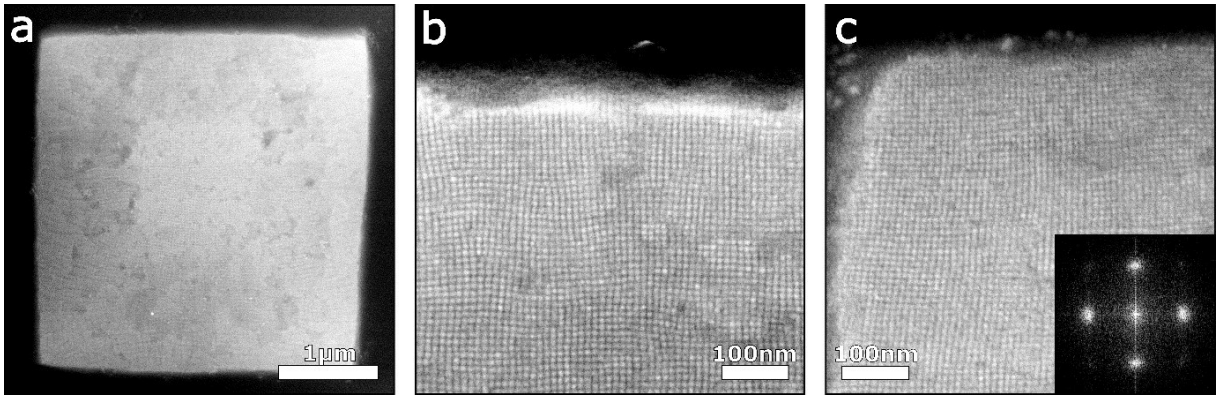

Figure S3.8: a) SEM micrograph of self-assembled supercrystals of $CsPbBr_2Cl$ NCs. The NC diameter is rather uniform over the whole crystal (7.3±0.4 nm), as indicated by the high-resolution micrograph of an edge **b)** and a corner **c)**. The inset of **c)** corresponds to the FFT of the corresponding micrograph, indicating a homogeneous four-fold symmetry of the NC arrangement.

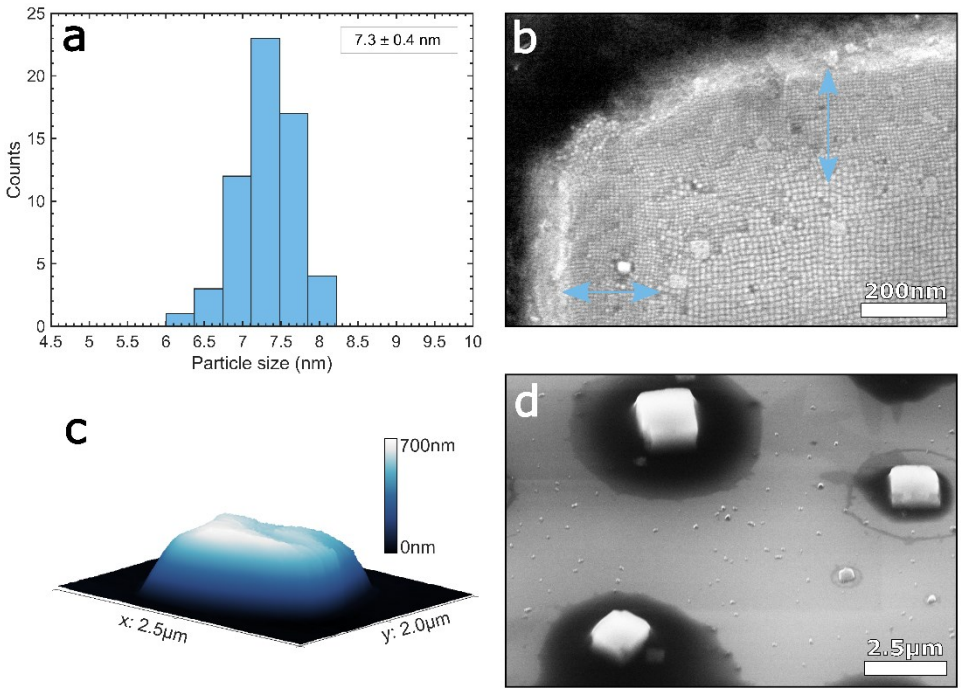

Figure S3.9: a) Distribution of the diameter of the $CsPbBr_2Cl$ NCs, measured by SEM. The mean value is 7.3±0.4 nm (size distribution of ~5%). **b)** SEM micrograph of the corner of a less faceted supercrystals occasionally featuring NCs of smaller size. The spatial extent of this subpopulation is limited to ~200 nm from the edges, indicated by the blue arrows. **c)** 3D AFM map of a supercrystal on a Kapton membrane. **d)** SEM micrograph of three supercrystals on a Si/SiOx wafer under a view angle of 45°. Typical supercrystal thicknesses of 580±120 nm can be observed.

Section S3.4 Atomic structure of the constituting $CsPbBr_2Cl$ NCs

The azimuthally averaged WAXS intensity calculated for the mean pattern for a supercrystal is shown in **Figure S3.10**. There are three prominent peaks originating from the atomic lattice of the $CsPbBr_2Cl$ NCs. The peaks can be attributed to 100_{AL}, 110_{AL} and 200_{AL} reflections of a cubic superlattice. The peaks at $q \sim 24.5$ nm^{-1} can be attributed to 210_{AL} reflection which is only partially covered by the detector. The structured background in the range of $q = 17$–20 nm^{-1} is from the Kapton film. It cannot be fully subtracted due to the anisotropy of scattering from the Kapton film in different spatial point of the scanned area. The peaks were simultaneously fitted by three Gaussian functions:

$$I\ q\ = \sum_{i=1}^{3} \frac{I_i}{\sqrt{2\pi\sigma_i^2}} \exp\left[-\frac{q - q_i\ ^2}{2\sigma_i^2}\right], \qquad \text{(S 3.1)}$$

where I_i is the integrated intensity, q_i is the momentum transfer and $w_i = 2\sqrt{2\ln 2}\sigma_i$ is the FWHM of the i-th Bragg peak. The peaks are at $q_{100} = 10.930 \pm 0.005$ nm^{-1}, $q_{110} = 15.442 \pm 0.002$ nm^{-1} and $q_{200} = 21.900 \pm 0.003$ nm^{-1} giving the unit cell parameter $a_{AL} = 0.574 \pm 0.001$ nm. The errorbars are the fitting errors. One should note that the expected atomic lattice structure for caesium lead halide perovskites at room temperature is orthorhombic.[184] However, the deviation of the unit cell parameters of such orthorhombic lattice from a cubic lattice is $< 2\%$. We are not able to resolve the peaks of the same order with so small separation due to the size-dependent Scherrer broadening of the Bragg peaks. Thus, we used the pseudocubic indexing of the Bragg peaks, where the 100_{AL} index corresponds to 110_{AL} and 002_{AL} reflections of the orthorhombic structure, the 110_{AL} – to 200_{AL} and 112_{AL}, the 200_{AL} – to 220_{AL} and 004_{AL}.

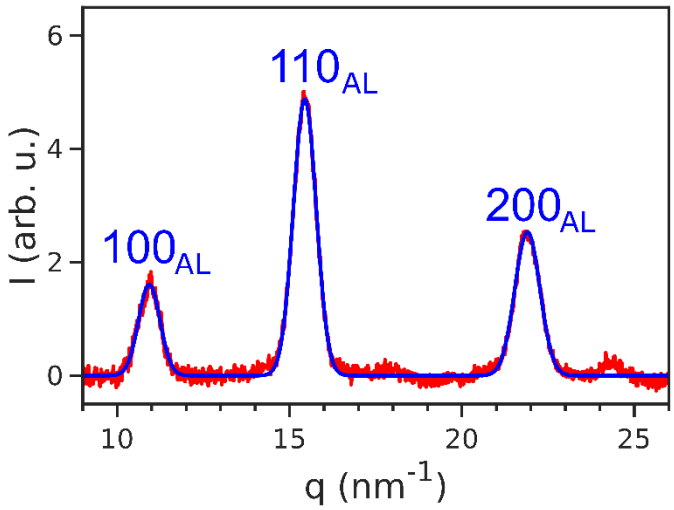

Figure S3.10: Azimuthally averaged intensity profile in WAXS region (red line) and Gaussian fitting including three peaks (blue line). The peaks are indexed according to a pseudocubic structure.

The FWHMs of the peaks extracted by the fitting are w_{100} = 0.736±0.011 nm^{-1}, w_{110} = 0.784±0.004 nm^{-1}, w_{200} = 0.856±0.08 nm^{-1}. We analyzed the FWHMs of the peaks by the Williamson-Hall method.[203] According to the method, the FWHMs of the Bragg peaks are defined by two factors: the size of coherently scattering domain L and the lattice distortion g (the ratio $\delta a_{AL}/a_{AL}$ of the FWHM δa_{AL} of the unit cell parameter distribution around the mean value a_{AL}). If we assume that the coherently scattering domain is a NC, the Williamson-Hall equation can be written as follows:

$$w^2\ q\ = \left(\frac{2\pi K}{L}\right)^2 + \ gq\ ^2, \qquad \text{(S 3.2)}$$

where $w(q)$ is the FWHM of the Bragg peak at momentum transfer q, K – a dimensionless shape factor, L – the NC size and g – the lattice distortion.

The first term is the pure Scherrer broadening, where the shape factor K is about 0.85 for the reflections of low orders for a cubic crystallite.[204] One should note, the size of coherently scattering domain can be bigger than a single NC if there are perfectly aligned NCs scattering coherently to the same direction. However, the fact that the WAXS Bragg peaks are much broader in the azimuthal direction than in the radial

(see the main text for the WAXS pattern), indicate a high degree of angular disorder of the NCs (will be discussed below) leading to low probability of such a scenario.

To extract the NC size L and the lattice distortion g, we fitted the experimentally obtained FWHMs and q-values for the present 100_{AL}, 110_{AL} and 200_{AL} peaks with **Equation (S 3.2)** as shown in **Figure S3.11**. The resulting parameters are L = 6.8±0.1 nm and g = 2.3±0.1%. The resulting NC size L is even smaller than the size L_{SEM} = 7.3±0.4 nm obtained from SEM measurement that indicates the correctness of the assumption that the coherently scattering domain consist of a single NC. The smaller size can be explained by the lattice twinning inside the NC leading to smaller domains and by the limits of the method.

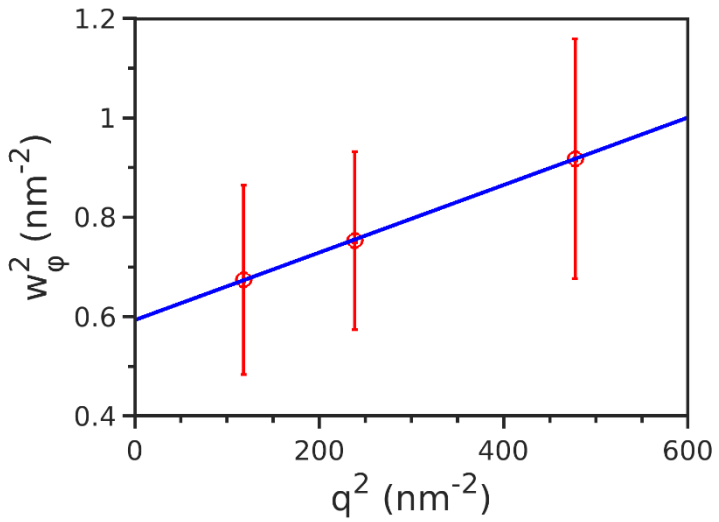

Figure S3.11: Williamson-Hall plot for the radial FWHM values of the WAXS Bragg peaks. The red points are experimental values, the blue straight line is the best fit.

Section S3.5. Local superlattice structure

The single SAXS diffraction patterns at different spatial points of the supercrystal are quite different from the average diffraction pattern shown in **Figure 3.3 c** in the main text. Examples of the single patterns are shown in **Figure S3.12**. Clearly, the Bragg peaks do not maintain their positions in both radial and azimuthal directions and change their shape from point to point.

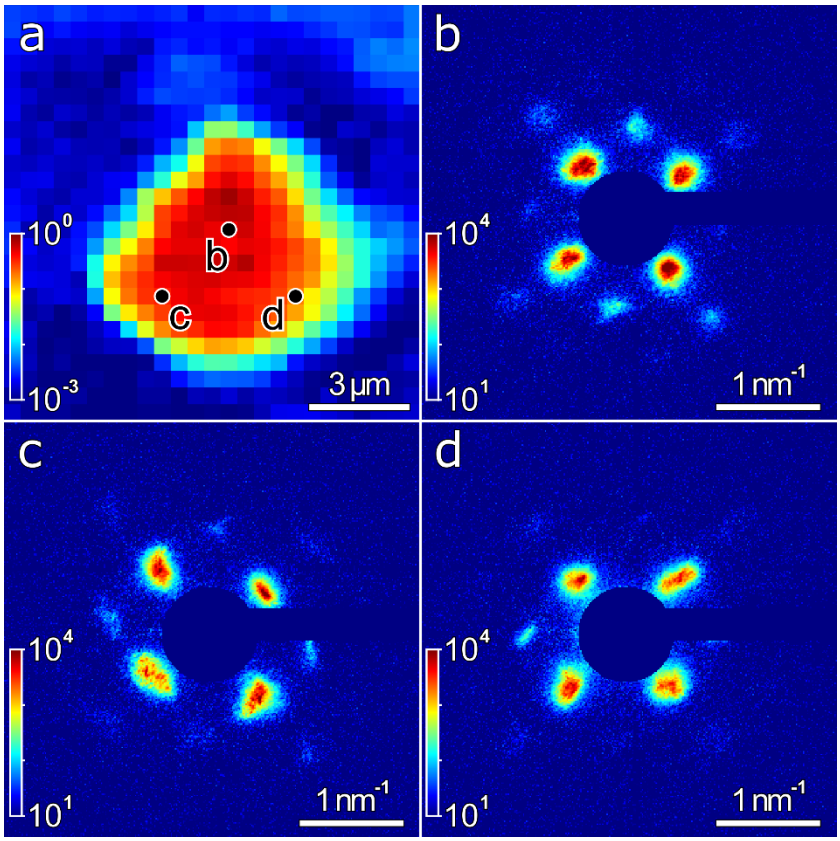

Figure S3.12: a) SAXS intensity-based map of the sample. The pixel size is 500 nm. **b) – d)** Examples of single SAXS diffractions patterns collected at the points indicated in panel **a).**

To study dependence of their parameters on the spatial position within the sample, we evaluated each single diffraction pattern separately. We fitted each of the first order Bragg peaks in the SAXS region by the Gaussian function:

$$I\ q,\varphi\ = \frac{I_0}{2\pi\sigma_q\sigma_\omega}\exp\left[-\frac{q-q_0\ ^2}{2\sigma_q^2}-\frac{\omega-\omega_0\ ^2}{2\sigma_\omega^2}\right], \qquad \text{(S 3.3)}$$

where I_0 is the integrated intensity, q_0 and ω_0 are the radial and azimuthal positions, $w_q = 2\sqrt{2\ln 2}\sigma_q$ and $w_\omega = 2\sqrt{2\ln 2}\sigma_\omega$ are the corresponding FWHMs of the Bragg peak. The fitting was done in the appropriate region of the polar coordinates with single isolated Bragg peak.

There are two Friedel pairs of the Bragg peaks corresponding to reflections from the $(100)_{SL}$ and $(010)_{SL}$ superlattice planes. Counting from the right-pointing horizontal axis, the 1st and 3rd peaks correspond to the $(100)_{SL}$ plane and the 2nd and 4th – to the $(010)_{SL}$

plane. We averaged the intensities, the radial and azimuthal positions and the FWHMs within each pair to get more reliable characteristics of the superlattice planes. The azimuthal coordinates of the 3rd and 4th peaks were corrected by -180° prior to the averaging. Finally, we have two sets of the characteristics defined in **Figure S3.13 a**. The reciprocal space coordinated were converted into the coordinates of the real-space basis vectors a_1 and a_2.

The azimuthal positions are converted into real space as follows:

$$\varphi_1 = \omega_2 - 90° \tag{S 3.4}$$

$$\varphi_2 = \omega_1 + 90° \tag{S 3.5}$$

The nearest-neighbor distances a_1 and a_2 are calculated as:

$$a_1 = \frac{2\pi}{q_1 \cdot \sin\gamma} \tag{S 3.6}$$

$$a_2 = \frac{2\pi}{q_2 \cdot \sin\gamma} \tag{S 3.7}$$

We also used additional azimuthal coordinates that are the azimuthal position of the mean line M between the a_1 and a_2:

$$\varphi = \frac{\varphi_1 + \varphi_2}{2} \tag{S 3.8}$$

and the angle γ between the real space basis vectors $\mathbf{a}_1$ and $\mathbf{a}_2$, calculated as:

$$\gamma = \varphi_2 - \varphi_1 \tag{S 3.9}$$

The definition of the real space coordinates is shown in **Figure S3.13 b**.

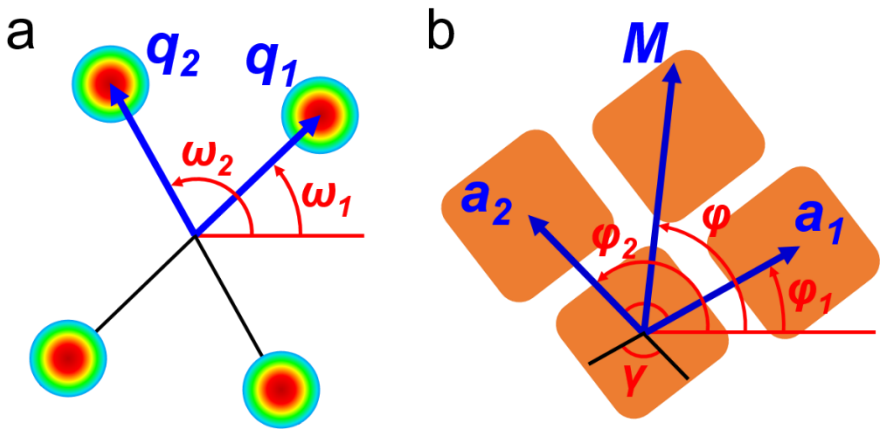

Figure S3.13: a) Scheme of the SAXS diffraction pattern from the superlattice. Only the first order Bragg peaks are shown. Two pairs of Bragg peaks are at momentum transfer values q_1 and q_2 and azimuthal positions ω_1 and ω_2, respectively. **b)** Scheme of the real space unit cell of the superlattice. The nearest neighbors are at distances a_1 and a_2 with azimuthal positions φ_1 and φ_2, respectively. The mean line M between a_1 and a_2 is at azimuthal position φ. The angle between a_1 and a_2 is equal to γ.

The extracted intensities I_1 and I_2 of the Bragg peaks are shown in **Figure S3.14 a,d**. The scattering areas basically coincide except the upper and right corners. Vanishing of the 1st Bragg peak possibly indicates out-of-plane rotation of the SL on these supercrystal edges as soon as such rotation bring the peak out of the Ewald sphere.

The extracted momentum transfers q_1 and q_2 associated with the superlattice plane spacings are shown in **Figure S3.14 b,e**. As it is clear from the figure, the momentum transfers grow on the edges of the supercrystal. It indicates contraction of the superlattice that is thoroughly discussed in the main text as well as its anisotropy.

The extracted azimuthal positions w_1 and w_2 are shown in **Figure S3.14 c,f**. They clearly indicate rotation of the superlattice around the incident beam (normal to the substrate). The rotation is also discussed in the main text.

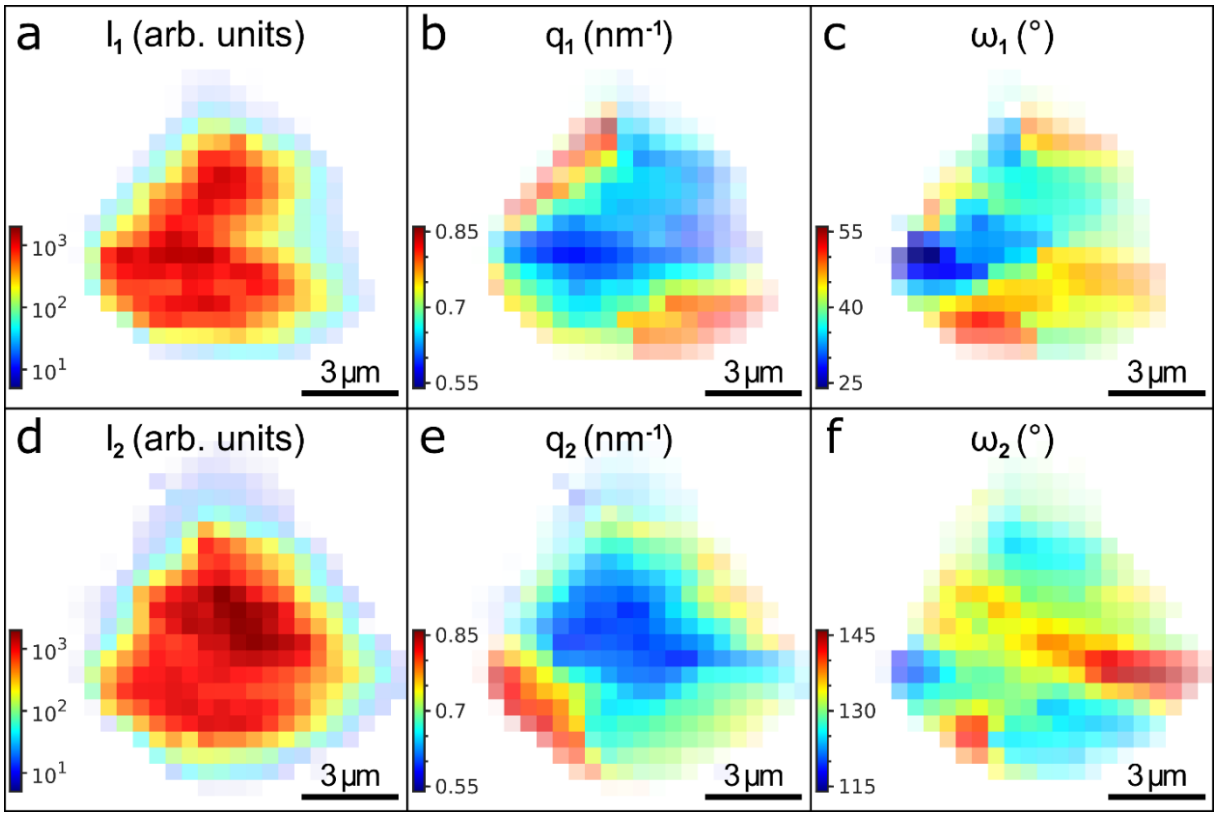

Figure S3.14: Mean extracted parameters: **a, d)** intensities, **b, e)** momentum transfer values and **c, f)** azimuthal positions of **a – c)** the 1st and 3rd and **d – f)** the 2nd and 4th Bragg peaks. The azimuthal positions are counted counterclockwise from a horizontal axis pointing to the right. The azimuthal position of the 3rd and 4th were corrected by -180° before averaging with their counterparts. The pixel size is 500 nm.

The extracted FWHMs in the radial direction w_{q1} and w_{q2} are shown in **Figure S3.15** a,c. Interestingly, in contrast to the momentum transfer values q_1 and q_2, the main deviations in FWHMs happen on the edges to which the crystallographic axes are perpendicular. This means lower dispersion in the superlattice plane separation normal to the edge of the supercrystal.

The extracted FWHMs in the azimuthal direction $w_{\omega 1}$ and $w_{\omega 2}$ are shown in **Figure S3.15 b,d**. There is no clear trend in the behavior of these parameters in respect to the spatial position inside the supercrystal. But most of the point having high FWHM values are located in the middle of the supercrystal, indicating higher dispersion of the angle γ between the lattice vectors a_1 and a_2 as well as of the superlattice orientation angle φ.

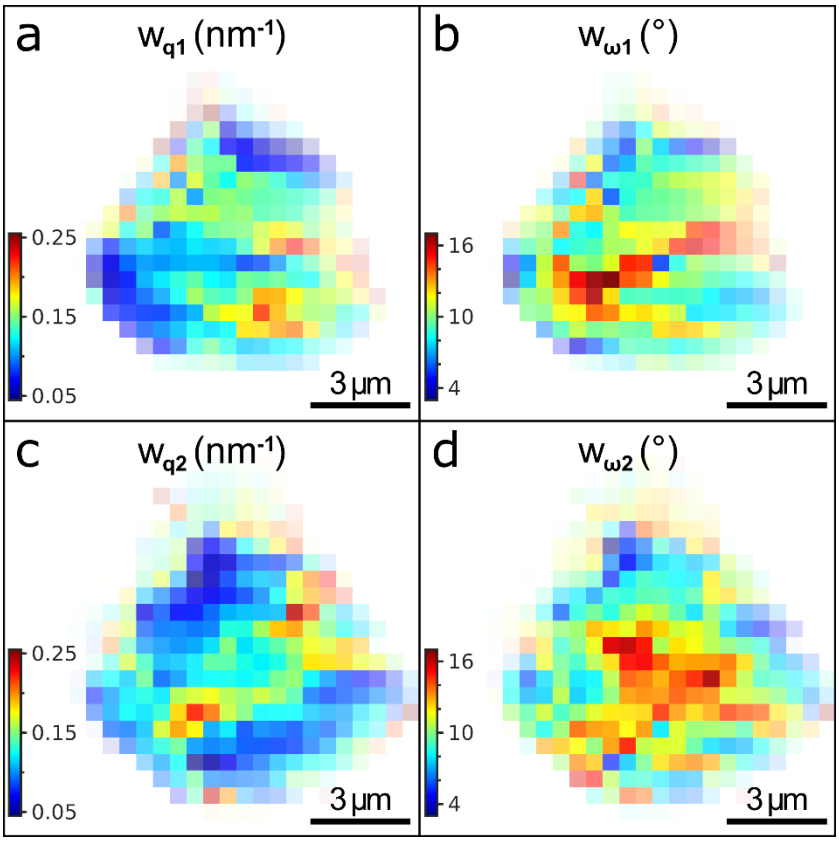

Figure S3.15: Mean extracted FWHMs in **a, c)** radial and **b, d)** azimuthal directions of **a,b)** the 1st and 3rd and **c,d)** the 2nd and 4th Bragg peaks. The pixel size is 500 nm.

The calculated lengths of the lattice vectors a_1 and a_2 are shown in **Figure S3.16**. The distance between the adjacent NCs decrease in both directions on the edges of the supercrystal, but the effect is higher in the direction parallel to the nearest supercrystal edge. For example, in the point 1 in **Figure S3.16**, the distance along $\mathbf{a}_1$, which is pointing to the top-right parallel to the nearest edge, is smaller than along $\mathbf{a}_2$, which is normal to the nearest edge. On the contrary, in the point 2, where $\mathbf{a}_2$ is parallel to the nearest edge, the distance along this direction is smaller than along $\mathbf{a}_1$. The anisotropy of the lattice shrinkage is better visible on the map of the a_2/a_1 ratio that is shown and discussed in the main text.

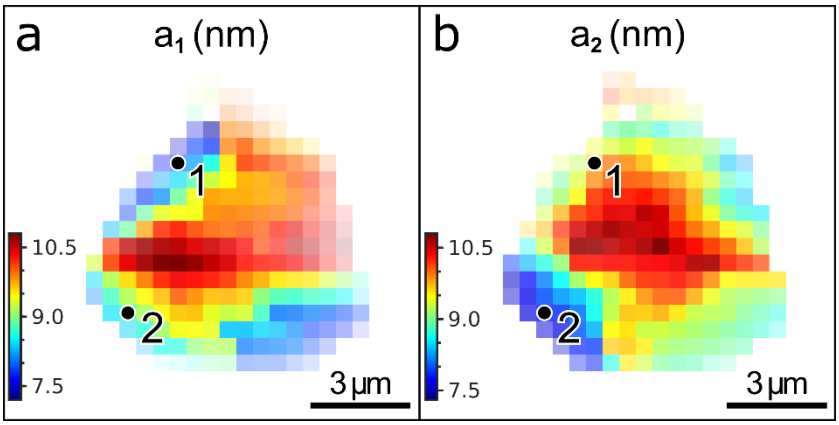

Figure S3.16: Maps of the calculated lengths of the lattice vectors a_1 and a_2. The points 1 and 2 are discussed in the text. The pixel size is 500 nm.

Section S6. NCs orientation inside the SL

In WAXS region, there are four Bragg peaks present on most of the diffraction pattern, as shown on the average one in **Figure S3.17**. Analogous to the SAXS analysis, we fitted each of the peaks separately for each spatial point within the sample with the 2D Gaussian functions (Eq. **(S 3.3)**).

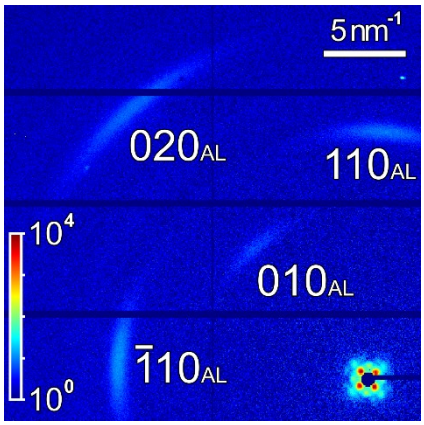

Figure S3.17: Average WAXS diffraction pattern with four prominent Bragg peaks. The indexes are given for pseudocubic atomic lattice oriented along [001] axis.

The intensities of the Bragg peaks extracted this way are shown in **Figure S3.18**. 010_{AL}, 020_{AL}, 110_{AL} and $\bar{1}10_{AL}$ peaks are detected in the spatial points within the supercrystal, though lower intensity of the WAXS reflections did not allow detecting them on the very edges. The 010_{AL} reflection is registered on even smaller area, because it has the lowest intensity among the peaks.

The intensities are not uniform within the supercrystal that can indicate different thickness of the sample or slight out-of-plane rotation of the NCs. The intensities of 010_{AL}, 020_{AL} and 110_{AL} reflections change the same way, while the intensity of $1\bar{1}0_{AL}$ reflection stay almost constant. The inhomogeneous thickness would lead to the similar changes in intensities of all reflections, thus, the change most likely is due to the out-of-plane rotation of the NCs. The constant intensity of $1\bar{1}0_{AL}$ reflection indicates that the rotation happens around an axis close to the $[110]_{AL}$ one. The changes in intensity of 010_{AL} and 020_{AL} reflections are qualitatively similar to the changes in intensity I_2 of 010_{SL} reflection (see **Figure S3.14 d**) that indicates simultaneous rotation of the NCs and SL keeping their mutual orientation. The changes in SAXS intensity are smaller due to lower effect of the Ewald's sphere curvature.

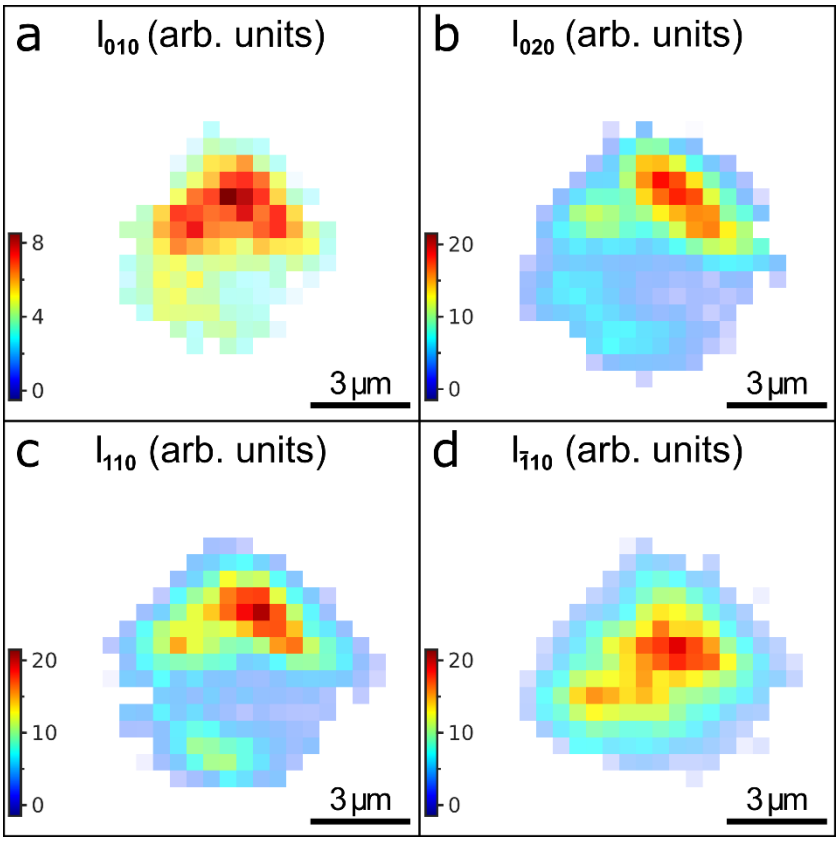

Figure S3.18: Extracted intensities of the WAXS Bragg peaks: **a)** 010_{AL}, **b)** 020_{AL}, **c)** 110_{AL} and **d)** $1\bar{1}0_{AL}$. The pixel size is 500 nm.

The mean extracted momentum transfer values are $q_{010} = 10.87 \pm 0.05$ nm^{-1}, $q_{110} = 10.85 \pm 0.05$ nm^{-1}, $q_{1\bar{1}0} = 10.91 \pm 0.03$ nm^{-1}, $q_{020} = 21.86 \pm 0.04$ nm^{-1}, that is in a

good agreement with the values obtained from the average radial profiles discussed above in **Section S3.5**. The errorbars here represent the standard deviation of the values across the sample. The momentum transfer values do not depend on the spatial position on the sample, as shown in **Figure S3.19**. The deviation is due to the noise together with the low intensities of the peaks themselves.

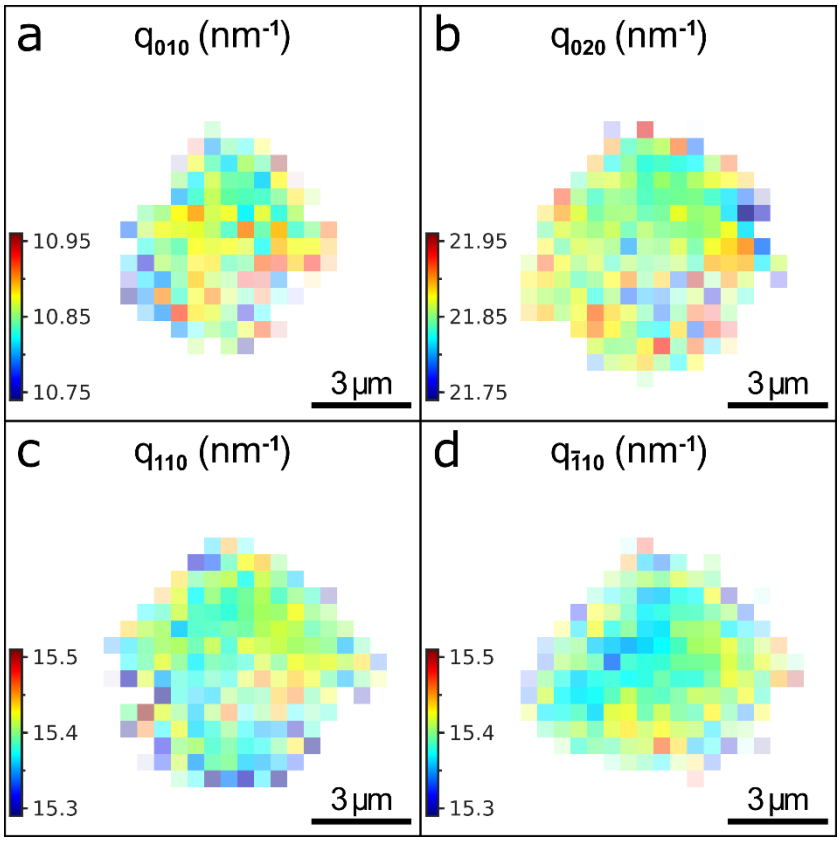

Figure S3.19: Extracted momentum transfers of the WAXS Bragg peaks: **a)** 010_{AL}, **b)** 020_{AL}, **c)** 110_{AL} and **d)**$1\bar{1}0_{AL}$. The pixel size is 500 nm.

The calculated from the q-values unit cell parameter is shown in **Figure S3.20 a**. It does not change within the supercrystal and remains constant at the value of $a_{AL} = 0.576 \pm 0.002$ nm. To better visualize the change in the unit cell parameter, we plot the values for each pixel against the distance of this pixel to the nearest supercrystal edge in **Figure S3.20 b**.

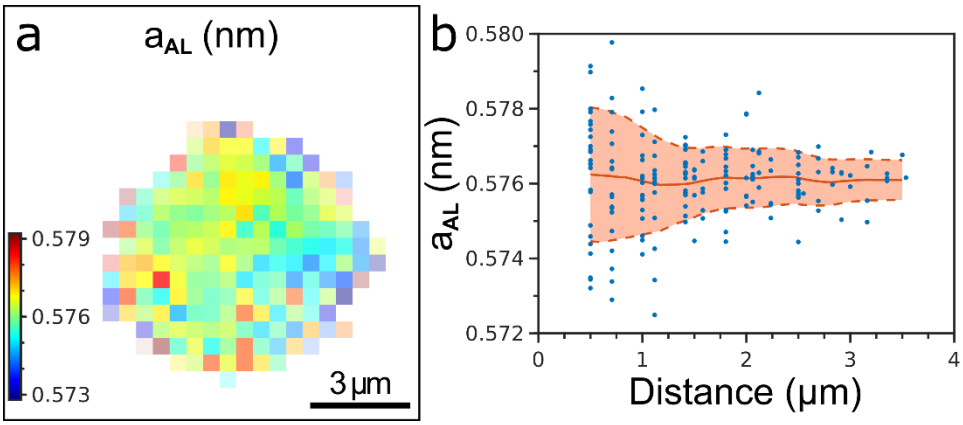

Figure S3.20: a) Calculated unit cell parameter a_{AL} of the pseudo-cubic atomic lattice of the NCs and **b)** the same value for each pixel against the distance from this pixel to the nearest edge of the supercrystal. The red line shows the mean value, the dashed lines indicate the confidence interval of $\pm\sigma$. The pixel size in **a)** is 500 nm.

The FWHMs in radial direction, shown in **Figure S3.21**, do not show any correlations with the spatial position on the sample as well. The mean values are $w_{q,010} = 0.73\pm0.10$ nm^{-1}, $w_{q,110} = 0.75\pm0.09$ nm^{-1}, $w_{q,110} = 0.73\pm0.07$ nm^{-1} and $w_{q,020} = 0.85\pm0.11$ nm^{-1}, that is in good agreement with the values from the average radial profile discussed above in **Section S3.4**. The errorbars here represent the standard deviation of the values across the sample.

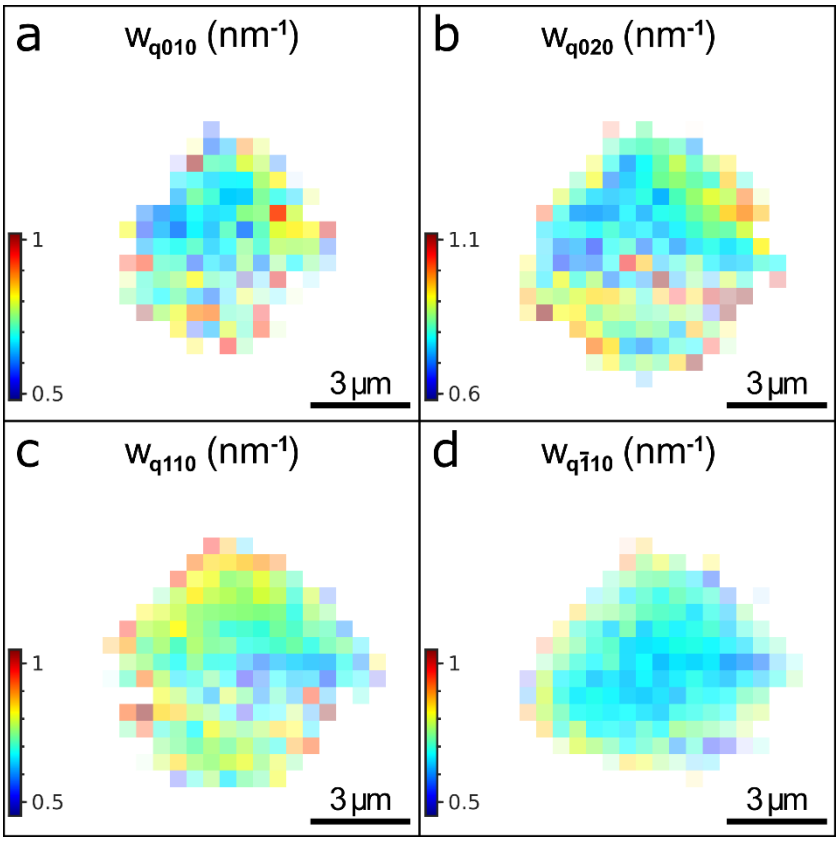

Figure S3.21: Extracted radial FWHMs of the WAXS Bragg peaks: **a)** 010_{AL}, **b)** 020_{AL}, **c)** 110_{AL} and **d)**$1\bar{1}0_{AL}$. The pixel size is 500 nm.

We used the radial FWHMs to extract the atomic lattice distortion of the NCs by the Williamson-Hall method (**Eq. (S 3.2)**). The lattice distortion g_q (the ratio $\delta a_{AL}/a_{AL}$ of the FWHM δa_{AL} of the unit cell parameter distribution around the mean value a_{AL}) was calculated as follows:

$$g_q = \left\langle \frac{1}{q_i} \sqrt{{w_i}^2 - \left(\frac{2\pi K}{L}\right)^2} \right\rangle_i , \qquad \text{(S 3.10)}$$

where w_i are the radial FWHMs for the present peaks, q_i are the momentum transfer values of the corresponding peaks, K is the shape constant, L is the NCs size and the averaging is performed over all present Bragg peaks. The shape constant K was discussed in **Section S3.4**; the NCs size was fixed at $L = 6.8$ nm obtained from the radial profile as described in the same **Section S3.4**. The resulting values of the atomic lattice distortion are shown in **Figure 3.6** in the main text. The mean value is $g_q = 1.5 \pm 0.9\%$ that is in good agreement with the values obtained from the average

radial profile discussed in **Section S3.1**. The distortion gets slightly higher on the edges of the supercrystal that can be explained by the contraction of the NCs together with the superlattice. To better visualize the change in distortion, we plot the values for each pixel against the distance of this pixel to the nearest supercrystal edge in **Figure 3.6 b** in the main text. The atomic lattice distortion grows from $< 1\%$ in the middle of the supercrystal up to $> 2\%$ on the edges. The trend is even more evident for another sample, described in **Section S3.7**. Here the effect is less pronounced, probably, because of lower intensity of the WAXS Bragg peaks causing higher noise.

Since the NCs have pseudocubic atomic lattice (all angles are equal to 90°), the azimuthal position of the WAXS Bragg peaks directly correspond to the azimuthal orientation of the supercrystal unit cell basis vectors $\mathbf{a}_1$ and $\mathbf{a}_2$. Thus, the azimuthal positions in real space are equal to the azimuthal positions in reciprocal space $\varphi_{hkl} = \omega_{hkl}$. The extracted azimuthal positions for all four peaks are shown in **Figure S3.22**. The NCs are clearly rotating in-plane as soon as the positions change for different peaks together from point to point. As expected, the difference between the positions remains constant, e.g. $\varphi_{110} - \varphi_{110} = 90°$, $\varphi_{110} - \varphi_{020} = 45°$ etc. We calculated the average azimuthal NC position Ψ collinear to the 010_{AL} vector as $\psi = \langle \varphi_{010}, \varphi_{020}, \varphi_{110} + 45°, \varphi_{110} - 45° \rangle$, where the angle brackets denote averaging over the four angles. The angle ψ is used to study the azimuthal position of the NCs. It is shown in **Figure 3.5 c** and discussed in the main text.

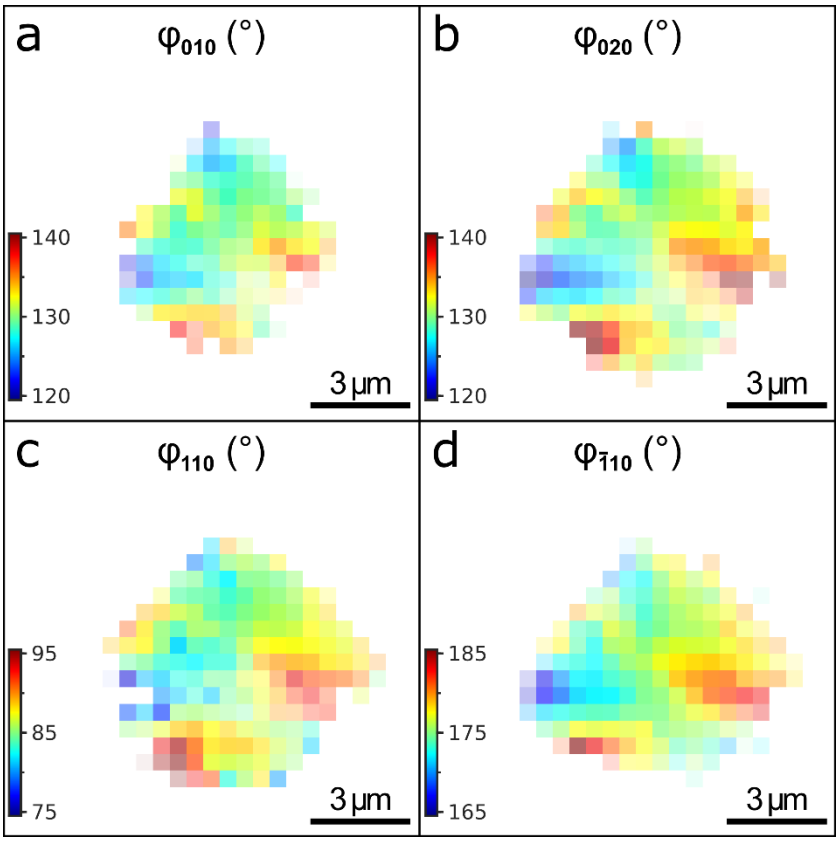

Figure S3.22: Extracted azimuthal positions of the WAXS Bragg peaks: **a)** 010_{AL}, **b)** 020_{AL}, **c)** 110_{AL} and **d)**$1\bar{1}0_{AL}$. The positions are counted counterclockwise from a horizontal axis pointing to the right. The pixel size is 500 nm.

We studied the relative azimuthal orientation of the NCs and the SL comparing the azimuthal positions of the lattice vectors obtained from the Bragg peak analysis described above. The differences in angles between the $[010]_{AL}$ axis of the NCs and the mean line **M** between the superlattice vectors $\mathbf{a}_1$ and $\mathbf{a}_2$ $\Delta = \Psi - \varphi$, between the $[010]_{AL}$ and $\mathbf{a}_1$ $\Delta_1 = \Psi - \varphi_1$; between the $[010]_{AL}$ and $\mathbf{a}_2$ $\Delta_2 = \Psi - \varphi_2$ are shown in **Figure S3.23**. Clearly, the angle Δ has narrower distribution with the mean value $\langle\Delta\rangle$ =45.2±1.7°. For comparison, the angles Δ_1 *and* Δ_2 have broader distribution with the mean values $\langle\Delta_1\rangle$ = 90.1±3.5° and $\langle\Delta_2\rangle$ = 0.8±3.8°. This is rather expected, because the angles between the NC crystallographic axes are constant, while the angle between the superlattice vectors changes from point to point in relatively broad range, as shown in **Figure 3.4 d** and discussed in the main text. At the same time, the angle between the mean lines between the superlattice vectors (e. g. **M** between $\mathbf{a}_1$ and $\mathbf{a}_2$ and **M'** between $\mathbf{a}_1$ and $-\mathbf{a}_2$) is always equal to 90° and does not depend on the length

and orientation of the vectors $\mathbf{a}_1$ and $\mathbf{a}_2$. It makes possible keeping the mutual orientation between the $[100]_{AL}$ and $[010]_{AL}$ axes and the mean lines **M** and **M'**.

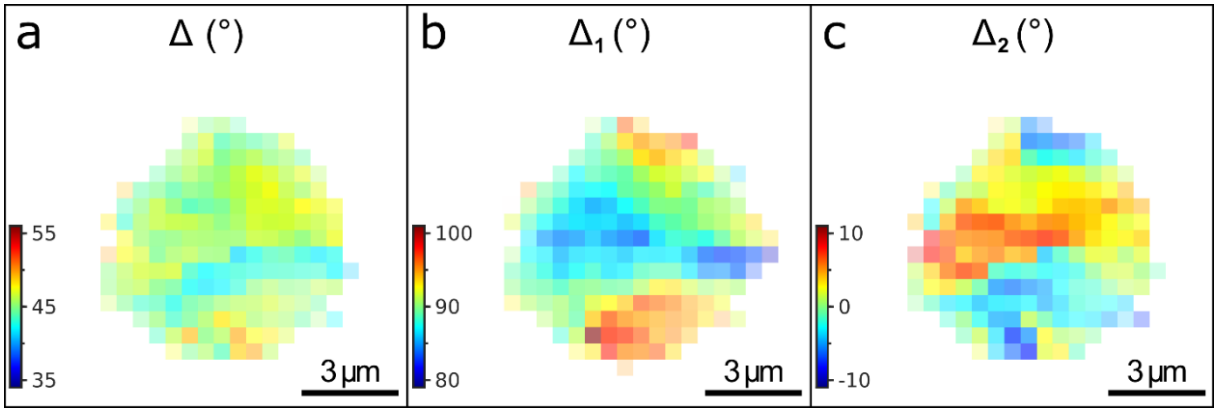

Figure S3.23: Relative angle between the direct lattice vectors of the NCs and the SL: **a)** between $[010]_{AL}$ and the mean line M between the a_1 and a_2; **b)** between $[010]_{AL}$ and a_1; **c)** between $[010]_{AL}$ and a_2. The pixel size is 500 nm.

The azimuthal FWHMs shown in **Figure S3.24** show clear dependence on the spatial position within the supercrystal. The FWHMs grow from 12° in the middle of the supercrystal up to 24° on the edges indicating higher azimuthal disorder of the NCs there.

We used the azimuthal FWHMs to extract the NCs angular disorder by the Williamson-Hall method. In this case, the lattice distortion g from **Eq. (S 3.2)** is the FWHM $\delta\Psi$ of angular distribution of the NCs around their mean position given by the azimuthal peak positions. The FWHM $\delta\Psi$ was calculated as follows:

$$\delta\psi = \left\langle \frac{1}{q_i} \sqrt{w_i q_i \,^2 - \left(\frac{2\pi K}{L}\right)^2} \right\rangle_i , \qquad \text{(S 3.11)}$$

where w_i are the azimuthal FWHMs (in radians) for the present peaks, q_i are the momentum transfer values of the corresponding peaks, K is the shape constant, L is the NCs size and the averaging is performed over all present Bragg peaks. The shape constant K was discussed in **Section S3.4**; the NCs size was fixed at $L = 6.8$ nm obtained from the radial profile as described in the same **Section S3.4**. The resulting values of the FWHM are shown in **Figure 3.5 d** and discussed in the main text.

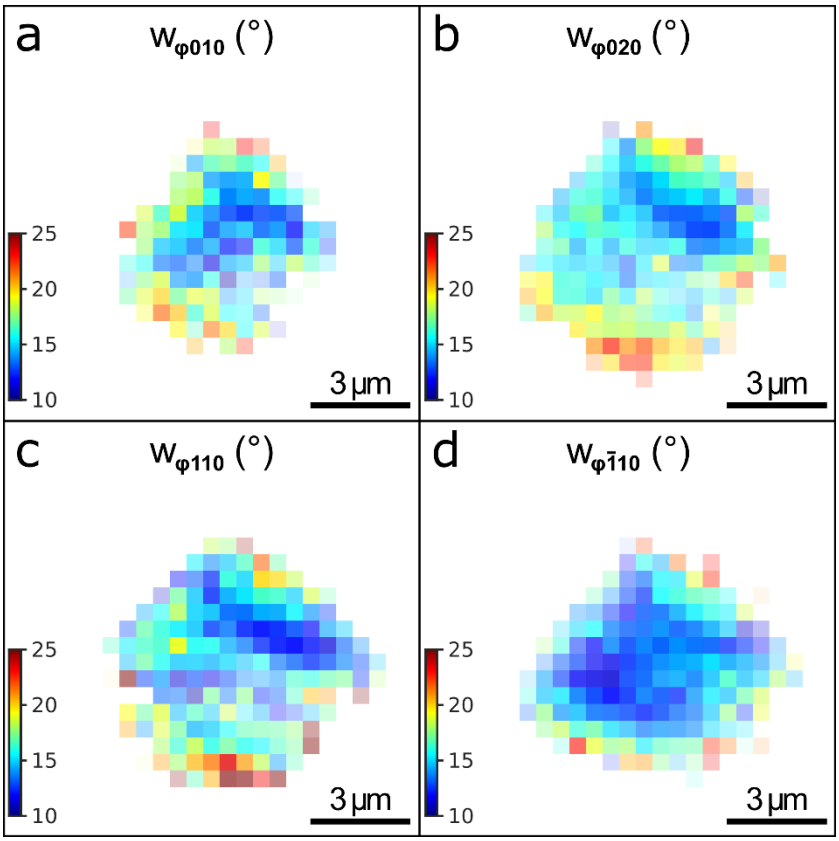

Figure S3.24: Extracted azimuthal FWHMs of the WAXS Bragg peaks: **a)** 010_{AL}, **b)** 020_{AL}, **c)** 110_{AL} and **d)** $1\bar{1}0_{AL}$. The pixel size is 500 nm.

Section S3.7. Another example of a supercrystal

All studied supercrystals behave similarly. Here we present the main results obtained for one more supercrystal. The average WAXS and SAXS patterns as well as the SAXS-based diffraction map are shown in **Figure S3.25**. The patterns look very similar to the ones observed for the sample described in the main text. The local structure was analyzed the same way as described above. The only difference is the WAXS analysis, performed only for three peaks 010_{AL}, 020_{AL} and 110_{AL}. The fourth $1\bar{1}0_{AL}$ peak hardly fitted into the detector in this case and was excluded from the consideration.

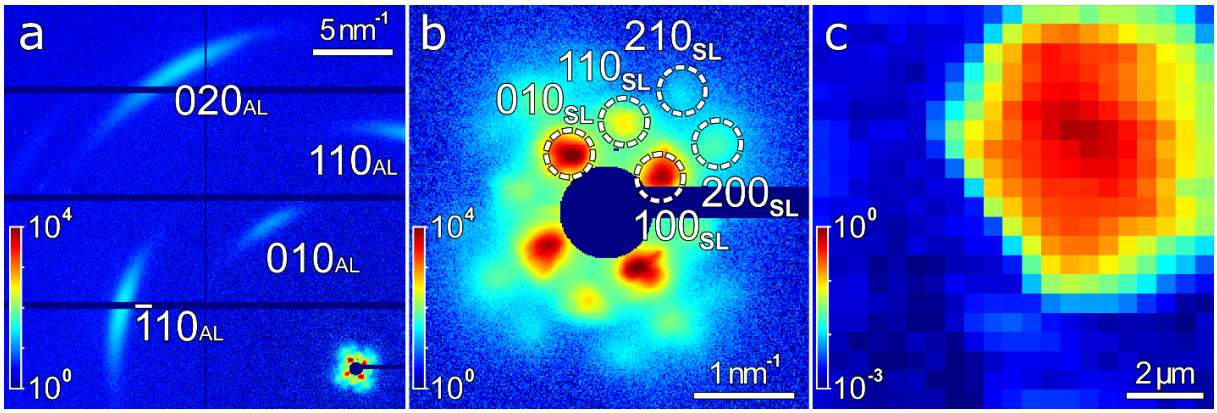

Figure S3.25: Average WAXS **a)** and SAXS **b)** patterns and **c)** SAXS-based diffraction map of the second sample. The Bragg peaks are indexed according to the "pseudocubic" structure of the atomic lattice and simple cubic structure of the superlattice. The pixel size in **c)** is 500 nm.

The main extracted parameters of the superlattice are shown in **Figure S3.26**. The main observations are the same as for the sample described in the main text. The superlattice anisotropically shrinks on the edges of the supercrystal. The contraction happens preferentially in the directions parallel to the nearest supercrystal edge. The angle between the basis vectors $\mathbf{a}_1$ and $\mathbf{a}_2$ changes in the range of 75–105° and the superlattice rotates in-plane as indicated by the azimuthal position φ of the mean line **M** between $\mathbf{a}_1$ and $\mathbf{a}_2$.

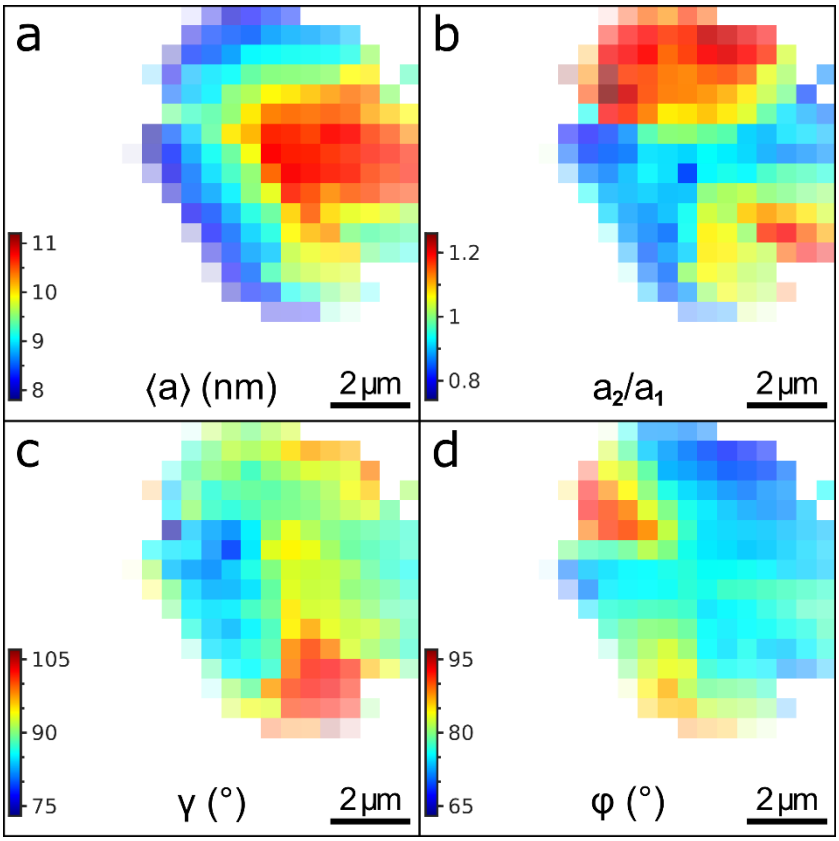

Figure S3.26: Extracted superlattice parameters: **a)** average unit cell parameter $\langle a \rangle = (a_1+a_2)/2$; **b)** ratio a_2/a_1 of the NC spacings along the basis vectors $\mathbf{a}_2$ and $\mathbf{a}_1$; **c)** angle Ψ between the basis vectors $\mathbf{a}_1$ and $\mathbf{a}_2$; **d)** azimuthal position φ of the mean line **M** between the basis vectors $\mathbf{a}_1$ and $\mathbf{a}_2$. The pixel size is 500 nm.

The main extracted parameters of the atomic lattice are shown in **Figure S3.27**. The main difference with the sample described in the main text is the homogeneous intensity of the WAXS Bragg peaks decreasing on the edges. It indicates absence of the out-of-plane rotations of the NCs. But the NCs rotate in-plane correlated with the mean line **M** between the $\mathbf{a}_1$ and $\mathbf{a}_2$ superlattice vectors as can be seen from the difference angle $\Delta = \Psi - \varphi$. The angular disorder of the NCs grows on the edges the same way as for the sample described in the main text.

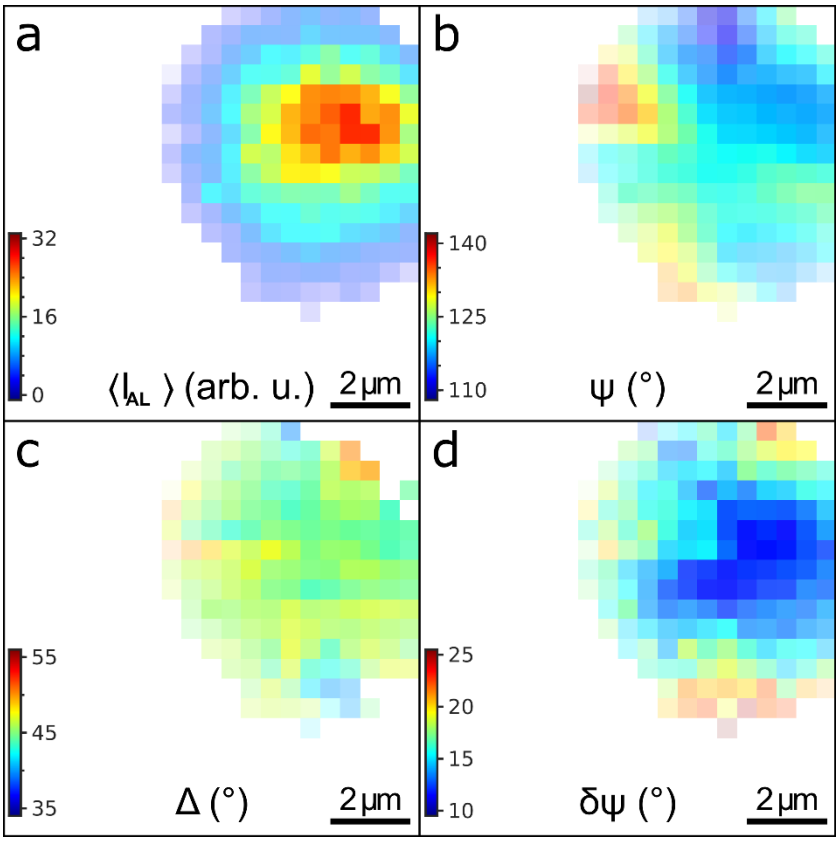

Figure S3.27: Extracted atomic lattice parameters: **a)** Average intensity of the WAXS Bragg peaks $<I_{AL}>$; **b)** azimuthal position Ψ of the 100_{AL} crystallographic directions of the NCs; **c)** the relative angle Δ between the $[010]_{AL}$ axis and the mean line **M** between the $\mathbf{a}_1$ and $\mathbf{a}_2$ basic vectors of the SL; **d)** FWHM $\delta\Psi$ of the angular disorder of the NCs around the mean azimuthal position Ψ. The pixel size is 500 nm.

The calculated unit cell parameter of the atomic lattice from the q-values of the WAXS Bragg peaks is shown in **Figure S3.28**. It doesn't show any correlation with the spatial position within the supercrystal and remains constant at the value of $a_{AL} = 0.576 \pm 0.002$ nm.

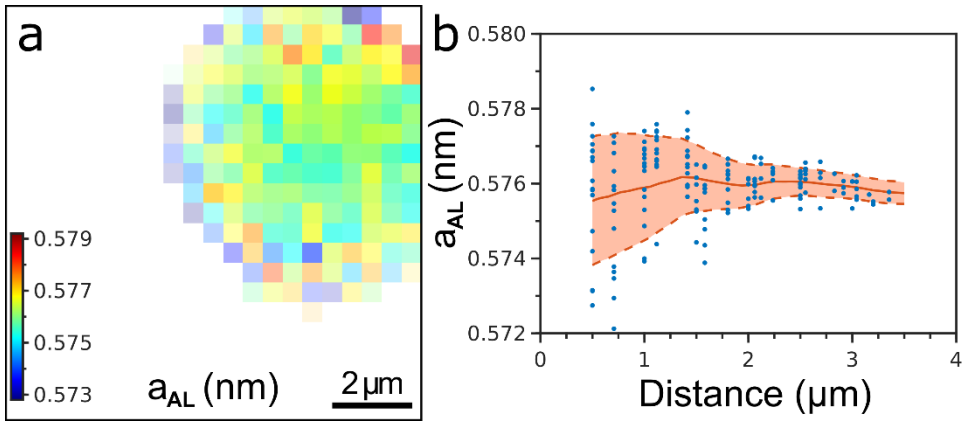

Figure S3.28: a) Calculated unit cell parameter a_{AL} of the pseudo-cubic atomic lattice of the NCs and **(b)** the same value for each pixel against the distance from this pixel to the nearest edge of the supercrystal. The red line shows the mean value, the dashed lines indicate the confidence interval of $\pm\sigma$. The pixel size in **a)** is 500 nm.

The atomic lattice distortion was calculated from the FWHMs of the present WAXS Bragg peaks by the Williamson-Hall method (**Eq. (S 3.10)**). The resulting values of the atomic lattice distortion are shown in **Figure S3.29**. The distortion gets slightly higher on the edges of the supercrystal that can be explained by the contraction of the NCs together with the superlattice. The atomic lattice distortion grows from about 0.5% in the middle of the supercrystal up to about 2.5% on the edges.

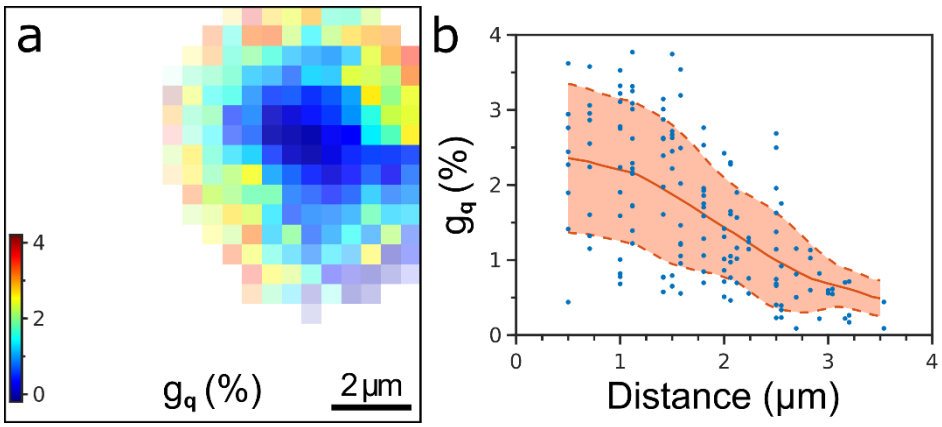

Figure S3.29: a) Atomic lattice distortion g_q extracted from the radial FWHMs of the WAXS Bragg peaks by the Williamson-Hall method and **(b)** the same value for each pixel against the distance from this pixel to the nearest edge of the supercrystal. The red line shows the mean value, the dashed lines indicate the confidence interval of $\pm\sigma$. The pixel size in **a)** is 500 nm.

Section S8. DFT-computed structures

The computation protocol used in this work is described in the main text. Cartesian coordinates of all computed structures can be accessed from the coordinate file (.xyz).

4. Zwitterionic Carbazole Ligands Enhance the Stability and Performance of Perovskite Nanocrystals in Light Emitting Diodes

Christopher Kirsch[1], *Tassilo Naujoks*[2], *Philipp Haizmann*[1], *Philipp Frech*[1], *Heiko Peisert*[1], *Thomas Chassé*[1], *Wolfgang Brütting*[2,*], *Marcus Scheele*[1,*].

[1] Institut für Physikalische und Theoretische Chemie, Universität Tübingen, 72076 Tübingen, Germany

[2] Institut für Physik, Universität Augsburg, Augsburg 86135, Germany

KEYWORDS Lead halide perovskites, Nanocrystals, Ligand exchange, Light-emitting diodes

This chapter is based on a manuscript, which is submitted to the Journal of ACS Applied Materials & Interfaces (as of 21.04.2023).

ChemRxiv Preprint: https://doi.org/10.26434/chemrxiv-2023-wjd4r (as of 12.05.2022)

4.1 Abstract

We introduce a new carbazole-based zwitterionic ligand (DCzGPC) synthesized via Yamaguchi esterification which enhances the efficiency of lead halide perovskite (LHP) nanocrystals (NCs) in light emitting diodes (LED). A facile ligand exchange of the native ligand shell, monitored by nuclear magnetic resonance (NMR), ultraviolet-visible (UV-vis), and photoluminescence (PL) spectroscopy, enables more stable and efficient LHP NCs. The improved stability is demonstrated in solution and solid-state LEDs, where the NCs exhibit prolonged luminescence lifetimes and improved luminance, respectively. These results represent a promising strategy to enhance the stability of LHP NCs and to tune their optoelectronic properties for further application in LEDs or solar cells.

4.2 Introduction

Colloidal nanocrystals (NCs) of all-inorganic lead halide perovskites (LHP) provide a variety of perspectives for application in optoelectronic devices. [29,213,214]. Due to their high luminescence quantum yields (50–99 %), defect tolerance and narrow full width at half maximum (FWHM, 12–40 nm for blue-to-red), as well as tunable emission color (by halide composition and size dependence), LHPs are ideal candidates for high-quality light sources in light emitting devices (LEDs) and full-color displays.[215,216] Despite these remarkable properties, their chemical instability constitutes a significant challenge for the long-term use in such applications.[89,217]

For LHP NCs, the chemical instability is particularly pronounced owing to their large surface-to-volume ratio. This natural disadvantage of colloidal NCs is partially compensated by tethering stabilizing organic ligands onto the surface of the NCs. However, the binding strengths of typical ligands, such as oleic acid or oleylamine, as well as their stability gain are relatively weak[67] , which has motivated the search for other

methods of stabilization, such as encapsulation[218,219], doping[220] or the use of ligands with a higher binding strength.[221,222] Krieg *et al.*[98] have demonstrated the advantages of using zwitterionic ligands, which bind strongly to LHP NCs and provide a significantly higher stabilization. However, these ligands contain long alkyl-chains which – just like the aforementioned encapsulation strategies – lead to electrically mostly insulating LHP NCs, severely hindering their application in LEDs.

We hypothesize that this issue may be resolved by replacing the long alkyl-chains with conjugated π-systems, which should increase the electrical conductivity of the NCs. To this end, a new ligand has to fulfil the same requirements as conventional charge transport layers: A match in energy levels for at least one carrier type, if the other is already transported sufficiently well between the NCs, paired with a higher bandgap than the LHP NCs ensures optimal operation. Here, we focus on enhancing the hole injection since we suspect an already sufficient electron mobility due to the n-type character of such NCs.[223] In this regard, the carbazole moiety matches the low valence band edge of LHPs, while featuring good solubility in organic solvents, a wide bandgap and high triplet level for application in conjunction with blue emitters.[224–226] Carbazoles have been incorporated in several stable, state-of-the-art opto-electronic devices with an extensive research background in that context.[227–229] Thus, we introduce a novel zwitterionic ligand (DCzGPC) based on a phosphocholine backbone with sidechains consisting of the conjugated carbazole π-system. We show that LEDs of LHP NCs stabilized with this ligand exhibit an increased operational lifetime, a higher external quantum yield and a lower turn-on voltage than the same LHP NCs with conventional ligand stabilization.

4.3 Results and Discussion

The ligand 1,2-Di((9H-carbazol-9-yl)propanoyl)-sn-glycero-3-phosphocholine (DCzGPC) is synthesized in a one-step-synthesis via Yamaguchi esterification[230,231] of

3-Carbazol-9-yl-propionic acid (CzPA) and sn-Glycero-3-phosphocholine (GPC) (**Figure 4.1 A**). A typical nuclear magnetic resonance (NMR) spectrum and selected peak areas are shown in **Figure 4.1 B (black data) and Figure S4.1Figure S4.3**, and further proof of the successful synthesis of DCzGPC is provided by high resolution mass spectrometry in the experimental section. UV-vis absorption and photoluminescence (PL) spectroscopy in **Figure 4.1 C (black data)** reveal a sharp absorption at 330 nm and 334 nm as well as an emission maximum located at 363 nm.

$CsPbBr_2Cl$ NCs capped with oleylamine/oleic acid are synthesized by established literature procedures. Absorption/PL characteristics (**Figure 4.1 C, blue data)** are compared to that of DCzGPC. The absorption of DCzGPC (dotted black line in **Figure 4.1 C**) is significantly outside the NC emission range (solid blue line in **Figure 4.1 C**), indicating that undesirable PL quenching of the NCs should be absent.[232] This is supported by the excitation spectrum in **Figure S4.4,** which exhibits comparable features for NCs with and without the presence of DCzGPC.

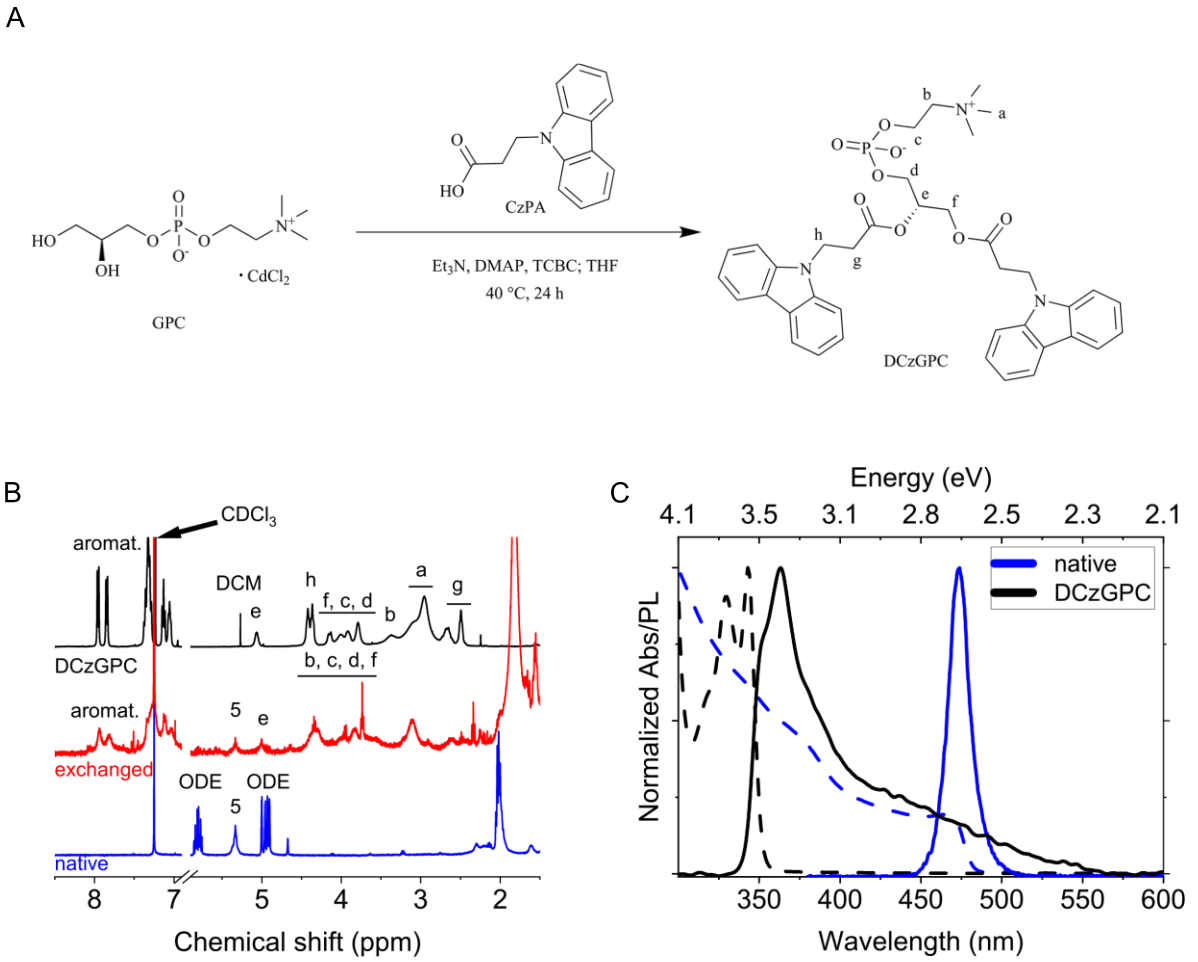

Figure 4.1: A) Reaction scheme of the synthesis resulting in the carbazole-based ligand (DCzGPC) with the zwitterionic anchoring group (latin letters (a–h) assigning the identified peaks in ^{1}H-NMR). **B)** ^{1}H-NMR analysis of the as-synthesized carbazole-based ligand (black), native $CsPbBr_2Cl$ NCs (blue) and with DCzGPC exchanged (26 wt %) $CsPbBr_2Cl$ NCs (red) in $CDCl_3$. Shown are the regions for the characteristic carbazolic proton peaks (7–8 ppm) and common DCzGPC peaks (a–h). A more detailed analysis can be found in **Figure S4.1**Figure **S4.3. C)** Optical spectroscopy (UV-vis (dotted lines) and photoluminescence (solid lines)) of the carbazol ligand (black) and the as synthesized $CsPbBr_2Cl$ NCs (blue). The spectra are normalized and were excited with 300 nm.

Successful ligand exchange of the NCs from oleylamine/oleic acid to DCzGPC as detailed in the experimental section is verified by ^{1}H-NMR spectroscopy. The ^{1}H-NMR spectrum of the exchanged NCs exhibits relatively broad signals in the region typical for the DCzGPC ligand (**Figure 4.1 B, red data**). Moreover, the peaks of the native ligand shell (oleic acid and oleylamine) decrease significantly compared to the spectrum of the native NCs before exposure to DCzGPC (**Figure 4.1 B, blue data**). A peak broadening is often attributed to an increased lateral relaxation due to neighboring

ligand molecules, indicating an attachment of this species to the NCs.[147,233] Taken together, these finding support a successful, partial replacement of oleylamine/oleic acid from the surface of the NCs by DCzGPC.

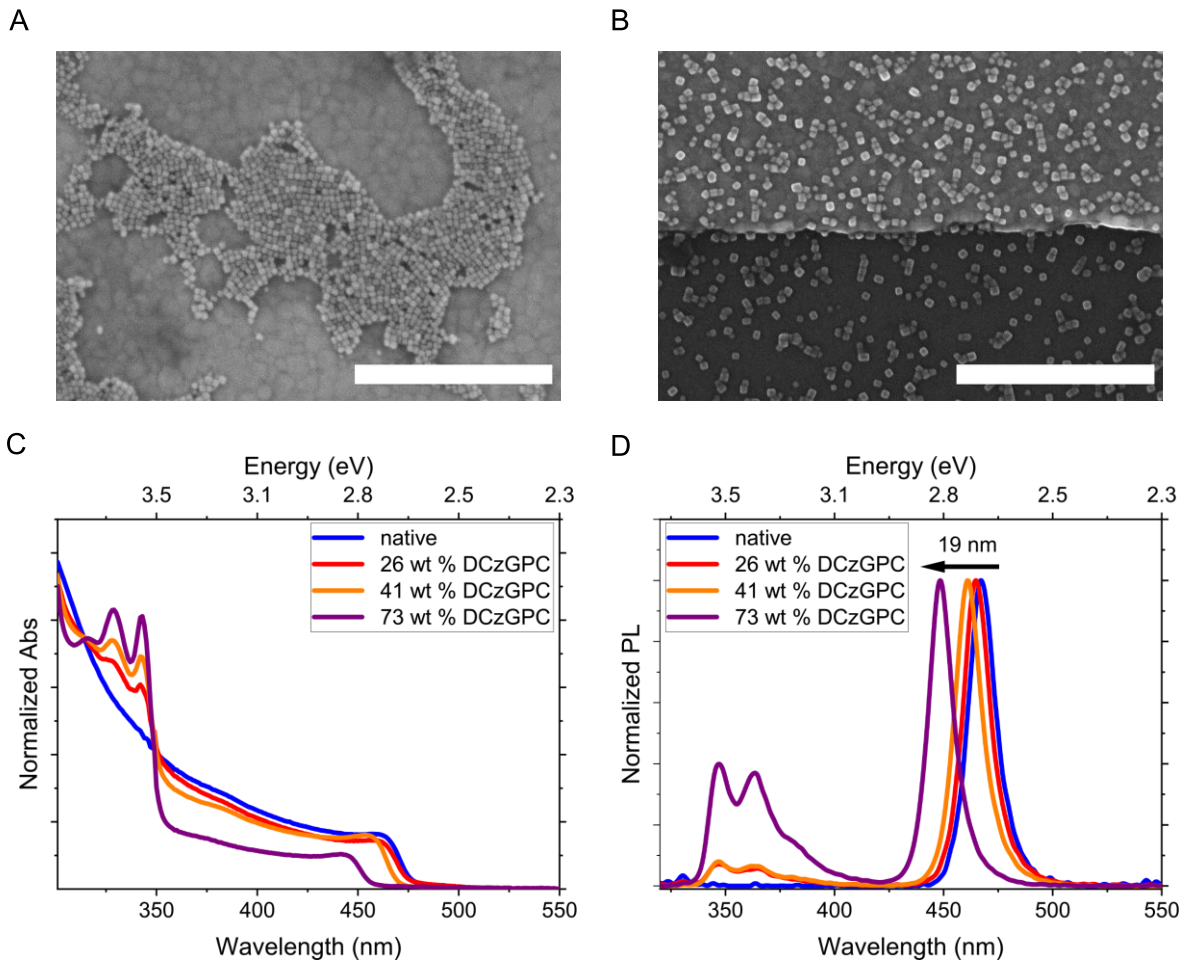

Figure 4.2: Scanning electron microscopy images displaying the preservation of the structural integrity during the preparation and ligand exchange processes. Different concentrations were used for film preparation. **A)** Untreated native $CsPbBr_2Cl$ NCs and **B)** after ligand exchange with the DCzGPC ligand (gold contact is visible in the upper, brighter section). Scale bars correspond to 500 nm. **C, D)** UV-vis and photoluminescence spectra of the $CsPbBr_2Cl$ nanocrystals before (blue) and after (red, orange, and purple) exchanging the ligand shell with different amounts of DCzGPC ligand.

By scanning electron microscopy (SEM) before and after ligand exchange, we find an increase in the average size of the NCs by ~1.5 nm (**Figure S4.5**) and an unaltered cubic shape (**Fig. 2B**). A comparison of the absorption and PL properties before and after ligand exchange reveals a significant hypsochromic shift, which increases upon adding more DCzGPC ligand (**Figure 4.2 C, D**). This shift prevails also in thin films and elec-

troluminescence experiments as well as for other perovskite nanocrystals, such as $CsPbBr_3$ (**Figure S4.6**), indicating that it is specific to the presence of DCzGPC and not, for instance, a solvent effect or a change in halide composition. By X-ray photoelectron spectroscopy (XPS), we exclude the presence of a chloride contamination in pure DCzGPC as a potential reason for the hypsochromic shift (**Figure S4.7**). We note that a concentration-dependent hypsochromic shift after addition of different bidendate ligands was also observed by other groups.[234–237] However, in those cases the NC size shrunk during ligand exchange, such that the shift was explained in terms of increased quantum confinement. In the present case, we observe the opposite, i.e., a slight increase in the NC size, which rules out increased quantum confinement as an explanation for the blue shift.

We find that the PL quantum yield (QY) increases from 61 % for the native NCs to a maximum of 73 % upon addition of DCzGPC. Further increase of the ligand concentration reduces the PLQY to 61 % (**Figure S4.10**). This finding further strengthens the conclusion of a substantial interaction between the NCs and the novel ligand.

Table 4.1: Summarized data from UPS and XPS spectra for pure ligand, native $CsPbBr_2Cl$ NCs and NCs exchanged with different concentrations of DCzGPC. All binding energies with respect to E_F.

Experiment	***F*** **(eV)**	***VBM*** **(eV)**	***IE*** **(eV)**	E_{Gap} **(Optical) (eV)**
DCzGPC	4.25	1.69	5.90	3.42
native	3.98	1.77	5.75	2.65
6.5 % wt DCzGPC	4.06	1.72	5.78	2.67
41 % wt DCzGPC	3.92	1.83	5.75	2.69
73 % wt DCzGPC	3.91	1.99	5.90	2.77

We perform XPS and UPS to gain a deeper understanding of the influence of DCzGPC on the electronic structure of the NCs and compare the results for the unexchanged NCs, the pure DCzGPC ligand as well as the exchanged NCs in **Table 4.1**. The measured work function (Φ) and valence band maximum (VBM) for the native

particles are in good agreement with literature data of mixed lead halide perovskites[223,238,239]. Minor variations in the results could stem from using different substrates[240], yet earlier measurements conducted on the same gold-coated substrate with $CsPbBrI_2$ showed strong consistency.[241] We find an ionization energy (IE) of 5.75 eV for the native particles and 5.9 eV for the pure DCzGPC ligand. The IE of the ligand-exchanged NCs ranges between 5.78 eV and 5.9 eV, indicating that states of the nanoparticle core contribute to valence band / 1Sh. Also, for the NCs exchanged with DCzGPC the VBM shifts towards higher $E–E_F$ values, and we find an enhanced density of states near the VBM while the work function after ligand exchange is nearly unaffected. The measured VBM shift is higher, (220 meV) than the observed hypsochromic shift (120 meV), indicating that the DCzGPC ligand also affects the position of the conduction band minimum. We note that both the shape and energetic position of the Pb4f core level spectra is almost identical for native and ligand-exchanged NCs (**Figure S4.8 C**), suggesting that no significant doping is induced by DCzGPC. N1s and C1s core level spectra and the concentration dependence of these signals confirm the presence of the ligand after exchange (**Figure** S4.8 **A, B**).

We conduct femtosecond transient absorption spectroscopy of thin films of the native and ligand-exchanged NCs following 90 fs excitation pulses at 325 nm (0.5 µJ/pulse). For both NC samples, we find the expected ground state bleach (GSB) close to the first excitonic transition of the NCs, a short-lived sub-band gap excited state absorption (ESA) feature as well as a weak broad ESA above the band gap energy (**Figure 4.3 A+ Figure S4.11**). While the absence of any new or strongly changed features in the presence of DCzGPC indicates no significant energy transfer between the ligand and the NCs, we observe overall shorter lifetimes **(Figure S4.12**). Biexponential fitting of the sub-band gap feature at 487 nm for the native and 477 nm for the exchanged system show a decrease of the second lifetime from 42 ps to 17 ps.

A previous report has attributed the sub-band gap feature below 1 ps to bandgap renormalization.[139] Based on this assumption, we compare the band gap renormalization energy of both NC samples by calculating the energy difference between the GSB and the sub-band gap ESA as indicated in **Figure 4.3 B**. Although slightly varying at different times, we consistently find higher renormalization energies between 3 - 15 % for the exchanged NCs (99 meV after 600 fs) compared to the native system (89 meV after 600 fs). These findings can be interpreted as evidence for stronger excitonic behavior and quantum confinement in the DCzGPC-exchanged NCs (**Figure 4.3 B + Table S4.1**).[139]

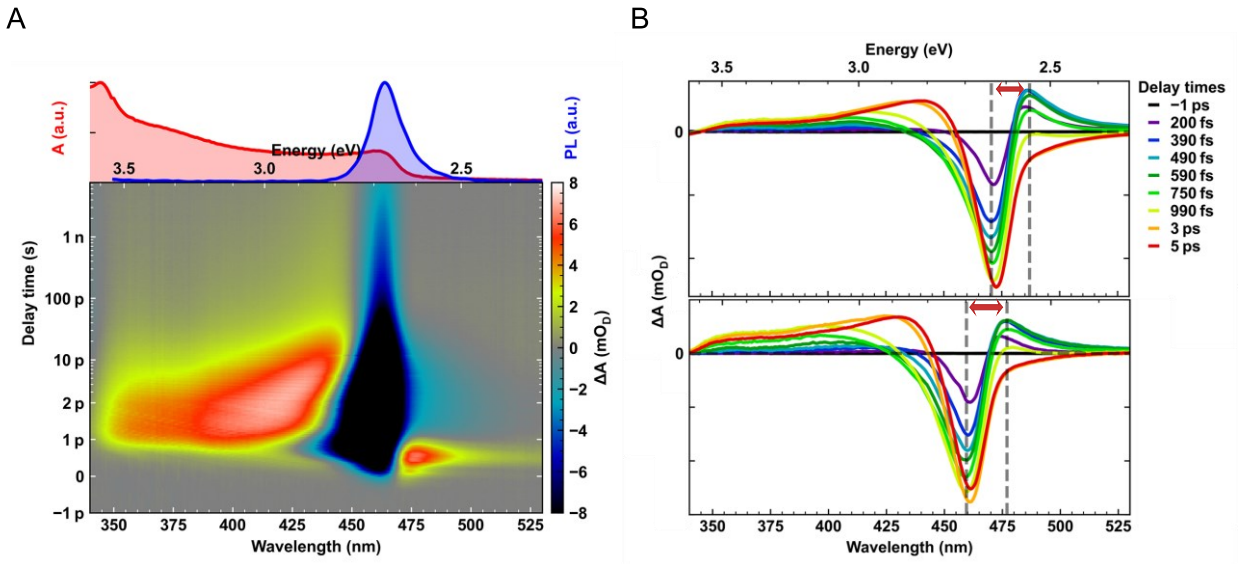

Figure 4.3: A) 2D transient absorption spectra of the exchanged perovskite system after excitation at 325 nm. After the first 2 ps, the delay time changes from a linear to a logarithmic scale. A steady-state absorption spectrum (red) and photoluminescence (PL, blue) spectrum is shown above the 2D plot. **B)** ΔA spectra of the native (top) and exchanged system (bottom) at selected delay times after excitation at 325 nm. The minimum of the GSB and maximum of the ESA are indicated with dashed lines.

LEDs with native as well as DCzGPC-exchanged $CsPbBr_2Cl$ NCs are prepared as described in the experimental part. We compare the current density-voltage-luminescence (jVL) curves in **Figure 4.4 A** and find an increase of the current densities by almost one order of magnitude as well as a reduction of the turn-on voltage from ~ 4 V to 3 V. The luminance in the ligand-exchanged sample increases by over one order

of magnitude, the maximum of the electroluminescence emission is shifted by 7 nm to smaller wavelengths (**Figure 4.4 B**) and the FWHM of the emitted light decreases from 22 nm to 16 nm, resulting in a more color-brilliant emission. We calculate the external quantum efficiency (EQE) from these results and display it for a range of luminances in **Figure 4.4 C** to find that the EQE approximately doubles upon ligand exchange. More importantly, the LEDs with ligand-exchanged NCs have their peak EQEs at much higher luminance.

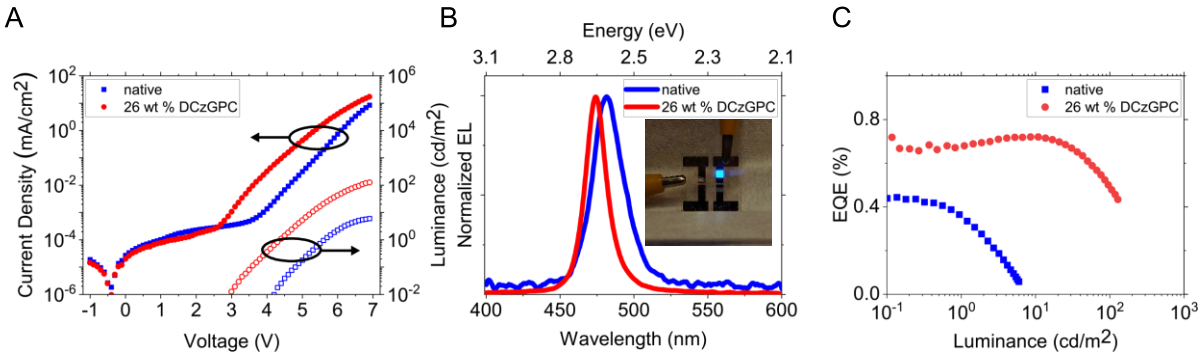

Figure 4.4: A) j-V-L curves of the as-prepared LEDs. The native case is depicted in blue and the exchanged sample in red. The current densities are shown as filled symbols and the luminance as empty symbols. **B)** Electroluminescence spectra of the native (blue) and exchanged (red) LED stacks (left) as well as a photograph of a working LED under 7 V operational bias as inset. The blue emission can be seen in the top right corner. **C)** Calculated external quantum efficiencies of the native (blue) and exchanged (red) LEDs.

With regard to the large chemical instability of perovskites, we perform stability tests in solution monitored by PL intensity changes upon water addition (**Figure 4.5 A**). For the native NCs and the DCzGPC passivation alike, we find the previously observed initial increase in PL, assigned to the passivation of surface defects.[218,242] However, this gain diminishes after 10 min without stirring the solution, which we attribute to the beginning water-mediated decomposition of the NCs. For the DCzGPC-exchanged NCs, this deterioration is significantly slowed down after 40 min, indicating a greater robustness against water. The stability of the particles exchanged with DCzGPC in polar solvents, such as THF or ethyl acetate, for at least two months without a significant loss in luminosity further supports their robustness.

We investigate the effect of this increased robustness on the performance in LEDs by performing stress tests under constant current operation and determine the operational lifetime LT_{50} (**Figure 4.5 B**). To this end, LEDs consisting of $CsPbBr_2Cl$ NCs with oleylamine/oleic acid or 26 wt % DCzGPC are operated at a current density of 1 mA/cm^2 in a N_2-filled glovebox at ambient temperature. While the LT_{50} of the native control device is 6 s, exchange with DCzGPC invokes a fifteen-fold increase to 91 s under the same test conditions. This demonstrates the improved stability of LEDs with the ligand exchanged NCs. Additionally, we also monitored changes of the voltage during device stressing. For the native devices the voltage, respectively the resistance, decreased monotonically by almost 1 V, while for the ligand-exchanged devices the voltage initially increases before it starts to slightly decrease after 5 minutes of operation, but the overall change is much less. This implies a fundamentally different degradation process (**Figure S3.13**).

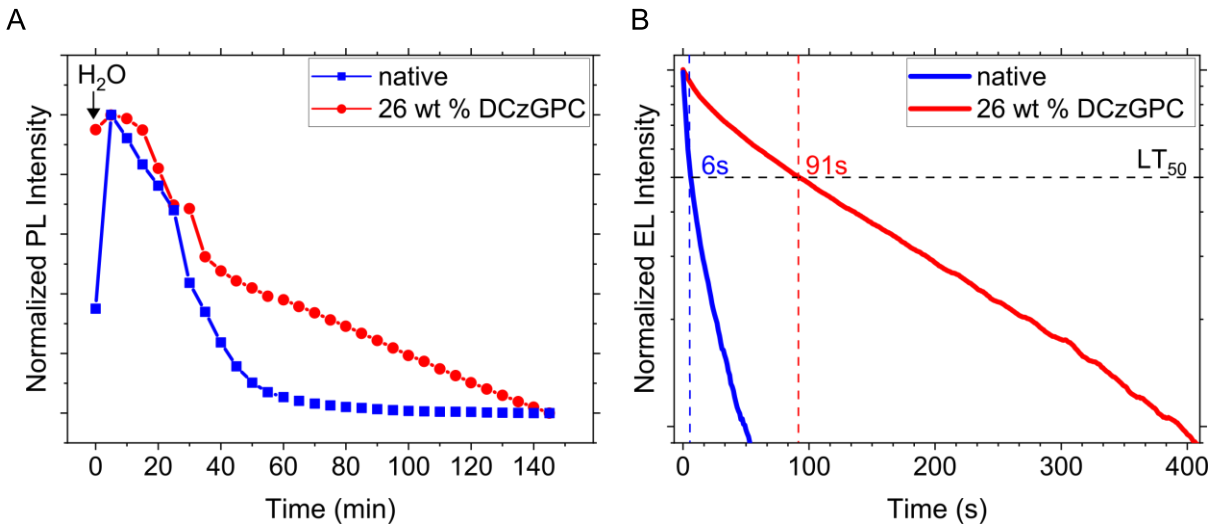

Figure 4.5: A) Normalized PL intensity change over time of native $CsPbBr_2Cl$ NCs (blue) and after ligand exchange with the DCzGPC ligand (red) upon the addition of 10 % water (by volume) without stirring for different times. **B)** LED operational lifetime of native $CsPbBr_2Cl$ NCs (blue) and after ligand exchange with the DCzGPC ligand (red) under 1 mA/cm^2 constant current operation bias. The black dotted line indicates luminance half-life time.

Our results indicate that DCzGPC as a ligand for LHP NCs (specifically $CsPbBr_2Cl$) combines the stability enhancement of the zwitterionic head group with the beneficial electronic properties of the carbazole π-system without significantly altering the size

and shape of the nanocrystals. The increased performance of DCzGPC-capped NCs is evident in solution through their long-term stability in polar solvents, while in the solid state, it prolongs the LED lifetime under bias stress. We attribute this stability improvement to a more robust attachment of the zwitterionic head group to the surface of the NCs, similar to previous demonstrations by others.[87,98]

The advantageous effects of DCzGPC on the electronic properties of $CsPbBr_2Cl$ NCs include an increase in the PLQY in solution as well as a largely improved electroluminescence characteristics in solid-state LEDs. While both effects are likely to result from the elimination of unsaturated surface defects compared to the native oleic acid/oleylamine ligands, the higher luminance and larger EQE of the LEDs indicate an additional facilitation of carrier injection, most likely due to the proximity of the π-conjugated carbazole moiety. We note that further improvements in the hole injection rate should be possible upon replacing the carbazole backbone of the DCzGPC ligand with other moieties that decrease the ionization energy.

To rationalize the hypsochromic shift of the NCs (both $CsPbBr_2Cl$ and $CsPbBr_3$) upon exchange with DCzGPC, we note that different capping ligands for NCs have been shown to not only affect the absolute energies of the band edges[243–245], but also the excitonic transition energy itself as described by the Brus equation.[105] Since the size of the NCs does not decrease during ligand exchange in our work, the only free parameters in the Brus equation for describing the excitonic transition energy are the relative dielectric constant and the carrier effective masses. Evidence for an increased dielectric constant due to DCzGPC is provided by the long-term colloidal stability in polar solvents. However, a simple estimate of the total exciton binding energy shows that a change in the dielectric environment alone cannot account for the full hypsochromic shift of 120 meV observed by us (see SI for details). Therefore, we propose that an additional reduction of the effective mass of the charge carriers is responsible for the increased excitonic transition energy. Similar effects were reported for comparable perov-

skite systems[246,247], for which density-functional theory (DFT) calculations indicated a drastic reduction of effective masses upon ligand exchange. Nevertheless, further research will be needed to fully understand such concentration-dependent hypsochromic shifts.

4.4 Conclusion

We have synthesized 1,2-Di((9H-carbazol-9-yl)propanoyl)-sn-glycero-3-phosphocholine (DCzGPC) via a one-step Yamaguchi esterification method and shown its potential as a ligand for $CsPbBr_2Cl$ nanocrystals (NCs) with enhanced stability against polar solvents and in thin film LEDs under bias stress. We have demonstrated that DCzGPC increases the photoluminescence quantum yield of the nanocrystals, preserves their structural integrity, and reduces the width of the emission peak. A concentration-dependent hypsochromic shift of the emission peak by up to 120 meV enables fine-tuning without changing the halogen composition of the NCs. In LEDs, the exchanged NCs demonstrated a fifteenfold longer operating lifetime, a 1.6-fold higher external quantum efficiency and a 25 % reduction in turn-on voltage to 3 V compared to the same NCs stabilized by oleic acid/oleylamine.

4.5 Experimental Section

Chemicals. 1-Octadecene (ODE), technical grade, 90 %, Sigma Aldrich; Oleic acid (OA), 97 %, Acros Organics; Oleylamine (OAm), 80–90 %, Acros Organics; Dichloromethane, 99.8 %, extra dry over molecular sieve, Stabilized, AcroSeal, Acros Organics; Tetrahydrofuran, 99.85 %, extra dry, unstabilized, AcroSeal, Acros; Caesium carbonate (Cs_2CO_3), 99.99 % (trace metal basis), Acros Organics; Lead(II) oxide (PbO), 99.999 % (trace metal basis), Sigma Aldrich; Toluene, 99.8 %, extra dry, AcroSeal, Acros Organics; sn-Glycero-3-phosphocholine 1:1 cadmium chloride adduct (GPC), 98 %, Sigma Aldrich; 3-(9H-Carbazol-9-yl)propanoic acid (CzPA), 95 %, abcr GmbH; 4-Dimethylaminopyridine (DMAP), 99 %, Sigma Aldrich; 2,4,6-Trichlorbenzoyl chloride

(TCBC), 97 %, Sigma Aldrich; PEDOT:PSS (poly(3,4-ethylenedioxythiophene) polystyrene sulfonate), Heraeus Germany GmbH & Co. KG; PVK (Poly(9-vinylcarbazole), Mw > 1 × 105, product ID LT-N4078), Luminescence Technology Corp. (Lumtec, Taiwan); B3PYMPM (4,6-Bis(3,5-di(pyridin-3-yl)phenyl)-2-methylpyrimidine, sublimed > 99 %, ProductID: LT-N876) and LiF (Lithium fluoride, > 99,99 %, ProductID: LT-E001) have been obtained from Luminescence Technology Corp. (Lumtec, Taiwan); All chemicals were used as purchased.

Nanoparticle and Device Preparation. *Preparation of Oleylammonium Halide (OLA-HX).* To prepare a 1.1 mmol/mL OLA-HX precursor solution, 10 mL of oleylamine (OAm) was placed in a 25-mL three-neck flask and either 1 mL of concentrated hydrochloric acid (HCl(aq.)) or 1.28 mL of concentrated hydrobromic acid (HBr(aq.)) was added slowly. Subsequently, the solidified reaction mixture was heated at 120 °C under nitrogen atmosphere for 2 h. The reaction temperature was then increased to 150 °C for 30 min and afterwards allowed to cool to room temperature. The mixture was kept in a glovebox and heated to 80 °C before injection.

Synthesis of $CsPbBr_2Cl$ Nanocrystals. $CsPbBr_2Cl$ Nanocrystals were made by a Hot-Injection synthesis using a modified literature method[248]. To synthesize ~ 12 nm $CsPbBr_2Cl$ nanocrystals, 49 mg (0.15 mmol) Cs_2CO_3, 67 mg (0.3 mmol) PbO and 1.5 mL oleic acid (OA) were degassed in 15 mL ODE in a 50 mL three-neck flask under reduced pressure at 120 °C for 1 h. Then the temperature increased to 260 °C under nitrogen atmosphere, 1 mL OLA-HBr and 0.5 mL OLA-HCl precursor were quickly injected and after 5 min the reaction mixture was cooled to room temperature (using an ice-bath below 180 °C).

Isolation and Purification of $CsPbBr_2Cl$ Nanocrystals. $CsPbBr_2Cl$ NCs were collected by centrifuging the suspension (7000 rpm, 10 min), decanting the supernatant, and collecting the precipitate. The precipitate was centrifuged again without addition of a

solvent (7000 rpm, 5 min), and the resulting supernatant was removed with a syringe, to separate the traces of residual supernatant. The precipitate was dissolved in 2 mL hexane and centrifuged again (2500 rpm, 5 min) to remove aggregates and larger particles. The resulting supernatant was filtered through a 0.2 µm PTFE syringe filter and stored as stock solution inside of a glovebox with a typically concentration of 10 mg/mL.

Zwitterionic Ligand Synthesis. The following DCzGPC ligand was synthesized using a modified literature method for the Yamaguchi-esterification.[230] A solution of 3-Carbazol-9-yl-propionic acid (220.1 mg, 0.92 mmol) in 12 mL anhydrous dichlormethane (DCM) was treated with sn-Glycero-3-phosphocholin 1:1 cadmium chloride adduct (GPC) (101.3 mg, 0.23 mmol), triethylamine (Et_3N) (256 mL, 1.84 mmol), 2,4,6-tricholrobenzoyl chloride (TCBC) (224 mL, 1.40 mmol) and 4-Dimethylaminopyridine (DMAP) (56.2 mg, 0.46 mmol). The reaction mixture was stirred for 24 h at 40 °C until TLC indicated disappearance of the starting material. The mixture was quenched with citric acid (10 % aqueous solution, 30 mL), and extracted with dichlormethane (DCM) (3x15 mL). The combined organic layers were washed with brine, dried over $MgSO_4$, filtered, and concentrated in vacuo. The crude product was purified by column chromatography on silica gel (CH_2Cl_2/CH_3OH/H_2O (65:25:4, v/v/v)) to give the desired colorless solid (63.5% yield, Rf 0.38); ^{1}H-NMR (400 MHz, $CDCl_3$),δ: 2.52 (m, 2H, g), 2.69 (m, 2H, g), 3.0 (s, 9H , a), 3.39 (m, 2H,b), 3.81–4.19 (m, 6H, f,c,d), 4.40 (m, 4H, h), 5.09 (m, 1H, e), 7.08 (m, 2H, C), 7.14 (m, 2H, C), 7.35 (m, 8H, A,B), 7.87 (m, 2H, D), 7.98 (m, 2H, D) ; ^{31}P-NMR(162 MHz, $CDCl_3$), δ: -0.81; HRMS (ESI-TOF): m/z calcd for $C_{38}H_{42}N_3O_8P$ $[M + Na]^+$ 722.26017; found 722.25982

Ligand Exchange Procedure. The DCzGPC stock solution was prepared by dissolving 140 mg of DCzGPC with 20 mL of Tetrahydrofuran (THF), resulting in a volume concentration of 7 mg/mL. The stock solution of $CsPbBr_2Cl$ NCs was precipitated before

ligand exchange with an equal volume of methyl acetate (MeOAc) at 7000 rpm and redispersed in hexane. To obtain a 41 wt % DCzGPC solution, equal volumes of 10 mg/mL $CsPbBr_2Cl$ NC solution in hexane and 7 mg/mL DCzGPC solution were mixed with a magnetic stir bar for 5 min to exchange the native ligands. After adding the ligand solution, the mixture became turbid and the resulting exchanged NCs could be precipitated at 7000 rpm using twice the volume of hexane. The precipitate could be redispersed in chloroform, ethyl acetate, chlorobenzene, or tetrahydrofuran to obtain a colloidal solution. All $CsPbBr_2Cl$ NC solutions were kept in a nitrogen-filled glovebox and exhibited stable luminescence for at least 4 months at room temperature.

Device Fabrication. The substrates for LEDs, sized 2x2 cm and coated with 90nm structured Indium tin oxide (ITO), were purchased from Kintec (Hong Kong). Initially, PEDOT:PSS was spin-coated in the cleanroom on top of the structured ITO substrates, at 4000 rpm for 30 s, and heated on a hot plate at 130 °C for 15 min, resulting in a smooth, approximately 40 nm thin film. The samples were transferred to a nitrogen-filled glovebox immediately. As a second layer, the approximately 20 nm thin PVK film was deposited by spin-coating a 3 mg/mL concentrated PVK-chlorobenzene solution at 3000 rpm for 30 s and heating at 175 °C for 30 min. The LHP NC solutions were spin-coated as described for the PL samples, after cooling the substrate to room temperature, resulting in a closed film of about 2–3 monolayers (effective thickness approximately 20 nm). To build a top contact, 55 nm B3PYMPM (rate: 100 pm/s) followed by 0.5 nm LiF (rate: 10 pm/s) were evaporated. The devices were finished with a 60 nm (rate: 100 pm/s) thick aluminum cathode, also deposited by thermal deposition. This fabrication is consistent with previously made perovskite LEDs published in reference [223].

Measurement Details. *UV-vis and Photoluminescence (PL) Spectroscopy.* Optical measurements were performed on a UV-vis-NIR spectrometer (Agilent Technologies, Cary 5000) and a fluorescence spectrometer (PerkinElmer FL8500). All spectra were

acquired under ambient conditions in a mixture of toluene and tetrahydrofuran (3:1) at room temperature (25 °C) in a cuvette of 1 cm pathlength. For thin-films, the solutions were dropcasted or spincoated on a thin glass coverslip.

Nuclear Magnetic Resonance (NMR) Spectroscopy. ^{1}H (400.160MHz) and ^{13}C (100.620MHz) spectra were recorded on a BrukerAvance400 III HD spectrometer. $CDCl_3$ was used as solvent at room temperature. The ^{1}H NMR spectra were referenced to the residual signal of the non-deuterated solvent component ($CDCl_3$ 7.25 ppm). Peak assignments were made by NMR spectroscopy (^{1}H, ^{31}P, ^{1}H-^{1}H-COSY).

High Resolution Mass Spectrometry (HRMS). HRMS (ESI-TOF) analysis was performed on a Bruker maXis 4G system.

Scanning Electron Microscopy (SEM). SEM imaging was performed on Si/SiO_x substrates with a HITACHI model SU8030 at 30 kV. SEM micrographs were taken of thin film samples, spincoated using 10 rps for 30 s with a 3 s ramp.

X-Ray Electron Spectroscopy (XPS) and Ultraviolet Photoelectron Spectroscopy (UPS). For characterization of the DCzGPC ligand and interaction after ligand exchange, we performed XPS and UPS measurements. The measuring system consisted of a multi-chamber UHV unit with a base pressure of pressure of 5×10^{-10} mbar. The analysis chamber was equipped with a monochromated Al K_α radiation source (XR 50 M, Specs), an ultraviolet source (UVS 300 SPECS), and a Phoibos 150 hemispherical photoelectron analyzer. For energy calibration of the analyzer, core-level spectra of Au and Cu foils were measured and the energy scale was set to the Au $4f_{7/2}$ (84.0 eV) and the Cu $2p_{3/2}$ (932.6 eV) peak positions respectively. UPS spectra were calibrated with respect to the metal (Au) Fermi-edge. An energy resolution of 400 and 150 meV for XPS and UPS was achieved, respectively.

Transient Absorption Spectroscopy (TA). Pump-probe spectroscopy was conducted with a femtosecond transient absorption spectrometer (HELIOS Fire) from Ultrafast Systems. An Astrella-F ultrafast Ti:sapphire amplifier from Coherent was used to generate 90 fs laser pulses at a repetition rate of 1 kHz at a central wavelength of 800 nm. A beam splitter was used to split the fundamental beam into a pump and a probe beam. The pump beam wavelength was altered to monochromatic 325 nm (0.5 µJ/pulse) by using the fourth harmonic of the signal in an Apollo-T optical parametric amplifier from Ultrafast Systems. The probe beam was directed to a mechanical delay-line from Ultrafast Systems to create time delays between the pump and probe up to 8 ns. The broadband probe spectrum from 320 to 640 nm was created subsequently through the use of a CaF_2 crystal. Thin films were prepared under inert conditions via dropcasting. A glass plate was used as a substrate sealed oxygen-free with a homemade sample holder. A reference channel for the probe was used to account for pulse-to-pulse energy fluctuations and multiple spectral scans were acquired and averaged for each experiment making sure no sample degradation occurred during the measurement.

Current Density-Voltage-Luminescence (j-V-L) and Lifetime (L-t). j-V-L and L-t curves were recorded with a Keithley 2612B source meter unit (SMU) at rates of 1V/s. A photodiode of known diameter at known distance was used for luminance detection. Angular dependent electroluminesce spectra were taken with a Phelos instrument (Fluxim AG, Switzerland). Using a Lambertian approximation, the EQE was determined. The validity of the EQE values was verified within a relative error of 10 % by random sampling with a calibrated integrating sphere.

Associated Content

Supporting Information. A listing of the contents of each file supplied as Supporting Information should be included. The following files are available free of charge. (**S1**) NMR spectra. (**S2**) Optical excitation spectra. (**S3**) Size histograms of the NCs.

(S4) Photoluminescence spectra. (S5) XPS and UPS. (S6) Photoluminescence Quantum Yield. (S7) Transient absorption spectroscopy. (S8) Device lifetime measurements. (S9) Calculations of the hypsochromic shift.

Corresponding Author

*marcus.scheele@uni-tuebingen and bruetting@physik.uni-augsburg.de

Author Contributions

The manuscript was written through contributions of all authors. All authors have given approval to the final version of the manuscript.

Funding Sources

This work was supported by the DFG under grants SCHE1905/8-1, BR1728/21-1 (project no. 424708673) and SCHE1905/9-1.

4.6 Supplementary Information

Enhancing the Stability and Performance of Perovskite Nanocrystal-Based Light-Emitting Devices by Zwitterionic Carbazole Functionalization

Christopher Kirsch[1], Tassilo Naujoks[2], Philipp Haizmann[1], Philipp Frech[1], Heiko Peisert[1], Thomas Chassé[1], Wolfgang Brütting[2], Marcus Scheele[1]

[1] Institut für theoretische und physikalische Chemie, Universität Tübingen, 72076 Tübingen, Germany

[2] Institut für Physik, Universität Augsburg, Augsburg 86135, Germany

Section S4.1 Overview NMR spectra

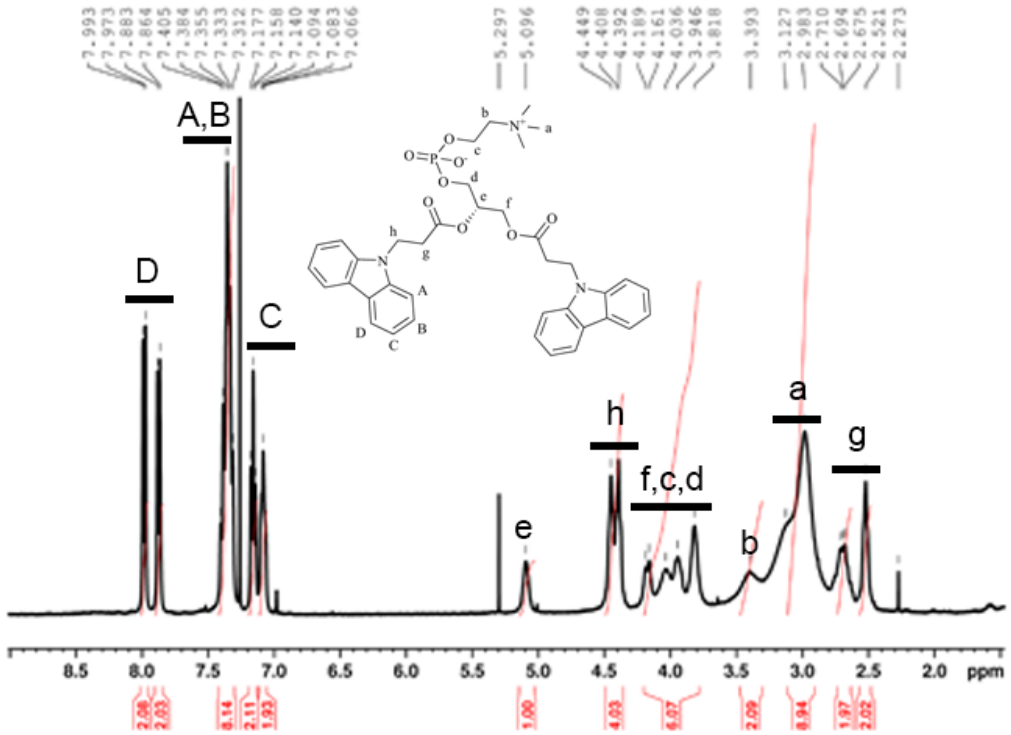

Figure S4.1: ^{1}H-NMR spectra of synthesized DCzGPC ligand in $CDCl_3$. Peaks common to all lecithin components were assigned according to the general pictogram.

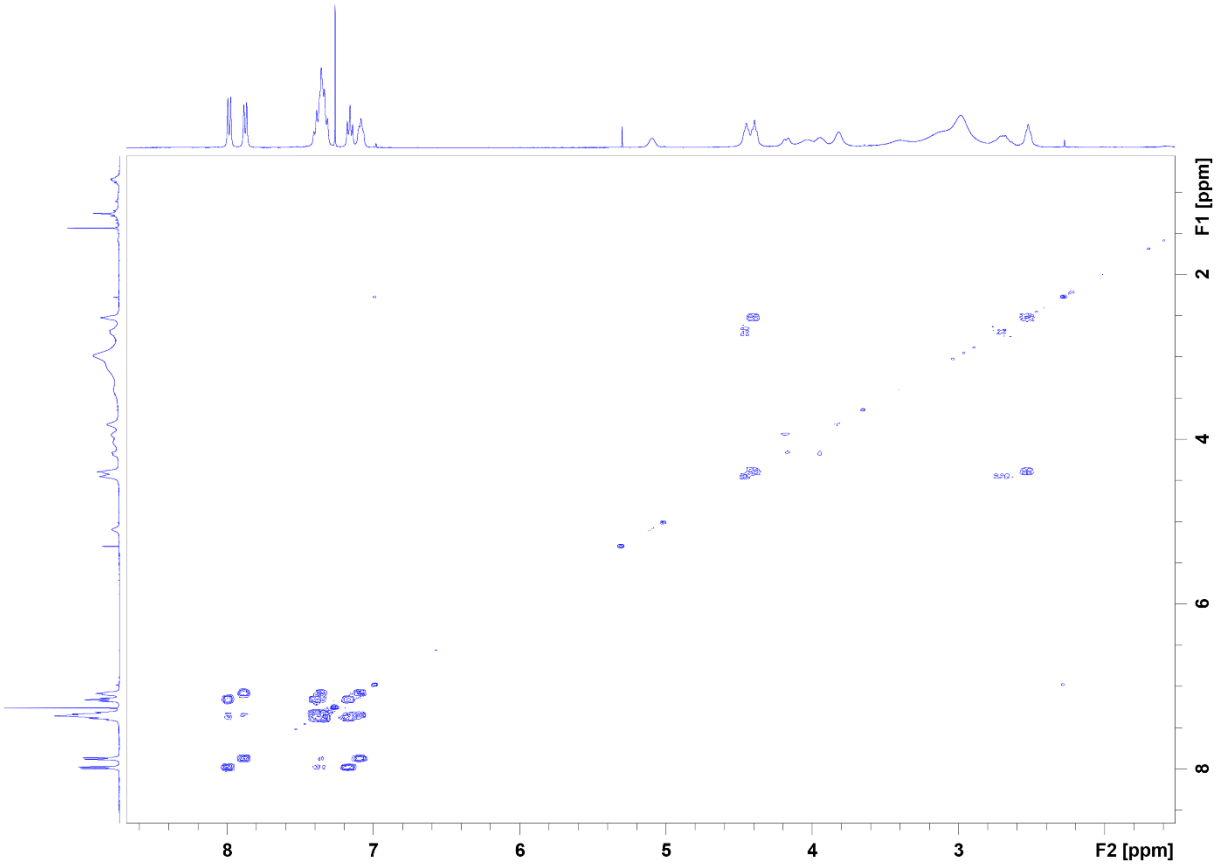

Figure S4.2: ^{1}H-^{1}H COSY-NMR spectra of synthesized DCzGPC ligand in $CDCl_3$.

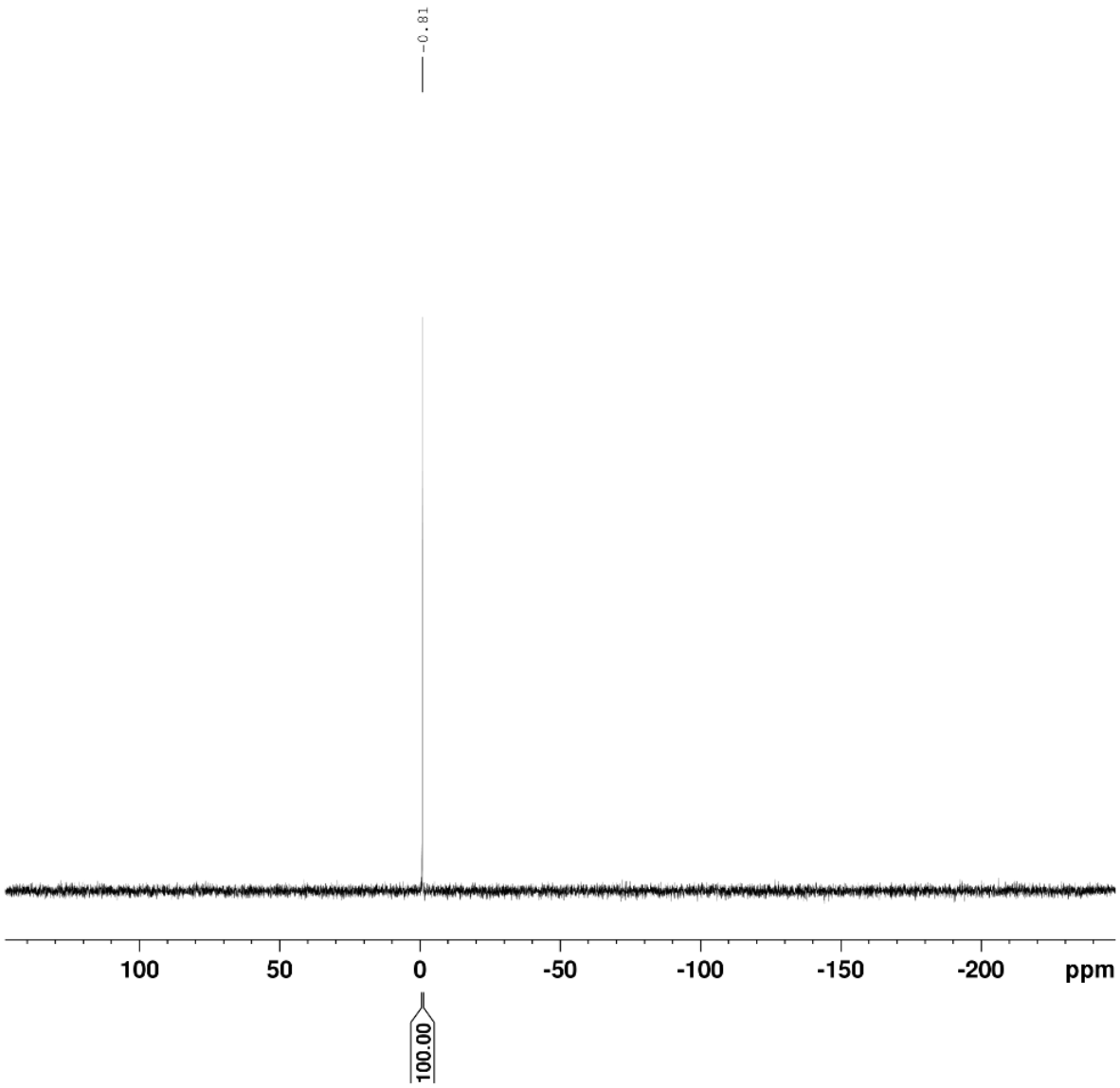

Figure S4.3: ^{31}P-NMR spectra of synthesized DCzGPC ligand in $CDCl_3$.

Section S4.2 Excitation Spectra of native $CsPbBr_2Cl$ NCs and ligand exchanged NCs

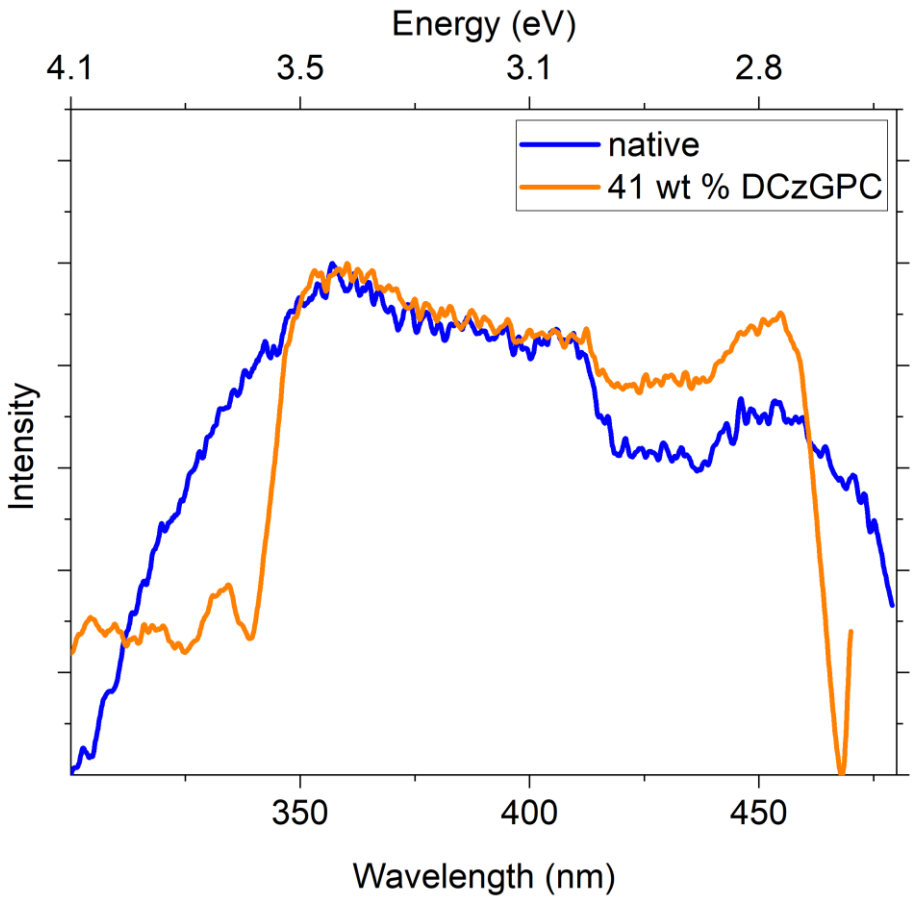

Figure S4.4: Excitation Spectra of $CsPbBr_2Cl$ NCs (blue) and with 41 wt % DCzGPC exchanged NCs (orange). For the detection wavelength, the respective emission maximum from the PL experiment was used.

Section S4.3 Size distribution determined from SEM micrographs

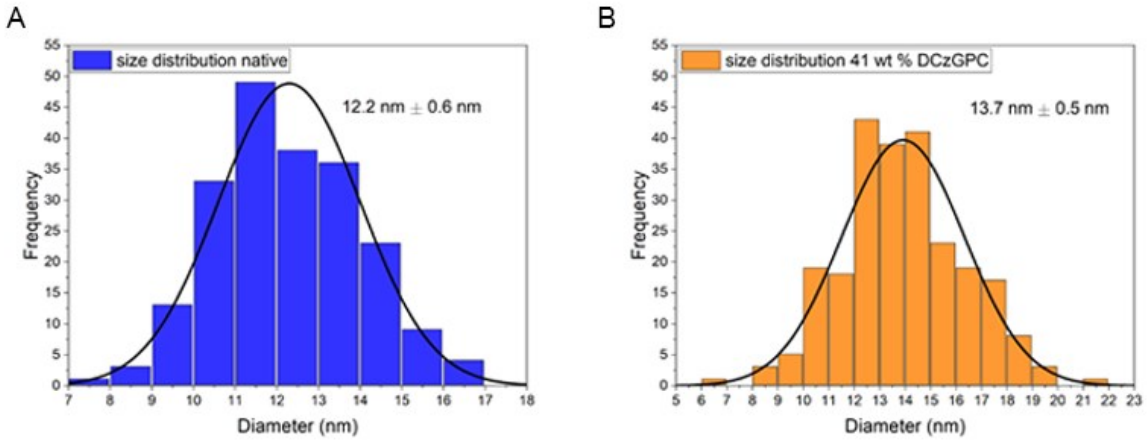

Figure S4.5: Size distribution determined from SEM micrographs of native $CsPbBr_2Cl$ (**A**) and with DCzGPC exchanged nanocrystals (**B**).

Section S4.4 Photoluminescence of green-emitting $CsPbBr_3$ NCs

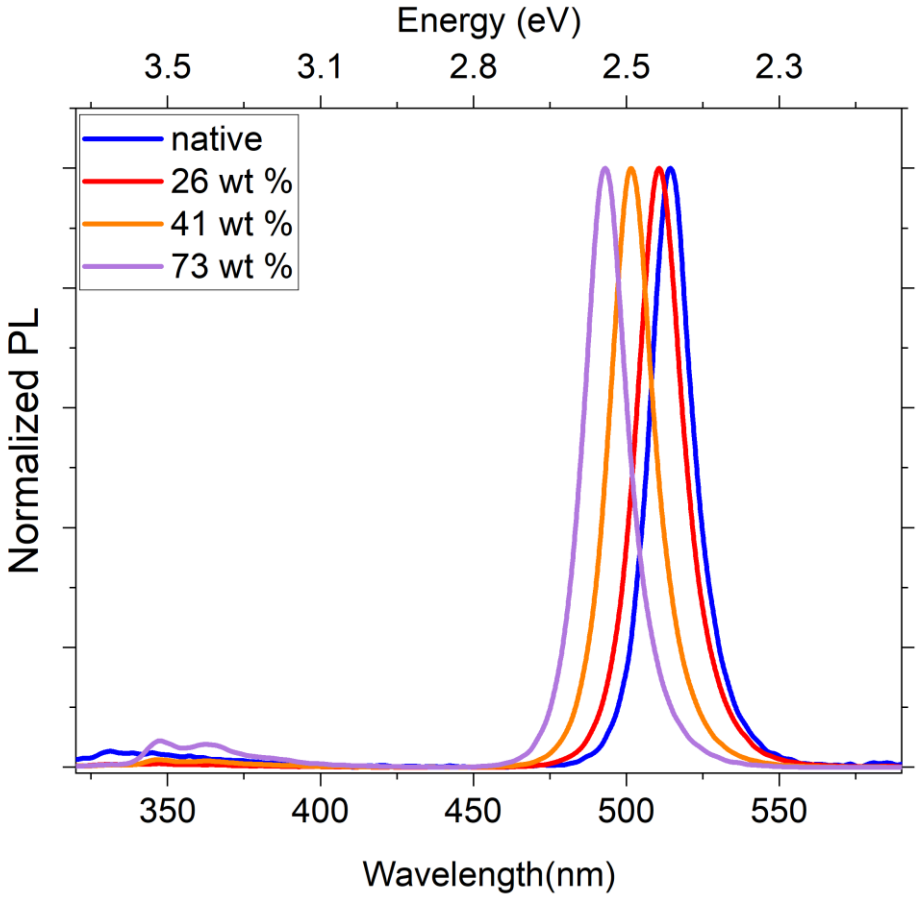

Figure S4.6: Photoluminescence spectra of the $CsPbBr_3$ nanocrystals before (blue) and after (red, orange, and purple) exchanging the ligand shell with different amounts of DCzGPC ligand.

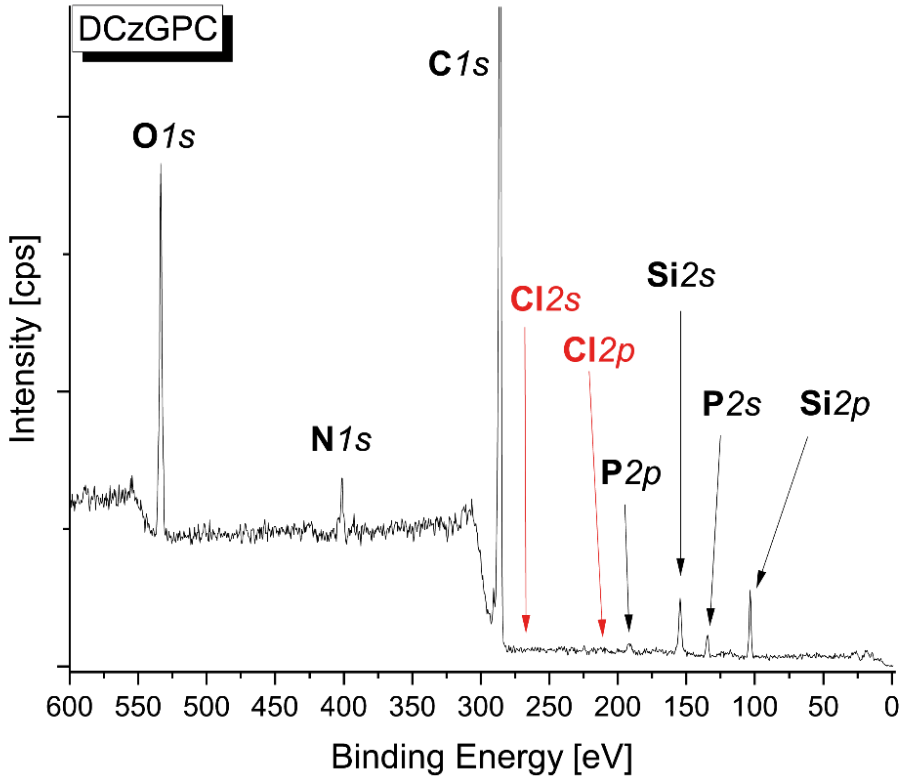

Figure S4.7: XPS survey spectra of pure DCzGPC ligand. All specific signals for the ligand (O1s, N1s, C1s and phosphor) are found. No signals are found for chlorine.

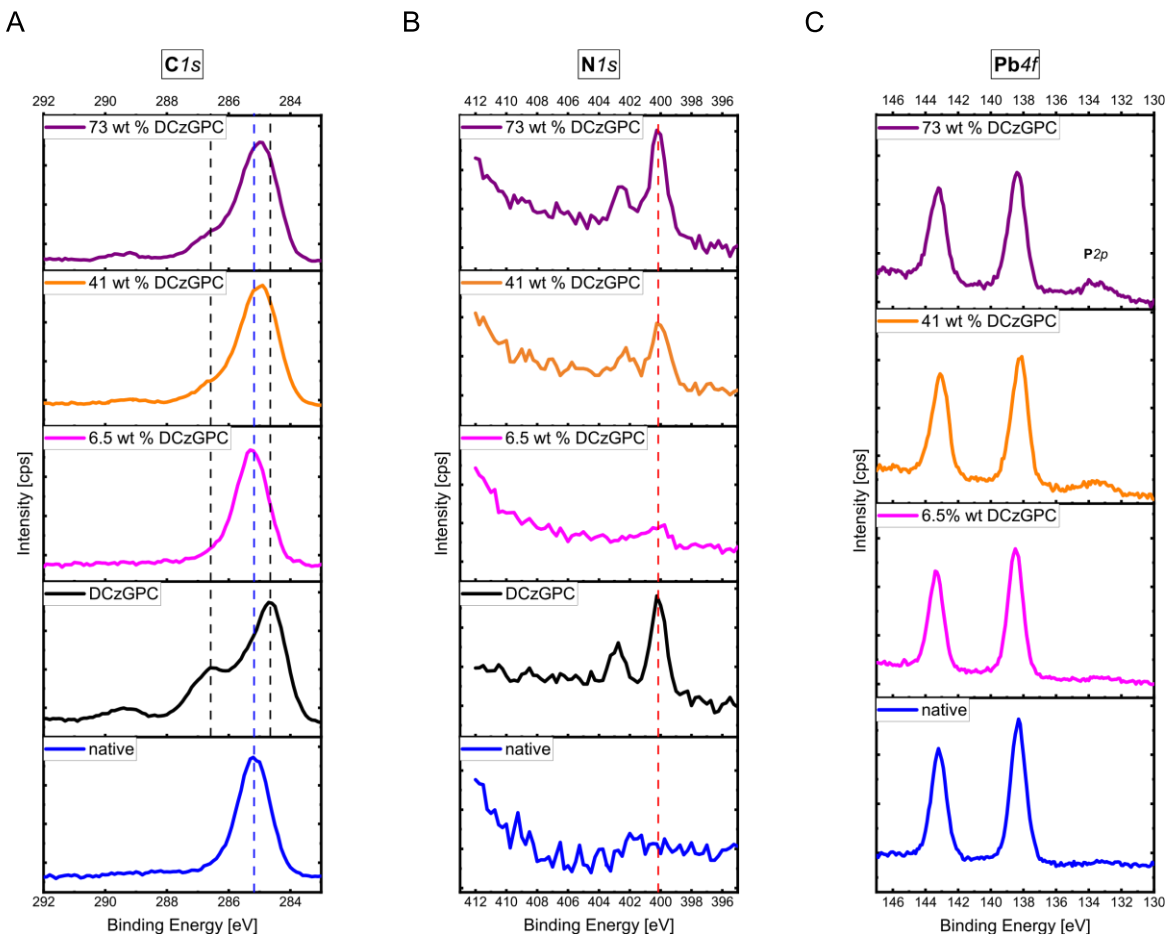

Figure S4.8: XPS Spectra of the core-level regions of C1s, N1s and Pb4f. Signals of the DCzGPC become more pronounced with increased addition. Analysis of the Pb4f core-level shows no change in binding energy or signal shape after ligand exchange. This excludes doping of the particle by the new ligand.

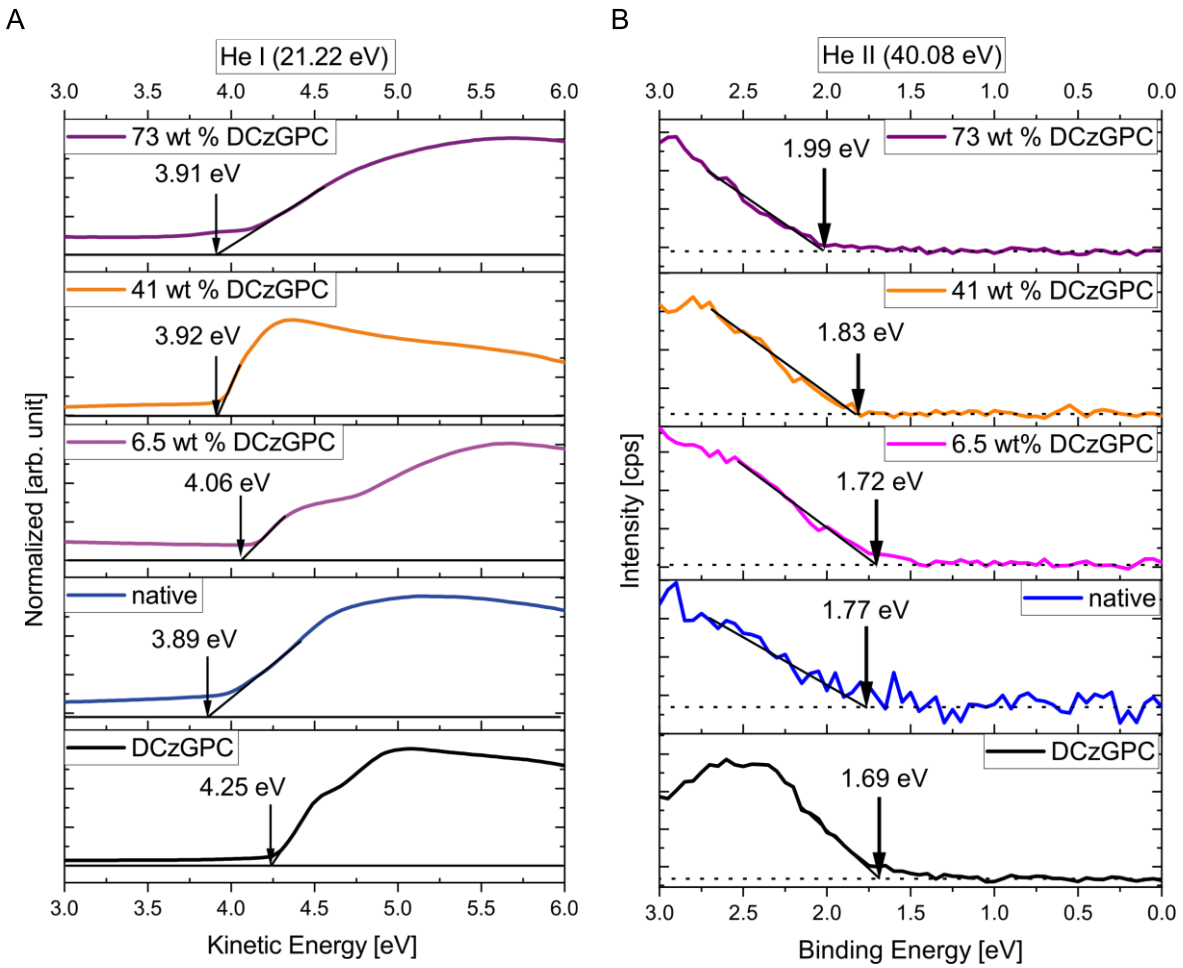

Figure S4.9: **A)** Secondary electron cut-off measurements with He I radiation (hν: 21.22 eV). **B)** Valence band maximum measurements with He II radiation (hν: 40.8 eV).

The determination of the secondary electron cut-off (SECO) of surfactant-stabilized nanoparticle samples is challenging due to inhomogeneous charging effects. Care was taken to prepare homogeneous single-layer films, but in the UPS spectra there are still areas where partial charging occurs due to stacked layers with insufficient charge transport. For the determination of the SECO, the intersection of the slope with the zero line was therefore used without background correction to eliminate the effect of partial charging. From the measurement of the pure DCzGPC ligand, where partial charging was practically absent and background correction theoretically feasible, the difference in the work function with/without background correction is approx. 30 meV, e.g. relatively small compared to the main conclusion that “the work function after ligand exchange is nearly unaffected”.

Section S4.6 absolute Photoluminescence Quantum Yield

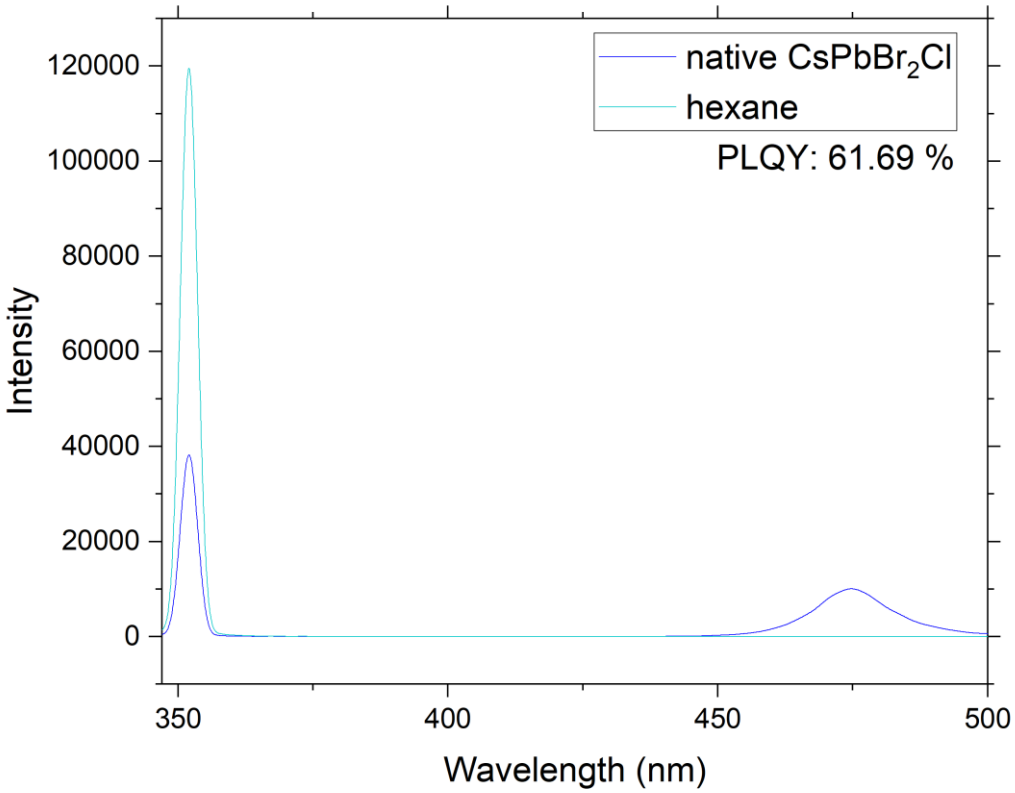

Figure S4.10: absolute PLQY measurement of pristine $CsPbBr_2Cl$ NCs in hexane.

Section S4.7 Transient Absorption Spectroscopy

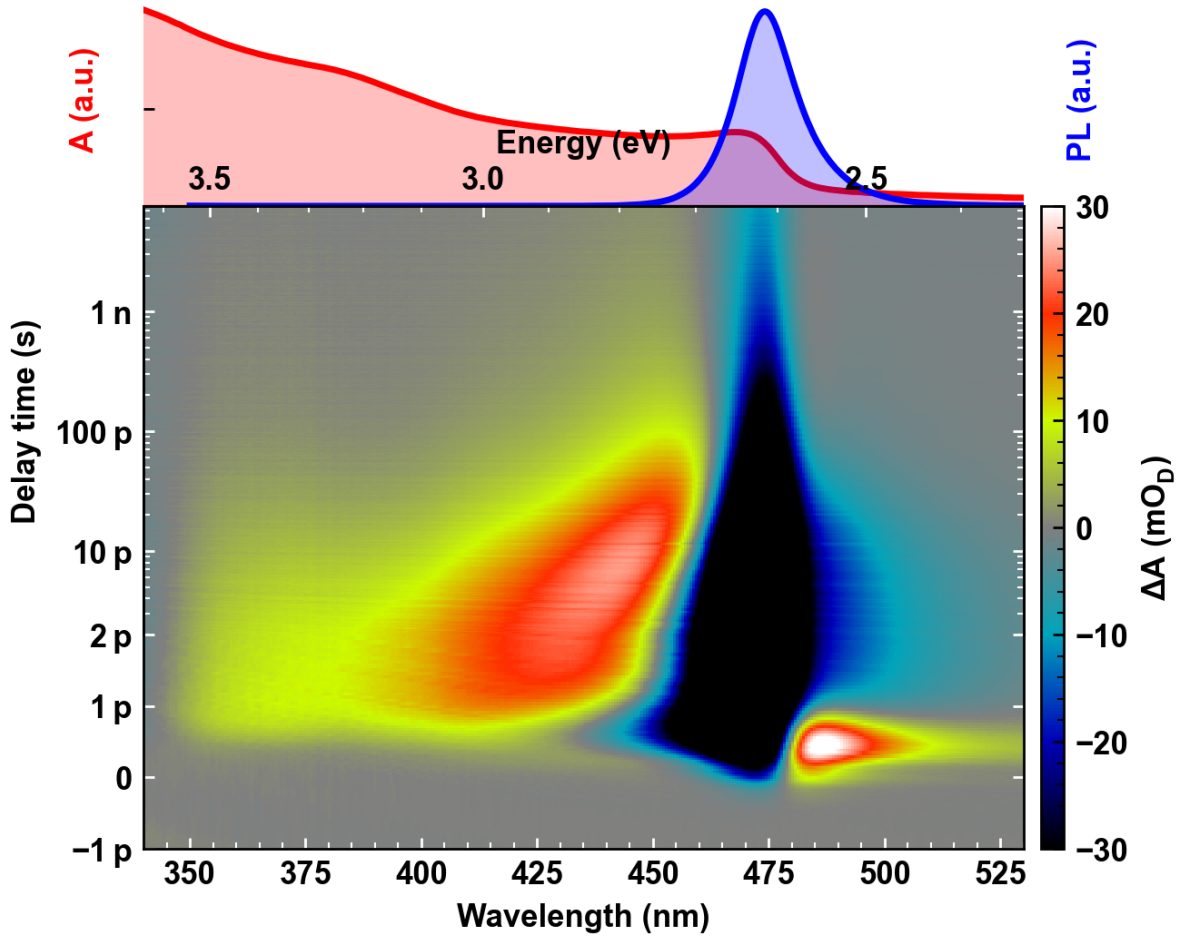

Figure S4.11:. 2D fs transient absorption plot of a thin film of the native perovskite system after excitation at 325 nm (0.5µJ/pulse). Steady-state absorption and photoluminescence spectra are shown in red and blue respectively above the 2D plot.

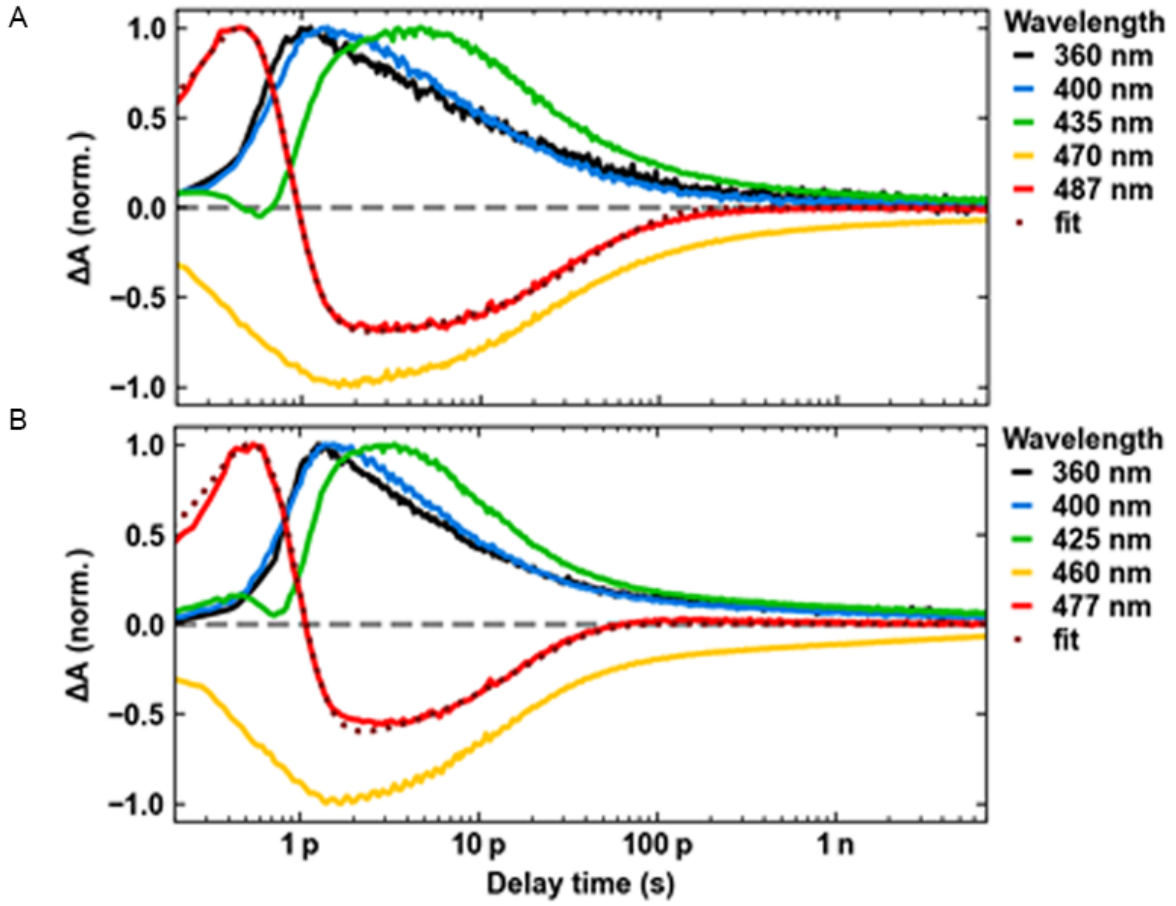

Figure S4.12: Kinetic traces at selected wavelengths of the native **A)** and exchanged system **B)** after excitation at 325 nm as well as the result of a biexponential fit at the maximum of the sub-band gap feature at 487 nm and 477 nm (red).

The following function (convolution of the instrument response function, IRF, and a sum of exponentials) was used to fit the sub-band gap feature at 487 nm for the native and 477 nm for the exchanged system where t_0 is the pump-probe delay, just before the signal starts rising, IRF the instrument response function ($\approx 0.4\ ps$), A_i being the amplitudes and t_i the decay times.

$$S\ t\ = e^{-\left(\frac{t-t_0}{\frac{IRF}{2\ln 2}}\right)^2} \cdot \sum_i A_i\, e^{-\frac{t-t_0}{t_i}} \tag{S4.1}$$

Biexponential fitting gives values of $t_1 = 0.3\ ps \pm 0.02\ ps$ and $t_2 = 42\ ps \pm 1\ ps$ for the native system at 487 nm and values of $t_1 = 0.3\ ps \pm 0.02\ ps$ and $t_2 = 17\ ps \pm 0.5\ ps$ for the exchanged system at 477 nm.

Table S4.1 Band gap renormalization energy $\boldsymbol{\Delta E}$ at different pump-probe delay times for the native and exchanged perovskite system

PUMP-PROBE DELAY (FS)	ΔE_{native} (meV)	$\Delta E_{exchanged}$ (meV)	Relative increase
200	74	76	3 %
300	76	80	5 %
400	82	90	10 %
500	87	93	7 %
600	89	99	11 %
700	86	99	15 %
800	89	101	13 %

Section S4.8 Lifetime measurements

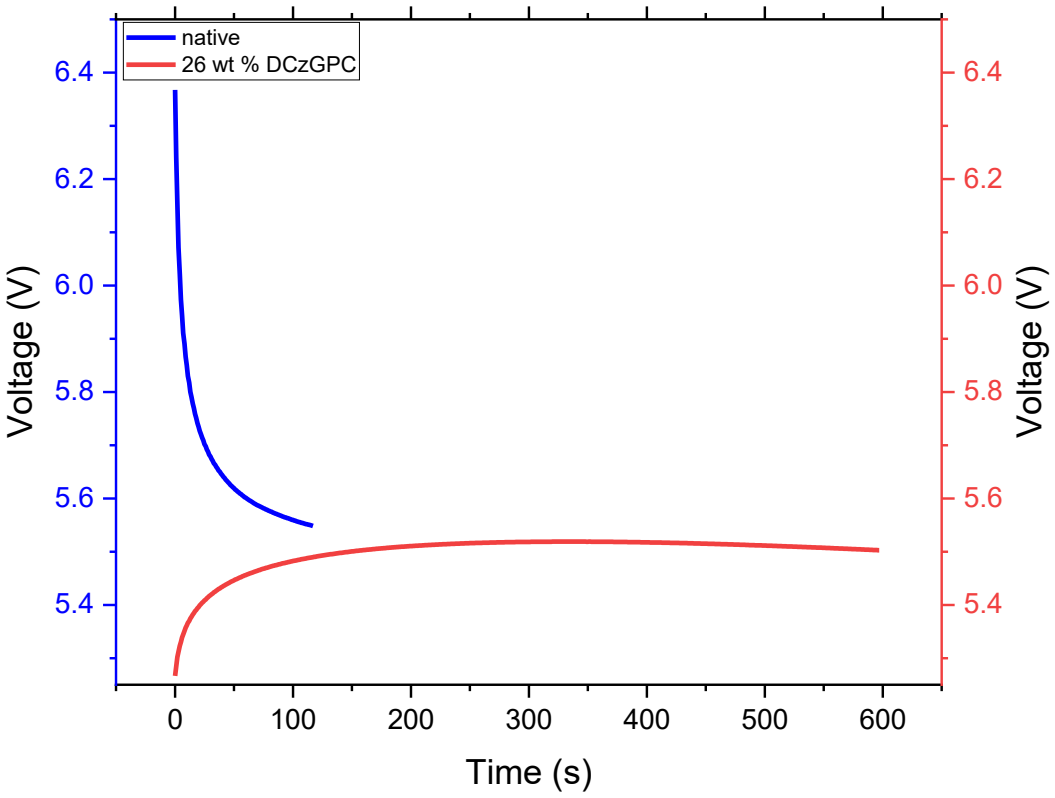

Figure S4.13: Voltage vs time dependence corresponding to the lifetime measurement (**Figure 4.5** main publication). Despite applying the same current, voltage responses differ between samples. Implied resistance (~1/V) decreases monotonically for native samples, and initially increases for DCzGPC treated samples.

Section S4.9 Estimating Blue-shift Contribution via Brus Equation

The origin of the blue shift induced by the DCzGPC ligand exchange remains elusive. However, some basic analytical considerations using Brus' equation may provide insight to the root of the influence. Overall, it implies that the hypsochromic shift may arise from a change of effective mass. As elucidated by Brus *et al.*[249], the energy gap of a nanoparticle in weak confinement regime can be predicted by taking the bulk gap and reducing it by the excitons binding energy and adding the confinement energy arising from a particle-in-a-box consideration:[250]

$$E_{gap,NC} = E_{gap,bulk} + E_{exciton} + E_{confinement} \tag{S4.2}$$

With the energy gap of the bulk LHP, $E_{gap,bulk}$, the exciton coulomb energy, $E_{exciton}$, and the confinement energy, $E_{confinement}$ While the bulk energy gap is determined by the halide composition, the exciton's attractive and therefore negative energy is determined by the reduced mass, $\mu = \frac{m_e \cdot m_h}{(m_e + m_h)}$, and the permittivity ε_r. The confinement energy of a nanocrystal is primarily determined by its size and the reduced mass of its constituent particles. This energy can be estimated using the 3-D particle in a box model, which is a widely used framework in quantum physics textbooks:

$$E_{exciton} = -\left(\frac{e^2}{4\pi\varepsilon_0\hbar}\right)^2 \cdot \frac{\mu}{2\varepsilon_r^2} = -\frac{\nu_{Ry}^2}{2} \cdot \frac{\mu}{\varepsilon_r^2} \tag{S4.3}$$

$$\mathrm{E_{confinement}} = \frac{\hbar^2 k^2}{2\mu} = \frac{\hbar^2}{2\mu} \cdot \sum_i^3 \left(\frac{n_i \pi}{a} e_i\right)^2 = \frac{3\hbar^2\pi^2}{2\mu a^2} \tag{S4.4}$$

$$\mathrm{E_{confinement}} = \frac{\hbar^2\pi^2}{2\mu\left(\frac{a}{\sqrt{3}}\right)^2} = \frac{\hbar^2\pi^2}{2\mu a^2} \tag{S4.5}$$

Using effective masses ($m_e = 0.15m_0$ and $m_h = 0.14m_0$) and permittivity ($\varepsilon_r = 4.96$) from Protesescu *et al.* [29] (**Table S4.2**) and bulk energy gaps from references [251,252], the individual contribution can be calculated as shown in **Table S4.2**.

Table S4.2 Energy contributions according to **eq. (S4.2)**. Reducing coulomb interaction via dielectric screening may only blue-shift as much as 40 meV.

Composition	$E_{gap,bulk}$	μ	$E_{exciton}$	$E_{confinement}$	$E_{gap,NC}$
$CsPbBr_3$	2.29 eV / 541.4 nm	$0.072m_0$	–40 meV	+156 meV	2.41 eV / 515.4 nm
$CsPbBr_2Cl$	2.59 eV / 478.1 nm	$0.072m_0$	–40 meV	+105 meV	2.65 eV / 467.1 nm

The calculated energy gap agrees very well with the measured PL peaks for the native $CsPbBr_3$ as well as $CsPbBr_2Cl$ NCs. However, it becomes evident that the measured blue-shift of 100 meV (22 nm) in case of $CsPbBr_3$ NCs and 120 meV (19 nm) in case of $CsPbBr_2Cl$ NCs cannot arise from dielectric screening, that is, an increase in the permittivity because the exciton energy is too small to account for these shifts. Apparently, the only term that shows the potential to induce such strong blue-shifts is $E_{confinement}$. However, as the particle size itself does not decrease, the only variable that is left is the reduced mass.

$$\Delta E := E_{gap} - E_{gap,bulk} = -\nu_{Ry}^2 \cdot \frac{\mu}{2\varepsilon_r^2} + \frac{\hbar^2\pi^2}{2\mu a^2} \tag{S4.6}$$

Equation (S4.6) leads to the quadratic equation:

$$0 = -\nu_{Ry}^2 \cdot \frac{\mu}{2\varepsilon_r^2} + \frac{\hbar^2\pi^2}{2\mu a^2} - \Delta E \tag{S4.7}$$

Or

$$0 = -\mu^2 \cdot \frac{\nu_{Ry}^2}{2\varepsilon_r^2} - \mu \cdot \Delta E + \frac{\hbar^2\pi^2}{2a^2} \qquad \mu \neq 0 \tag{S4.8}$$

Solving **eq. (S4.8)** by using the experimentally determined shift of the optical gap ΔE, an estimate for the change in reduced mass can be obtained. As shown in **Table S4.3,** in the case of $CsPbBr_3$ the decrease in reduced mass from 0.072 to 0.045 can be achieved by halving for example the effective hole mass to $0.072m_e$. Similarly, for $CsPbBr_2Cl$ an even stronger reduction can take place, while the electron mass could also be concurrently reduced.

Table S4.3 Reduced mass and the implied energies after ligand exchange with 73 wt. % DCzGPC.

Composition	$E_{gap,bulk}$	μ_{DCzGPC}	$E_{exc..,DCzGPC}$	$E_{conf.,DCzGPC}$	$E_{gap.,DCzGPC}$
$CsPbBr_3$	2.29 eV / 541.4 nm	$0.045m_0$	–25 meV	+250 meV	2.51 eV / 493.0 nm
$CsPbBr_2Cl$	2.59 eV / 478.1 nm	$0.031m_0$	–17 meV	+195 meV	2.77 eV / 448.0 nm

5. Quantum Efficiency Enhancement of Lead-Halide Perovskite Nanocrystal LEDs by Organic Lithium Salt Treatment

Tassilo Naujoks [1] *Roshini Jayabalan* [1] *Christopher Kirsch* [2] *Fengshuo Zu* [3] *Mukunda Mandal* [4] *Jan Wahl* [2] *Martin Waibel* [1] *Andreas Opitz* [3] *Norbert Koch* [3,5] *Denis Andrienko* [4] *Marcus Scheele* [2] *and Wolfgang Brütting* *[,1]

[1] Institut für Physik, Universität Augsburg, 86135 Augsburg, Germany

[2] Institut für Physikalische und Theoretische Chemie, Universität Tübingen, 72076 Tübingen, Germany

[3] Institut für Physik & IRIS Adlershof, Humboldt-Universität zu Berlin, 12489 Berlin, Germany

[4] Max Planck Institute für Polymerforschung, Ackermannweg 10, 55128 Mainz, Germany

[5] Helmholtz-Zentrum Berlin für Materialien und Energie GmbH, 12489 Berlin, Germany

*E-mail: wolfgang.bruetting@physik.uni-augsburg.de

This chapter is based on the publication published in ACS Applied Materials & Interfaces: *ACS Appl. Mater. Interfaces* 2022, 14, 25, 28985–28996, DOI: 10.1021/acsami.2c04018

5.1 Abstract

Surface-defect passivation is key to achieving high photoluminescence quantum yield in lead halide perovskite nanocrystals. However, in perovskite light-emitting diodes these surface ligands also have to enable balanced charge injection into the nanocrystals to yield high efficiency and operational lifetime. In this respect, alkaline halides have been reported to passivate surface trap states and increase the overall stability of perovskite light emitters. On the one side, the incorporation of alkaline ions into the lead halide perovskite crystal structure is considered to counterbalance cation vacancies, while on the other side, the excess halides are believed to stabilise the colloids. Here, we report an organic lithium salt, viz. LiTFSI, as a halide-free surface passivation on perovskite nanocrystals. We show that treatment with LiTFSI has multiple beneficial effects on lead halide perovskite nanocrystals and LEDs derived from them. We obtain higher photoluminescence quantum yield and longer exciton lifetime, and a radiation pattern that is more favourable for light outcoupling. The ligand-induced dipoles on the nanocrystal surface shift their energy levels toward lower hole-injection barrier. Overall, these effects add up to a four- to seven-fold boost of the external quantum efficiency in proof-of-concept LED structures, depending on the colour of the used lead halide perovskite nanocrystal emitters.

5.2 Introduction

Electroluminescent perovskite light-emitting devices (PeLED) were first reported in the 1990s and achieved external quantum efficiencies similar to state-of-the-art fluorescent organic LEDs at that time;[253] however, because of severe temperature-induced efficiency drop they have been operated at low temperature only, typically in liquid nitrogen.[254] Triggered by their success in photovoltaics, perovskites with the general formula ABX_3 (where A is a monovalent organic or inorganic cation, B a

bivalent cation – typically Pb^{2+} – and X a halide anion) have been "rediscovered" as light emitters less than a decade ago[255] and have developed into a rapidly progressing LED technology ever since.[256–259] Narrow emission bands, which are easily tunable by perovskite composition and size in the case of nanostructured materials, paired with high photo- and electroluminescence efficiency over the entire visible and near-infrared spectral range make them attractive candidates for next-generation displays and lighting. However, despite external quantum efficiencies of PeLEDs being close to organic LEDs, their practical use is still severely limited by insufficient operational lifetimes being on the order of a few 10–100 h at best.[260,261]

In the focus of this work are electroluminescent lead halide perovskite (LHP) nanocrystals (NC), which are, beside 3D bulk and 2D layered perovskites, an emerging class of active light emitters for PeLEDs. They share attractive features like solution processability, ease of bandgap tuning and defect tolerance, however, with potentially higher radiative decay rates and, thus, higher photoluminescence quantum yield in the case of LHP NCs even in the absence of a core–shell structure. Nevertheless, NCs have particularly large surface-area-to-volume ratio, which makes them very sensitive toward surface defects and, thus, strategies to develop defect passivation are particularly important.[262] Consequently, surface chemistry plays a pivotal role in the optoelectronic properties of LHP NCs.

LHP NCs are typically synthesized as colloidal suspensions stabilized by organic ligands, such as oleic acid and oleylamine (see **Figure 5.1**).[29] Despite their high photoluminescence, these pristine "solutions" cannot be used directly for film fabrication and implementation in PeLEDs because of the electrically insulating nature of the ligands. Moreover, nonbinding excess ligands, required to stabilize the suspensions, even deteriorate charge injection into the NCs further.[263–265] "Washing" the nanocrystals before film deposition removes these ligands partially; however, it is at the expense of creating a large density of surface defects with the concomitant

formation of nonradiative exciton decay channels mainly caused by A- and X-site vacancies, as well as inducing stability issues. To overcome these problems, researchers have developed a variety of different surface passivation strategies and employed them in LHP NCs, including halide salts, strongly binding organic ligands, and zwitterionic species.[266–268] In particular, the use of lithium halides has been shown to increase the photoluminescence yield as well as their stability.[269] Therein, its passivation is mostly attributed to the excess halides that fill the corresponding vacancies at the NC surface and, thus, reduce nonradiative defects and, at the same time, suppress ion migration via these vacancies. Nevertheless, the role of the Li^+ cation itself has largely remained elusive. [270] Thus, it is worth studying the effect of halide-free lithium salts, like lithium bis(trifluoromethanesulfonyl)imide (LiTFSI, see **Figure 5.1**), which has already been investigated as a beneficial additive in perovskite solar cells.[271–273] In this work, we show that by adding LiTFSI to various LHP NC solutions, with emission colors ranging from deep red to green to sky blue, their optoelectronic properties are tuned toward a higher photoluminescence quantum yield, better hole injection and transport, and a lower electroluminescence turn-on voltage. Overall, this results in a 4- to 7-fold increase of the external quantum efficiency of PeLEDs.

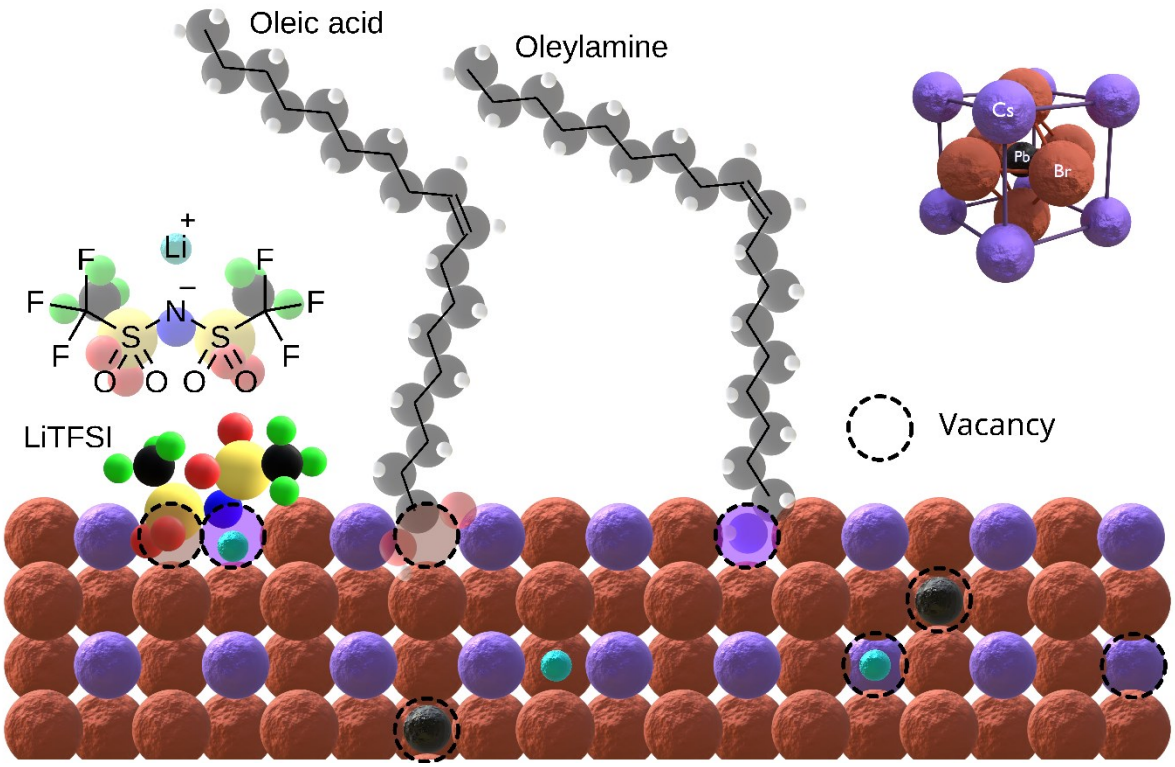

Figure 5.1: Schematic $CsPbBr_3$ NC surface with possible interaction mechanisms by oleic acid, oleylamine, and the organic lithium salt, LiTFSI. Li^+ may fill a vacancy or may be intercalated. On the upper right, a full $PbBr_6$ octahedron with adjacent Cs ions is depicted to illustrate the ABX_3 crystal structure.

5.3 Results and Discussion

5.3.1 Surface Ligand Exchange

LHP NCs with different stoichiometry and emission color, ranging from sky blue ($CsPbBr_2Cl$) to green ($CsPbBr_3$) to red ($MAPbBrI_2$, where MA stands for methylammonium), have been obtained commercially or synthesized as described in the **Methods** section. The native NC solutions with oleylamine and oleic acid surface ligands (10 mg/mL solid NC contents in toluene) have subsequently been mixed with equal volumes of LiTFSI solutions in chlorobenzene; see **Methods** for details. This has resulted in different weight concentrations of LiTFSI relative to the LHP NCs, such as 0.1, 1, 9, and 50 wt %. Thin films have been prepared by spin-coating under an inert atmosphere using these LiTFSI:NC mixed solutions, and their properties were compared with corresponding thin films made from the native NC solutions. In the following, we focus on green $CsPbBr_3$NCs; blue and red NCs are only discussed in the

LED part of this manuscript, but we anticipate that they behave qualitatively similar regarding the effect of LiTFSI on optical, electronic, and charge transport behavior. We mostly consider the 1 wt % LiTFSI doped thin films for characterization, because PeLEDs with this LiTFSI content show the highest luminance while being close to the optimal efficiency, as will be discussed later.

In general, film formation without and with LiTFSI is found to be very similar (see **Figure S5.5**) so that we will not discuss this in detail here. $CsPbBr_3$ NCs of size 7–8 nm arrange in a cubic packing of the NCs on the surface of various kinds of substrates. We do not find a significant difference in NC arrangement and coverage, indicating that the addition of LiTFSI to the NC solutions preserves a certain fraction of the native oleylamine and oleic acid ligands, as schematically shown in **Figure 5.1**. It is important to note that we do not see a significant shrinkage of the NC size upon LiTFSI treatment, in contrast to the findings of Liu *et al.*, where they observe etching of the NC surface by the acidic (H)TFSI.[274] These films were subsequently studied by photoluminescence, photoelectron spectroscopy, density functional theory modeling, and in PeLEDs.

Arguments for successful ligand exchange come from changes of photoluminescence (PL) spectra and lifetimes as well as from photoelectron spectroscopy, as will be discussed in the following two sections.

5.3.2 Photoluminescence

Photoluminescence spectra, quantum yield (PLQY), and lifetime are key indicators for the structural intactness of the LHP NC surfaces, both in solution as well as in thin films. Thereby, not only does ligand passivation play a key role but also the dielectric environment and the substrate on which the NCs are deposited. **Figure 5.2 a** shows a comparison of PLQY of native, i.e., oleylamine/oleic acid-capped, $CsPbBr_3$ NCs on various substrates relative to glass (BK7). When using highly conductive substrates

like metals, ITO, ZnO, or PEDOT:PSS, the PLQY is significantly lowered compared with glass. For PEDOT:PSS, the quantum yield reduction can be ascribed to residual water content, which may degrade the LHP NC significantly and quench luminescence.[275,276] The reduction for ZnO and ITO however originates from a different mechanism; e.g., their high carrier densities may enable exciton-carrier quenching or the oxides could lead to degradation of the LHPs.[277] And even in the case of the organic polymer polyvinylcarbazole (PVK), used as hole transporting layer (HTL) in PeLEDs, the PLQY is slightly lowered with respect to glass. However, by introducing LiTFSI as dopant in PVK the impairment is overcome. LiTFSI as dopant in HTLs is reported to increase their electrical conductivity rendering this effect rather unexpected.[278] Another Li-based substrate treatment is a thin film of LiF evaporated on glass before spin-coating of the LHP NCs, which proves to be even more beneficial on the PLQY (see **Figure 5.2 a**). A positive effect of an LiF interlayer has already been observed for light emission from bulk perovskites. Bigger grain sizes and reduced pinholes in the film were identified as the main cause for a better optical performance.[279] For LHP NCs the grain sizes are predefined during synthesis and not expected to change upon spin-coating on a substrate.[29] Consequently, it is reasonable to assume a different mechanism for the PLQY enhancement.

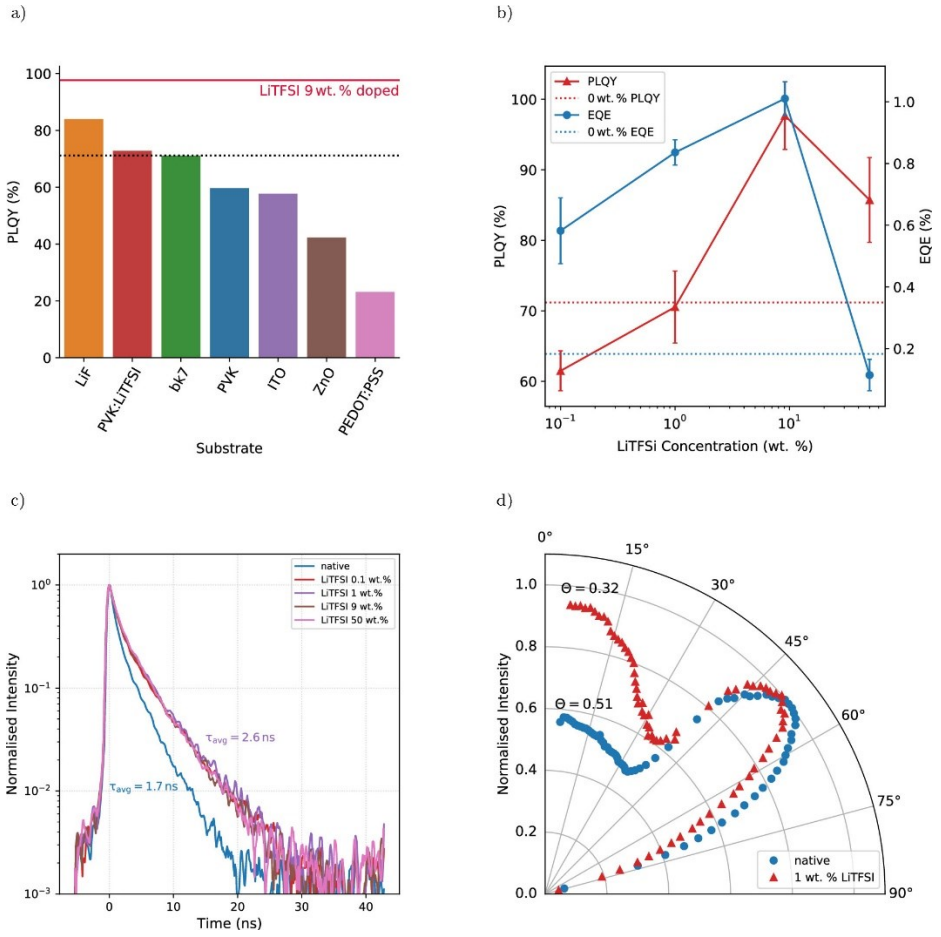

Figure 5.2: **(a)** PLQY of $CsPbBr_3$ NC thin films on various substrates; **(b)** LiTFSI doping concentration dependent PLQY and EQE; **(c)** TRPL decay curves; **(d)** p-polarized ADPL spectra.

This raises the question, whether the nature of the substrate alone affects the PLQY, or if there is interdiffusion from the underlying material into the LHP NC thin film. Thus, to study the influence of LiTFSI on the $CsPbBr_3$ NCs, we directly add the Li salt to the solution prior to spin-coating on glass. Even though a more polar solvent, viz. chlorobenzene, is needed to mix the two substances, an increase in PLQY can be observed, both, in solution and as a thin film. **Figure 5.2 b** shows the PLQYs of thin-films fabricated with different LiTFSI mass percentage mixing ratios. At very low concentrations, the PLQY is slightly decreased with respect to the pristine (0 wt %) LHP NC film, which has a PLQY of about 70%. In contrast to that, at concentrations higher than 1 wt %, the PLQY is significantly increased reaching near unity at 9 wt %, before it decreases again for a 1:1 mixture of both components. The PLQY impairment at low concentrations is comparable to a solvent mixture of toluene and chlorobenzene

(but no LiTFSI), which may imply that some of the NCs are irreversibly degraded by the polar solvent before this detrimental effect is outweighed at higher LiTFSI content.[280]

Together with the changes in the PLQY of LiTFSI-treated $CsPbBr_3$ NC films, we also observed a slight red shift of their PL emission spectra (**Figure S5.1**), which is indicative of ligand exchange by the addition of LiTFSI to the NC solutions prior to spin-coating. Similar observations were recently reported on red-emitting LHP NC and were assigned to the highly dynamic/labile binding situation of oleic acid and oleylamine on the perovskite NC surface.[243,281] Therefore, both the enhanced PLQY and the spectral PL red shift indicate that the new ligand must be in spatial proximity to the NC surface, which is only possible if the native ligand (oleic acid/oleylamine) is replaced.

Because we assumed a surface trap passivation effect by the LiTFSI, time-resolved photoluminescence (TRPL) was measured on the same films (**Figure 5.2 c**). As detailed in the Supporting Information (**Figure S5.2 and Figure** S5.3), the PL transients show a double-exponential decay with a fast initial lifetime of about 1 ns and a slower one with several nanoseconds. Weighting the lifetimes with their relative amplitudes, one obtains an average lifetime, as explained in the context of **Figure S5.2 and Figure** S5.3. For the native sample $\tau_{avg} = 1.7$ ns is obtained, whereas all the LiTFSI-doped ones have similar $\tau_{avg} = 2.6$ ns, with only minor variation $\Delta\tau_{avg} = 0.1$ ns (see **Figure 5.2 c**), which is surprising in view of the observed changes in the PLQY over the same concentration range. However, as discussed above, the PLQY is reduced if there are solvent-degraded LHP NCs in the film, which contribute to absorption of the incident UV light but not to light emission in the visible range. On the other hand, the PL lifetimes do not necessarily have to be affected by degraded LHP NC; if they do not interact with the optically active ones, the obtained lifetimes originate only from intact NCs because the degraded ones are not detected, in contrast to the PLQY measurement.

As the double-exponential fits on the intensity decay (see **Figure S5.2 and Figure** S5.3) reveal, the individual PL lifetimes are concentration independent (just like the average, τ_{avg}). However, a comparison of the amplitudes exhibits a shift of weights toward the longer lifetime with increasing LiTFSI concentration. Together with the PLQY measurements, this implies that within the short lifetime there are more nonradiative decay processes. Furthermore, this could indicate that trap-assisted recombination is suppressed by the presence of LiTFSI. There have been several reports about surface trap passivation featuring various halide salts. They agree on a passivation mechanism by halide abundance, which has also been reported by groups using lithium-free halide salts.[27,248,282,283] However, in our case, the halide-free LiTFSI seems to have a similar effect.

In addition to the changes in PLQY and PL lifetime, we observe a change of the radiation pattern of LHP NC films upon addition of LiTFSI. **Figure 5.2 d** shows the parallelly polarized (p-pol.) angular dependent photoluminescence (ADPL) of a native and a 1 wt % LiTFSI-treated $CsPbBr_3$ NC thin film. As studied in great detail for organic light emitters[284] as well as for some LHP NCs,[73,285] such radiation patterns contain information about the average orientation of the transition dipole moments (TDM) of the electronically active optical transition from the excited state to the ground state. This parameter is key to understanding and improving light outcoupling from thin-film light-emitting structures, such as organic LEDs[284] or PeLEDs.[145] In particular, the orientation parameter Θ (which is defined as the fraction of power emitted by vertical TDMs) directly indicates the degree of anisotropy of the TDM orientation distribution, with $\Theta = 0.33$ being the isotropic case, and larger (smaller) values indicating more vertical (horizontal) TDM orientation. By comparing native $CsPbBr_3$ and LiTFSI-treated NCs we notice a significant change of the TDM orientation. After fitting with an appropriate dipole model (details in the **Supplementary Information**) a TDM orientation parameter of $\Theta_{native} = 0.51$ is obtained, proving more vertical TDM orientation for the

native NCs, in contrast to $\Theta_{LiTFSI} = 0.32$ being close to isotropic for the 1 wt % LiTFSI-treated NCs. This means that the unfavorable vertical TDM orientation of the native NC film is changed to an isotropic emission profile corresponding to the cubic structure of LHP. A similar behavior has also been found by an Al_2O_3 overcoating of LHP nanoplatelets.[285,286] Thus, we suppose that LiTFSI acts as a dielectric layer to screen the asymmetry in the electrostatics between the substrate and the free surface of the NCs.

5.3.3 Energy Level Alignment

To elucidate the impact of LiTFSI on the electronic properties of LHP NCs, ultraviolet and X-ray photoelectron spectroscopy (UPS and XPS) measurements have been conducted on the PVK/$CsPbBr_3$–NC and PVK/$CsPbBr_3$–NC:LiTFSI films, respectively. As shown in **Figure 5.3 a** by the valence region and the secondary electron cutoff spectra, the PVK film exhibits an initial work function of 4.59 eV and the highest occupied molecular orbital (HOMO) level is found at 1.37 eV binding energy (with respect to E_F). Upon deposition of $CsPbBr_3$ NCs, the work function decreases to 4.25 eV, likely due to the formation of band bending and/or an interface dipole at the buried interface.[287] The valence band (VB) onset of $CsPbBr_3$ is then extrapolated at 1.68 eV with respect to E_F. Given the energy gap of $CsPbBr_3$ of about 2.4 eV (515 nm), this shows that E_F is located above midgap which is due to a strong n-type character on the surface of the NCs. Additional surface photovoltage measurements under white light illumination shows no shifts of $CsPbBr_3$ NC energy levels, indicating a flat band condition through the LHP NC layer.[288] Hence, the surface energy levels are then expected to also reflect the electronic properties within the LHP NC thin-film. With the addition of LiTFSI to the $CsPbBr_3$ NCs, a shift of the valence band toward lower binding energy by 0.25 eV is observed, which is accompanied by an increase in sample work function, leading to a decrease in VB onset to 1.43 eV with respect to E_F.

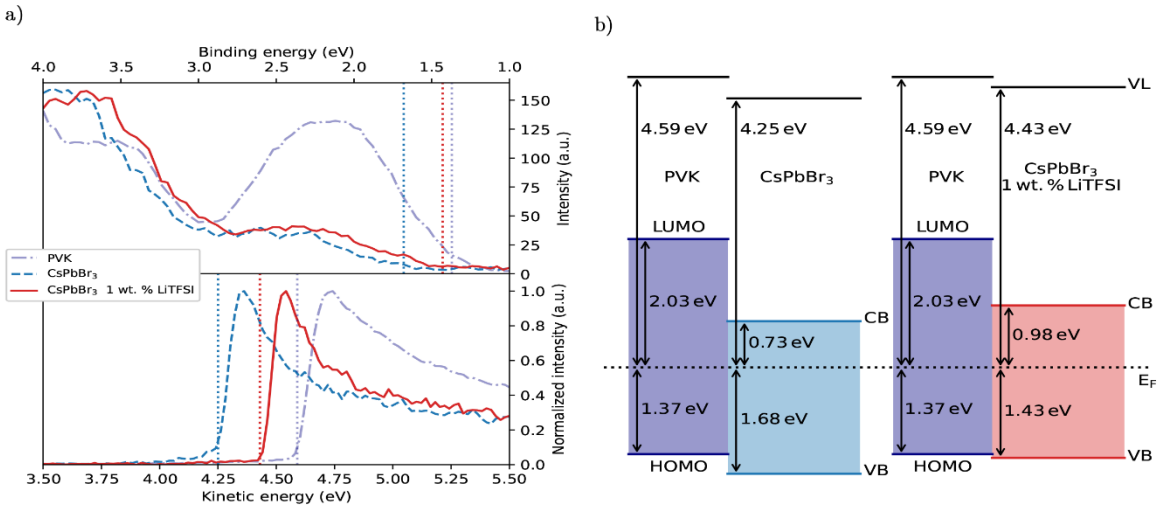

Figure 5.3: (a) UPS spectra of PVK and PVK/$CsPbBr_3$–NC films with and without the addition of LiTFSI. Top panel, valence band spectra; bottom panel, secondary electron cutoff region. **(b)** Energy level diagram at the PVK/$CsPbBr_3$ interface with and without addition of LiTFSI. VL and E_F refer to vacuum level and Fermi level (set at 0 eV binding energy). Bandgaps are taken from the optical gap for the perovskite and from literature for PVK.[289]

A similar shift of the core levels was observed in XPS (see **Figure S5.6**). Such a rigid shift of all $CsPbBr_3$–NC energy levels distinctly demonstrates a p-doping effect by the addition of LiTFSI. It is worth mentioning that the use of substantially attenuated UV flux (attenuation of more than 100 times compared to the standard helium discharge lamp) is required for the UPS measurement, as a high UV flux is found to cause irreversible changes of the electronic structure. However, this leads to insufficient signal-to-noise ratio at the top VB region, which keeps us from extracting the LHP NC valence band onset on a logarithmic intensity scale of the photoelectron signal, as is known to accurately infer the band edge position of perovskite films due to the low density of states at the top of the valence band.[238,290] However, the shift of the electronic levels is not affected by this procedure.

Furthermore, XPS can serve as another proof for successful ligand exchange. Similar to Liu *et al.*, we find a fluorine peak (F 1s) in the XPS spectrum of the LiTFSI-treated NC film (see **Figure S5.6 d**), which could not be observed in the native sample.[274]

However, because of the low X-ray intensity used in our experiments, nitrogen and sulfur peaks could not be identified. Nevertheless, following the consideration of Liu *et al.*, it can be concluded that $TFSI^-$ is attached at the surface of the NCs.[274]

The resulting energy level diagram of the PVK/$CsPbBr_3$ NC stack is shown in Figure 5.3 b. It can be clearly seen that the PVK/$CsPbBr_3$–NC interface initially exhibits a large energy barrier of ca. 0.31 eV for hole injection. Because of the p-doping effect by addition of LiTFSI, such an energy barrier is reduced to 0.06 eV with $CsPbBr_3$ NC VB edge shifting closer to the HOMO level of PVK. With such reduction, the hole injection can be significantly improved.

The reduced hole injection barrier is manifested in the electrical transport behavior as well. As expected, a single carrier hole-only device (layer stack shown in the inset of **Figure 5.4**) with 1% LiTFSI doping shows a significant increase, respectively doubles the current density when operated at 4 V (see **Figure 5.4**). We note that this current enhancement is not caused by a change in the layer morphology (including its thickness). As shown in the Supporting Information (**Figure S5.5**), both native and LiTFSI-treated $CsPbBr_3$–NC films have similar morphology with a partially closed uppermost NC monolayer on top of fully closed layer(s) underneath. If at all, the LiTFSI treatment even slightly improves the film morphology so that the increase of current cannot originate from insufficient NC coverage. Further, one can also expect to obtain different electronic coupling among the $CsPbBr_3$ NCs by replacing (part of) the insulating oleylamine/oleic acid ligands by LiTFSI so that an improved bulk charge transport might also contribute to the observed current enhancement. We also note that electron injection is apparently not affected by the energy level shift, as electron-only devices (see **Figure S5.7 d**) show a negligible difference in current.

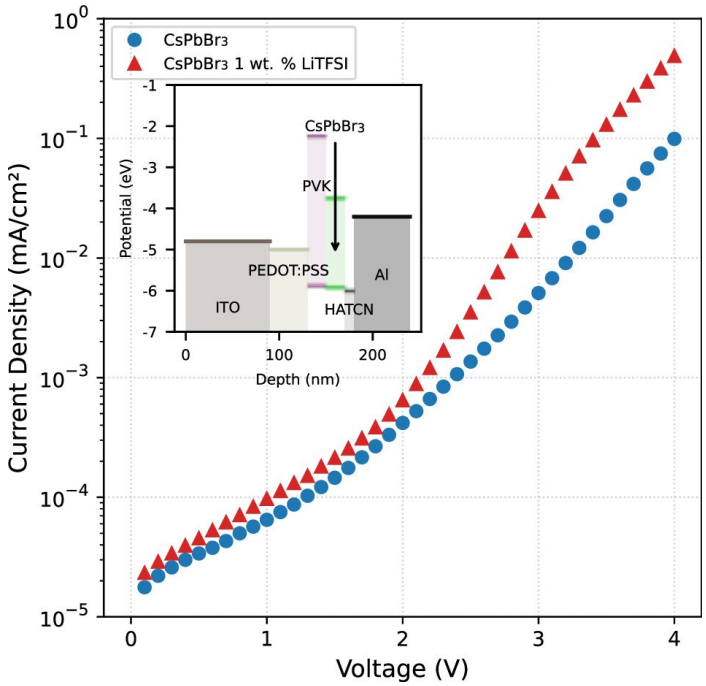

Figure 5.4: Hole-only j–V curve with the schematic device stack as inset.

5.3.4 Density Functional Theory Modeling

Density functional theory (DFT) modeling of four slab models was performed (see the **Supplementary Information** for computational details) to understand the structural changes upon LiTFSI treatment and its consequent impact on the electronic structure of the $CsPbBr_3$ NCs. As shown in **Figure 5.5 a**, model A consists of pristine $CsPbBr_3$, whereas in model B, a Li^+ ion replaces a Cs^+ ion together with a $TFSI^-$ replacing a Br^- ion over the surface. Model C considers intercalation of a Li^+ ion, with one $TFSI^-$ placed over the CsBr-terminated surface, whereas model D is a system analogous to model C, but with the two $-CF_3$ groups of the $TFSI^-$ ion having been replaced with two $-CH_3$ groups.

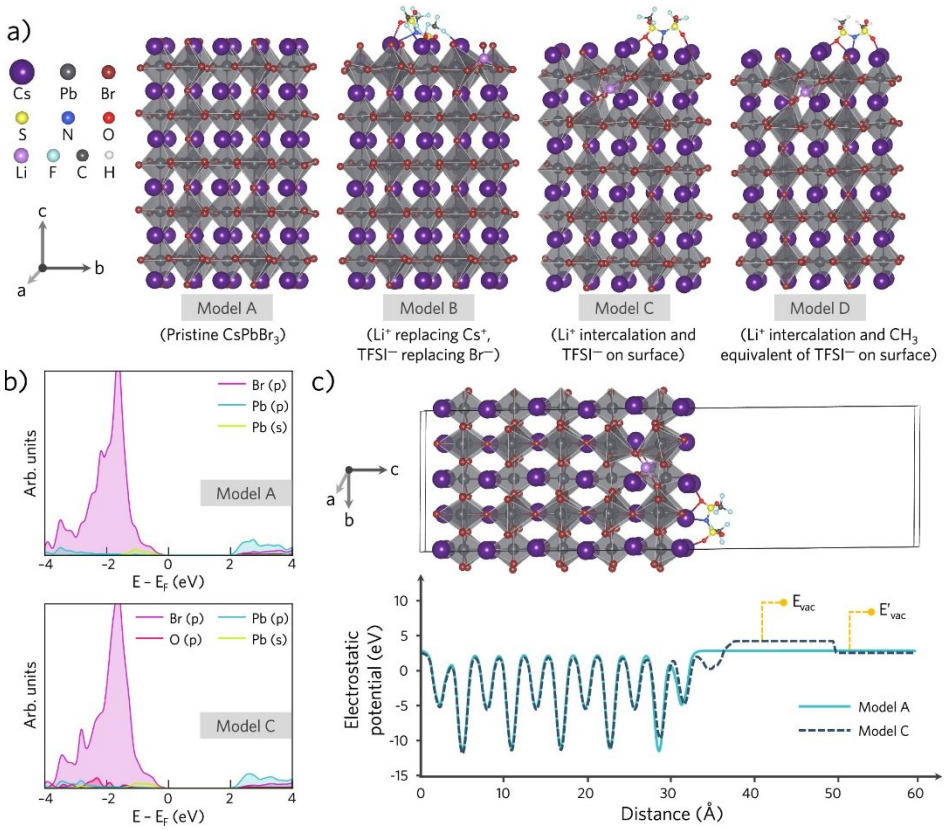

Figure 5.5: **(a)** Slab models of orthorhombic $CsPbBr_3$ ($1 \times 2 \times 3$ supercell; 5 PbI layers) exposing the CsBr-terminated surfaces, **(b)** projected density of states plots for model A and C (E_F = Fermi energy), **(c)** planar average electrostatic potential for determining the vacuum energy level, E_{vac}. In the diagram, E_{vac} corresponds to the (near) vacuum level of the TFSI-deposited surface and E'_{vac} represents the undoped (far) vacuum level.

Even though model D is not relevant experimentally, we explored this system computationally to disentangle the effect of C–F bond polarity on work function (WF), by closely comparing it with its C–H analogue.

We found that both pristine and LiTFSI-doped systems exhibit a very similar density of states (**Figure 5.5 b**), and the orbital contributions from the $TFSI^-$ ions are quite deep-lying, appearing only near −2.0 eV. On the other hand, the $TFSI^-$ ligands were found to alter the surface dipole moment of the particle significantly, causing a substantial shift in the vacuum level (**Figure 5.5 c**). Consequently, the mere presence of a surface $TFSI^-$ ion in model B replacing a Br^- ion increased the work function of the NC from 4.51 eV in pristine model A to 5.54 eV in model B. The vacuum level-shift is even more prominent in model C, partly attributable to the fact that the dipoles caused by the surface $TFSI^-$ ions are now exclusively outside the inorganic core, as

opposed to model B, where the O atom from TFSI binds to a Pb^{2+} ion from the core and hence, the dipole is partly compensated. In model D, we show that when the highly polar C–F bonds in TFSI are replaced with C–H bonds, the vacuum level shift is drastically reduced (E_{vac} = 4.23 eV and WF = 6.20 eV for $-CF_3$ groups in model C vs E_{vac} = 3.83 eV and WF = 5.69 eV for $-CH_3$ groups in model D). We recognize that the computed change in the work function is rather substantial compared to the experiment (UPS measured hole stabilization being around 0.25 eV, **Figure 5.3 b**). We attribute this discrepancy to (i) a higher $TFSI^-$ coverage in the model system compared to the experiment and (ii) the fact that in the slab model only one surface is asymmetrically covered with organic ligand as opposed to all six-side coverage in an actual NC.

In addition to the change in work function, the topotactic intercalation of the Li^+ ion, regardless of whether in a tetrahedral or octahedral site, has been demonstrated to increase interaction with neighboring halide ions (see Li–Br bonding in addition to the usual Cs–Br bonds in model C and D in **Figure 5.5 a**),[270] and thus the activation barrier for halide ion migration is expected to increase.[291] We anticipate a similar effect of the Li^+ ion on preventing ion migration and improving the structural integrity of the LiTFSI-treated $CsPbBr_3$ particles. Finally, we speculate that the availability of electronegative O atoms from the $TFSI^-$ ligand, which is quite mobile over the surface, would also coordinate to Pb atoms, as seen in model B, and contribute toward preventing detrimental Pb^{2+} to Pb^0 reduction over the surface.[292]

5.3.5 Perovskite Light-Emitting Diodes

Finally, we have employed native and LiTFSI-treated $CsPbBr_3$ NCs in PeLEDs, where PVK is used as polymeric hole transport layer and B3PYMPM as electron transport layer, followed by a LiF/Al cathode as depicted in the inset of **Figure 5.6 a**, the corresponding current–voltage–luminance characteristics is also shown in **Figure 5.6 a**. The native $CsPbBr_3$ NCs show two onsets for the current, with the first

occurring slightly above 1 V which can be assigned to electrons due to the n-type position of the Fermi level; the second onset with a much steeper increase of current is located at about 3.5 V and would accordingly correspond to the onset of hole injection. This is supported by the fact that detectable luminance (>1 × 10^{-2} cd/m^2) occurs not before the applied voltage exceeds 4 V.

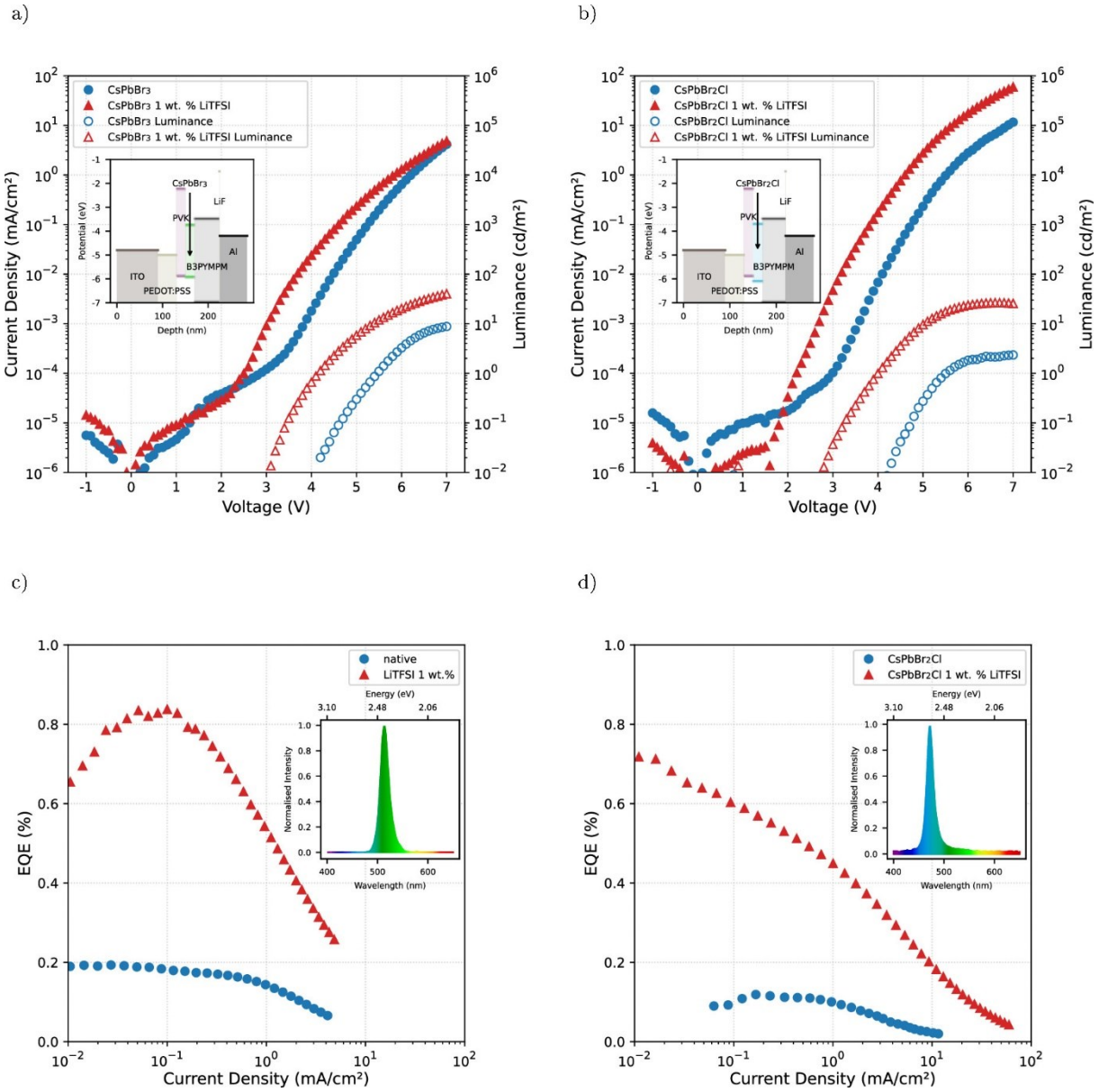

Figure 5.6: *j–V–L* curves of **(a)** $CsPbBr_3$ and **(b)** $CsPbBr_2Cl$ PeLEDs with and without LiTFSI-doping; **(c, d)** corresponding EQE vs current density curves. The insets depict their stack structures and their emission spectra.

For the 1 wt % LiTFSI-doped NCs, the double-step feature in the current disappears; rather, there is a steep increase starting above 2 V and luminance is detected already

at 3 V. With further increasing voltage, both current and luminance increase much steeper in the LiTFSI-doped PeLED as compared to the untreated one. Finally, at 7 V both devices reach the same current, but the luminance in the LiTFSI-doped PeLED stays several times above the native one, indicating higher external quantum efficiency (EQE). This is shown in **Figure 5.6 c** where the maximum EQE increases by more than a factor of 4 from 0.2% to above 0.8%. We also note that both, native and LiTFSI-treated $CsPbBr_3$, PeLEDs have the same narrow green electroluminescence spectrum shown in the inset of **Figure 5.6 c**.

Similar to the PLQY series, we have also fabricated PeLEDs with other LiTFSI doping concentrations (see **Figure S5.7**). We find that the highest EQE is reached for a LiTFSI concentration of 5 wt %; however, this device (just like the 9 wt %) does not reach the same level of luminance as the 1 wt % device, indicating some kind of overdoping by LiTFSI that leads to irreversible device degradation at high current densities, while lower concentrations lack sufficiently high PLQY.

As a proof of concept, we also applied LiTFSI doping to sky-blue emitting $CsPbBr_2Cl$ NCs (results shown in **Figure 5.6 b, d**). In this case, the reduction of the turn-on voltages for current and luminance induced by LiTFSI doping is even bigger, as detectable luminance sets in already below 3 V. The EQE is enhanced by a factor 7 from 0.1 to 0.7%, proving an even stronger effect of LiTFSI doping in the wider band gap, sky-blue PeLEDs.

Furthermore, a red methylammonium-$PbBrI_2$ NC PeLED can also be improved by LiTFSI, without an evident current-density increase (see **Figure S5.8**). In this case, the red NC emitter does not face the same hole injection barriers as its blue and green counterparts, such that an increase in hole-injection is not expected to play a major role. Nevertheless, the device EQE is boosted by a similar factor through the LiTFSI treatment.

5.3.6 Discussion

The overall increase in PeLED performance with various LHP species implies a very versatile mechanism. The increase in PLQY and exciton lifetime with the LiTFSI concentration suggests a surface passivation mechanism. This has already been reported with lithium halides, where the lithium ions as well as the halides have shown surface trap passivation.[269,270,293] However, the influence of Li^+ has not been completely disentangled from that of the halide. Here we use the organic $TFSI^-$ anion, proving that a halide-free passivation is possible. As sulfonic moieties have been reported to fill halide vacancies, a similar interaction from LiTFSI seems plausible and has already been reported.[262,274,294] In particular, $TFSI^-$ has been suggested to act as surface passivation by coordinating with Pb and Cs cations on the NC surface. Additionally, suppressed hysteresis of the j–V characteristics (see **Figure S5.7 c**) implies that ions have been demobilized to some extent. Although neither a significant shrinkage of the NCs nor a spectral blue-shift has been observed, as reported by Liu *et al.* upon (H)TFSI treatment,[274] an analogous chemical reaction may still take place on the NC surface: $CsPbBr_3$ + LiTFSI → $CsPbBr_2TFSI$ + LiBr. The main difference to the (H)TFSI passivation is that the resulting lithium halide salt is not as volatile as the corresponding halide acid (HBr in this case), effectively blocking a prolonged decomposition of the NC surface, thus avoiding shrinkage. Br^- having a higher affinity to bind Li^+ than $TFSI^-$ renders this process energetically favorable.[295] This could explain why the addition of LiTFSI passivates $CsPbBr_3$ NCs without degrading their shape and size. Apart from that, an enhanced stability to polar solvents as reported by Liu *et al.* is also exhibited by our LiTFSI-treated NCs. [274]

Though, upon considering the PLQY and EQE depending on LiTFSI concentration (**Figure 5.2 b**) it becomes evident, that apart from surface trap passivation another beneficial consequence arises from the LiTFSI treatment. The different dependence on

LiTFSI concentration between EQE and PLQY cannot fully be explained by a surface trap passivation mechanism, because the EQE (η_{EQE}) is proportional to the PLQY:

$$\eta_{EQE} = \eta_{out} \cdot q_{PLQY} \cdot \gamma \quad (5.1)$$

However, at small doping concentrations the drop in EQE is not as pronounced as it is for the PLQY. Other factors only influencing the EQE are the outcoupling factor (η_{out}) and the charge carrier balance (γ).[284] So an emitter orientation change can enhance the EQE compared to the PLQY, by a limited amount. This change in radiation pattern is observed as shown in **Figure 5.2 d**, but the change of orientation is simulated to result in an EQE increase factor of only 1.3. Considering the PeLED fabricated with a 1 wt % LiTFSI doping, as compared to the one with native $CsPbBr_3$ NCs, the PLQY does not change significantly but the EQE does from about 0.2 to 0.8% by a factor of 4. The orientation alone cannot account for such large enhancement, but the last factor, the charge carrier balance can. Consequently, the doping procedure modifies the charge carrier balance in favor of EQE. Further investigations into that have been made by designing a hole-only device. This device exhibits hole-currents up to a factor 6 higher for the doped sample (see **Figure 5.4**), implying an increased hole injection of roughly the same factor. The leveraged hole-injection can be ascribed to an improved VB alignment with the adjacent PVK's HOMO level, as measured by UPS and XPS (see **Figure** 5.3). The injection barrier is reduced from 0.31 to 0.06 eV, which is in accordance with the increased hole current in the devices. At that, not only the VB onset is shifted but the entire density of states by 0.25 eV, raising the CB level by the same amount and rendering the $CsPbBr_3$–NC semiconducting thin film less n-type.

This energy-level shift is expected when considering the reports of using LiTFSI as a p-dopant in organic semiconductors. In that case, oxygen plays a key role in enabling the doping process, which is proven by lithium oxide residuals after successful doping.[296,297] Even though the LiTFSI treatment here is realized in the absence of oxy-

gen, a comparable reaction may lead to p-doping of the NCs. However, direct signatures of charge transfer could not be found in photoelectron spectroscopy, which is understandable, as these NC films have a very large surface area-to-volume ratio, making the detection of new electronic states upon charge transfer hard. Nevertheless, the observed rigid shift of all energy levels (including the core levels) clearly proves p-doping upon LiTFSI treatment of the $CsPbBr_3$NCs.

The significance of the VB alignment can be seen when comparing the differently colored LEDs: For the blue $CsPbBr_2Cl$, the enhancement of current and EQE is highest, it decreases in green $CsPbBr_3$ to no significant current increase for the red $MAPbBrI_2$. The sky-blue $CsPbBr_2Cl$ has a VB onset reported to be even lower,[298]rendering a potential p-doping even more beneficial as observed. The red device presumably does not benefit by the energy level shift, because of its small bandgap[298] the injection barrier has not been the limiting factor, even though the EQE is still significantly increased.

When considering the higher doping concentrations, 5 wt %and more, a drop in luminance at elevated currents can be observed (see **Figure S5.7 a, b**). Although the currents are further increasing, the luminance does not exceed 20 cd/m^2. A drastic EQE drop occurs at this critical luminance value. This drop is proven to be irreversible by multiple measurement runs of the LEDs. Apparently, there is a degradation induced by an excess of LiTFSI doping. Different interactions of lithium ions with the LHP NCs ranging from residing on an interstitial position over cation exchange (Cs^+ for $CsPbBr_3$) to filling lead vacancies have been explored.[270] Upon excess doping multiple of these interactions may mix and change the LHP NCs properties toward lower stability and quantum yields. Even though this drop in quantum yield is observed in PLQY measurements at 50 wt % doping only, the drop in operational stability is already dominant for the PeLEDs starting from 5 wt %. The degradation above a certain luminance together with the fact that $CsPbBr_3$ is optically stable even upon strong excitations[299,300] leads to the conclusion that the degradation has to originate from an inter-

action between charge carriers and the excited state. Because of the revealed n-type nature of the LHP NCs and the different current onsets observed in the *j*–*V*–*L* curves, it is evident that there is an electron abundance in the device during light-emission. Several reports suggest a chemical reduction reaction of lead as a major degradation path in LHPs,[301,302] which may be facilitated by this surplus of electrons in PeLEDs during operation. Finally the trion state, consisting of two electrons and one hole, may be the main cause of degradation. LiTFSI seems to have no influence on this proposed electron-induced degradation, because it plays only a minor role in the mitigation of electrons, if at all. Its major contribution is ascribed to the easier hole injection into the LHP NCs not necessarily caused by the slightly less n-type energy alignment but rather by the reduced hole injection barrier. As a consequence, the degradation seems to affect the EQE in PeLEDs significantly. With the red and blue device, the LiTFSI has proven to be very versatile, increasing the performance of simple all-inorganic tribromide LHP NCs as well as mixed halide or organic perovskite NCs. However, the degradation of PeLEDs cannot be prevented by the use of LiTFSI, because its major influence is related to hole injection and increased PL quantum efficiency.

5.4 Conclusion

Surface defect passivation has already been recognized as key to enhance the performance of LHP NCs regarding its optoelectronic properties. Here we investigate surface treatment with a p-dopant, viz. the organic lithium salt LiTFSI, and show that the efficiency in PeLEDs is tremendously enhanced. We trace this enhancement back to positive effects on three decisive properties considering their EQE: the emitter's quantum yield is proven to be brought close to unity. This is achieved by most surface passivation techniques on LHP NCs. Additionally, the angular emission pattern is changed in favor of better light outcoupling. Although these two effects contribute to the increased efficiency to a certain extent, the most pronounced influence is identified to be the simultaneous tuning of the charge carrier balance to promote hole injection.

Enhancement in these three key factors is a remarkable feature that can be attributed to the LiTFSI treatment. However, there are still challenges concerning stability, which is a major issue for LHP NCs in LEDs in general. At the same time the interaction as well as degradation of LHP NCs in conjunction with LiTFSI is not entirely understood. Nevertheless, a 4–7 fold increase in EQE can be achieved for PeLEDs of various colors and chemistry, rendering the LiTFSI treatment a very promising procedure to further investigate.

5.5 Methods

5.5.1 Materials

ITO (indium tin oxide) substrates with dimensions 2 × 2 cm were purchased by Kintec (Hong Kong) with and without a custom layer thickness pattern of 100 nm on a 23 nm SiO2 buffer on a 0.7 mm thick glass substrate. Fused silica (SiO2) substrates with dimensions 2 × 2 cm with a thickness of 0.7 mm were bought from Nano Quarz Wafer Germany GmbH. PEDOT:PSS in a low-conductive ratio of 1:20 was used, having the descriptor CH8000, by Heraeus Germany GmbH & Co. KG. ZnO was synthesized from zinc acetate using the sol–gel method.[303] $CsPbBr_3$ solution (c = 10 mg/mL in toluene, product ID 900746) and LiTFSI (Lithium bis(trifluormethane)sulfonimide, 99.95% trace metal basis, product ID 544094) were ordered from Merck Germany KGaA. PVK (Poly(9-vinylcarbazole), Mw > 1 × 105, product ID LT-N4078) was obtained from Luminescence Technology Corp. (Lumtec, Taiwan).

5.5.2 Nanoparticle Preparation

Preparation of Oleylammonium Halide (OLA-HX)

To prepare a 1.1 mmol/mL OLA-HX precursor solution, we placed 10 mL of oleylamine (OAm) in a 25 mL three-neck flask and slowly added either 1 mL of concentrated hydrochloric acid (HCl(aq.)) or 1.28 mL of concentrated hydrobromic acid (HBr(aq.)).

Subsequently, the solidified reaction mixture was heated at 120 °C under nitrogen atmosphere for 2 h. The reaction temperature has then been increased to 150 °C for 30 min and afterward allowed to cool to room temperature. The mixture was kept in a glovebox and heated to 80 °C before injection.

CsPbBr2Cl Nanocrystals

$CsPbBr_2Cl$ nanocrystals were prepared by a hot-injection synthesis using a modified literature method.[248] To synthesize 7 nm $CsPbBr_2Cl$ nanocrystals, 49 mg (0.15 mmol) of Cs_2CO_3, 67 mg (0.3 mmol) of PbO, and 1.5 mL of oleic acid (OA) were degassed in 15 mL of ODE in a 50 mL three-neck flask under reduced pressure at 120 °C for 1 h. The temperature was increased to 240 °C under a nitrogen atmosphere, 1 mL of OLA-HBr and 0.5 mL of OLA-HCl precursor were quickly injected, and after 1 min, the reaction mixture was cooled to room temperature using an ice bath (below 180 °C). $CsPbBr_2Cl$ NCs were collected by centrifuging the suspension (7000 rpm, 10 min.), decanting the supernatant, and collecting the precipitate. The precipitate was centrifuged again without the addition of a solvent (7000 rpm, 5 min.), and the resulting supernatant was removed with a syringe to separate the traces of residual supernatant. The precipitate was dissolved in 2 mL of hexane and centrifuged again (2500 rpm, 5 min) to remove aggregates and larger particles. The resulting supernatant was filtered through a 0.2 μm PTFE syringe filter and stored as stock solution inside of a glovebox with a typical concentration of 25 mM following Maes *et al.*[201]

LiTFSI Treatment

The LiTFSI solution was diluted from a stock that was created by dissolving 200 mg of LiTFSI with 2 mL of dimethylformamide (DMF) and 18 mL of chlorobenzene (CB) by stirring overnight, resulting in a volume concentration of 10 mg/mL. Dilution to 1, 0.1, and 0.01 mg/mL concentrations was done with CB only.

Equal volumes of LHP NC solution and LiTFSI solutions were mixed to obtain a LiTFSI-doped solution. Mixing equal volumes of 10 mg/mL LHP NC and 10 mg/mL LiTFSI yielded a 5 mg/mL LHP NC solution with 50 wt % LiTFSI doping. Analogously, 9.09, 0.990, and 0.099 wt % doped solutions were obtained by using 1, 0.1, and 0.01 mg/mL concentrated LiTFSI solution and mixing with the 10 mg/mL LHP NC solution in equal volumes. All LHP NC solutions were created within a nitrogen-filled glovebox and exhibited stable luminescence for at least 3 months at room temperature.

5.5.3 Sample Preparation

Photoluminescence

Fused silica was used as a substrate for all PL measurements, that is PLQY, TRPL, and ADPL. The substrates were spin-coated in a nitrogen-filled glovebox by dropping 50 μL (p.r.n. LiTFSI-doped) of LHP NC solution before starting the rotation of the spin-coater. After a settling time of 30 s, it was accelerated to 500 rpm and kept at that speed for another 30 s. To remove residuals from the edges, spinning for 5 s at 2000 rpm was applied before the procedure was stopped.

UPS/XPS, SEM, LEDs, and Single-Carrier Devices

For UPS/XPS and SEM, unpatterned ITO substrates were used, and for the electrical devices, patterned ITO substrates were used. For the electron-only device, a fused-silica substrate was smoothed with a 0.8 μm thick PMMA layer before depositing 7.5 nm aluminum and 1 nm LiF as a bottom electrode. Initially, PEDOT:PSS was spin-coated in the cleanroom, at 4000 rpm for 30 s, and heated on a hot plate at 130 °C for 15 min, resulting in a smooth approximately 40 nm thin film. The samples were transferred to a nitrogen-filled glovebox immediately. As a second layer, the approximately 20 nm thin PVK film was deposited by spin-coating a 3 mg/mL concentrated PVK-chlorobenzene solution at 3000 rpm for 30 s and heating at 175 °C for 30 min. The

LHP NC solutions are spin-coated as described for the PL samples, after cooling the substrate to room temperature, resulting in a closed film of about 2–3 monolayers (effective thickness approximately 20 nm).

The sample in the current state, that is, the bottom-half LED, was used for UPS/XPS and SEM investigations. For devices, the samples were transferred without ambient exposure into a high vacuum chamber, with a pressure less than 1 × 10–6 mbar. For the hole-only device, 10 nm HATCN (rate: 50 pm/s) was evaporated, and for LEDs and the electron-only device, 55 nm B3PYMPM (rate: 100 pm/s) followed by 0.5 nm LiF (rate: 10 pm/s) were evaporated. The devices were finished with a 60 nm (rate: 100 pm/s) thick aluminum cathode, also deposited by thermal deposition.

5.5.4 Measurement Details

PLQY

The PLQY was determined by a two-step method of measurement featuring a $BaSO_4$-coated integrating sphere.[304] The excitation source was a HeCd laser's 442 nm light. The excitation signal as well as the sample fluorescence was collected with a fiber and guided into a Princeton Instruments Acton2300i spectrometer, which was connected to a nitrogen-cooled CCD camera (Princeton Instruments Pylon BRX100). An absolute calibration of the integrating-sphere CCD system was performed with a lamp calibrated for spectral irradiance according to the NIST standard by GigaHertz Optik GmbH Germany. With that system, spectra could be evaluated to its amount of photons and consequently a PLQY was calculated.

ADPL

The ADPL measurement and analysis were performed as previously reported by our group.[145] The spectrum was recorded with the same CCD spectrometer system as explained for the PLQY.

TRPL

Transient photoluminescence was recorded by the C5680 streak camera system by Hamamatsu, after being delayed by a Stanford Instruments DG535 while being spectrally analyzed by an Acton Spectra Pro 2300i. Excitation was done with the EKSPLA PT400 diode pumped solid-state laser set to wavelength 355 nm.

UPS/XPS

Ultraviolet photoelectron spectroscopy (UPS) measurements have been conducted using a SPECS PHOIBOS 100 hemispherical electron analyzer equipped with a monochromatized helium discharge lamp (21.22 eV). The UV flux was attenuated significantly by the monochromator to avoid UV-induced sample degradation. A sample bias of −10 V was applied to acquire the secondary electron cutoff spectra. The base pressure of the analysis chamber has been kept below 1×10^{-9} mbar. X-ray photoelectron spectroscopy (XPS) measurements were performed at a JEOL JPS-9030 ultrahigh vacuum system (base pressure of 1×10^{-9} mbar) using monochromatized Al Kα (1486.6 eV) radiation. Anode power of 30 W was applied for XPS measurements, which has not been found to induce noticeable sample degradation.

LEDs and Hole-Only Devices

j–V(−L) curves are recorded with a Keithley 2612B source meter unit (SMU). A photodiode of known diameter at known distance is used for luminance detection. The electroluminescent spectrum is taken with the Phelos system by Fluxim AG (Switzer-

land). With that and a Lambertian approximation, the EQE was determined. The integrity of the Lambertian approximation was ensured by random sampling with a calibrated integrating sphere (same setup as for PLQY). The sampling revealed that the photodiode's and consequently in this manuscript reported EQE was about 10% underestimated, relatively. For instance, the EQE of the 9 wt % LiTFSI-doped sample in **Figure 5.2 b** showed 1.1% EQE in the integrating sphere, whereas it was 1% in the photodiode setup.

5.6 Supplementary Information

Quantum Efficiency Enhancement of Lead-Halide Perovskite Nanocrystal LEDs by Organic Lithium Salt Treatment

Tassilo Naujoks [1] *Roshini Jayabalan* [1] *Christopher Kirsch* [2] *Fengshuo Zu* [3] *Mukunda Mandal* [4] *Jan Wahl* [2] *Martin Waibel* [1] *Andreas Opitz* [3] *Norbert Koch* [3,5] *Denis Andrienko* [4] *Marcus Scheele* [2] *and Wolfgang Brütting* *[,1]

[1] Institut für Physik, Universität Augsburg, 86135 Augsburg, Germany

[2] Institut für Physikalische und Theoretische Chemie, Universität Tübingen, 72076 Tübingen, Germany

[3] Institut für Physik & IRIS Adlershof, Humboldt-Universität zu Berlin, 12489 Berlin, Germany

[4] Max Planck Institute für Polymerforschung, Ackermannweg 10, 55128 Mainz, Germany

[5] Helmholtz-Zentrum Berlin für Materialien und Energie GmbH, 12489 Berlin, Germany

*E-mail: wolfgang.bruetting@physik.uni-augsburg.de

Section S5.1 Photoluminescence Spectra

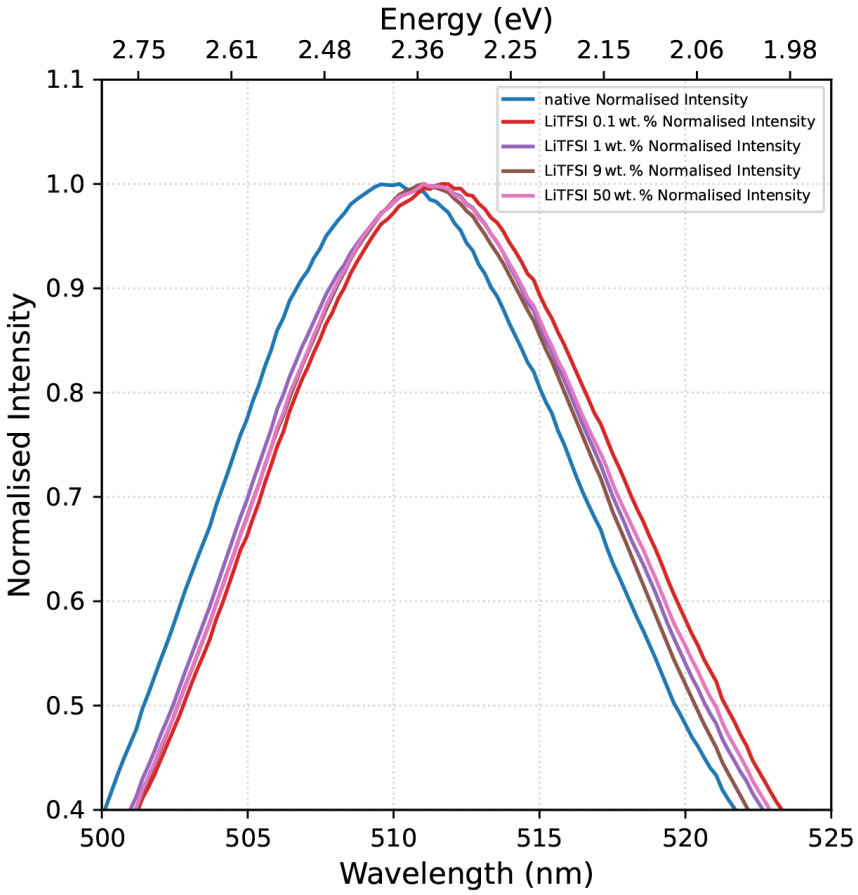

Figure S5.1: Normalised photoluminescence spectra of native and LiTFSI-treated $CsPbBr_3$ NC films. The spectra of LiTFSI-doped samples show a red-shift by about 2–3 nm.

Section S5.2 Transient Photoluminescence Spectroscopy

The normalized transient PL data has been fitted with a double exponential decay function.

$$\boldsymbol{I\ t\ = A_1 \cdot \exp\left[-\frac{t}{\tau_1}\right] + A_2 \cdot \exp\left[-\frac{t}{\tau_2}\right]} \tag{S5.1}$$

with individual amplitudes A_x and lifetimes τ_x. The reciprocal lifetimes yield the respective decay rates:

$$k_x = \frac{1}{\tau_x} \tag{S5.2}$$

Additionally, for comparison, an amplitude-weighted average lifetime τ_{avg} is defined (with the amplitudes summed being one):

$$\tau_{avg} = \sum_{i=0}^{n} A_i \cdot \tau_i \tag{S5.3}$$

The data shown in **Figure S5.2 and Figure** S5.3 indicate a significant difference between native and all the LiTFSI-treated films. In detail, though, the average PL lifetimes do not vary with LiTFSI concentration, but there is a trend towards stronger contribution of the slower decay type with increasing concentration.

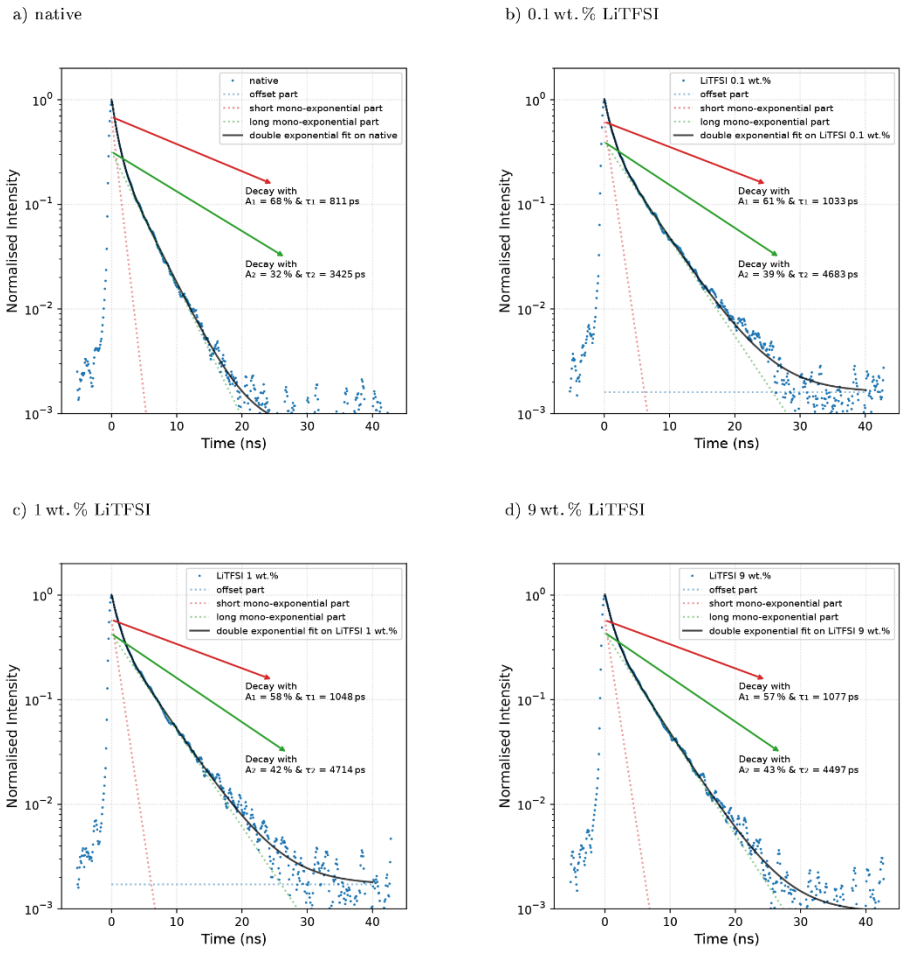

Figure S5.2: Transient PL of a $CsPbBr_3$-NC film with **a)** no, **b)** 0.1 wt. %, **c)** 1 wt. % and **d)** 9 wt. % LiTFSI doping.

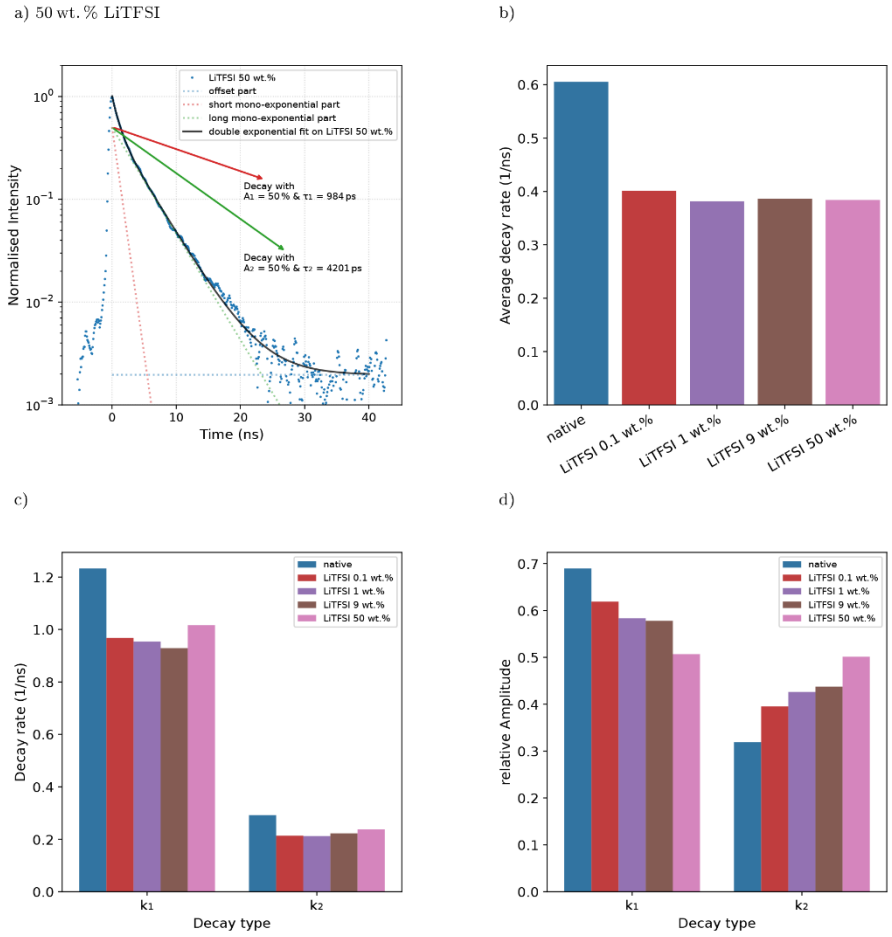

Figure S5.3: Transient PL of a $CsPbBr_3$ NC film with **a)** 50 wt. % LiTFSI doping. **b)** average decay rate, **c)** individual decay rates and **d)** relative amplitudes against LiTFSI doping concentration.

Section S5.3 Angular Dependent Photoluminesence Spectroscopy

Angular Dependent Photoluminesence Spectroscopy (ADPL) data is recorded in two steps: the orthogonal (s-pol.) and the parallel (p-pol.) part of the PL signal is recorded sequentially. The p-pol. part contains contributions from transition dipole moments (TDM) that are perpendicular ($p_\perp$) as well as parallel ($p_\parallel$) to the substrate surface, and thus provides the relevant information about the TDM orientation. Therefore it is used for determining the orientation parameter according to equation:

$$\boldsymbol{\Theta} = \frac{\boldsymbol{p}_{\perp}^{2}}{\boldsymbol{p}_{\perp}^{2} + \boldsymbol{p}_{\parallel}^{2}} \tag{S5.4}$$

Θ can take values between 0 and 1, while the former denotes fully horizontal orientation and the latter fully vertical orientation. Isotropic orientation is obtained if one third of the TDMs is perpendicular, that is $\Theta = \frac{1}{3}$. The fits result in TDM values of $\Theta_{\text{native}} = 0.51$ (vertical) and $\Theta_{\text{LiTFSI}} = 0.32$ (isotropic) see **Figure S5.4 c, d**. More details on this method can be found in the publication of Jurow *et al.*,[286,305] as well as in the original publication for organic semiconductors by Frischeisen *et al.*[305] The s-pol. part, however, contains only contributions of the TDMs that are parallel to the substrate; it is thus only used for tting the layer thickness and verifying the refractive index of the LHP NC layers, **Figure S5.4 a, b**: $d_{\text{native}} = 31$ nm and $n_{\text{native}}(\lambda = 510\text{ nm}) = 1.75$, respectively $d_{\text{LiTFSI}} = 10$ nm and n_{LiTFSI} ($\lambda = 510$ nm) $= 1.75$. The thickness difference can be explained by a deviating film coverage on fused silica compared to on PVK (as shown in **Figure S5.5**).

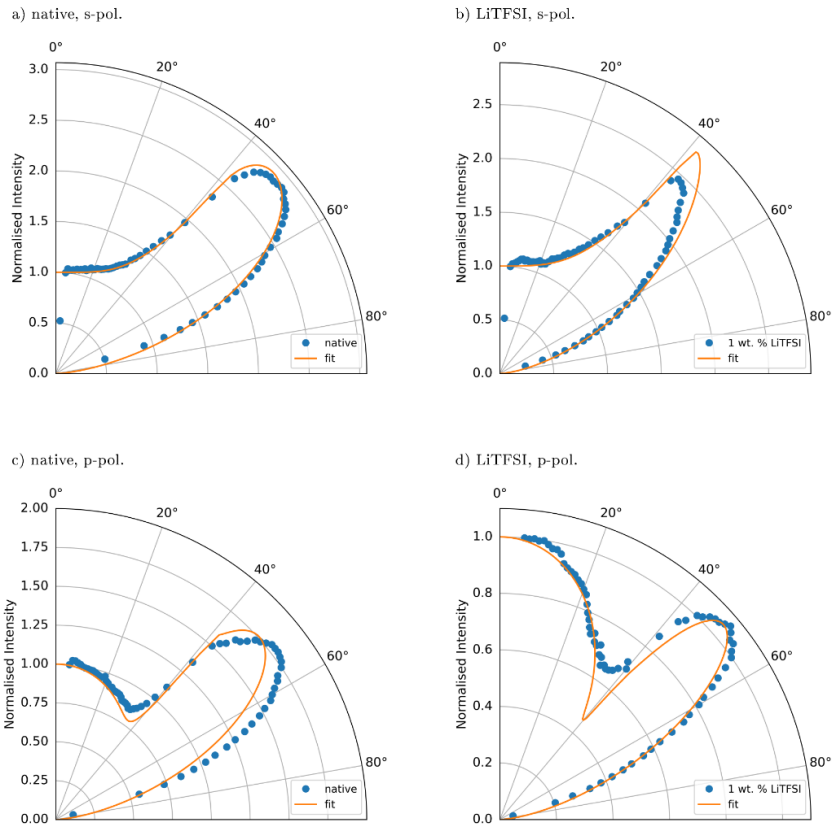

Figure S5.4: s-polarised ADPL spectrum taken at 510 nm with a matrix-transfer fit of **a)** native **b)** 1 wt. % LiTFSI doped $CsPbBr_3$ thin-film on glass (fused silica); the corresponding curves for p-polarised ADPL are shown in **c)** and **d)**.

Section S5.4 Scanning Electron Microscopy (SEM)

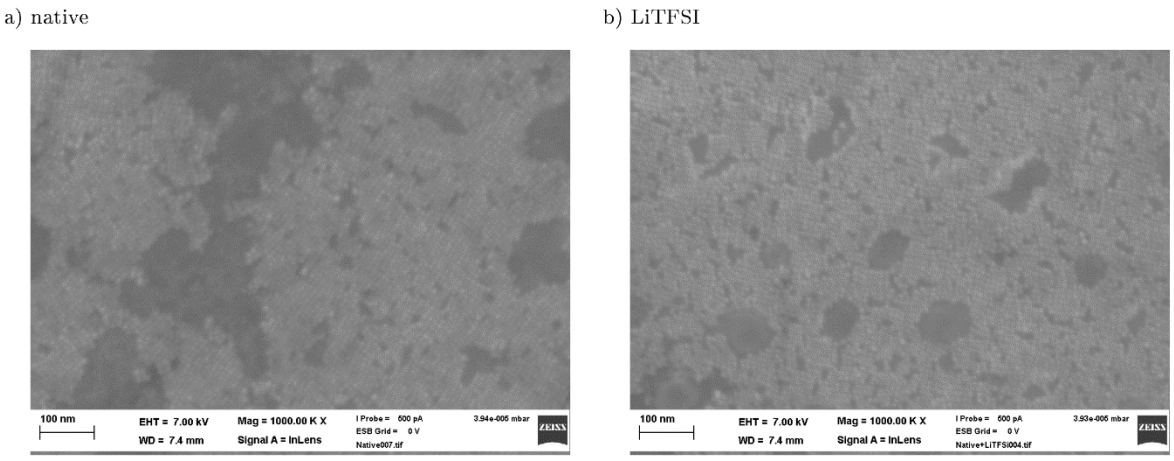

Figure S5.5: SEM image of $CsPbBr_3$ NCs spin-coated on PVK **a)** without and **b)** with 1 wt. % LiTFSI doping. The dark areas have been verified to be another layer of LHP NCs by EDX. Nevertheless the LiTFSI doped sample shows slightly better yet comparable film coverage

Section S5.5 XPS

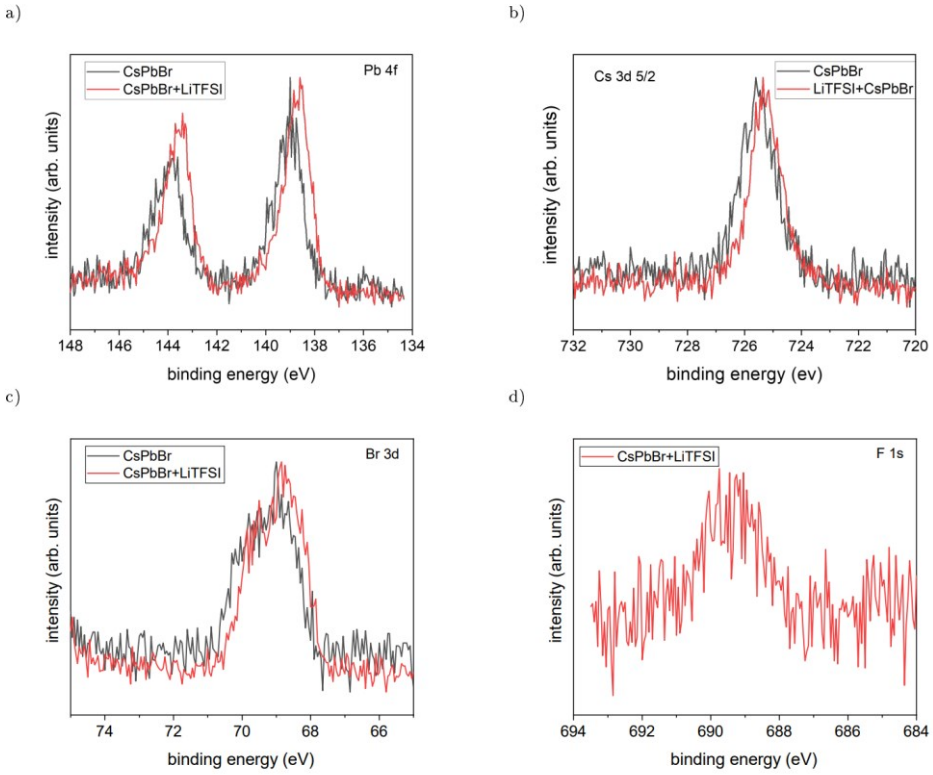

Figure S5.6: XPS spectra considering the core levels of $CsPbBr_3$ at **a)** Pb 4f, **b)** Cs 3d 5/2, **c)** Br 3d and **d)** F 1s. All the core levels are shifted by the same amount as the VB onset shown in the main publication of around 0.25 eV. Note that for native $CsPbBr_3$ NCs no F 1s signal could be detected, as expected in the absence of LiTFSI.

Section S5.6 Density Functional Theory Calculations

Slab models are constructed from orthorhombic $CsPbBr_3$ structure considering a 1 x 2 x 3 supercell having 5 Pb–Br layers and exposing the Cs–Br terminated surface. Consecutive slabs in the c-direction have been separated by a vacuum of approximately 20 Åto ensure decoupling with its periodic image. Periodic calculations are performed using a plane wave basis set implementation of density functional theory within the Vienna Ab initio Simulation Package (VASP, version 6.1)[306] employing the PBE exchange-correlation functional,[307] and van der Waals interactions have been incorporated employing Grimme's D3 method.[308] The valence-core interactions are described with the projected augmented wave (PAW) method.[309,310] Valence electrons of each type of atom considered during calculations are: N (5), S (6), O (6), C (4), F (7), Li (3), Cs (9), Pb (14), and Br (7). A plane-wave energy cutoff of 520 eV is used in all calculations. Forces of each atom smaller than 0.02 eV/Å are used during geometry relaxation. The structural relaxation has been done by sampling the Brillouin zone over a 3 x 3 x 1 k-point grid centered at the Γ-point. Structure visualisation and the projected density of states plots are performed using the VESTA[310] and Sumo[311] packages. VASPKIT[312] is used for plotting planar average electrostatic potentials and obtain vacuum level energy.

Table S5.1: Calculated Energy levels for the models elaborated in the main article.

	Vacuum-Level (eV)	E_{Fermi} (eV)	Workfunction (eV)
model A	2.87	-1.64	4.51
model B	3.71	-1.83	5.54
model C	4.23	-1.97	6.20
model D	3.83	-1.87	5.69

Section S5.7 PeLEDS

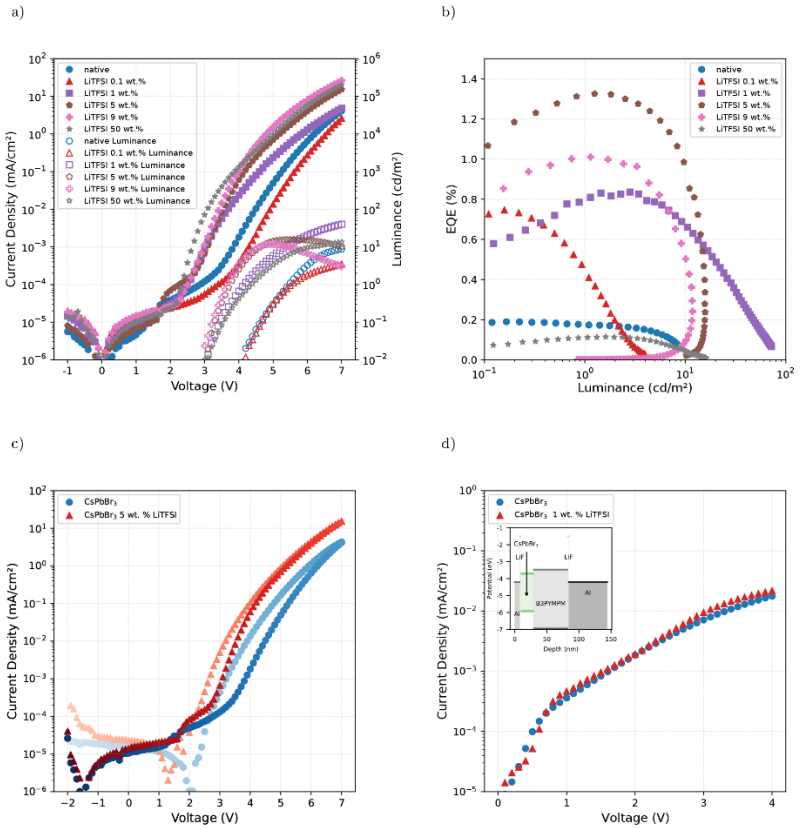

Figure S5.7: a): j-V-L curves of $CsPbBr_3$ NC-LEDs with and without various LiTFSI doping, with **b**) its corresponding EQE vs current density curves. **c)** The 5 wt. % sample's sweepback j-V curves (dark symbols measured before brighter ones). **d)** $CsPbBr_3$ NC electron-only device, as shown in the inset.

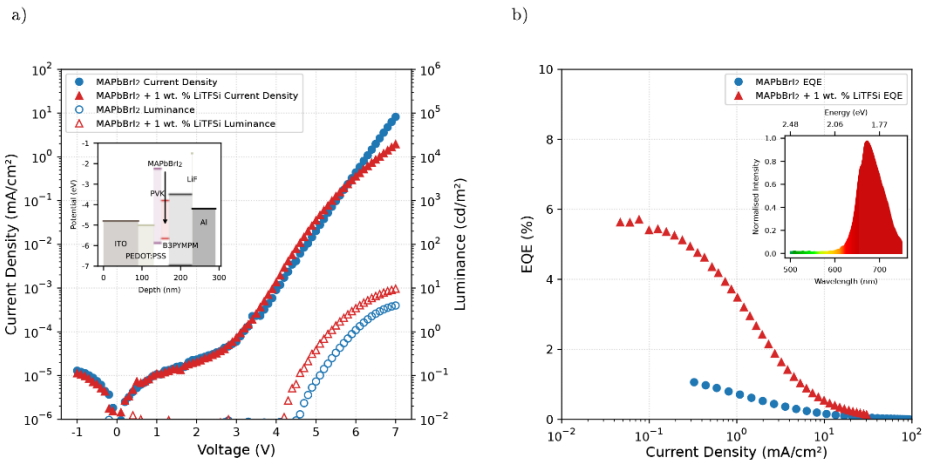

Figure S5.8: a): j-V-L curves of $MAPbBrI_2$ NC LEDs with and without LiTFSI doping, with **b)** its corresponding EQE vs current density curves. The insets depict their stack structures and their partly degraded emission spectra, respectively.

Section S5.8 Additional Details

Substrate cleaning procedure

All substrates are cleaned in a cleanroom by the same procedure: 4 sequential ultrasonic baths in different liquids for 5 minutes each is the initial cleaning step. The sequence of solvents is: Aloconox (detergent) enriched rinsing water, de-ionised water followed by UV-grade acetone and UV-grade isopropanol. After drying completely, the substrates are put in an UV-Ozone cleaner, for 15 minutes.

Additional materials

HATCN (Dipyrazino[2,3-f:2',3'-h] quinoxaline-2,3,6,7,10,11- hexacarbonitrile, sublimed > 99 %, ProductID: LT-N221), B3PYMPM (4,6-Bis(3,5-di(pyridin3-yl)phenyl)-2-methylpyrimidine, sublimed > 99 %, ProductID: LT-N876) and LiF (Lithium Fluoride, > 99,99 %, ProductID: LT-E001) have been obtained from Luminescence Technology Corp. (Lumtec, Taiwan). 1-Octadecene (ODE), technical grade, 90 %, Sigma Aldrich; Oleic acid (OA), 97 %, Acros Organics; Oleylamine (OAm), 80 - 90 %, Acros Organics; Caesium carbonate (Cs_2CO_3), 99.99 % (trace metal basis), Acros Organics; Lead(II) oxide (PbO), 99.999 % (trace metal basis), Sigma Aldrich; Toluene, 99.8 %, extra dry, AcroSeal, Acros; Acetonitrile (ACN) , 99.9 %, extra dry, AcroSeal, Acros; Lead(II) iodide (PbI_2), 99 %, Acros Organics; Methylammonium bromide (MABr), 98 %, Sigma Aldrich; Methylamine (MA) solution, 33 wt. % in absolute Ethanol, Sigma Aldrich; Disodium ethylenediaminetetraacetic acid dihydrate (Na_2EDTA), Sigma Aldrich; All chemicals were used as purchased.

$MAPbBrI_2$ nanocystals preparation

The perovskite precursor solution has been prepared exactly as mentioned by Hassan *et. al.*.[313] In order to obtain 12 nm $CH_3NH_3PbBrI_2$ perovskite nanoparticles emitting at 650 nm, 5 ml of anhydrous toluene has been mixed with 4 ml of oleic acid and 0.4 ml of oleylamine in a three-neck ask under nitrogen atmosphere at 70 °C. At this

temperature 0.4 ml of the previously made ACN/MA perovskite precursor solution has been swiftly injected into the toluene/ligand mixture under vigorous stirring. After one minute, the reaction vessel has been cooled to room temperature using an ice-bath. $MAPbBrI_2$ NCs have been collected by centrifuging the suspension without addition of an antisolvent (7000 rpm, 10 min.), decanting the supernatant, and collecting the precipitate. The precipitate has been centrifuged again without addition of a solvent (7000 rpm, 5 min), and the resulting supernatant has been removed with a syringe, to separate the traces of residual supernatant. The precipitate has been dissolved in 5 ml anhydrous toluene and centrifuged again (7000 rpm, 5 min) to remove aggregates and larger particles. The resulting supernatant has been filtered through a 0.2 µm PTFE syringe filter and stored as stock solution inside of a glovebox. The as obtained $MAPbBrI_2$ solutions have been subsequently treated with Na_2ETDA. The solid EDTA salt has been added to the toluene solution of NCs and stirred for 24 hours. In a typical exchange reaction 10 times the amount of salt was used.[214] Afterwards, the samples have been filtered with a 0.2 µm syringe filter.

6. Mitigating the Photodegradation of All- Inorganic Mixed-Halide Perovskite Nanocrystals by Ligand Exchange

*Jan Wahl[$,‡], Philipp Haizmann[$,‡], **Christopher Kirsch[$],** Rene Frecot[$], Nastasia Mukharamova[#], Dameli Assalauova[#], Young Yong Kim[#], Ivan Zaluzhnyy[+], Thomas Chassé[$,ß], Ivan A. Vartanyants[#,&], Heiko Peisert[$,]*, Marcus Scheele[$,ß,]**

[$] Institut für physikalische und theoretische Chemie, Universität Tübingen, Auf der Morgenstelle 18, 72076 Tübingen, Germany

[#] Deutsches Elektronen-Synchrotron DESY, Notkestraße 85, 22607 Hamburg, Germany

[+] Institut für Angewandte Physik, Universität Tübingen, Auf der Morgenstelle 10, 72076 Tübingen, Germany

[ß] Center for Light-Matter Interaction, Sensors & Analytics LISA[+], Universität Tübingen, Auf der Morgenstelle 15, 72076 Tübingen, Germany

[&] National Research Nuclear University MEPhI (Moscow Engineering Physics Institute), Kashirskoe shosse 31, 115409 Moscow, Russia

[‡] These authors contributed equally

This chapter is based on a publication published in Physical Chemistry Chemical Physics (PCCP), DOI: 10.1039/d2cp00546h

6.1 Abstract

We show that the decomposition of caesium lead halide perovskite nanocrystals under continuous X- ray illumination depends on the surface ligand. For oleic acid/oleylamine, we observe a fast decay accompanied by the formation of elemental lead and halogen. Upon surface functionalization with a metal porphyrin derivate, the decay is markedly slower and involves the disproportionation of lead to Pb^0 and Pb^{3+}. In both cases, the decomposition is preceded by a contraction of the atomic lattice, which appears to initiate the decay. We find that the metal porphyrin derivative induces a strong surface dipole on the nanocrystals, which we hold responsible for the altered and slower decomposition pathway. These results are important for application of lead halide perovskite nanocrystals in X-ray scintillators.

6.2 Introduction

Lead halide perovskites are an important class of materials for use in light harvesting and light emitting devices.[314,315] Another promising application of perovskites are scintillators, where they have already shown good performance in X-ray detection.[316–318] However, the instability of perovskite- based materials is a significant drawback for the application in optoelectronic and scintillating devices.[87,148,317,319–322] To address this issue, the photodegradation of methylammonium lead iodide ($MAPbI_3$) thin films has been thoroughly investigated, including the postulation of a decay mechanism.[323–325] Recently, these photodegradation studies have been extended to caesium mixed- halide perovskites ($CsPbX_3$)[326–328] in view of their improved stability against long-term light exposure.[329] However, even the most stable mixed halide perovskites, such as $CsPbBrI_2$, undergo slow photodegradation in intense visible light.[326–328] The aim of this work is to use the tunable surface chemistry of nanocrystals (NCs) to further mitigate this instability with a particular focus on photodegradation with X-ray photons to aid the application in scintillators.[87,323] To this end, we introduce zinc-(5-monocarboxyphenyl-

10,15,20-triphenylporphyrin) (mZnTPP) as surface ligand and investigate its effect on the decomposition of the NCs under X-ray illumination. As NCs, we use two model systems, namely $CsPbBrI_2$ and $CsPbBr_2Cl$, based on their light emitting properties hereafter referred to as red and blue perovskites, respectively. If not explicitly stated otherwise, these NCs are surface-functionalized with oleic acid/oleylamine, referred here to as the "native ligand". As previously reported, perovskites experience drastic changes under continuous X-ray exposure.[151,330] One analytical method that utilizes X-ray irradiation is X-ray photoelectron spectroscopy (XPS). Here, a sample is continuously irradiated with X-rays, and electrons, released from the sample due to the external photoelectric effect, are detected based on their kinetic energy. The core-level binding energy of an emitted electron is directly related to the detected kinetic energy. Previous XPS experiments on

perovskites reported a shift of the binding energies to higher values with ongoing measurement time. This was mostly attributed to either surface, substrate or charging effects.[148] In this work, we observe a similar shift for the red and blue perovskite NCs. However, we demonstrate by a combination of XPS and wide-angle X-ray scattering (WAXS) that the core-level energy shift originates from a contraction of the atomic lattice. For the red and blue perovskite NCs with native ligands, we find a similar decay mechanism as recently postulated for thin films.[326] While morphology and chemical composition are maintained in the red perovskites, the blue perovskites exhibit a loss of chlorine and undergo recrystallization. Most importantly, we observe a greatly altered and slower decay mechanism after surface functionalization with the porphyrin derivative mZnTPP.

6.3 Results

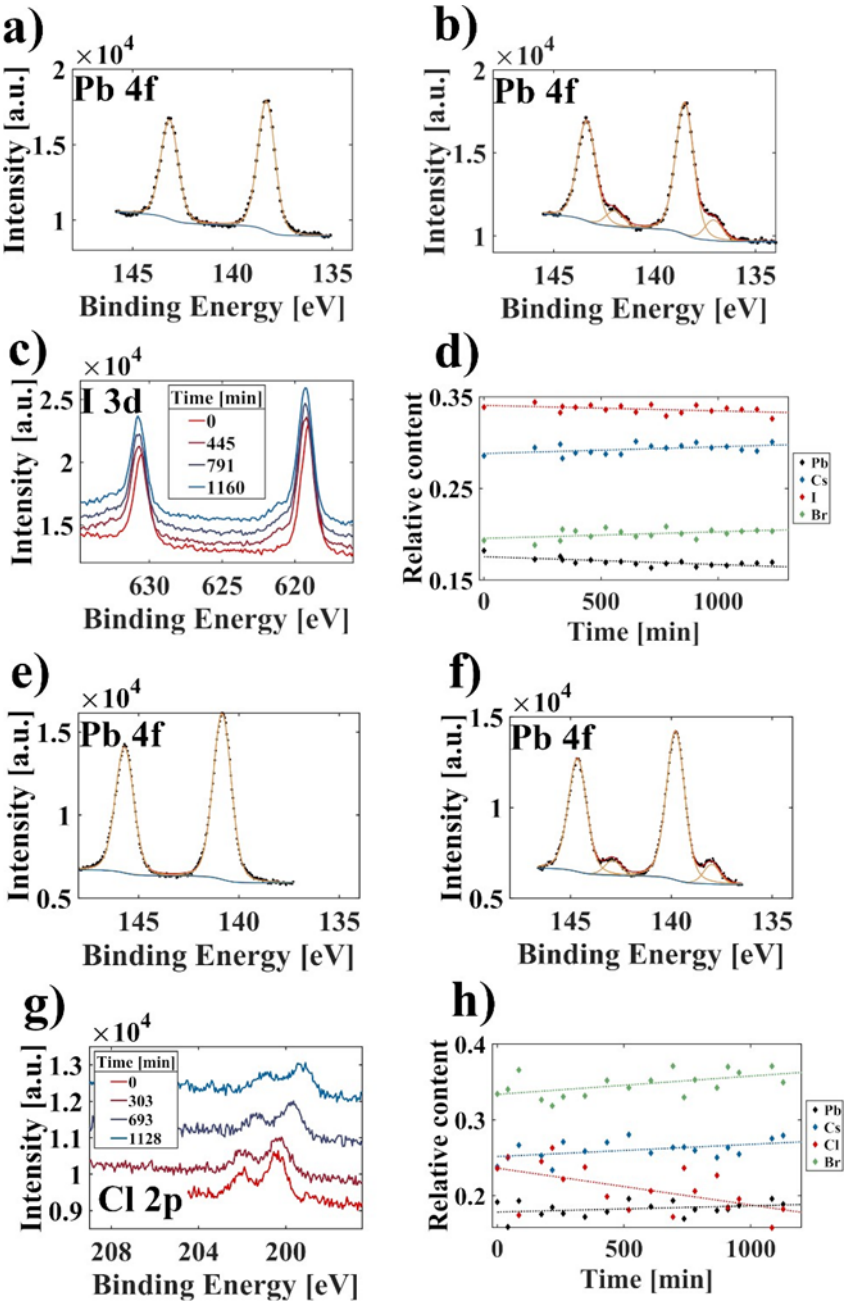

Figure 6.1: Pb 4f core level XPS spectra of $CsPbBrI_2$ **a)** at the start (0 min) and **b)** after 1160 min of X-ray exposure. Fit components are shown in orange, the overall fit is depicted in red. All spectra were fitted by applying a Shirley-type background (blue). **c)** I 3d spectra at different times during the illumination with the evolution of a shoulder at higher binding energy (621 eV). **d)** Relative stoichiometric content and linear regression (dotted lines) during the exposure for $CsPbBrI_2$. Pb 4f spectra of $CsPbBr_2Cl$ **e)** at the start (0 min) and **f)** after 1128 min of exposure. **g)** Cl 2p spectra (~ 200 eV) exhibit a decrease over time without the formation of a novel peak. **h)** Relative stoichiometric content for $CsPbBr_2Cl$ during the experiment.

The decomposition of both perovskite systems was analyzed under continuous X-ray illumination for at least 20 h by XPS and ultraviolet photoelectron spectroscopy (UPS). Core level and valence spectra were recorded at regular time intervals. Exemplarily, spectra of Pb 4f doublet peaks recorded at the beginning and end of the illumination are shown in **Figure 6.1 a + b**. The Pb 4f main peak at a binding energy of 138.25 eV in **Figure 6.1 a** corresponds to Pb^{2+} in the red perovskites. Over the course of this investigation, all samples, independent of stoichiometry and ligand shell, developed an additional Pb species visible in the corresponding Pb 4f-core level spectra of **Figure 6.1 a + b**. The signal occurred at lower binding energies (~137 eV), which indicates a lowering of the oxidation state. Therefore, and in agreement with literature, we attribute this peak to the formation of elemental lead (Pb^0).[148,324,331] The formation of the Pb^0 component is detected after illuminating the sample for few hours. The intensity of the Pb^0 peak increases continuously with time, the relative Pb^0/Pb^{2+} content as a function of the illumination time is summarized in **Figure S6.3** for the red perovskites. Corresponding peak fits are shown for the first and last measurement of the experiment in **Figure 6.1 a + b**, respectively. Additionally, we tracked the lead content over the course of the experiment, as shown in **Figure S6.3**. After 20 h, we observe the formation of 13.2 % Pb0 for the red perovskites (**Figure S6.3**). As a source of electrons for the reduction of Pb2+, we consider the halides in the NCs. While the bromide peak in all samples experienced no significant change (see **Figure S6.1**), we find strong changes in the core level spectra of the other halides, *i.e.*, I- for the red perovskites (**Figure 6.1 c + g**. We observe the formation of a distinct shoulder at high binding energy in the I 3d region for the red perovskites, suggesting that I- is indeed oxidized during the reduction of Pb^{2+} (**Figure 6.1 c**). By tracking the stoichiometric composition, we find the iodide content to stay constant throughout the experiment (**Figure 6.1 d**), suggesting that the new iodine/iodide species remains in the sample during the decomposition even in ultra-high vacuum. To calculate the amount of newly formed species, we first determined the percentages of such from the detail spectra fits. However, the intensities

therein are not directly comparable, therefore we multiplied the percentage with the survey spectrum intensities, *i.e.*, peak areas, to calculate a comparable value for the amount of all newly formed species. The ratio of the novel iodine (621 eV) to Pb^0 (137 eV) species is 1.61 ± 0.23, *i.e.*, close to 2:1, supporting our hypothesis of a redox reaction between I- and Pb^{2+}. For a more detailed derivation of the ratio, see supporting information section S6.2.

We observed similar changes in the XPS core level spectra for the blue perovskites, *e.g.*, the formation of Pb^0 (**Figure 6.1 e + f**), however to a lesser extent compared to the red perovskites. After 20 h of irradiation, a total of 10.2 % Pb^0 was observed for the blue perovskites (**Figure S6.3**). Additionally, we measured a drastic decrease by ~20–25 % (**Figure 6.1 h**) in the Cl 2p peak intensity, suggesting chloride as the redox partner for Pb^{2+} since this is roughly twice the amount of Pb^0 formed. Finally, the Cs 4d orbital was monitored and no formation of novel peaks could be observed (**Figure 6.1 d + h**), suggesting that Cs remains in a relatively stable environment in both cases.

We probed the morphology of both NC samples after X-ray exposure by scanning electron microscopy (SEM). While the red perovskites maintained the cubic, nanocrystalline morphology, the blue perovskites recrystallized to larger agglomerates (see **Figure S6.4**). Therefore, we determine the structure before (**Figure 6.2 a**) and after X-ray exposure by WAXS. (Note that the flux and exposure times during synchrotron-based WAXS are vastly different from those during XPS, and the cross- section is substantially higher for the XPS experiments with their lower photon energies, such that a quantitative comparison is not possible. We believe, however, that qualitative considerations may still be made.) We index the WAXS patterns observed here according to the cubic perovskite phase, although previous scattering experiments have shown a pseudocubic annotation to be more appropriate.[23,332] However, the limited q-range and the broad reflections, which are typical for NCs, prevent such a refinement. From **Figure 6.2 b** one can see that one of the 200 peaks shifted to higher q values, while

another remains at the same position. This indicates a contraction of this part of the sample. For further analysis, we integrate the diffraction maps over all angular coordinates to obtain an azimuthally-independent scattering pattern. In **Figure 6.2 c**, we display the differential intensity, obtained by subtracting the azimuthally integrated diffraction pattern after X-ray exposure from the first pattern. In this Figure, positive differential intensities refer to reflections which weakened during X-ray exposure, while negative differential intensities indicate newly evolved reflections. From the differential pattern, a change of the lattice constant from 6.11 Å to 5.67 Å could be obtained (see **Figure 6.2 c**) and Supporting information, S6.5, for more details).

Upon exposing the red perovskites to X-rays during XPS, we observed a shift of all sample peaks to higher binding energies (**Figure 6.3**). We argue that this shift is not primarily caused by electric charging since 1) the Au 4f substrate peaks remain at constant energies throughout the experiment (**Figure 6.3 a + b**), 2) the perovskite films were rather thin to enable the release of a large number of secondary electrons from the Au substrate underneath to suppress charging,[333,334] and 3) the magnitude of the shift of the sample peaks was different for different elements (Pb 4f: +0.63 eV, Cs 4d: +0.71 eV). The shifts remained constant after illumination for approximately 7 h (**Figure 6.3 c+ d**).

We probed the influence of X-ray irradiation on the work function by measuring UPS before and after 20 h exposure (**Figure S6.5**). We find a shift of the high binding cutoff by 0.12 eV to higher energies, indicating a decrease of the work function. At the same time, the energy of the valence state maximum (1Sh) referenced to the Fermi level remains constant (see **Figure S6.8**). These findings suggest that the energy levels of the nanocrystal are shifted by 0.12 eV toward the vacuum level.

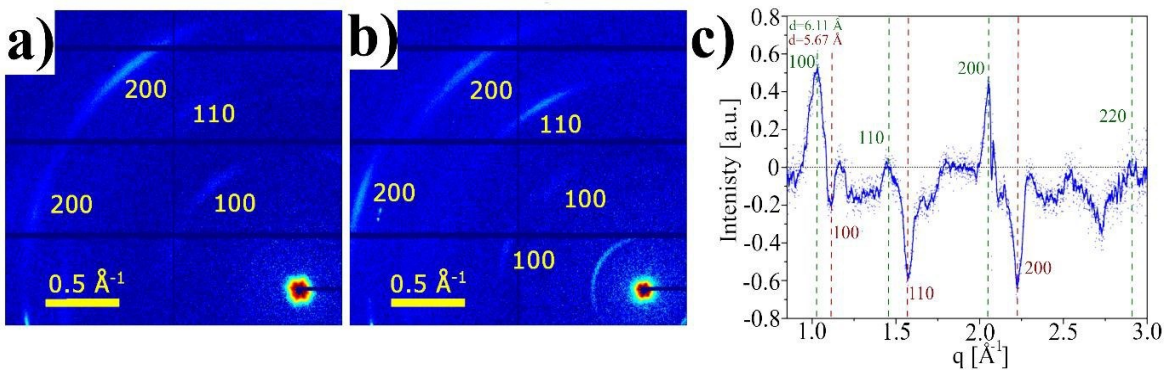

Figure 6.2: a) First WAXS measurement of $CsPbBrI_2$ nanocrystal superlattices and b) subsequent measurement after the spot was already exposed to radiation. c) Differential scattering intensity obtained by subtracting the azimuthally integrated diffraction pattern after X-ray exposure from the first pattern. Positive differential intensities refer to reflections which weakened during X-ray exposure, while negative differential intensities indicate newly evolved reflections. Indexing of old (green) and new (brown) peaks according to a cubic perovskite phase.

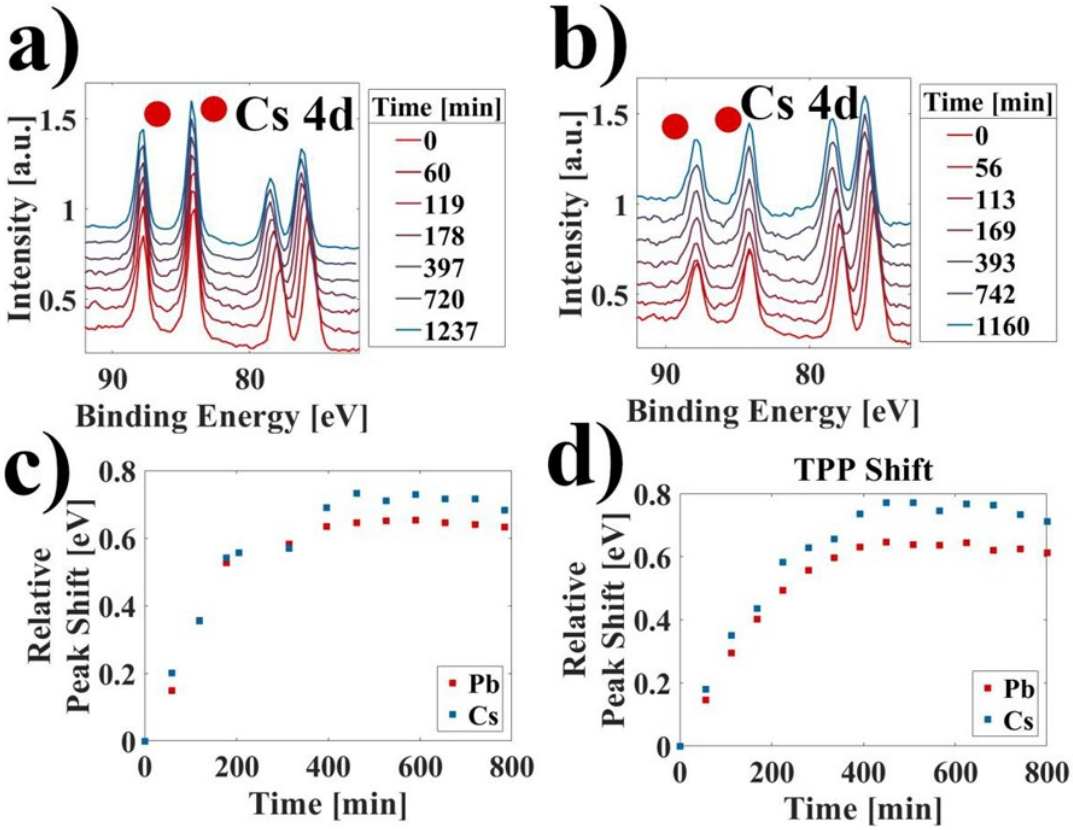

Figure 6.3: Cs 4d (75 eV) and Au 4f (84 eV) XPS spectra for **a)** native ligands and **b)** mZnTPP exchanged samples after different X-ray radiation exposure times. The substrate-related Au signals are denoted by red dots and did not change throughout the experiment in both cases. Relative peak position of the Pb 4f and Cs 3d signals compared to the binding energy at the start of the experiment for **c)** native and **d)** mZnTPP exchanged samples.

Motivated by the previous finding that ligand exchange with mZnTPP can enhance the stability of red perovskites in light emitting devices,[243] we studied the effect of this ligand on the decomposition of the red perovskites under X-ray illumination. (Note: the loss of structural integrity of the blue perovskites due to chlorine evaporation did not allow for an analogous analysis.) With the mZnTPP ligand shell, we again found the formation of Pb^0, but its formation is slower and yields only 8.1 % compared to 13.2 % after 20 h for the native ligand. An additional lead species occurred at higher binding energy for this ligand at ~140.9 eV, indicating a higher oxidation state than Pb^{2+} (**Figure 6.4 a + b**). The intensity ratio between this new peak and the evolving Pb^0 peak in the Pb 4f spectrum is roughly 2:1 for all irradiation times, implying that their formation is correlated (**Figure 6.4 e**). In contrast to the sample stabilized with the native ligand (*cf.* **Figure 6.1**), we did not find a similar shoulder in the iodide signal (Supporting information section S6.7), suggesting a different decomposition mechanism as a result of the ligand exchange. Before investigating this mechanism in more detail, we verify by SEM the structural integrity of the mZnTPP-stabilized red perovskites after X-ray exposure (**Figure 6.4 c**) and note that the stoichiometric composition remained roughly constant (**Figure 6.4 d**). We found the same shift in binding energies for all core-level peaks of the sample as already described for the red perovskites with the native ligand, suggesting that the shift is independent of the ligand shell and related to the NCs itself. UPS measurements before X-ray exposure revealed a shift to lower cutoff binding energies by ~0.5 eV compared to the NCs with native ligand stabilization (**Figure S6.7**). After X-ray exposure, the cutoff binding energies increase by 0.1 eV (**Figure S6.5**), reproducing the same effect as observed with the native ligand.

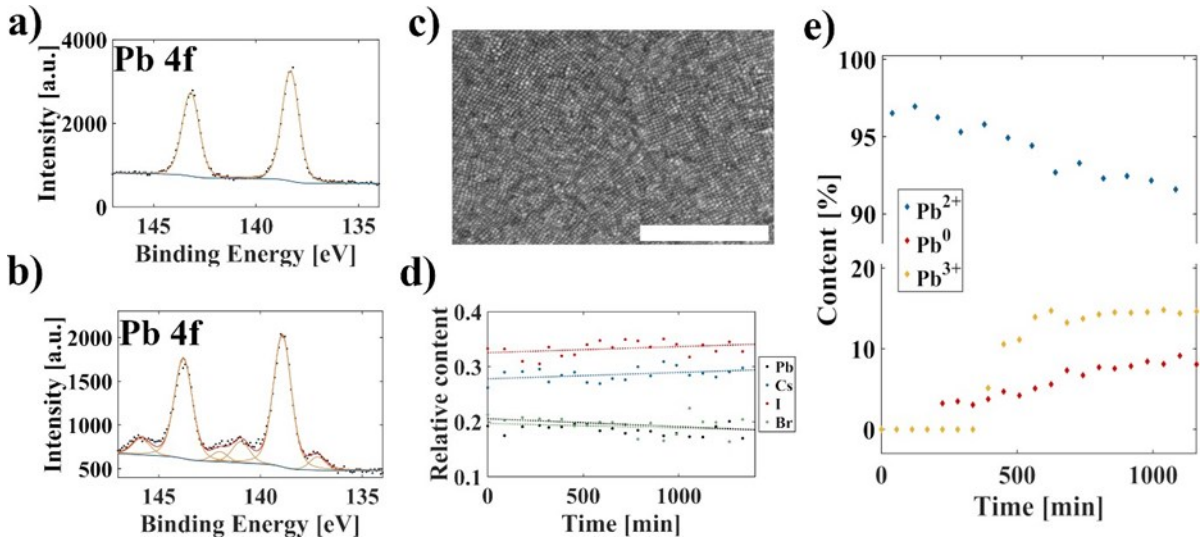

Figure 6.4: XPS of the Pb 4f orbital for $CsPbBrI_2$ with an mZnTPP ligand shell at the **a)** start and **b)** end of the experiment. Two new lead species occurred, at lower and higher binding energies. **c)** SEM micrograph of the mZnTPP exchanged sample after X-ray exposure for approximately 20 h. Scale bar corresponds to 500 nm. **d)** Relative stoichiometric content and linear regression (dotted lines) of the exchanged $CsPbBrI_2$ sample over time. **e)** Temporal evolution of the observed lead species, the novel formed peaks are attributed to Pb^0 (~ 137 eV) and Pb^{3+} (~ 141 eV).

6.4 Discussion

Based on the XPS and WAXS results, we now propose a mechanism for the X-ray radiation-related degradation of the red and blue perovskite NCs with their native ligands. Our findings suggest a redox reaction during which Pb^0 and molecular iodine ($CsPbBrI_2$) or chlorine ($CsPbBr_2Cl$) are formed. While iodine resides within the sample after 20 h in ultra-high vacuum, chlorine is removed. This suggests the following decomposition reaction for the red perovskites:

$$\begin{aligned} CsPbBrI_2(xl) &\rightarrow CsBr(s) \; + \; PbI_2(s) \\ PbI_2(s) &\rightarrow Pb^0(s) \; + \; I_2(s) \end{aligned} \tag{6.1}$$

where (xl) refers to the crystalline and (s) to the solid state. Similar mechanisms are postulated for $MAPbI_3$ and $CsPbBrI_2$ thin films, where a comparable Pb peak was found.[319,326–328,330] The first reaction is facilitated by the low enthalpy of formation for $CsPbBrI_2$ as shown by calorimetry.[335] We believe that the second reaction is enabled by the high energy radiation. In view of the high volatility of I_2, particular in ultra-high

vacuum, we note that the formation of polyiodides, such as I_3^-, is possible under these conditions which greatly reduces its volatility.[326,336]

We suggest a similar decay mechanism for the blue perovskites based on the analogous formation of a Pb^0 signal (**Figure 6.1 f**). We interpret the absence of a novel chlorine peak (**Figure 6.1 g**) and the strong decrease in chlorine content (**Figure 6.1 h**) as indirect evidence for the oxidation of chloride, since Cl_2 is highly volatile and polychlorides are less stable than polyiodides. In this scenario, chlorine would immediately evaporate and remain undetected by XPS. The crystal decomposition expected from such a loss in material is consistent with the greatly altered morphology found by SEM (**Figure S6.4**). Our finding that, in the red and blue perovskites alike, bromide is neither oxidized nor removed from the sample, can be rationalized in terms of the oxidation potentials and enthalpies of decomposition for all three halides. Firstly, the oxidation potential of bromide (E^0 = –1.087 V) is larger than that of iodide (E^0 = –0.5355 V) and triiodide (E^0 = –0.536 V), favoring the oxidation of the latter. In contrast, the oxidation potential of chloride (E^0 = –1.396 V) is higher than for bromide. However, the enthalpy of decomposition is roughly 0.22 eV larger for $CsPbBr_3$ than for $CsPbCl_3$, which we hold responsible for the observed overall oxidation and removal of chloride.[337] We now discuss the shift of the core-levels in XPS upon X-ray illumination, for which we focus on the red-emitting perovskites since the decomposition of the blue perovskites prevents a similar analysis. A core-level shift in XPS is generally attributed to a variety of origins, such as changes in the chemical environment of specific atoms, an altered electrostatic or Madelung potential, surface effects at the sample substrate interface or charging effects.[148,323–325] Firstly, we rule out any surface effects due to the very prominent gold substrate signal (**Figure 6.3**) which remains unaltered throughout the entire experiment. Secondly, charging effects are unlikely due to several reasons: The gold substrate signal is clearly visible, indicating a very thin perovskite film that can be assumed to be grounded. Closely

related is the high secondary electron count, originating from the substrate that we correlate to a suppression of sample charging. Lastly, the conductivities of the native as well as the mZnTPP exchanged sample are known.[243] The electric resistance in the porphyrin-containing sample is lower and should result in a smaller shift. However, we find the same shifts independent of the ligand shell and can thus assume that the shift does not originate from charging. Therefore, only two possible explanations remain: changes in either the electrostatic potential or the chemical environment. We argue that a change of the electrostatic potential in the sample is the origin of the peak shifts, which is justified in the following. The electrostatic potential in an ionic solid for an ion i is given as

$$V_i = \frac{e^2}{4\pi\varepsilon_0 r_0} \sum_{j \neq i} \frac{z_j}{r_{ij}/r_0} = \frac{e^2}{4\pi\varepsilon_0 r_0} M_i \tag{6.2}$$

with the elementary charge e, vacuum permittivity ε_0, equilibrium lattice constant r_0, effective charge z_j of the j-th atom, the distance between the respective atoms r_{ij} and the Madelung constant M_i. To quantify the change in V_i for Pb and Cs according to **(6.2)**), we calculate the changes of the radii during the contraction of the unit cell by 0.44 Å as determined from WAXS (**Figure 6.2 a**) and compare the results to the core-level shifts in XPS. The excellent agreement suggests that the lattice contraction is the reason for the measured core-level shift. We attribute the remaining small discrepancies to the inhomogeneous composition of the mixed halide system, as well as the simultaneously occurring decomposition mechanisms.

Table 6.1: Influence of irradiation by X-rays on the lattice constants and resulting distances for the $CsPbBrI_2$ NCs. The calculated electrostatic potential for Pb and Cs as well as the difference are given, experimental value in brackets.

	$CsPbBrI_2$					
	a_0=6.11Å	a_1=5.67Å	Difference [eV]	a_0=6.11Å	a_1=5.67 Å	Difference [eV]
Atom	**Pb**			**Cs**		
d_{CsA} [Å]	5.2395	4.8497		n.a.	n.a.	
d_{AX} [Å]	3.025	2.8		4.2780	3.9598	
d_{PbA} [Å]	n.a.	n.a.		5.2395	4.8497	
V_{el} [eV]	7.5	8.1	0.6 (0.630)	8.9	9.6	0.7 (0.711)

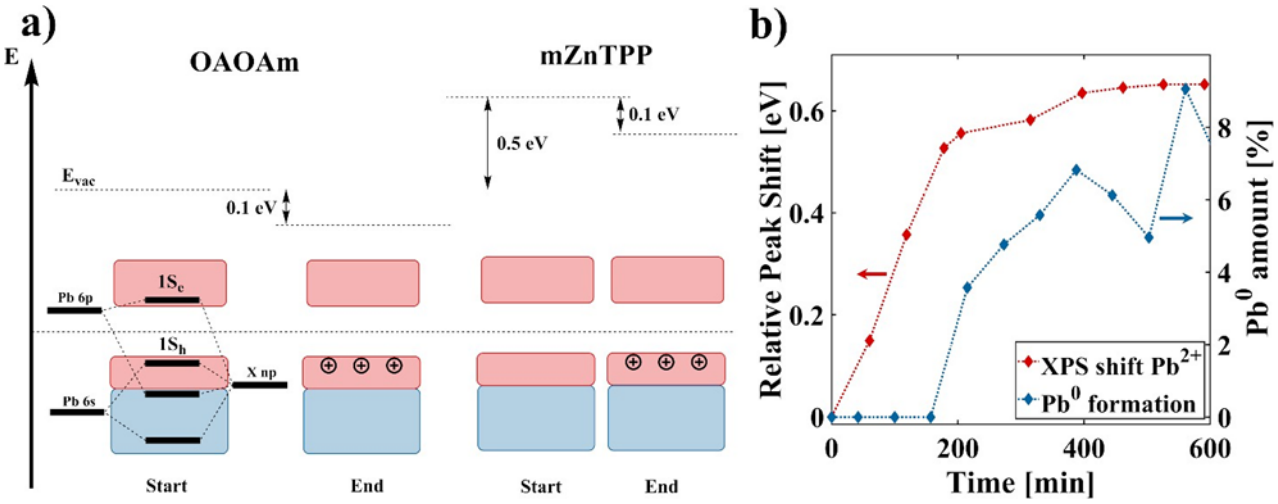

Figure 6.5: a) Energy level scheme obtained from UPS measurements for the native shell (left) and mZnTPP functionalized nanocrystals (right), all energies are referenced against the Fermi level of the instrument. The conduction state minimum ($1S_e$) and valence state maximum ($1S_h$) are indicated, respectively. The character of the states is depicted as red and blue for antibonding and bonding orbitals, respectively. The contraction of the crystal lattice resulted in a shift to higher energies by 0.1 eV for the native ligand as well as for mZnTPP. In addition, mZnTPP functionalization lowered the binding energy by 0.5 eV compared to the native functionalization. **b)** Temporal evolution of the XPS shift induced by the lattice contraction (red) and the formation of elemental lead (blue).

We now discuss the effect of ligand exchange with mZnTPP on the stability of the red perovskites under X-ray irradiation. Based on our XPS results, which involve the occurrence of two novel lead species (**Figure 6.4 b**), supposedly Pb^0 and Pb^{3+}, and a constant Pb^0:Pb^{3+} ratio of 1:2 during the experiment (**Figure 6.4 e**), we suggest the following disproportionation reaction:

$$3CsPbBrI_2 \rightarrow Cs_3Pb_2Br_3I_6 \; + \; Pb^0 \qquad \textbf{(6.3)}$$

This disproportionation is consistent with our finding that no other iodide species occurred (**Figure S6.9**) under these conditions, that is, this degradation pathway does not involve halide oxidation. Despite the low stability of Pb^{3+}, this oxidation state has previously been postulated for perovskites.[325,338] In addition, the specialized experimental conditions (continuous X-ray radiation in ultra-high vacuum) may facilitate its detection. Most notably, this new degradation pathway is substantially slower than the degradation with native ligand functionalization (compare **Figure S6.3** with **Figure 6.4 e**) and proceeds solely via the reaction of lead. To rationalize this surprising effect of the mZnTPP ligand, we note a recent work on the stabilizing effect of ligands with strong (surface) dipoles on CdSe NCs against irreversible reduction during charging.[339] During XPS, the NCs are subject to substantial charging and, while not all considerations for the reduction of Cd in CdSe may be transferable to Pb in $CsPbBrI_2$, we argue that the general rational outlined by du Fossé *et al.* is of central importance also in the present case: mZnTPP invokes a 0.5 eV increase in work function (**Figure 6.5 a**) and provides better dielectric screening (a higher permittivity)[243] compared to the native ligand. As du Fossé *et al.* have shown, a reduced work function affects primarily the overall crystal and only to a lesser extent a localized state, such as Pb^0. [339] This stabilizes the NCs during charging and inhibits the irreversible reduction of lead. Thus, a promising strategy to further enhance the stability of perovskite NCs is the search for ligands that induce even larger work functions.

We note that both degradation pathways – with and without mZnTPP – are preceded by the same core level energy shifts of Pb and Cs (**Figure 6.3 c + d**), which we were able to correlate with a lattice contraction (**Figure 6.2 a** and **Table 6.1**). A likely scenario for such a contraction could be either a phase transition or halide segregation.[328] The latter is a well-known phenomenon in $CsPbI_2Br$, leading to bromine-enriched crystal domains (of smaller lattice constant) with iodine-rich segregations at the boundaries.[328] **Figure 6.5 b** suggests that this transformation is a prerequisite for the redox reaction of Pb^{2+} to occur according to either **Equation (6.1)** or ((6.3).

Upon comparing the decomposition of our samples with the response of mixed-halide perovskites under UV radiation some similarities were found. The phase segregation / lattice contraction and iodine evaporation were found for superlattices of $CsPb(Br_xI_{1-x})_3$ NCs and could be reproduced under X-ray illumination.[152] However, we did not observe the formation of distinct $CsPbBr_3$ nanocrystals under the presented conditions, which we rationalize by the possibility of forming triiodide under the extreme environment of XPS.[326,336] Mainly this can be seen in the reduction of the photoluminescence signal and absence of bright green emission (**Figure S6.10**).

In conclusion, we have shown that the mechanism of photodegradation under X-ray radiation of all-inorganic mixed lead halide perovskite nanocrystals depends on the ligand shell. With the ligands oleic acid/oleylamine, we found a fast decomposition into elemental lead and halogen, similar to previous studies on bulk thin films. After ligand exchange with a metal porphyrin derivative, photodegradation was significantly slower and progressed *via* a disproportionation of Pb^{2+} to Pb^0 and Pb^{3+}. We hold an increase in work function of the nanocrystal film by 0.5 eV responsible for the altered photodegradation behavior, which was induced by the metal porphyrin derivative. This work highlights the advantageous tunability of the ligand shell of lead halide perovskite nanocrystals as an additional means to improve their photostability and suggests sur-

face ligands that introduce strong dipoles as a general paradigm toward mitigating photodegradation.

Author information

The manuscript was written through contributions of all authors. All authors have given approval to the final version of the manuscript.

Acknowledgments

This work was supported by the DFG under grants SCHE1905/8-1 (project no. 424708673) and SCHE1905/9-1 as well as the Carl Zeiss Stiftung (Forschungsstruktur-konzept "Interdisziplinäres nanoBCP-Lab"). I.A.V. acknowledges the financial support of the Russian Federation represented by the Ministry of Science and Higher Education of the Russian Federation (Agreement No. 075-15- 2021-1352). The Authors would like to thank Dmitry Lapkin and Jerome Carnis for help with the WAXS measurements. We acknowledge DESY (Hamburg, Germany), a member of the Helmholtz Association HGF, for the provision of experimental facilities. Parts of this research were carried out at PETRA III synchrotron facility and we would like to thank the beamline staff for assistance in using the Coherence Application P10 beamline.

6.5 Supplementary Information

Mitigating the Photodegradation of All-Inorganic Mixed-Halide Perovskite Nanocrystals by Ligand Exchange

*Jan Wahl[$,‡], Philipp Haizmann[$,‡], **Christopher Kirsch[$],** Rene Frecot[$], Nastasia Mukharamova[#], Dameli Assalauova[#], Young Yong Kim[#], Ivan Zaluzhnyy[+], Thomas Chassé[$,ß], Ivan A. Vartanyants[#,&], Heiko Peisert[$,]*, Marcus Scheele[$,ß,]**

[$] Institut für physikalische und theoretische Chemie, Universität Tübingen, Auf der Morgenstelle 18, 72076 Tübingen, Germany

[#] Deutsches Elektronen-Synchrotron DESY, Notkestraße 85, 22607 Hamburg, Germany

[+] Institut für Angewandte Physik, Universität Tübingen, Auf der Morgenstelle 10, 72076 Tübingen, Germany

[ß] Center for Light-Matter Interaction, Sensors & Analytics LISA[+], Universität Tübingen, Auf der Morgenstelle 15, 72076 Tübingen, Germany

[&] National Research Nuclear University MEPhI (Moscow Engineering Physics Institute), Kashirskoe shosse 31, 115409 Moscow, Russia

[‡] These authors contributed equally

Materials and methods Materials

1-Octadecene (ODE), technical grade, 90%, Sigma Aldrich; Oleic acid (OA), 97%, Acros Organics; Oleylamine (OAm), 80-90%, Acros Organics; Caesium carbonate (Cs_2CO_3), 99.99% (trace metal basis), Acros Organics; Lead(II)iodide (PbI_2), 99.999% (trace metal basis), Sigma Aldrich; Lead(II)bromide (PbBr2), ≥98%, Sigma Aldrich; Lead(II)chloride (PbCl2), Puratronic™, 99.999% (metal trace), Crystalline, Alfa Aesar; Toluene, HPLC grade, 99.8%; Toluene, 99.8%, extra dry, AcroSeal, Acros Organics; zinc-(5-monocarboxyphenyl-10,15,20-triphenylporphyrin) (mZnTPP), TriPorTech; Tetrachloroethylene (TCE), ≥99%, Acros Organics; Kapton® polyimide membranes (125 µm thickness), DuPont

$CsPbX_3$ nanocrystal synthesis

The used nanocrystals were synthesized with two different stoichiometries, namely $CsPbBrI_2$ and $CsPbBr_2Cl$, following the published synthesis route by Protesescu *et al.*[68] with slight adjustments. For $CsPbBrI_2$ a 20ml glass reaction vial was used which could be heated to the reaction temperature of 160°C in a custom-made aluminum heating block. Generally, the syntheses were carried out with twice the concentration of precursors compared to literature.

Ligand exchange and thin film preparation

Following the purification, the nanocrystals (NC) were either used as obtained or post- synthetically modified by ligand exchange with zinc-(5-monocarboxyphenyl-10,15,20- triphenylporphyrin) (mZnTPP). The exchange was effectively carried out in solution by adding 0.25 stoichiometric equivalents of mZnTPP to the NC solution. An immediate color change was observed upon addition. The ligand exchange procedure and corresponding analysis is given in more detail in another paper.[243]

The as-synthesized and exchanged NCs were subsequently spin-coated onto custom-made gold substrates under nitrogen atmosphere to prepare thin films. The coating parameters were chosen to be 10 rps for 30 s with a 3 s ramp.

The used substrates were custom made at the LISA$^+$ center Tübingen. A commercially available four-inch silicon wafer with native oxide layer was coated with 10 nm chromium in an evaporation chamber, followed by deposition of a 50 nm gold layer.

Self-assembly into superlattices

To prepare superlattices for the X-ray scattering measurements, the perovskite samples were prepared as 1-3 mM solutions in toluene ($CsPbBrI_2$) or tetrachloroethylene ($CsPbBr_2Cl$) and drop- casted onto Kapton® substrates under inert atmosphere. The substrates were placed inside a petri dish with an additional reservoir of solvent (1-2 ml) to slow down the evaporation process and covered with a lid. The samples were allowed to dry for 24 h before the lid was removed and an additional drying process for 5–6 h was allowed.

Scanning electron microscopy (SEM)

SEM was carried out at a HITACHI SU8030 electron microscope, utilizing an acceleration voltage of 30 kV. SEM micrographs were taken of thin film samples.

X-ray photoelectron spectroscopy and ultraviolet photoelectron spectroscopy

The thin film samples were analyzed inside an ultrahigh vacuum chamber (base pressure: 2 x 10^{-10} mbar) with a XR-50M X-ray source from SPECS utilizing monochromatic Al Kα radiation ($h\nu$ = 1486.7 eV) with a flux of $2.3 \cdot 10^{11}$ photons/s. For photoelectron detection a Phoibos 150 DLD hemispherical photoelectron energy analyzer (SPECS) was used. The spectrometer was calibrated to reproduce the binding energy of Au $4f_{7/2}$ (84.0 eV) and Cu $2p_{3/2}$ (932.6 eV) signals, with photoionization cross sections

of 0.2511 and 0.3438, respectively.[340] Measurements were performed under fixed analyzer transmission mode, with an energy resolution of 400 meV and 150 meV for XPS and Ultraviolet photoelectron spectroscopy (UPS), respectively. Custom written scripts were used to measure overview and detailed spectra at specified times during the experiment. Peak fitting was done using the Unifit software package.[341] Peaks are expected to show Voigt profile, meaning a convolution of Lorentzian and Gaussian peaks. The background was modeled with an iterative algorithm to apply Shirley background.

UPS was carried out with similar conditions as XPS measurements. A helium ultraviolet source with an energy of 21.22 eV was used in combination with a Phoibos 150 DLD electron analyzer.

XPS and UPS experiments were conducted on thin film samples.

Small- and wide-angle X-ray scattering

The small- and wide-angle X-ray scattering (SAXS and WAXS) were carried out at the Coherence Applications beamline P10 of the PETRA III synchrotron source at the Deutsche Elektronen-Synchrotron (DESY). The X-ray source provided a beam with a wavelength of λ=0.0898nm or an energy of 13.8 keV, the beam was focused on a spot size of roughly 400x400 nm^2 with a focal depth of 0.5 mm. A two-dimensional EIGER X4M (Dectris) detector with 2070x2167 pixels of size 75x75 μm^2 was used, it was located 412 mm away from the sample plane. The detector was positioned in a way to allow simultaneous measurements of SAXS and WAXS. The exposure time of the samples was 0.5 s. The obtained diffraction patterns were analyzed by Bragg peak assignment and radial profiles could be achieved by averaging over the angular coordinates. For SAXS and WAXS measurements superlattice samples were used.

S6.1: Low Binding energy survey from XPS

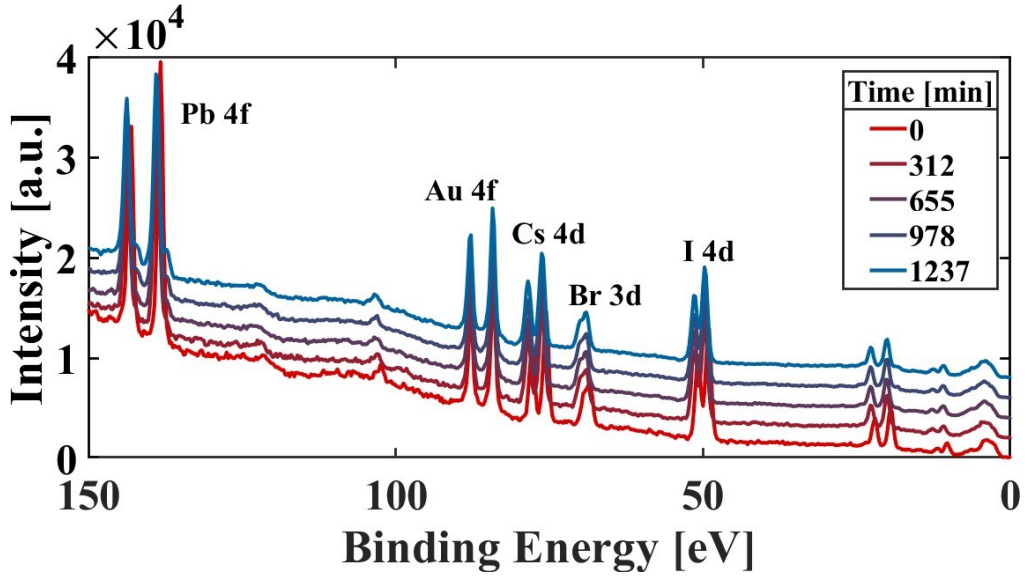

Figure S6.1: Survey spectra at different times during the X-ray illumination. A shift in peak position for all elements associated with the perovskites can be observed. As the perovskites were deposited on a gold substrate, the Au 4f core level peak serves as a reference for the binding energies. Another interesting feature is the occurrence of an additional novel peak in the Pb 4f region, visible at lower binding energies after illumination, indicating the decomposition of the nanocrystals (*cf.* **Figure 6.1** of the manuscript). Beside of the energetic shift of the Br 3d peak no further change could be observed, *i.e.*, it was not possible to detect an additional species for this element arising from the degradation.

S6.2: Calculation of the I:Pb ratio and temporal evolution of novel lead species

As detail XPS spectra are generally not comparable, the ratio of formed elemental lead and iodine was calculated as follows. The percentages were taken from the ratio of the areas fitted to the detail spectra as shown in **Figure S6.2**. Subsequently, the areas from the survey spectra were fitted as described in the methods section. The as obtained areas were then multiplied with the percentages from the detail spectra, resulting in areas that are quantitatively comparable.

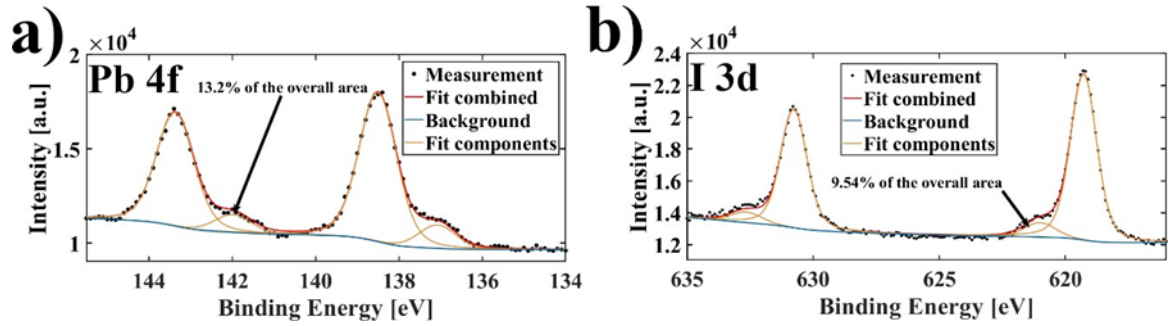

Figure S6.2: Percentages of the novel formed species after illuminating the native sample for ~20h for **a**) lead and **b**) iodide. The amount of newly formed species is given as a percentage of the overall peak area in both cases.

Generally, an error of 10% per fitted peak area is assumed.[342] Additionally, a Gaussian error propagation was carried out since multiple calculations were done with the measured values. The precise error calculation is given by:

$$\Delta\left(\frac{I_2}{Pb^0}\right) = \Delta R = \sqrt{\left(\frac{\partial R}{\partial A_{I_2}} \cdot \Delta A_{I_2}\right)^2 + \left(\frac{\partial R}{\partial A_{Pb^0}} \cdot \Delta A_{Pb^0}\right)^2} \tag{S6.1}$$

With the ratio of formed iodine to elemental lead R, the Area of iodine A_{I_2} and elemental lead A_{Pb^0} as well as the corresponding uncertainties denoted by Δ. The error calculation resulted in an error of the ratio of 0.23.

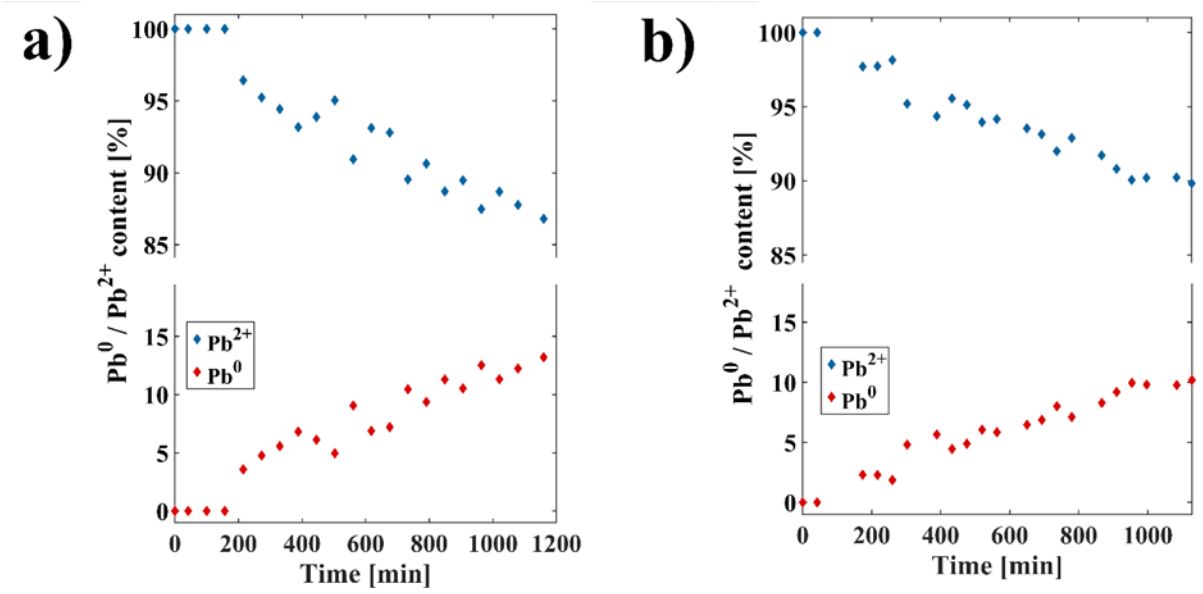

Figure S6.3: Temporal evolution of elemental lead (Pb^0) for a) $CsPbBrI_2$ and b) $CsPbBr_2Cl$ obtained by fitting the Pb 4f XPS spectra in **Figure 6.1** of the manuscript.

S6.3: Structural integrity probed by SEM for $CsPbBrI_2$ and $CsPbBr_2Cl$

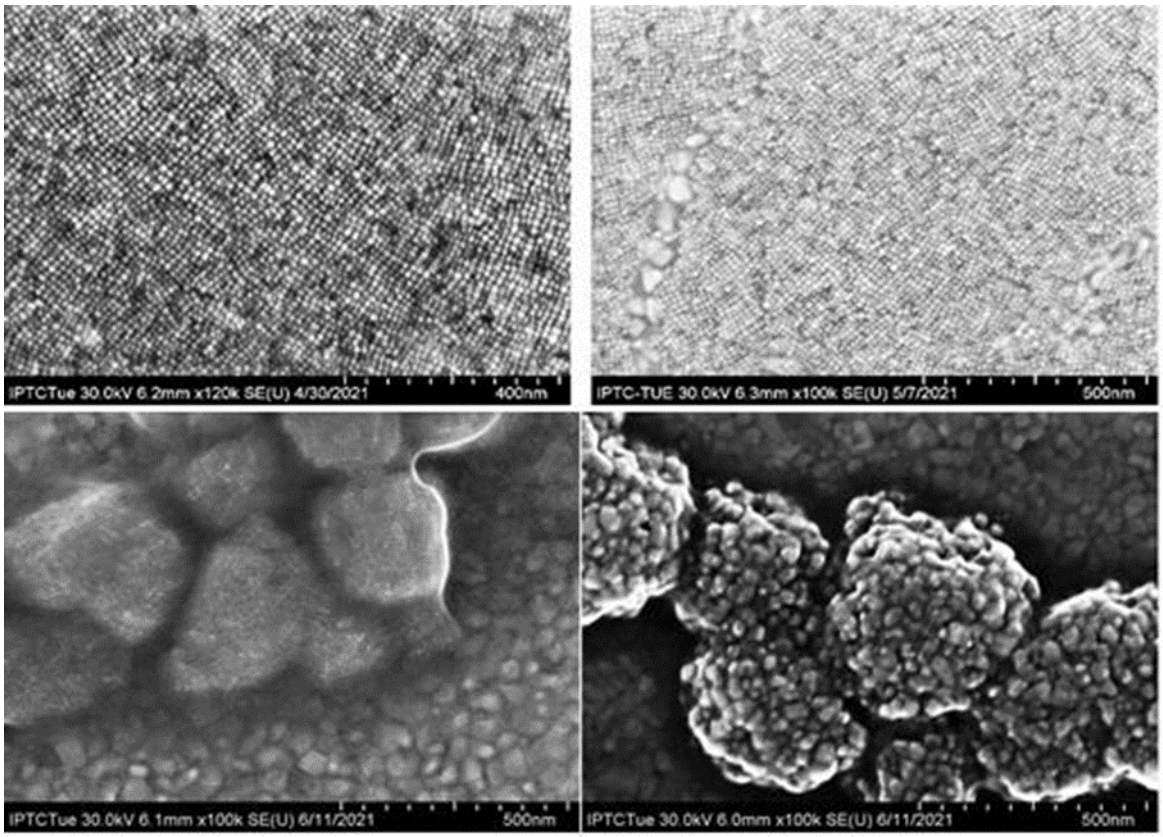

Figure S6.4: SEM of $CsPbBrI_2$ (top) and $CsPbBr_2Cl$ (bottom) before (left) and after (right) X-ray exposure.

S6.4: UPS of native and exchanged $CsPbBrI_2$ before and after X-ray illumination

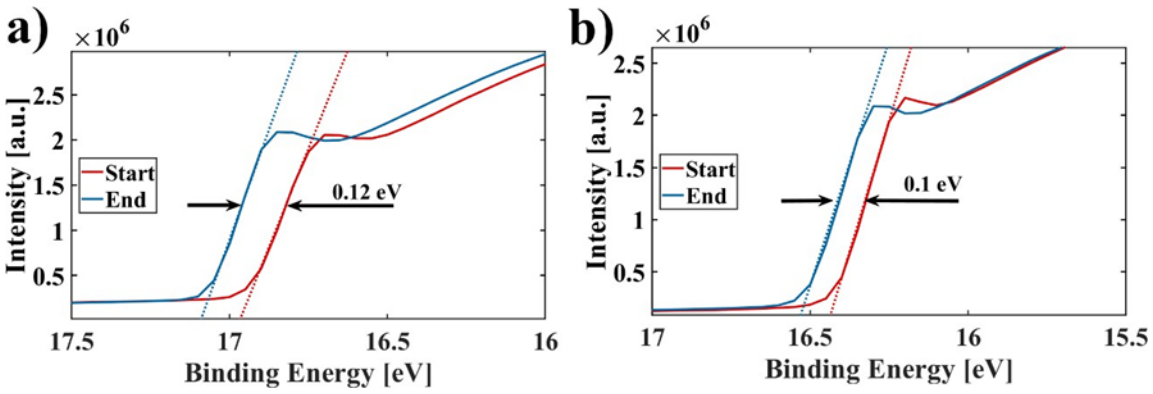

Figure S6.5: UPS cut-off energies of **a**) native and **b**) exchanged $CsPbBrI_2$. The shift in the cut-off energy of ~0.1 eV in both cases is found from a linear extrapolation, the shift indicates a reduction of the work function by the same amount. The fits are indicated as dotted lines.

The shifts of the UPS onset were found to be $\Delta native = 0.12333\ eV$ and $\Delta TPP = 0.0947\ eV$ from fitting. However, as UPS has a resolution limit of one decimal, the value for both shifts was taken to be ~ 0.1 eV.

S6.5: Further example of the lattice contraction

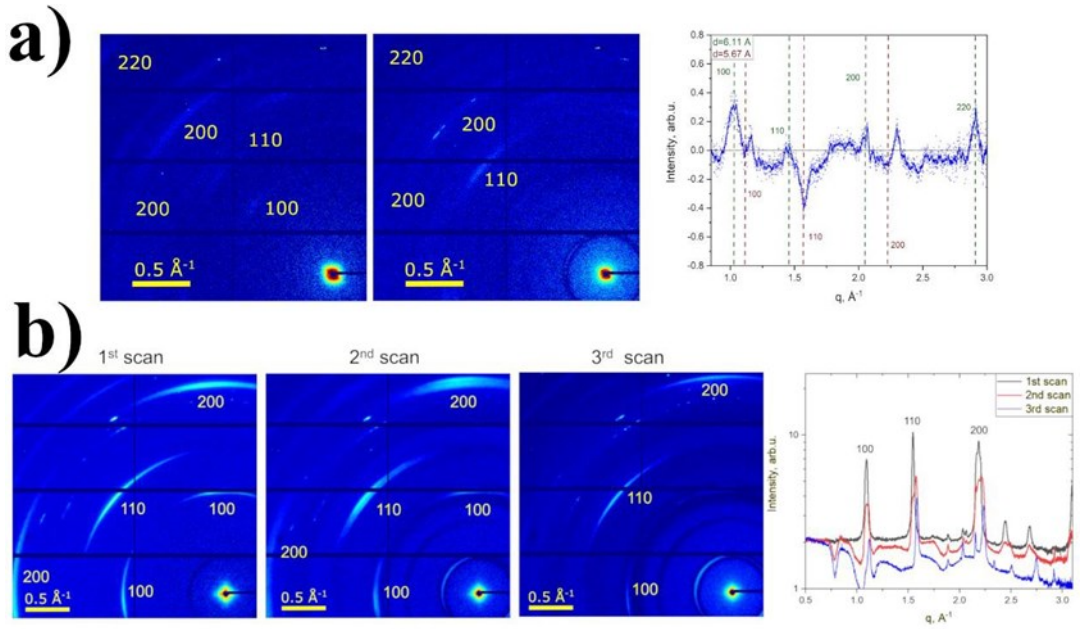

Figure S6.6: More examples of the isotropic lattice contraction for **a**) $CsPbBrI_2$ and **b**) $CsPbBr_2Cl$

S6.6: UPS overview spectra and onset

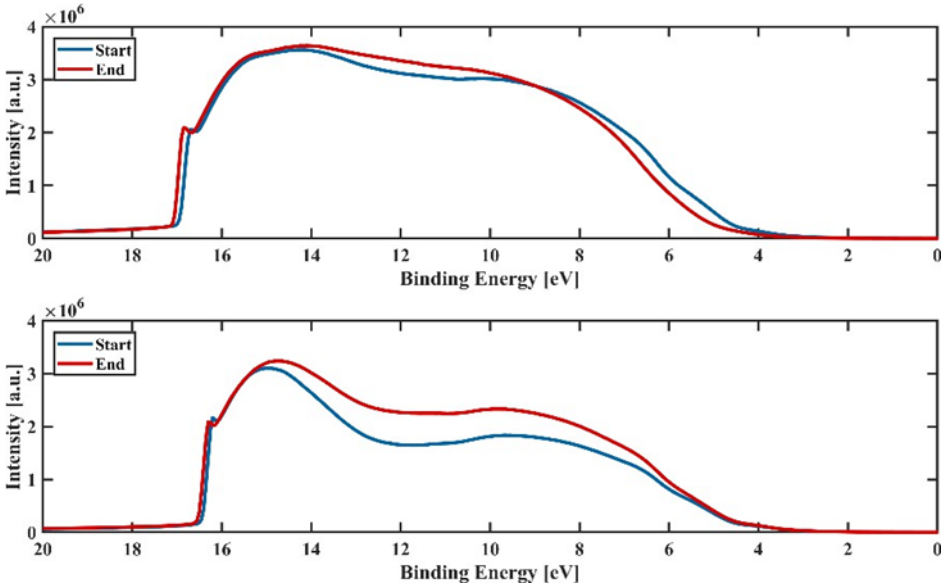

Figure S6.7: UPS overview spectra of the native CsPbBrI2 sample (top) and the mZnTPP exchanges sample (bottom). The cutoff energies are shifted by ~0.5 eV.

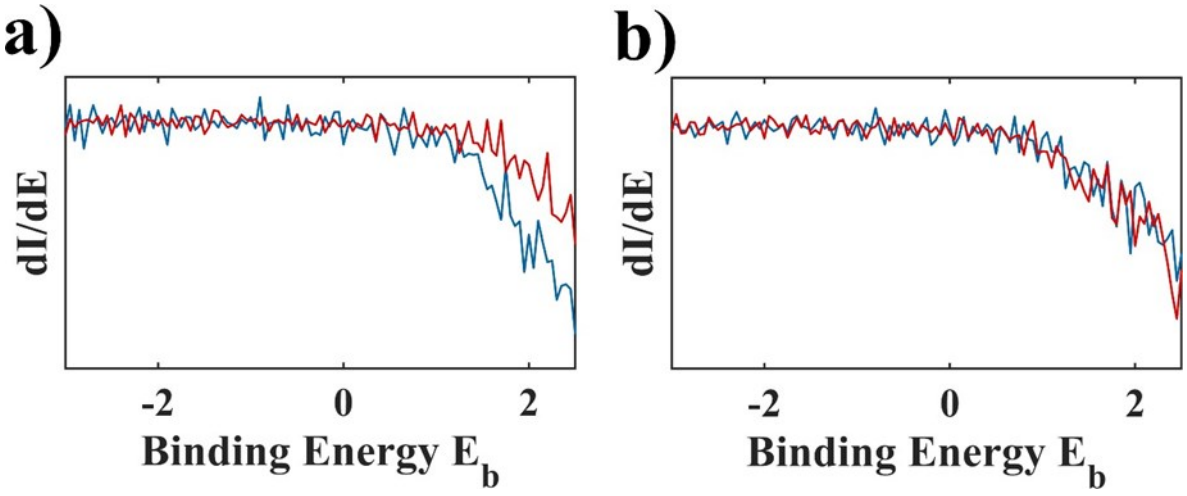

Figure S6.8: The onset remained constant at ~1 eV, shown by the derivative of the UPS spectrum for **a)** native and **b)** mZnTPP functionalized $CsPbBrI_2$. The constant onset refers to the Fermi level being located in the middle of the band gap before and after the illumination. Therefore, a shift of the energy states in their entirety is at hand.

S6.7: Iodide preservation for $CsPbBrI_2$ functionalized with mZnTPP

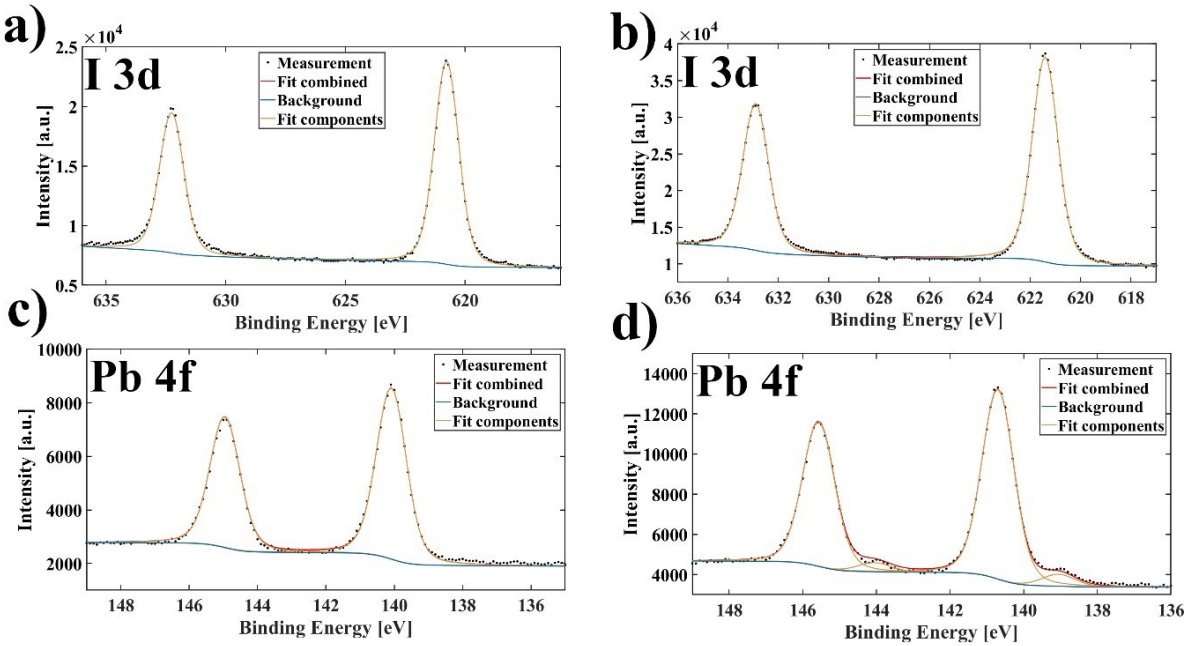

Figure S6.9: : I 3d (**a** + **b**) and Pb 4f (**c** + **d**) XPS detail spectra for the mZnTPP exchanged sample. The decomposition of the NCs started as indicated by the formation of elemental lead. However, there are no novel peaks for the iodide signal.

S6.8: Photoluminescence loss after X-ray illumination

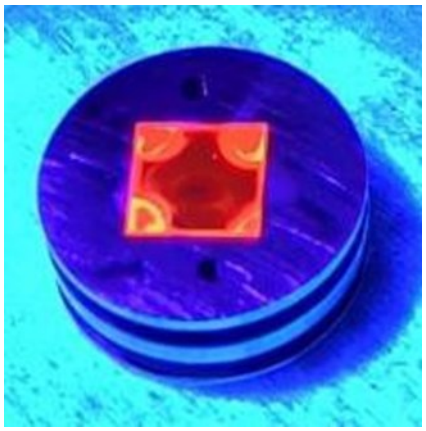

Figure S6.10: $CsPbBrI_2$ sample after exposure to X-ray radiation for ~21 h. The middle of the sample was illuminated, the area exhibits a darker spot corresponding to a loss of PL response.

7. Conclusion & Outlook

This chapter summarizes the main results of this work, which aims to optimize the efficiency of light-emitting diodes by improving the structure, optoelectronic properties, and stability of blue-emitting perovskite nanoparticles.

Initially, spatially resolved fluorescence (lifetime) measurements and high-precision X-ray nanodiffraction were performed to correlate the influence of structural misalignment and fluorescence (lifetime) properties of inorganic $CsPbX_3$ (X- = Br-, Cl-) perovskites. The nanoparticles self-assembled from colloidal solution into superlattices exhibited strong differences in their emission properties at the edges compared to the core of the superlattice. When approaching an edge of the supercrystal, a blue shift as strong as 20 meV and an approximately 20 % reduction in lifetime were observed. In collaboration with the group of Prof. Ivan A. Vartanyants, a comprehensive structural investigation of these regions was performed at DESY by X-ray nanodiffraction measurements. This allowed us to detect a reduction in the distance between the nanoparticles, a loss of structural coherence and orientation order, and a compressive strain near the surfaces of the supercrystal. These structural distortions correlated strongly with the blue-shifted fluorescence and reduced radiation lifetimes. This correlation highlights the importance of structure on the emission properties of perovskites for application in optoelectronic devices, such as LEDs.

Subsequently, the focus was on optimizing the nanoparticles themselves, with emphasis on the ligand shell of the nanocrystals. Due to the synthesis, native ligands in perovskite nanocrystals consist of oleic acid and oleylamine, which not only bind weakly to the surface, but also have an insulating effect due to their long alkyl chains. Therefore, a new ligand was designed and prepared by Yamaguchi esterification. This showed more stable binding to the particle surface due to its zwitterionic nature and bidentate binding ability. In addition, this ligand possesses the advantageous electronic

properties of the carbazole-π system. In LEDs, the exchanged NCs showed a 15-fold longer lifetime, a 1.6-fold higher external quantum efficiency, and a 25% reduction in turn-on voltage to 3 V compared to the same NCs stabilized with oleic acid/oleylamine. Thus, this work highlights the relevance of the ligand shell on the optoelectric properties of the nanoparticle.

In continuation, the effect of doping the nanoparticles with the organic lithium salt LiTFSI on the efficiency of the LEDs was investigated. Using time-resolved and parallel-polarized angle-dependent photoluminescence spectroscopy, it was shown that the doping increases the quantum efficiency and improves the light outcoupling compared to the native nanoparticle system. Further investigations by X-ray photoelectron spectroscopy revealed that p-doping is induced by the addition of LiTFSI. This lowered the energy barrier for hole injection from 0.31 eV to 0.06 eV, which improved the charge carrier balance. Ultimately, the efficiency of blue LEDs was 7 times higher than that of untreated nanoparticles.

Finally, the stability under continuous X-ray irradiation of all inorganic mixed lead halide perovskite nanocrystals was investigated. It was found that surface functionalization with a porphyrin derivative called mZnTPP as a ligand resulted in an altered and slower decay mechanism. The addition of the ligand increased the work function by 0.5 eV compared to the native system. This significantly slowed down the reduction of Pb^{2+} to Pb^{0} and thus the photoinduced decay of the perovskites.

In summary, this work has developed suitable methods to improve the efficiency and stability of blue electroluminescent LEDs based on perovskite nanoparticles. The knowledge gained from this work will guide future work to further optimize optoelectronic devices. Surface ligands have been shown to significantly influence the structure, stability, and optoelectronic properties of perovskite nanoparticles and thus optoelectronic devices.

It should be noted, however, that both the intrinsic and extrinsic stability of perovskites can only be partially improved by ligands. Although the work in Chapters 4 and 6 has made the particles more stable against external influences, degradation still occurs over time. In addition, the efficiencies of less than 2 % achieved so far are not yet sufficient for an industrial application of this illumination technology. In this respect, further improvements are needed.

A possible further improvement in efficiency could be to further optimize the ligand system developed in Chapter 4. The synthesis used in this chapter offers the possibility of replacing the carbazole backbone with an even more suitable organic semiconductor. Theoretical calculations could identify a ligand system that, in addition to the previous improvements similar to Chapter 5, raises the energy levels of the valence band towards the hole transport layer to enable more efficient hole injection.

In addition to the aforementioned optimization options, the backbone of the ligand could be modified to activate a possible cycloaddition that leads to coupled structures by UV light during the spin coating process, as outlined in Figure 7.1. This would not only allow better coupling between the particles, but also significantly increase the stability of the films.

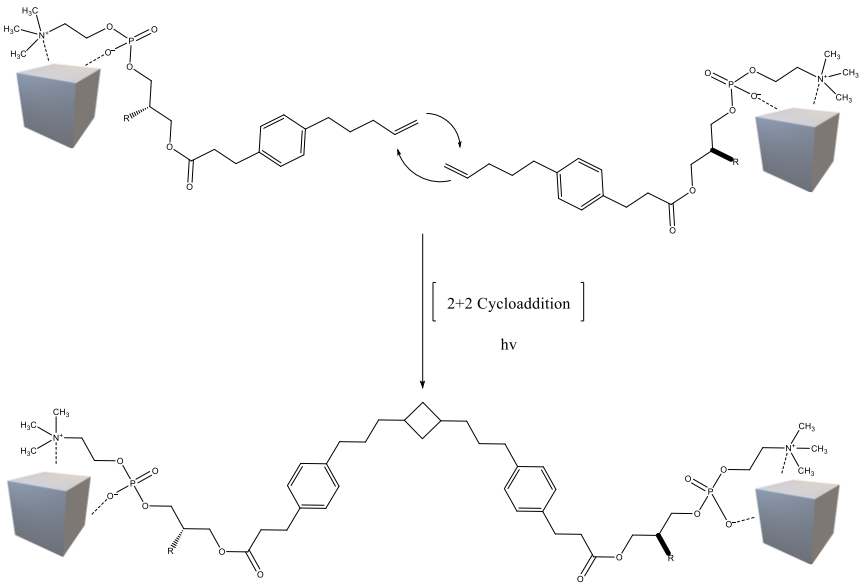

Figure 7.1: Schematic of a potential light-triggered cycloaddition process for synthesizing interconnected nanocrystal films.

In conclusion, the field of lead halide perovskite nanocrystals is gaining increasing significance, and our understanding of their physical and chemical properties is gradually developing.

List of Abbreviations

1Sh	Valence state maximum
AFM	Atomic force microscopy
AL	Atomic lattice
B3PYMPM	(4,6-Bis(3,5-di(pyridin-3-yl)phenyl)-2-methylpyrimidine
CaF_2	Calcium fluoride
$CaTiO_3$	Calcium titanate
CB	Conduction band
CBM	Conduction band minimum
Cd	Cadmium
CNT	Classical nucleation theory
Cs	Caesium
Cs2CO3	Caesium carbonate
$CsPbBr_3$	Caesium lead bromide
$CsPbX_3$	All-inorganic caesium lead perovskites
CTL	Charge transport layer
DCM	Dichloromethane
DCzGPC	1,2-Di((9H-carbazol-9-yl)propanoyl)-sn-glycero-3-phosphocholine
DESY	Deutsches Elektronen Synchrotron (German electron synchrotron)
DFG	Deutsche Forschungsgemeinschaft (German research foundation)
DFT	Density functional theory
DMAP	4-(dimethylamino)pyridine
DOS	Density of states
ELQLEDs	Electroluminescent quantum dot light-emitting device
EML	Emission layer
EQE	External quantum efficiency
ESI-TOF	Electrospray ionization time-of-flight
ETL	Electron transport layer
$FAPbI_3$	Formamidinium lead Iodide
FLIM	Fluorescence lifetime imaging microscopy

FWHM	Full width at half maximum
GaAs	Gallium *a*, Gallium arsenide
GPC	L-α-glycerophosphorylcholine
HI	Hot-injection
HOMO	Highest occupied molecular orbital
HRMS	High resolution mass spectrometry
HRTEM	High-resolution transmission electron microscopy
HTL	Hole transport layer
IRF	Instrument response function
ITO	Indium tin oxide
LARP	Ligand-assisted reprecipitation
LED	Light emitting diodes
LHP	Lead halide perovskites
LUMO	Lowest unoccupied molecular orbital
$MAPbI_3$	Methylammonium lead iodide
MeOAc	Methyl acetate
MgSO4	Magnesium sulfate
MHP	Metal halide perovskites
MO	Molecular orbital
NC	Nanocrystal
NMR	Nuclear magnetic resonance spectroscopy
NPL	Nanoplatelets
OA	Oleic acid
ODE	Octadecene
OLA	Oleylamin
$Pb(OOCR)_2$	Lead oleate
PbX_2	Lead halide
PEDOT:PSS	Poly(3,4-ethylenedioxythiophene) polystyrene sulfonate
PL	Photoluminescence
PLQY	Photoluminescence quantum yield
PTFE	Polytetrafluoroethylene

PV	Photovoltaic
PVK	Polyvinylcarbazole
QDLEDs	Quantum dot light-emitting diodes
SAXS	Small angle X-ray scattering
Se	Selenide
SEM	Scanning electron microscopy
SL	Superlattice
TA	Transient Absorption Spectroscopy
TCBC	2,4,6-Trichlorbenzoylchlorid
TCSPC	Time-correlated single photon counting
TEM	Transmission electron microscopy
UPS	Ultraviolet photoelectron spectroscopy
VB	Valence band
VBM	Valence band maximum
WAXS	Wide-angle X-ray scattering
XPS	X-Ray Electron Spectroscopy
XRD	X-ray diffraction

List of Figures and Tables

Bibliography

[1] *Gen 1, 3, LU* **2023**, https://www.die-bibel.de/bibeln/online-bibeln/lesen/LU17/GEN.1/1.-Mose-1.

[2] L. Aschoff, *Kurze Übersichtstabelle zur Geschichte der Medizin*, Springer Berlin Heidelberg, Berlin **2013**.

[3] N. Holonyak, S. F. Bevacqua, *Appl. Phys. Lett.* **1962**, *1*, 82.

[4] S. Nakamura, *Ann. Phys.* **2015**, *527*, 335.

[5] J. Wahl, *Coupled organic inorganic nanostructures (COIN) of core-shell Indium Phosphide / Zinc Sulfide qunatum dots prepared via reactive surface passivation* **2018**, Master thesis, Eberhard Karls Universität Tübingen.

[6] Z. Liu, W. Qiu, X. Peng, G. Sun, X. Liu, D. Liu, Z. Li, F. He, C. Shen, Q. Gu, F. Ma, H.-L. Yip, L. Hou, Z. Qi, S.-J. Su, *Advanced materials (Deerfield Beach, Fla.)* **2021**, *33*, e2103268.

[7] T. Chiba, Y. Hayashi, H. Ebe, K. Hoshi, J. Sato, S. Sato, Y.-J. Pu, S. Ohisa, J. Kido, *Nature Photon* **2018**, *12*, 681.

[8] Y. Dong, Y.-K. Wang, F. Yuan, A. Johnston, Y. Liu, D. Ma, M.-J. Choi, B. Chen, M. Chekini, S.-W. Baek, L. K. Sagar, J. Fan, Y. Hou, M. Wu, S. Lee, B. Sun, S. Hoogland, R. Quintero-Bermudez, H. Ebe, P. Todorovic, F. Dinic, P. Li, H. T. Kung, M. I. Saidaminov, E. Kumacheva, E. Spiecker, L.-S. Liao, O. Voznyy, Z.-H. Lu, E. H. Sargent, *Nature nanotechnology* **2020**, *15*, 668.

[9] G. Rose, *De novis quibusdam fossilibus, quae in montibus uraliis inveniuntur. I. De Perowskite, fossili novo.*, Berlin **1839**.

[10] G. Rose, Journal für praktische Chemie **1840**, 19, 459.

[11] M. M. Lee, J. Teuscher, T. Miyasaka, T. N. Murakami, H. J. Snaith, *Science (New York, N.Y.)* **2012**, *338*, 643.

[12] M. A. Green, E. D. Dunlop, G. Siefer, M. Yoshita, N. Kopidakis, K. Bothe, X. Hao, *Progress in Photovoltaics* **2023**, *31*, 3.

[13] P. Basumatary, P. Agarwal, *Materials Research Bulletin* **2022**, *149*, 111700.

[14] O. Almora, D. Baran, G. C. Bazan, C. I. Cabrera, S. Erten-Ela, K. Forberich, F. Guo, J. Hauch, A. W. Y. Ho-Baillie, T. J. Jacobsson, R. A. J. Janssen, T. Kirchartz, N. Kopidakis, M. A. Loi, R. R. Lunt, X. Mathew, M. D. McGehee, J. Min, D. B. Mitzi, M. K. Nazeeruddin, J. Nelson, A. F. Nogueira, U. W. Paetzold, B. P. Rand, U. Rau, H. J. Snaith, E. Unger, L. Vaillant-Roca, C. Yang, H.-L. Yip, C. J. Brabec, *Adv. Energy Mater.* **2023**, *13*, 2203313.

[15] Z. L. Wang, Z. C. Kang, *Functional and Smart Materials*, Springer US, Boston, MA **1998**.

[16] V. M. Goldschmidt, *Naturwissenschaften* **1926**, *14*, 477.

[17] R. J. D. Tilley, *Perovskites: Structure-property relationships*, Wiley, Chichester, West Sussex **2016**.

[18] L. Liang, L. Wencong, C. Nianyi, *Journal of Physics and Chemistry of Solids* **2004**, *65*, 855.

[19] P. Cottingham, R. L. Brutchey, *Chem. Mater.* **2018**, *30*, 6711.

[20] C. L. Jackson, G. B. McKenna, *The Journal of Chemical Physics* **1990**, *93*, 9002.

[21] S. C. Riha, B. A. Parkinson, A. L. Prieto, *J. Am. Chem. Soc.* **2009**, *131*, 12054.

[22] S. H. Tolbert, A. P. Alivisatos, *Science (New York, N.Y.)* **1994**, *265*, 373.

[23] F. Bertolotti, L. Protesescu, M. V. Kovalenko, S. Yakunin, A. Cervellino, S. J. L. Billinge, M. W. Terban, J. S. Pedersen, N. Masciocchi, A. Guagliardi, *ACS nano* **2017**, *11*, 3819.

[24] C. Li, X. Lu, W. Ding, L. Feng, Y. Gao, Z. Guo, *Acta crystallographica. Section B, Structural science* **2008**, *64*, 702.

[25] R. E. Brandt, V. Stevanović, D. S. Ginley, T. Buonassisi, *MRS Communications* **2015**, *5*, 265.

[26] W. Geng, Le Zhang, Y.-N. Zhang, W.-M. Lau, L.-M. Liu, *J. Phys. Chem. C* **2014**, *118*, 19565.

[27] Q. A. Akkerman, V. D'Innocenzo, S. Accornero, A. Scarpellini, A. Petrozza, M. Prato, L. Manna, *J. Am. Chem. Soc.* **2015**, *137*, 10276.

[28] Q. A. Akkerman, G. Rainò, M. V. Kovalenko, L. Manna, *Nature materials* **2018**, *17*, 394.

[29] L. Protesescu, S. Yakunin, M. I. Bodnarchuk, F. Krieg, R. Caputo, C. H. Hendon, R. X. Yang, A. Walsh, M. V. Kovalenko, *Nano letters* **2015**, *15*, 3692.

[30] M. R. Filip, G. E. Eperon, H. J. Snaith, F. Giustino, *Nature communications* **2014**, *5*, 5757.

[31] G. J. Man, C. Kamal, A. Kalinko, D. Phuyal, J. Acharya, S. Mukherjee, P. K. Nayak, H. Rensmo, M. Odelius, S. M. Butorin, *Nature communications* **2022**, *13*, 3839.

[32] G. E. Eperon, S. D. Stranks, C. Menelaou, M. B. Johnston, L. M. Herz, H. J. Snaith, *Energy Environ. Sci.* **2014**, *7*, 982.

[33] R. Prasanna, A. Gold-Parker, T. Leijtens, B. Conings, A. Babayigit, H.-G. Boyen, M. F. Toney, M. D. McGehee, *J. Am. Chem. Soc.* **2017**, *139*, 11117.

[34] C. Giansante, I. Infante, *J. Phys. Chem. Lett.* **2017**, *8*, 5209.

[35] S. G. Motti, D. Meggiolaro, S. Martani, R. Sorrentino, A. J. Barker, F. D. Angelis, A. Petrozza, *Advanced materials (Deerfield Beach, Fla.)* **2019**, *31*, e1901183.

[36] H. Huang, M. I. Bodnarchuk, S. V. Kershaw, M. V. Kovalenko, A. L. Rogach, *ACS energy letters* **2017**, *2*, 2071.

[37] S. D. Stranks, G. E. Eperon, G. Grancini, C. Menelaou, M. J. P. Alcocer, T. Leijtens, L. M. Herz, A. Petrozza, H. J. Snaith, *Science (New York, N.Y.)* **2013**, *342*, 341.

[38] Q. Dong, Y. Fang, Y. Shao, P. Mulligan, J. Qiu, L. Cao, J. Huang, *Science (New York, N.Y.)* **2015**, *347*, 967.

[39] H. Zhu, K. Miyata, Y. Fu, J. Wang, P. P. Joshi, D. Niesner, K. W. Williams, S. Jin, X.-Y. Zhu, *Science (New York, N.Y.)* **2016**, *353*, 1409.

[40] W.-J. Yin, T. Shi, Y. Yan, *J. Phys. Chem. C* **2015**, *119*, 5253.

[41] M. A. Becker, R. Vaxenburg, G. Nedelcu, P. C. Sercel, A. Shabaev, M. J. Mehl, J. G. Michopoulos, S. G. Lambrakos, N. Bernstein, J. L. Lyons, T. Stöferle, R. F. Mahrt, M. V. Kovalenko, D. J. Norris, G. Rainò, A. L. Efros, *Nature* **2018**, *553*, 189.

[42] M. Vert, Y. Doi, K.-H. Hellwich, M. Hess, P. Hodge, P. Kubisa, M. Rinaudo, F. Schué, *Pure and Applied Chemistry* **2012**, *84*, 377.

[43] N. Baig, I. Kammakakam, W. Falath, *Mater. Adv.* **2021**, *2*, 1821.

[44] R. van Noorden, *Nature* **2012**, *483*, S32-3.

[45] Vijay K Varadan, *Nanoscience and nanotechnology in engineering*, World Scientific, New Jersey **2010**.

[46] C. B. Murray, D. J. Norris, M. G. Bawendi, *J. Am. Chem. Soc.* **1993**, *115*, 8706.

[47] X. Peng, J. Wickham, A. P. Alivisatos, *J. Am. Chem. Soc.* **1998**, *120*, 5343.

[48] V. K. LaMer, R. H. Dinegar, *J. Am. Chem. Soc.* **1950**, *72*, 4847.

[49] J. J. de Yoreo, Reviews in Mineralogy and Geochemistry **2003**, 54, 57.

[50] L. C. Schmidt, A. Pertegás, S. González-Carrero, O. Malinkiewicz, S. Agouram, G. Mínguez Espallargas, H. J. Bolink, R. E. Galian, J. Pérez-Prieto, *J. Am. Chem. Soc.* **2014**, *136*, 850.

[51] M. V. Kovalenko, M. I. Bodnarchuk, *Chimia* **2017**, *71*, 461.

[52] I. Lignos, S. Stavrakis, G. Nedelcu, L. Protesescu, A. J. deMello, M. V. Kovalenko, *Nano letters* **2016**, *16*, 1869.

[53] Y. Li, H. Huang, Y. Xiong, S. V. Kershaw, A. L. Rogach, *Angewandte Chemie (International ed. in English)* **2018**, *57*, 5833.

[54] C. Sun, Z. Gao, H. Liu, C. Geng, H. Wu, X. Zhang, C. Fan, W. Bi, *Dalton transactions (Cambridge, England 2003)* **2018**, *47*, 16218.

[55] S. G. Kwon, T. Hyeon, Small (Weinheim an der Bergstrasse, Germany) **2011**, 7, 2685.

[56] J. C. Dahl, X. Wang, X. Huang, E. M. Chan, A. P. Alivisatos, *J. Am. Chem. Soc.* **2020**, *142*, 11915.

[57] M. Piotrowski, Z. Ge, Y. Wang, A. K. Bandela, U. Thumu, *Nanoscale* **2022**, *14*, 16806.

[58] Q. A. Akkerman, S. Park, E. Radicchi, F. Nunzi, E. Mosconi, F. D. Angelis, R. Brescia, P. Rastogi, M. Prato, L. Manna, *Nano letters* **2017**, *17*, 1924.

[59] S. K. Balakrishnan, P. V. Kamat, *Chem. Mater.* **2018**, *30*, 74.

[60] J. Shamsi, A. S. Urban, M. Imran, L. de Trizio, L. Manna, *Chemical reviews* **2019**, *119*, 3296.

[61] D. V. Talapin, J.-S. Lee, M. V. Kovalenko, E. V. Shevchenko, *Chemical reviews* **2010**, *110*, 389.

[62] D. Vanmaekelbergh, *Nano Today* **2011**, *6*, 419.

[63] W. H. Evers, B. de Nijs, L. Filion, S. Castillo, M. Dijkstra, D. Vanmaekelbergh, *Nano letters* **2010**, *10*, 4235.

[64] M. D. Eldridge, P. A. Madden, D. Frenkel, *Nature* **1993**, *365*, 35.

[65] P. Bartlett, R. H. Ottewill, P. N. Pusey, *Phys. Rev. Lett.* **1992**, *68*, 3801.

[66] C. B. Murray, C. R. Kagan, M. G. Bawendi, *Science (New York, N.Y.)* **1995**, *270*, 1335.

[67] J. de Roo, M. Ibáñez, P. Geiregat, G. Nedelcu, W. Walravens, J. Maes, J. C. Martins, I. van Driessche, M. V. Kovalenko, Z. Hens, *ACS nano* **2016**, *10*, 2071.

[68] G. Nedelcu, L. Protesescu, S. Yakunin, M. I. Bodnarchuk, M. J. Grotevent, M. V. Kovalenko, *Nano letters* **2015**, *15*, 5635.

[69] Y. Yuan, J. Huang, *Acc. Chem. Res.* **2016**, *49*, 286.

[70] J. Liu, K. Song, Y. Shin, X. Liu, J. Chen, K. X. Yao, J. Pan, C. Yang, J. Yin, L.-J. Xu, H. Yang, A. M. El-Zohry, B. Xin, S. Mitra, M. N. Hedhili, I. S. Roqan, O. F. Mohammed, Y. Han, O. M. Bakr, *Chem. Mater.* **2019**, *31*, 6642.

[71] Y. Zhang, R. Sun, X. Ou, K. Fu, Q. Chen, Y. Ding, L.-J. Xu, L. Liu, Y. Han, A. V. Malko, X. Liu, H. Yang, O. M. Bakr, H. Liu, O. F. Mohammed, *ACS nano* **2019**, *13*, 2520.

[72] D. Zhang, Y. Yu, Y. Bekenstein, A. B. Wong, A. P. Alivisatos, P. Yang, *J. Am. Chem. Soc.* **2016**, *138*, 13155.

[73] J. Jagielski, S. F. Solari, L. Jordan, D. Scullion, B. Blülle, Y.-T. Li, F. Krumeich, Y.-C. Chiu, B. Ruhstaller, E. J. G. Santos, C.-J. Shih, *Nature communications* **2020**, *11*, 387.

[74] G. Rainò, M. A. Becker, M. I. Bodnarchuk, R. F. Mahrt, M. V. Kovalenko, T. Stöferle, *Nature* **2018**, *563*, 671.

[75] J. Liu, X. Zheng, O. F. Mohammed, O. M. Bakr, *Acc. Chem. Res.* **2022**, *55*, 262.

[76] M. A. Boles, D. Ling, T. Hyeon, D. V. Talapin, *Nature materials* **2016**, *15*, 141.

[77] N. C. Anderson, M. P. Hendricks, J. J. Choi, J. S. Owen, *J. Am. Chem. Soc.* **2013**, *135*, 18536.

[78] J. Owen, *Science (New York, N.Y.)* **2015**, *347*, 615.

[79] M. L. H. Green, G. Parkin, *J. Chem. Educ.* **2014**, *91*, 807.

[80] N. Fiuza-Maneiro, K. Sun, I. López-Fernández, S. Gómez-Graña, P. Müller-Buschbaum, L. Polavarapu, *ACS energy letters* **2023**, *8*, 1152.

[81] D. Yang, X. Li, W. Zhou, S. Zhang, C. Meng, Y. Wu, Y. Wang, H. Zeng, *Advanced materials (Deerfield Beach, Fla.)* **2019**, *31*, e1900767.

[82] J. Shi, F. Li, Y. Jin, C. Liu, B. Cohen-Kleinstein, S. Yuan, Y. Li, Z.-K. Wang, J. Yuan, W. Ma, *Angewandte Chemie (International ed. in English)* **2020**, *59*, 22230.

[83] G. Almeida, L. Goldoni, Q. Akkerman, Z. Dang, A. H. Khan, S. Marras, I. Moreels, L. Manna, *ACS nano* **2018**, *12*, 1704.

[84] A. Pan, B. He, X. Fan, Z. Liu, J. J. Urban, A. P. Alivisatos, L. He, Y. Liu, *ACS nano* **2016**, *10*, 7943.

[85] S. C G, J. Mannekote Shivanna, J. D. Schiffman, S. Mohan, S. Budagumpi, R. G. Balakrishna, *ACS applied materials & interfaces* **2022**, *14*, 38471.

[86] M. Han, Y.-Y. Noh, *Phys. Status Solidi A* **2021**, *218*, 2100366.

[87] F. Krieg, Q. K. Ong, M. Burian, G. Rainò, D. Naumenko, H. Amenitsch, A. Süess, M. J. Grotevent, F. Krumeich, M. I. Bodnarchuk, I. Shorubalko, F. Stellacci, M. V. Kovalenko, *Journal of the American Chemical Society* **2019**, *141*, 19839.

[88] A. Dutta, N. Pradhan, *ACS energy letters* **2019**, *4*, 709.

[89] C. Otero-Martínez, N. Fiuza-Maneiro, L. Polavarapu, *ACS applied materials & interfaces* **2022**, *14*, 34291.

[90] J. Ye, Z. Li, D. J. Kubicki, Y. Zhang, L. Dai, C. Otero-Martínez, M. A. Reus, R. Arul, K. R. Dudipala, Z. Andaji-Garmaroudi, Y.-T. Huang, Z. Li, Z. Chen, P. Müller-Buschbaum, H.-L. Yip, S. D. Stranks, C. P. Grey, J. J. Baumberg, N. C. Greenham, L. Polavarapu, A. Rao, R. L. Z. Hoye, *J. Am. Chem. Soc.* **2022**, *144*, 12102.

[91] S. Masi, A. F. Gualdrón-Reyes, I. Mora-Seró, *ACS energy letters* **2020**, *5*, 1974.

[92] A. Swarnkar, W. J. Mir, A. Nag, *ACS energy letters* **2018**, *3*, 286.

[93] Encyclopedia of Nanomaterials, Elsevier **2023**.

[94] Y. Shynkarenko, M. I. Bodnarchuk, C. Bernasconi, Y. Berezovska, V. Verteletskyi, S. T. Ochsenbein, M. V. Kovalenko, *ACS energy letters* **2019**, *4*, 2703.

[95] P.-L. Chu, W.-L. Huang, S.-Y. Chu, *ACS Appl. Opt. Mater.* **2023**, *1*, 513.

[96] E. T. Vickers, E. E. Enlow, W. G. Delmas, A. C. DiBenedetto, A. H. Chowdhury, B. Bahrami, B. W. Dreskin, T. A. Graham, I. N. Hernandez, S. A. Carter, S. Ghosh, Q. Qiao, J. Z. Zhang, *ACS energy letters* **2020**, *5*, 817.

[97] B. Zhang, L. Goldoni, J. Zito, Z. Dang, G. Almeida, F. Zaccaria, J. de Wit, I. Infante, L. de Trizio, L. Manna, *Chem. Mater.* **2019**, *31*, 9140.

[98] F. Krieg, S. T. Ochsenbein, S. Yakunin, S. ten Brinck, P. Aellen, A. Süess, B. Clerc, D. Guggisberg, O. Nazarenko, Y. Shynkarenko, S. Kumar, C.-J. Shih, I. Infante, M. V. Kovalenko, *ACS energy letters* **2018**, *3*, 641.

[99] C.-H. Kuan, S.-H. Yang, *Mater. Adv.* **2022**, *3*, 7824.

[100] A. Papangelis, T. Ulven, *The Journal of organic chemistry* **2022**, *87*, 8194.

[101] K. Ichihara, H. Iwasaki, K. Ueda, R. Takizawa, H. Naito, M. Tomosugi, *Chemistry and physics of lipids* **2005**, *137*, 94.

[102] A. Hermetter, H. Stütz, R. Franzmair, F. Paltauf, *Chemistry and physics of lipids* **1989**, *50*, 57.

[103] P. Wang, D. H. Blank, T. A. Spencer, *The Journal of organic chemistry* **2004**, *69*, 2693.

[104] Quinten Adriaan Akkerman, Perovskite Nanocrystals: A New Age of Semiconductuctive Nanocrystals, Genova **2018**.

[105] L. Brus, *J. Phys. Chem.* **1986**, *90*, 2555.

[106] T. C. Damen, J. Shah, D. Y. Oberli, D. S. Chemla, J. E. Cunningham, J. M. Kuo, *Physical review. B, Condensed matter* **1990**, *42*, 7434.

[107] N. F. Mott, *Trans. Faraday Soc.* **1938**, *34*, 500.

[108] G. H. Wannier, *Phys. Rev.* **1937**, *52*, 191.

[109] J. Frenkel, *Phys. Rev.* **1931**, *37*, 17.

[110] J. Tilchin, D. N. Dirin, G. I. Maikov, A. Sashchiuk, M. V. Kovalenko, E. Lifshitz, *ACS nano* **2016**, *10*, 6363.

[111] L. M. Herz, Annual review of physical chemistry **2016**, 67, 65.

[112] W. Demtröder, *Experimentalphysik*, Springer, Berlin **2003**-.

[113] A. B. Sproul, M. A. Green, *Journal of Applied Physics* **1991**, *70*, 846.

[114] A. K. Guria, S. K. Dutta, S. D. Adhikari, N. Pradhan, *ACS energy letters* **2017**, *2*, 1014.

[115] M. Liu, G. Zhong, Y. Yin, J. Miao, K. Li, C. Wang, X. Xu, C. Shen, H. Meng, *Advanced science (Weinheim, Baden-Wurttemberg, Germany)* **2017**, *4*, 1700335.

[116] D. Parobek, B. J. Roman, Y. Dong, H. Jin, E. Lee, M. Sheldon, D. H. Son, *Nano letters* **2016**, *16*, 7376.

[117] N. Phung, R. Félix, D. Meggiolaro, A. Al-Ashouri, G. Sousa E Silva, C. Hartmann, J. Hidalgo, H. Köbler, E. Mosconi, B. Lai, R. Gunder, M. Li, K.-L. Wang, Z.-K. Wang, K. Nie, E. Handick, R. G. Wilks, J. A. Marquez, B. Rech, T. Unold, J.-P. Correa-Baena, S. Albrecht, F. D. Angelis, M. Bär, A. Abate, *J. Am. Chem. Soc.* **2020**, *142*, 2364.

[118] C.-H. Lu, G. V. Biesold-McGee, Y. Liu, Z. Kang, Z. Lin, *Chemical Society reviews* **2020**, *49*, 4953.

[119] H. Liu, Z. Wu, J. Shao, D. Yao, H. Gao, Y. Liu, W. Yu, H. Zhang, B. Yang, *ACS nano* **2017**, *11*, 2239.

[120] Q. A. Akkerman, D. Meggiolaro, Z. Dang, F. D. Angelis, L. Manna, *ACS energy letters* **2017**, *2*, 2183.

[121] E. Amerling, H. Lu, B. W. Larson, A. E. Maughan, A. Phillips, E. Lafalce, L. Whittaker-Brooks, J. J. Berry, M. C. Beard, Z. V. Vardeny, J. L. Blackburn, *ACS energy letters* **2021**, *6*, 1104.

[122] S. F. Solari, L.-N. Poon, M. Wörle, F. Krumeich, Y.-T. Li, Y.-C. Chiu, C.-J. Shih, *J. Am. Chem. Soc.* **2022**, *144*, 5864.

[123] M. Saliba, T. Matsui, K. Domanski, J.-Y. Seo, A. Ummadisingu, S. M. Zakeeruddin, J.-P. Correa-Baena, W. R. Tress, A. Abate, A. Hagfeldt, M. Grätzel, *Science (New York, N.Y.)* **2016**, *354*, 206.

[124] C. Liu, J. Sun, W. L. Tan, J. Lu, T. R. Gengenbach, C. R. McNeill, Z. Ge, Y.-B. Cheng, U. Bach, *Nano letters* **2020**, *20*, 1240.

[125] Y. Zhou, J. Chen, O. M. Bakr, H.-T. Sun, *Chem. Mater.* **2018**, *30*, 6589.

[126] L. Xu, S. Yuan, H. Zeng, J. Song, *Materials Today Nano* **2019**, *6*, 100036.

[127] D. Amgar, T. Binyamin, V. Uvarov, L. Etgar, *Nanoscale* **2018**, *10*, 6060.

[128] H. Wu, Y. Yang, D. Zhou, K. Li, J. Yu, J. Han, Z. Li, Z. Long, J. Ma, J. Qiu, *Nanoscale* **2018**, *10*, 3429.

[129] W. Liu, Q. Lin, H. Li, K. Wu, I. Robel, J. M. Pietryga, V. I. Klimov, *J. Am. Chem. Soc.* **2016**, *138*, 14954.

[130] M. Lu, X. Zhang, Y. Zhang, J. Guo, X. Shen, W. W. Yu, A. L. Rogach, *Advanced materials (Deerfield Beach, Fla.)* **2018**, *30*, e1804691.

[131] W. van der Stam, J. J. Geuchies, T. Altantzis, K. H. W. van den Bos, J. D. Meeldijk, S. van Aert, S. Bals, D. Vanmaekelbergh, C. de Mello Donega, *J. Am. Chem. Soc.* **2017**, *139*, 4087.

[132] Z.-J. Yong, S.-Q. Guo, J.-P. Ma, J.-Y. Zhang, Z.-Y. Li, Y.-M. Chen, B.-B. Zhang, Y. Zhou, J. Shu, J.-L. Gu, L.-R. Zheng, O. M. Bakr, H.-T. Sun, *J. Am. Chem. Soc.* **2018**, *140*, 9942.

[133] R. Begum, M. R. Parida, A. L. Abdelhady, B. Murali, N. M. Alyami, G. H. Ahmed, M. N. Hedhili, O. M. Bakr, O. F. Mohammed, *J. Am. Chem. Soc.* **2017**, *139*, 731.

[134] G. Pan, X. Bai, D. Yang, X. Chen, P. Jing, S. Qu, L. Zhang, D. Zhou, J. Zhu, W. Xu, B. Dong, H. Song, *Nano letters* **2017**, *17*, 8005.

[135] F. Zeng, Y. Tan, W. Hu, X. Tang, X. Zhang, H. Yin, *Journal of Luminescence* **2022**, *245*, 118788.

[136] D. Zhou, D. Liu, G. Pan, X. Chen, D. Li, W. Xu, X. Bai, H. Song, *Advanced materials (Deerfield Beach, Fla.)* **2017**, *29*.

[137] T. J. Milstein, D. M. Kroupa, D. R. Gamelin, *Nano letters* **2018**, *18*, 3792.

[138] D. L. Dexter, *Phys. Rev.* **1957**, *108*, 630.

[139] J. Butkus, P. Vashishtha, K. Chen, J. K. Gallaher, S. K. K. Prasad, D. Z. Metin, G. Laufersky, N. Gaston, J. E. Halpert, J. M. Hodgkiss, *Chem. Mater.* **2017**, *29*, 3644.

[140] M. Li, X. Zhang, S. Lu, P. Yang, *RSC Adv.* **2016**, *6*, 103382.

[141] D. Zhang, Y. Yang, Y. Bekenstein, Y. Yu, N. A. Gibson, A. B. Wong, S. W. Eaton, N. Kornienko, Q. Kong, M. Lai, A. P. Alivisatos, S. R. Leone, P. Yang, *J. Am. Chem. Soc.* **2016**, *138*, 7236.

[142] L. Dou, M. Lai, C. S. Kley, Y. Yang, C. G. Bischak, D. Zhang, S. W. Eaton, N. S. Ginsberg, P. Yang, *Proceedings of the National Academy of Sciences of the United States of America* **2017**, *114*, 7216.

[143] D. Parobek, Y. Dong, T. Qiao, D. Rossi, D. H. Son, *J. Am. Chem. Soc.* **2017**, *139*, 4358.

[144] T. Tsutsui, E. Aminaka, C. P. Lin, D.-U. Kim, Philosophical Transactions of the Royal Society of London. Series A: Mathematical, Physical and Engineering Sciences **1997**, 355, 801.

[145] T. Morgenstern, C. Lampe, T. Naujoks, M. Jurow, Y. Liu, A. S. Urban, W. Brütting, *Journal of Luminescence* **2020**, *220*, 116939.

[146] C.-K. Lin, Y. Zhang, M. Gao, J.-A. Lin, H. K. D. Le, Z. Lin, P. Yang, *Nano letters* **2022**, *22*, 2437.

[147] R. Grisorio, M. E. Di Clemente, E. Fanizza, I. Allegretta, D. Altamura, M. Striccoli, R. Terzano, C. Giannini, M. Irimia-Vladu, G. P. Suranna, *Nanoscale* **2019**, *11*, 986.

[148] W. Xiang, S. Liu, W. Tress, *Energy Environ. Sci.* **2021**, *14*, 2090.

[149] Y.-H. Ko, P. Prabhakaran, M. Jalalah, S.-J. Lee, K.-S. Lee, J.-G. Park, *J. Mater. Chem. C* **2018**, *6*, 7803.

[150] S. Huang, Z. Li, B. Wang, N. Zhu, C. Zhang, L. Kong, Q. Zhang, A. Shan, L. Li, *ACS applied materials & interfaces* **2017**, *9*, 7249.

[151] C. Das, M. Wussler, T. Hellmann, T. Mayer, W. Jaegermann, *Physical chemistry chemical physics PCCP* **2018**, *20*, 17180.

[152] M. C. Brennan, S. Toso, I. M. Pavlovetc, M. Zhukovskyi, S. Marras, M. Kuno, L. Manna, D. Baranov, *ACS energy letters* **2020**, *5*, 1465.

[153] S. Lou, T. Xuan, J. Wang, *Optical Materials: X* **2019**, *1*, 100023.

[154] X. Yuan, X. Hou, J. Li, C. Qu, W. Zhang, J. Zhao, H. Li, *Physical chemistry chemical physics PCCP* **2017**, *19*, 8934.

[155] S. Wang, A. A. Yousefi Amin, L. Wu, M. Cao, Q. Zhang, T. Ameri, *Small Structures* **2021**, *2*, 2000124.

[156] Y. Wei, Z. Cheng, J. Lin, *Chemical Society reviews* **2019**, *48*, 310.

[157] S. Toso, D. Baranov, D. Altamura, F. Scattarella, J. Dahl, X. Wang, S. Marras, A. P. Alivisatos, A. Singer, C. Giannini, L. Manna, *ACS nano* **2021**, *15*, 6243.

[158] X. Ye, J. Chen, M. Eric Irrgang, M. Engel, A. Dong, S. C. Glotzer, C. B. Murray, *Nature materials* **2017**, *16*, 214.

[159] N. Goubet, M. P. Pileni, *J. Phys. Chem. Lett.* **2011**, *2*, 1024.

[160] M. Cargnello, A. C. Johnston-Peck, B. T. Diroll, E. Wong, B. Datta, D. Damodhar, V. V. T. Doan-Nguyen, A. A. Herzing, C. R. Kagan, C. B. Murray, *Nature* **2015**, *524*, 450.

[161] A. Dreyer, A. Feld, A. Kornowski, E. D. Yilmaz, H. Noei, A. Meyer, T. Krekeler, C. Jiao, A. Stierle, V. Abetz, H. Weller, G. A. Schneider, *Nature materials* **2016**, *15*, 522.

[162] F. Fetzer, A. Maier, M. Hodas, O. Geladari, K. Braun, A. J. Meixner, F. Schreiber, A. Schnepf, M. Scheele, *Nature communications* **2020**, *11*, 6188.

[163] N. Yazdani, M. Jansen, D. Bozyigit, W. M. M. Lin, S. Volk, O. Yarema, M. Yarema, F. Juranyi, S. D. Huber, V. Wood, *Nature communications* **2019**, *10*, 4236.

[164] Y. Tong, E.-P. Yao, A. Manzi, E. Bladt, K. Wang, M. Döblinger, S. Bals, P. Müller-Buschbaum, A. S. Urban, L. Polavarapu, J. Feldmann, *Advanced materials (Deerfield Beach, Fla.)* **2018**.

[165] I. Cherniukh, G. Rainò, T. Stöferle, M. Burian, A. Travesset, D. Naumenko, H. Amenitsch, R. Erni, R. F. Mahrt, M. I. Bodnarchuk, M. V. Kovalenko, *Nature* **2021**, *593*, 535.

[166] R. Hoffmann, Angewandte Chemie (International ed. in English) **2013**, 52, 93.

[167] G. A. Somorjai, Y. Li, *Introduction to surface chemistry and catalysis*, Wiley, Hoboken, NJ **2010**.

[168] C. Kastl, R. J. Koch, C. T. Chen, J. Eichhorn, S. Ulstrup, A. Bostwick, C. Jozwiak, T. R. Kuykendall, N. J. Borys, F. M. Toma, S. Aloni, A. Weber-Bargioni, E. Rotenberg, A. M. Schwartzberg, *ACS nano* **2019**, *13*, 1284.

[169] H. Y. Jeong, Y. Jin, S. J. Yun, J. Zhao, J. Baik, D. H. Keum, H. S. Lee, Y. H. Lee, *Advanced materials (Deerfield Beach, Fla.)* **2017**, *29*.

[170] H. R. Gutiérrez, N. Perea-López, A. L. Elías, A. Berkdemir, B. Wang, R. Lv, F. López-Urías, V. H. Crespi, H. Terrones, M. Terrones, *Nano letters* **2013**, *13*, 3447.

[171] M. S. Kim, S. J. Yun, Y. Lee, C. Seo, G. H. Han, K. K. Kim, Y. H. Lee, J. Kim, *ACS nano* **2016**, *10*, 2399.

[172] M. R. Rosenberger, H.-J. Chuang, K. M. McCreary, C. H. Li, B. T. Jonker, *ACS nano* **2018**, *12*, 1793.

[173] H. Ding, Y. Dong, S. Li, N. Pan, X. Wang, *Optics express* **2018**, *26*, 7797.

[174] D.-D. Ren, J.-K. Qin, Y. Li, P. Miao, Z.-Y. Sun, P. Xu, L. Zhen, C.-Y. Xu, *Optical Materials* **2018**, *80*, 203.

[175] J. G. Bohnet, Z. Chen, J. M. Weiner, D. Meiser, M. J. Holland, J. K. Thompson, *Nature* **2012**, *484*, 78.

[176] K. D. B. Higgins, S. C. Benjamin, T. M. Stace, G. J. Milburn, B. W. Lovett, E. M. Gauger, *Nature communications* **2014**, *5*, 4705.

[177] F. Mattiotti, M. Kuno, F. Borgonovi, B. Jankó, G. L. Celardo, *Nano letters* **2020**, *20*, 7382.

[178] F. Krieg, P. C. Sercel, M. Burian, H. Andrusiv, M. I. Bodnarchuk, T. Stöferle, R. F. Mahrt, D. Naumenko, H. Amenitsch, G. Rainò, M. V. Kovalenko, *ACS central science* **2021**, *7*, 135.

[179] S. Toso, D. Baranov, C. Giannini, S. Marras, L. Manna, *ACS materials letters* **2019**, *1*, 272.

[180] J. S. van der Burgt, J. J. Geuchies, B. van der Meer, H. Vanrompay, D. Zanaga, Y. Zhang, W. Albrecht, A. V. Petukhov, L. Filion, S. Bals, I. Swart, D. Vanmaekelbergh, *J. Phys. Chem. C* **2018**, *122*, 15706.

[181] I. A. Zaluzhnyy, R. P. Kurta, A. André, O. Y. Gorobtsov, M. Rose, P. Skopintsev, I. Besedin, A. V. Zozulya, M. Sprung, F. Schreiber, I. A. Vartanyants, M. Scheele, *Nano letters* **2017**, *17*, 3511.

[182] N. Mukharamova, D. Lapkin, I. A. Zaluzhnyy, A. André, S. Lazarev, Y. Y. Kim, M. Sprung, R. P. Kurta, F. Schreiber, I. A. Vartanyants, M. Scheele, *Small (Weinheim an der Bergstrasse, Germany)* **2019**, *15*, e1904954.

[183] A. Maier, D. Lapkin, N. Mukharamova, P. Frech, D. Assalauova, A. Ignatenko, R. Khubbutdinov, S. Lazarev, M. Sprung, F. Laible, R. Löffler, N. Previdi, A. Bräuer, T. Günkel, M. Fleischer, F. Schreiber, I. A. Vartanyants, M. Scheele, *Advanced materials (Deerfield Beach, Fla.)* **2020**, *32*, e2002254.

[184] M. Zhang, Z. Zheng, Q. Fu, Z. Chen, J. He, S. Zhang, L. Yan, Y. Hu, W. Luo, *CrystEngComm* **2017**, *19*, 6797.

[185] A. Swarnkar, R. Chulliyil, V. K. Ravi, M. Irfanullah, A. Chowdhury, A. Nag, *Angew. Chem.* **2015**, *127*, 15644.

[186] T. G. Liashenko, E. D. Cherotchenko, A. P. Pushkarev, V. Pakštas, A. Naujokaitis, S. A. Khubezhov, R. G. Polozkov, K. B. Agapev, A. A. Zakhidov, I. A. Shelykh, S. V. Makarov, *Physical chemistry chemical physics PCCP* **2019**, *21*, 18930.

[187] M. Kapuscinski, M. Agthe, Z.-P. Lv, Y. Liu, M. Segad, L. Bergström, *ACS nano* **2020**, *14*, 5337.

[188] H. M. van der Kooij, G. T. van de Kerkhof, J. Sprakel, *Soft matter* **2016**, *12*, 2858.

[189] A. Leineweber, Journal of applied crystallography **2016**, 49, 1632.

[190] D.-J. Xue, Y. Hou, S.-C. Liu, M. Wei, B. Chen, Z. Huang, Z. Li, B. Sun, A. H. Proppe, Y. Dong, M. I. Saidaminov, S. O. Kelley, J.-S. Hu, E. H. Sargent, *Nature communications* **2020**, *11*, 1514.

[191] D. Baranov, S. Toso, M. Imran, L. Manna, *The journal of physical chemistry letters* **2019**, *10*, 655.

[192] D. Baranov, A. Fieramosca, R. X. Yang, L. Polimeno, G. Lerario, S. Toso, C. Giansante, M. D. Giorgi, L. Z. Tan, D. Sanvitto, L. Manna, *ACS nano* **2021**, *15*, 650.

[193] Y. Tang, L. Gomez, A. Lesage, E. Marino, T. E. Kodger, J.-M. Meijer, P. Kolpakov, J. Meng, K. Zheng, T. Gregorkiewicz, P. Schall, *Nano letters* **2020**, *20*, 5997.

[194] C. Stavrakas, A. A. Zhumekenov, R. Brenes, M. Abdi-Jalebi, V. Bulović, O. M. Bakr, E. S. Barnard, S. D. Stranks, *Energy Environ. Sci.* **2018**, *11*, 2846.

[195] D. W. deQuilettes, S. M. Vorpahl, S. D. Stranks, H. Nagaoka, G. E. Eperon, M. E. Ziffer, H. J. Snaith, D. S. Ginger, *Science (New York, N.Y.)* **2015**, *348*, 683.

[196] Y. Wang, Z. Tang, M. A. Correa-Duarte, I. Pastoriza-Santos, M. Giersig, N. A. Kotov, L. M. Liz-Marzán, *J. Phys. Chem. B* **2004**, *108*, 15461.

[197] P. Asbeck, *Journal of Applied Physics* **1977**, *48*, 820.

[198] Y. Fang, H. Wei, Q. Dong, J. Huang, *Nature communications* **2017**, *8*, 14417.

[199] L. M. Pazos-Outón, M. Szumilo, R. Lamboll, J. M. Richter, M. Crespo-Quesada, M. Abdi-Jalebi, H. J. Beeson, M. Vrućinić, M. Alsari, H. J. Snaith, B. Ehrler, R. H. Friend, F. Deschler, *Science (New York, N.Y.)* **2016**, *351*, 1430.

[200] D. Lapkin, C. Kirsch, J. Hiller, D. Andrienko, D. Assalauova, K. Braun, J. Carnis, Y. Y. Kim, M. Mandal, A. Maier, A. J. Meixner, N. Mukharamova, M. Scheele, F. Schreiber, M. Sprung, J. Wahl, S. Westendorf, I. A. Zaluzhnyy, I. A. Vartanyants, *Nature communications* **2022**, *13*, 892.

[201] J. Maes, L. Balcaen, E. Drijvers, Q. Zhao, J. de Roo, A. Vantomme, F. Vanhaecke, P. Geiregat, Z. Hens, *The journal of physical chemistry letters* **2018**, *9*, 3093.

[202] S. Kalbfleisch, H. Neubauer, S. P. Krüger, et al. (Eds.), *The Göttingen Holography Endstation of Beamline P10 at PETRA III/DESY*, AIP **2011**.

[203] G. Williamson, W. Hall, *Acta Metallurgica* **1953**, *1*, 22.

[204] J. I. Langford, A. J. C. Wilson, *Journal of applied crystallography* **1978**, *11*, 102.

[205] T. D. Kühne, M. Iannuzzi, M. Del Ben, V. V. Rybkin, P. Seewald, F. Stein, T. Laino, R. Z. Khaliullin, O. Schütt, F. Schiffmann, D. Golze, J. Wilhelm, S. Chulkov, M. H. Bani-Hashemian, V. Weber, U. Borštnik, M. Taillefumier, A. S. Jakobovits, A. Lazzaro, H. Pabst, T. Müller, R. Schade, M. Guidon, S. Andermatt, N. Holmberg, G. K. Schenter, A. Hehn, A. Bussy, F. Belleflamme, G. Tabacchi, A. Glöß, M. Lass, I. Bethune, C. J. Mundy, C. Plessl, M. Watkins, J. VandeVondele, M. Krack, J. Hutter, *The Journal of Chemical Physics* **2020**, *152*, 194103.

[206] Perdew, Burke, Ernzerhof, *Phys. Rev. Lett.* **1996**, *77*, 3865.

[207] G. Lippert, M. Parrinello, Hutter, Jurg, *Molecular Physics* **2010**, *92*, 477.

[208] J. VandeVondele, J. Hutter, *The Journal of Chemical Physics* **2007**, *127*, 114105.

[209] M. Krack, *Theor Chem Acc* **2005**, *114*, 145.

[210] S. Grimme, J. Antony, S. Ehrlich, H. Krieg, *The Journal of Chemical Physics* **2010**, *132*, 154104.

[211] S. ten Brinck, I. Infante, *ACS energy letters* **2016**, *1*, 1266.

[212] L. Genovese, T. Deutsch, A. Neelov, S. Goedecker, G. Beylkin, *The Journal of Chemical Physics* **2006**, *125*, 74105.

[213] H. Huang, L. Polavarapu, J. A. Sichert, A. S. Susha, A. S. Urban, A. L. Rogach, *NPG Asia Mater* **2016**, *8*, e328-e328.

[214] Y. Hassan, J. H. Park, M. L. Crawford, A. Sadhanala, J. Lee, J. C. Sadighian, E. Mosconi, R. Shivanna, E. Radicchi, M. Jeong, C. Yang, H. Choi, S. H. Park, M. H. Song, F. Angelis, C. Y. Wong, R. H. Friend, B. R. Lee, H. J. Snaith, *Nature* **2021**, *591*, 72.

[215] A. Dey, J. Ye, A. De, E. Debroye, S. K. Ha, E. Bladt, A. S. Kshirsagar, Z. Wang, J. Yin, Y. Wang, L. N. Quan, F. Yan, M. Gao, X. Li, J. Shamsi, T. Debnath, M. Cao, M. A. Scheel, S. Kumar, J. A. Steele, M. Gerhard, L. Chouhan, K. Xu, X.-G. Wu, Y. Li, Y. Zhang, A. Dutta, C. Han, I. Vincon, A. L. Rogach, A. Nag, A. Samanta, B. A. Korgel, C.-J. Shih, D. R. Gamelin, D. H. Son, H. Zeng, H. Zhong, H. Sun, H. V. Demir, I. G. Scheblykin, I. Mora-Seró, J. K. Stolarczyk, J. Z. Zhang, J. Feldmann, J. Hofkens, J. M. Luther, J. Pérez-Prieto, L. Li, L. Manna, M. I. Bodnarchuk, M. V. Kovalenko, M. B. J. Roeffaers, N. Pradhan, O. F. Mohammed, O. M. Bakr, P. Yang, P. Müller-Buschbaum, P. V. Kamat, Q. Bao, Q. Zhang, R. Krahne, R. E. Galian, S. D. Stranks, S. Bals, V. Biju, W. A. Tisdale, Y. Yan, R. L. Z. Hoye, L. Polavarapu, *ACS nano* **2021**, *15*, 10775.

[216] K. Lin, J. Xing, L. N. Quan, F. P. G. Arquer, X. Gong, J. Lu, L. Xie, W. Zhao, Di Zhang, C. Yan, W. Li, X. Liu, Y. Lu, J. Kirman, E. H. Sargent, Q. Xiong, Z. Wei, *Nature* **2018**, *562*, 245.

[217] S. Zhang, G. Han, *Prog. Energy* **2020**, *2*, 22002.

[218] Y. Liu, Z. Wang, S. Liang, Z. Li, M. Zhang, H. Li, Z. Lin, *Nano letters* **2019**, *19*, 9019.

[219] G. H. Ahmed, J. Yin, O. M. Bakr, O. F. Mohammed, *ACS energy letters* **2021**, *6*, 1340.

[220] J. Ye, M. M. Byranvand, C. O. Martínez, R. L. Z. Hoye, M. Saliba, L. Polavarapu, *Angewandte Chemie (International ed. in English)* **2021**, *60*, 21636.

[221] J. Shamsi, D. Kubicki, M. Anaya, Y. Liu, K. Ji, K. Frohna, C. P. Grey, R. H. Friend, S. D. Stranks, *ACS energy letters* **2020**, *5*, 1900.

[222] M. Imran, P. Ijaz, L. Goldoni, D. Maggioni, U. Petralanda, M. Prato, G. Almeida, I. Infante, L. Manna, *ACS energy letters* **2019**, *4*, 819.

[223] T. Naujoks, R. Jayabalan, C. Kirsch, F. Zu, M. Mandal, J. Wahl, M. Waibel, A. Opitz, N. Koch, D. Andrienko, M. Scheele, W. Brütting, *ACS applied materials & interfaces* **2022**, *14*, 28985.

[224] J. He, H. Liu, Y. Dai, X. Ou, J. Wang, S. Tao, X. Zhang, P. Wang, D. Ma, *J. Phys. Chem. C* **2009**, *113*, 6761.

[225] W. Cho, Y. Kim, C. Lee, J. Park, Y.-S. Gal, J. W. Lee, S.-H. Jin, *Dyes and Pigments* **2014**, *108*, 115.

[226] Y. Lin, Y. Firdaus, F. H. Isikgor, M. I. Nugraha, E. Yengel, G. T. Harrison, R. Hallani, A. El-Labban, H. Faber, C. Ma, X. Zheng, A. Subbiah, C. T. Howells, O. M. Bakr, I. McCulloch, S. Wolf, L. Tsetseris, T. D. Anthopoulos, *ACS energy letters* **2020**, *5*, 2935.

[227] T. Hatakeyama, K. Shiren, K. Nakajima, S. Nomura, S. Nakatsuka, K. Kinoshita, J. Ni, Y. Ono, T. Ikuta, *Advanced materials (Deerfield Beach, Fla.)* **2016**, *28*, 2777.

[228] Y. Lu, Z. Wang, J. Chen, Y. Peng, X. Tang, Z. Liang, F. Qi, W. Chen, *Journal of Luminescence* **2021**, *234*, 117952.

[229] W. Wang, Z. Wu, T. Ye, S. Ding, K. Wang, Z. Peng, X. W. Sun, *J. Mater. Chem. C* **2021**, *9*, 2115.

[230] D. Liu, S. A. Kozmin, *Organic letters* **2002**, *4*, 3005.

[231] S. Majhi, *ChemistrySelect* **2021**, *6*, 4178.

[232] N.-T. Chen, S.-H. Cheng, C.-P. Liu, J. S. Souris, C.-T. Chen, C.-Y. Mou, L.-W. Lo, *International journal of molecular sciences* **2012**, *13*, 16598.

[233] B. Fritzinger, R. K. Capek, K. Lambert, J. C. Martins, Z. Hens, *J. Am. Chem. Soc.* **2010**, *132*, 10195.

[234] B. A. Koscher, J. K. Swabeck, N. D. Bronstein, A. P. Alivisatos, *J. Am. Chem. Soc.* **2017**, *139*, 6566.

[235] S. R, H. V. Vishaka, K. J, R. G. Balakrishna, *ACS Appl. Nano Mater.* **2020**, *3*, 6089.

[236] H. Xiao, Y. Wei, P. Dang, S. Liang, Z. Cheng, G. Li, J. Lin, *J. Mater. Chem. C* **2020**, *8*, 9968.

[237] M. Vallés-Pelarda, A. F. Gualdrón-Reyes, C. Felip-León, C. A. Angulo-Pachón, S. Agouram, V. Muñoz-Sanjosé, J. F. Miravet, F. Galindo, I. Mora-Seró, *Advanced Optical Materials* **2021**, *9*, 2001786.

[238] J. Endres, D. A. Egger, M. Kulbak, R. A. Kerner, L. Zhao, S. H. Silver, G. Hodes, B. P. Rand, D. Cahen, L. Kronik, A. Kahn, *J. Phys. Chem. Lett.* **2016**, *7*, 2722.

[239] P. Schulz, E. Edri, S. Kirmayer, G. Hodes, D. Cahen, A. Kahn, *Energy Environ. Sci.* **2014**, *7*, 1377.

[240] Y. Zou, Q. Meng, H. Mao, D. Zhu, *Organic Electronics* **2017**, *41*, 307.

[241] J. Wahl, P. Haizmann, C. Kirsch, R. Frecot, N. Mukharamova, D. Assalauova, Y. Y. Kim, I. Zaluzhnyy, T. Chassé, I. A. Vartanyants, H. Peisert, M. Scheele, *Physical chemistry chemical physics PCCP* **2022**, *24*, 10944.

[242] Z. Li, Q. Hu, Z. Tan, Y. Yang, M. Leng, X. Liu, C. Ge, G. Niu, J. Tang, *ACS applied materials & interfaces* **2018**, *10*, 43915.

[243] J. Wahl, M. Engelmayer, M. Mandal, T. Naujoks, P. Haizmann, A. Maier, H. Peisert, D. Andrienko, W. Brütting, M. Scheele, *Advanced Optical Materials* **2021**.

[244] M. Soreni-Harari, N. Yaacobi-Gross, D. Steiner, A. Aharoni, U. Banin, O. Millo, N. Tessler, *Nano letters* **2008**, *8*, 678.

[245] P. R. Brown, D. Kim, R. R. Lunt, N. Zhao, M. G. Bawendi, J. C. Grossman, V. Bulović, *ACS nano* **2014**, *8*, 5863.

[246] S. Silver, S. Xun, H. Li, J.-L. Brédas, A. Kahn, *Adv. Energy Mater.* **2020**, *10*, 1903900.

[247] Y. Zheng, Z. Fang, M.-H. Shang, Z. Du, Z. Yang, K.-C. Chou, W. Yang, S. Wei, X. Hou, *ACS applied materials & interfaces* **2020**, *12*, 34462.

[248] A. Dutta, R. K. Behera, P. Pal, S. Baitalik, N. Pradhan, *Angew. Chem.* **2019**, *131*, 5608.

[249] A. L. Efros, L. E. Brus, *ACS nano* **2021**, *15*, 6192.

[250] T. Kippeny, L. A. Swafford, S. J. Rosenthal, *J. Chem. Educ.* **2002**, *79*, 1094.

[251] R. G. Niemann, A. G. Kontos, D. Palles, E. I. Kamitsos, A. Kaltzoglou, F. Brivio, P. Falaras, P. J. Cameron, *J. Phys. Chem. C* **2016**, *120*, 2509.

[252] D. B. Straus, R. J. Cava, *ACS applied materials & interfaces* **2022**, *14*, 34884.

[253] M. Era, S. Morimoto, T. Tsutsui, S. Saito, *Appl. Phys. Lett.* **1994**, *65*, 676.

[254] Michael Coelle, Wolfgang Bruetting, Markus Schwoerer, Masayuki Yahiro, Tetsuo Tsutsui, in *SPIE Proceedings* (Ed.: Zakya H. Kafafi), SPIE **2001**.

[255] Zhi-Kuang Tan, Reza Saberi Moghaddam, May Ling Lai, Pablo Docampo, Ruben Higler, Felix Deschler, Michael Price, Aditya Sadhanala, Luis M. Pazos, Dan Credgington, Fabian Hanusch, Thomas Bein, Henry J. Snaith, Richard H. Friend, *Nature nanotechnology* **2014**, *9*, 687.

[256] Yang Liu, Jieyuan Cui, Kai Du, He Tian, Zhuofei He, Qiaohui Zhou, Zhaoliang Yang, Yunzhou Deng, Dong Chen, Xiaobing Zuo, Yang Ren, Liang Wang, Haiming Zhu, Baodan Zhao, Dawei Di, Jianpu Wang, Richard H. Friend, Yizheng Jin, *Nature Photon* **2019**, *13*, 760.

[257] Xiao-Ke Liu, Weidong Xu, Sai Bai, Yizheng Jin, Jianpu Wang, Richard H. Friend, Feng Gao, *Nature materials* **2020**, *20*, 10.

[258] Min-Ho Park, Joo Sung Kim, Jung-Min Heo, Soyeong Ahn, Su-Hun Jeong, Tae-Woo Lee, *ACS energy letters* **2019**, *4*, 1134.

[259] Kangyu Ji, Miguel Anaya, Anna Abfalterer, Samuel D. Stranks, *Advanced Optical Materials* **2021**, *9*, 2002128.

[260] Seung-Je Woo, Joo Sung Kim, Tae-Woo Lee, *Nature Photon* **2021**, *15*, 630.

[261] Y.-H. Kim, S. Kim, A. Kakekhani, J. Park, J. Park, Y.-H. Lee, H. Xu, S. Nagane, R. B. Wexler, D.-H. Kim, S. H. Jo, L. Martínez-Sarti, P. Tan, A. Sadhanala, G.-S. Park, Y.-W. Kim, B. Hu, H. J. Bolink, S. Yoo, R. H. Friend, A. M. Rappe, T.-W. Lee, *Nature Photon* **2021**, *15*, 148.

[262] Junzhi Ye, Mahdi Malekshahi Byranvand, Clara Otero Mart\'ınez, Robert L. Z. Hoye, Michael Saliba, Lakshminarayana Polavarapu, *Angew. Chem.* **2021**, *133*, 21804.

[263] Leyre Gomez, Chris de Weerd, Jose L. Hueso, Tom Gregorkiewicz, *Nanoscale* **2017**, *9*, 631.

[264] Naresh Kumar Kumawat, Abhishek Swarnkar, Angshuman Nag, Dinesh Kabra, *J. Phys. Chem. C* **2018**, *122*, 13767.

[265] Wei Yan, Jianhua Shen, Yihua Zhu, Yiqing Gong, Jingrun Zhu, Zheng Wen, Chunzhong Li, *Nano Research* **2021**, *14*, 4038.

[266] Guopeng Li, Jingsheng Huang, Hanwen Zhu, Yanqing Li, Jian-Xin Tang, Yang Jiang, *Chem. Mater.* **2018**, *30*, 6099.

[267] Fei Li, Ying Liu, Hongliang Wang, Qian Zhan, Quanlin Liu, Zhiguo Xia, *Chem. Mater.* **2018**, *30*, 8546.

[268] Navendu Mondal, Apurba De, Anunay Samanta, *ACS energy letters* **2018**, *4*, 32.

[269] Tian Wu, Junnan Li, Yatao Zou, Hao Xu, Kaichuan Wen, Shanshan Wan, Sai Bai, Tao Song, John A. McLeod, Steffen Duhm, Feng Gao, Baoquan Sun, *Angewandte Chemie International Edition* **2020**, *59*, 4099.

[270] Hao Wu, Jianbei Qiu, Jing Wang, Yugeng Wen, Qi Wang, Zhangwen Long, Dacheng Zhou, Yong Yang, Dazhao Wang, *Inorg. Chem. Front.* **2021**, *8*, 658.

[271] Cong Chen, Guang Yang, Junjie Ma, Xiaolu Zheng, Zhiliang Chen, Qi Zhang, Guojia Fang, *J. Mater. Chem. C* **2017**, *5*, 10280.

[272] Hui Luo, Jihuai Wu, Quanzhen Liu, Mingjing Zhang, Pengqiang Yuan, Miaoliang Huang, *ChemistrySelect* **2018**, *3*, 12320.

[273] Ngoc Duy Pham, Jing Shang, Yang Yang, Minh Tam Hoang, Vincent Tiing Tiong, Xiaoxiang Wang, Lijuan Fan, Peng Chen, Liangzhi Kou, Lianzhou Wang, Hongxia Wang, *Nano Energy* **2020**, *69*, 104412.

[274] Mengyuan Liu, Le Ma, Kehan Xie, Piaopiao Zeng, Shijing Wei, Feng Zhang, Chao Li, Feijiu Wang, *J. Phys. Chem. Lett.* **2022**, *13*, 1519.

[275] T.P. Nguyen, P. Le Rendu, P.D. Long, S.A. De Vos, *Surface and Coatings Technology* **2004**, *180-181*, 646.

[276] Xue-Feng Peng, Xiao-Yan Wu, Xia-Xia Ji, Jie Ren, Qi Wang, Guo-Qing Li, Xiao-Hui Yang, *J. Phys. Chem. Lett.* **2017**, *8*, 4691.

[277] Selina Olthof, in *Organic and Hybrid Light Emitting Materials and Devices XXV* (Eds.: Tae-Woo Lee, Franky So, Chihaya Adachi), SPIE **2021**.

[278] Kiwoong Kim, Junkyeong Jeong, Minju Kim, Donghee Kang, Sang Wan Cho, Hyunbok Lee, Yeonjin Yi, *Applied Surface Science* **2019**, *480*, 565.

[279] Baodan Zhao, Yaxiao Lian, Linsong Cui, Giorgio Divitini, Gunnar Kusch, Edoardo Ruggeri, Florian Auras, Weiwei Li, Dexin Yang, Bonan Zhu, Rachel A. Oliver, Judith L. MacManus-Driscoll, Samuel D. Stranks, Dawei Di, Richard H. Friend, *Nature Electronics* **2020**, *3*, 704.

[280] Yifang Sun, Huidan Zhang, Kai Zhu, Weiguang Ye, Lushuang She, Ximing Gao, Wenyu Ji, Qinghui Zeng, *RSC Adv.* **2021**, *11*, 27333.

[281] Katie Hills-Kimball, Hanjun Yang, Tong Cai, Junyu Wang, Ou Chen, *Advanced Science* **2021**, *8*, 2100214.

[282] Francesco Di Stasio, Sotirios Christodoulou, Nengjie Huo, Gerasimos Konstantatos, *Chem. Mater.* **2017**, *29*, 7663.

[283] Ju Young Woo, Youngsik Kim, Jungmin Bae, Tae Gun Kim, Jeong Won Kim, Doh C. Lee, Sohee Jeong, *Chem. Mater.* **2017**, *29*, 7088.

[284] Tobias D. Schmidt, Thomas Lampe, Daniel Sylvinson M. R., Peter I. Djurovich, Mark E. Thompson, Wolfgang Brütting, *Physical Review Applied* **2017**, *8*, 37001.

[285] M. J. Jurow, T. Morgenstern, C. Eisler, J. Kang, E. Penzo, M. Do, M. Engelmayer, W. T. Osowiecki, Y. Bekenstein, C. Tassone, L.-W. Wang, A. P. Alivisatos, W. Brütting, Y. Liu, *Nano letters* **2019**, *19*, 2489.

[286] M. J. Jurow, T. Lampe, E. Penzo, J. Kang, M. A. Koc, T. Zechel, Z. Nett, M. Brady, L.-W. Wang, A. P. Alivisatos, S. Cabrini, W. Brütting, Y. Liu, *Nano letters* **2017**, *17*, 4534.

[287] Selina Olthof, Klaus Meerholz, *Scientific reports* **2017**, *7*, 40267.

[288] Fengshuo Zu, Christian M. Wolff, Maryline Ralaiarisoa, Patrick Amsalem, Dieter Neher, Norbert Koch, *ACS applied materials & interfaces* **2019**, *11*, 21578.

[289] Tiago B. Tavares, Francisco F. de Sousa, Maria J. A. Sales, Leonardo G. Paterno, Waldomiro Paschoal, Sanclayton G. C. Moreira, *Applied Physics A* **2021**, *127*, 855.

[290] Fengshuo Zu, Patrick Amsalem, David A. Egger, Rongbin Wang, Christian M. Wolff, Honghua Fang, Maria Antonietta Loi, Dieter Neher, Leeor Kronik, Steffen Duhm, Norbert Koch, *J. Phys. Chem. Lett.* **2019**, *10*, 601.

[291] Jie Cao, Shu Xia Tao, Peter A. Bobbert, Ching-Ping Wong, Ni Zhao, *Advanced Materials* **2018**, *30*, 1707350.

[292] Rui An, Fengying Zhang, Xianshao Zou, Yingying Tang, Mingli Liang, Ihor Oshchapovskyy, Yuchen Liu, Alireza Honarfar, Yunqian Zhong, Chuanshuai Li, Huifang Geng, Junsheng Chen, Sophie E. Canton, Tõnu Pullerits, Kaibo Zheng, *ACS applied materials & interfaces* **2018**, *10*, 39222.

[293] Zhishan Fang, Haiping He, Lu Gan, Jing Li, Zhizhen Ye, *Advanced Science* **2018**, *5*, 1800736.

[294] Alex I. Pointon, Nicholas E. Grant, Ruy S. Bonilla, Evangeline C. Wheeler-Jones, Marc Walker, Peter R. Wilshaw, Claire E. J. Dancer, John D. Murphy, *ACS Applied Electronic Materials* **2019**, *1*, 1322.

[295] Hyunwon Chu, Hyungjun Noh, Yun-Jung Kim, Seongmin Yuk, Ju-Hyuk Lee, Jinhong Lee, Hobeom Kwack, YunKyoung Kim, Doo-Kyung Yang, Hee-Tak Kim, *Nature communications* **2019**, *10*, 188.

[296] Francesco Lamberti, Teresa Gatti, Enrico Cescon, Roberto Sorrentino, Antonio Rizzo, Enzo Menna, Gaudenzio Meneghesso, Moreno Meneghetti, Annamaria Petrozza, Lorenzo Franco, *Chem* **2019**, *5*, 1806.

[297] Jaemin Kong, Yongwoo Shin, Jason A. Röhr, Hang Wang, Juan Meng, Yueshen Wu, Adlai Katzenberg, Geunjin Kim, Dong Young Kim, Tai-De Li, Edward Chau, Francisco Antonio, Tana Siboonruang, Sooncheol Kwon, Kwanghee Lee, Jin Ryoun Kim, Miguel A. Modestino, Hailiang Wang, André D. Taylor, *Nature* **2021**, *594*, 51.

[298] Vikash Kumar Ravi, Ganesh B. Markad, Angshuman Nag, *ACS energy letters* **2016**, *1*, 665.

[299] Gabriele Rainò, Annelies Landuyt, Franziska Krieg, Caterina Bernasconi, Stefan T. Ochsenbein, Dmitry N. Dirin, Maryna I. Bodnarchuk, Maksym V. Kovalenko, *Nano letters* **2019**, *19*, 3648.

[300] Stefano Pierini, Marianna D'Amato, Mayank Goyal, Quentin Glorieux, Elisabeth Giacobino, Emmanuel Lhuillier, Christophe Couteau, Alberto Bramati, *ACS Photonics* **2020**, *7*, 2265.

[301] Gergely F. Samu, Rebecca A. Scheidt, Prashant V. Kamat, Csaba Janáky, *Chem. Mater.* **2017**, *30*, 561.

[302] Jence T. Mulder, Indy du Fossé, Maryam Alimoradi Jazi, Liberato Manna, Arjan J. Houtepen, *ACS energy letters* **2021**, *6*, 2519.

[303] J.N. Hasnidawani, H.N. Azlina, H. Norita, N.N. Bonnia, S. Ratim, E.S. Ali, *Procedia Chemistry* **2016**, *19*, 211.

[304] S. Leyre, E. Coutino-Gonzalez, J. J. Joos, J. Ryckaert, Y. Meuret, D. Poelman, P. F. Smet, G. Durinck, J. Hofkens, G. Deconinck, P. Hanselaer, *Review of Scientific Instruments* **2014**, *85*, 123115.

[305] Jörg Frischeisen, Daisuke Yokoyama, Ayataka Endo, Chihaya Adachi, Wolfgang Brütting, *Organic Electronics* **2011**, *12*, 809.

[306] G. Kresse, J. Furthmüller, *Physical Review B* **1996**, *54*, 11169.

[307] John P. Perdew, Kieron Burke, Matthias Ernzerhof, *Phys. Rev. Lett.* **1996**, *77*, 3865.

[308] G. Kresse, J. Furthmüller, *Computational Materials Science* **1996**, *6*, 15.

[309] G. Kresse, D. Joubert, *Physical Review B* **1999**, *59*, 1758.

[310] Koichi Momma, Fujio Izumi, *Journal of applied crystallography* **2011**, *44*, 1272.

[311] Alex M Ganose, Adam J Jackson, David O Scanlon, *Journal of Open Source Software* **2018**, *3*, 717.

[312] Vei Wang, Nan Xu, Jin-Cheng Liu, Gang Tang, Wen-Tong Geng, *Computer Physics Communications* **2021**, *267*, 108033.

[313] Y. Hassan, O. J. Ashton, J. H. Park, G. Li, N. Sakai, B. Wenger, A.-A. Haghighirad, N. K. Noel, M. H. Song, B. R. Lee, R. H. Friend, H. J. Snaith, *Journal of the American Chemical Society* **2019**, *141*, 1269.

[314] L. N. Quan, B. P. Rand, R. H. Friend, S. G. Mhaisalkar, T.-W. Lee, E. H. Sargent, *Chemical reviews* **2019**, *119*, 7444.

[315] L. Chouhan, S. Ghimire, C. Subrahmanyam, T. Miyasaka, V. Biju, *Chemical Society reviews* **2020**, *49*, 2869.

[316] Q. Chen, J. Wu, X. Ou, B. Huang, J. Almutlaq, A. A. Zhumekenov, X. Guan, S. Han, L. Liang, Z. Yi, J. Li, X. Xie, Y. Wang, Y. Li, D. Fan, D. B. L. Teh, A. H. All, O. F. Mohammed, O. M. Bakr, T. Wu, M. Bettinelli, H. Yang, W. Huang, X. Liu, *Nature* **2018**, *561*, 88.

[317] F. Zhou, Z. Li, W. Lan, Q. Wang, L. Ding, Z. Jin, *Small Methods* **2020**, *4*, 2000506.

[318] Y. Zhou, J. Chen, O. M. Bakr, O. F. Mohammed, *ACS energy letters* **2021**, *6*, 739.

[319] B. Conings, J. Drijkoningen, N. Gauquelin, A. Babayigit, J. D'Haen, L. D'Olieslaeger, A. Ethirajan, J. Verbeeck, J. Manca, E. Mosconi, F. D. Angelis, H.-G. Boyen, *Adv. Energy Mater.* **2015**, *5*, 1500477.

[320] S. Mazumdar, Y. Zhao, X. Zhang, *Front.Electron.* **2021**, *2*, 2572.

[321] A. Xie, C. Hettiarachchi, F. Maddalena, M. E. Witkowski, M. Makowski, W. Drozdowski, A. Arramel, A. T. S. Wee, S. V. Springham, P. Q. Vuong, H. J. Kim, C. Dujardin, P. Coquet, M. D. Birowosuto, C. Dang, *Commun Mater* **2020**, *1*, 444.

[322] S. Kishimoto, K. Shibuya, F. Nishikido, M. Koshimizu, R. Haruki, Y. Yoda, *Appl. Phys. Lett.* **2008**, *93*, 261901.

[323] M. Scheele, W. Brütting, F. Schreiber, *Physical chemistry chemical physics PCCP* **2015**, *17*, 97.

[324] J. Endres, M. Kulbak, L. Zhao, B. P. Rand, D. Cahen, G. Hodes, A. Kahn, *Journal of Applied Physics* **2017**, *121*, 35304.

[325] S. Colella, M. Todaro, S. Masi, A. Listorti, D. Altamura, R. Caliandro, C. Giannini, E. Carignani, M. Geppi, D. Meggiolaro, G. Buscarino, F. D. Angelis, A. Rizzo, *ACS energy letters* **2018**, *3*, 1840.

[326] L. A. Frolova, S. Y. Luchkin, Y. Lekina, L. G. Gutsev, S. A. Tsarev, I. S. Zhidkov, E. Z. Kurmaev, Z. X. Shen, K. J. Stevenson, S. M. Aldoshin, P. A. Troshin, *Adv. Energy Mater.* **2021**, *11*, 2002934.

[327] A. F. Akbulatov, L. A. Frolova, N. N. Dremova, I. Zhidkov, V. M. Martynenko, S. A. Tsarev, S. Y. Luchkin, E. Z. Kurmaev, S. M. Aldoshin, K. J. Stevenson, P. A. Troshin, *The journal of physical chemistry letters* **2020**, *11*, 333.

[328] L. A. Frolova, Q. Chang, S. Y. Luchkin, D. Zhao, A. F. Akbulatov, N. N. Dremova, A. V. Ivanov, E. E. M. Chia, K. J. Stevenson, P. A. Troshin, *J. Mater. Chem. C* **2019**, *7*, 5314.

[329] R. E. Beal, D. J. Slotcavage, T. Leijtens, A. R. Bowring, R. A. Belisle, W. H. Nguyen, G. F. Burkhard, E. T. Hoke, M. D. McGehee, *The journal of physical chemistry letters* **2016**, *7*, 746.

[330] J. D. McGettrick, K. Hooper, A. Pockett, J. Baker, J. Troughton, M. Carnie, T. Watson, *Materials Letters* **2019**, *251*, 98.

[331] S. Tao, I. Schmidt, G. Brocks, J. Jiang, I. Tranca, K. Meerholz, S. Olthof, *Nature communications* **2019**, *10*, 2560.

[332] P. Cottingham, R. L. Brutchey, *Chemical communications (Cambridge, England)* **2016**, *52*, 5246.

[333] D. R. Baer, K. Artyushkova, H. Cohen, C. D. Easton, M. Engelhard, T. R. Gengenbach, G. Greczynski, P. Mack, D. J. Morgan, A. Roberts, *Journal of Vacuum Science & Technology A* **2020**, *38*, 31204.

[334] J. Cazaux, Journal of Electron Spectroscopy and Related Phenomena **2000**, 113, 15.

[335] B. Wang, A. Navrotsky, *J. Phys. Chem. C* **2020**, *124*, 8639.

[336] P. S. Mathew, G. F. Samu, C. Janáky, P. V. Kamat, *ACS energy letters* **2020**, *5*, 1872.

[337] R. A. Evarestov, E. A. Kotomin, A. Senocrate, R. K. Kremer, J. Maier, *Physical chemistry chemical physics PCCP* **2020**, *22*, 3914.

[338] D. Cortecchia, J. Yin, A. Bruno, S.-Z. A. Lo, G. G. Gurzadyan, S. Mhaisalkar, J.-L. Brédas, C. Soci, *J. Mater. Chem. C* **2017**, *5*, 2771.

[339] I. Du Fossé, S. Lal, A. N. Hossaini, I. Infante, A. J. Houtepen, *J. Phys. Chem. C* **2021**, *125*, 23968.

[340] J. J. Yeh, I. Lindau, *Atomic Data and Nuclear Data Tables* **1985**, *32*, 1.

[341] R. Hesse, M. Weiß, R. Szargan, P. Streubel, R. Denecke, *Journal of Electron Spectroscopy and Related Phenomena* **2013**, *186*, 44.

[342] K. Harrison, L. B. Hazell, *Surf. Interface Anal.* **1992**, *18*, 368.

Declaration of Contribution

The following list describes the contributions to the papers discussed in this thesis.

Publication 1: Spatially Resolved Fluorescence of Caesium Lead Halide Perovskite Supercrystals Reveals Quasi-Atomic Behavior of Nanocrystals.

I synthesized and characterized samples for the measurements conducted at the DESY P10 beamline. The characterization mainly involved the determination of the size distribution, optical properties (absorption and photoluminescence), and structure analysis. The self-assembly into superlattices and corresponding characterization was carried out partly by me, including optical microscopy and sample preparation for scanning electron microscopy. Additionally, I synthesized multiple beamline samples and prepared them for shipping to the synchrotron. On site I coordinated the measurement planning and made fresh samples.

Total estimated contribution: ~30 %

Publication 2: Zwitterionic Carbazole Ligands Enhance the Stability and Performance of Perovskite Nanocrystals in Light Emitting Diodes.

For this work I carried out the synthesis of the nanocrystals and performed the ligand exchange. The design concept of the ligand was developed by me considering all the authors' suggestions, and the design and synthesis of the new ligand was carried out by me. Most preparative and analytical steps were carried out by me, including the optical, electrical, and structural measurements. I additionally prepared the samples for measurements, which could not be conducted in our lab, like SEM, NMR, and device measurements. The manuscript was written entirely by me, supported by a critical review especially by Marcus Scheele.

Total estimated contribution: ~90 %

Publication 3: Quantum Efficiency Enhancement of Lead-Halide Perovskite Nanocrystal LEDs by Organic Lithium Salt Treatment

For this publication I prepared the NC samples, including synthesis and characterization. I assisted in the analysis and interpretation of the data.

Total estimated contribution: ~15 %

Publication 4: Mitigating the Photodegradation of All-Inorganic Mixed-Halide Perovskite Nanocrystals by Ligand Exchange.

Herein, I synthesized and fabricated all $CsPbBr_2Cl$ perovskite nanoparticles, including the fabrication of superlattices. I assisted in the analysis and interpretation of the data.

Total estimated contribution: ~10 %

Acknowledgements

This is finally the right place to express my gratitude. While writing this thesis, it would have been impossible for me to do it alone without the great support of my colleagues and friends. Therefore, I would like to take this opportunity to thank them all from the bottom of my heart.

First and foremost, I would like to thank my supervisor and group leader Prof. Dr. Marcus Scheele who gave me the necessary support and freedom to succeed. He was always available for discussions and always found enough time to deal in detail with topics that I had brought in. In addition, Marcus Scheele always gave me the feeling that he supported my work and my plans. During this time, I not only developed scientifically, but also gained valuable insights into team leadership that I will take with me.

I would like to express my gratitude to my second supervisor, Prof. Dr. Alfred J. Meixner, for his support and the opportunity to work with his students on optical setups. His help was valuable to me. Special thanks are due to Prof. Dr. Reinhold Fink, who served as second reviewer of this thesis and was a member of the examination board. Furthermore, I would like to thank Prof. Dr. Heiko Peisert and Prof. Dr. Thomas Chassé for their support during the XPS and UPS measurements. Through their expertise and provision of the instruments, I was able to gain important insights. In particular, I would like to thank Heiko Peisert for the extremely interesting and enlightening discussions on this topic. In addition, I would like to express my gratitude to Heiko Peisert for serving as a member of the review committee. His contribution was of great importance.

I would like to thank all colleagues and friends at the chair for the pleasant and friendly working atmosphere: Dr. Andre Maier, Kai Wurst, Dr. Christine Schedel, Philipp Frech, Theresa Hettinger, Dr. Björn Märker, Dr. Michelle Weber, Fabian Strauss, Sophia Westendorf, Dr. Kai Braun, Dr. Krishan Kumar, Patrick Michel, and Jonas Hiller. The mutual helpfulness and the constant exchange of knowledge were not only a professional enrichment. In particular, the numerous discussions with Jan Wahl and Philipp Haizmann contributed decisively to the knowledge gained and the progress of the work. Thank you to Jan Wahl for proofreading this thesis.

Special thanks also go to the partners from Augsburg and Mainz: Tassilo Naujoks, Manuel Engelmayer, Roshini Jayabalan, Prof. Dr. Wolfang Brütting and, Dr. Mukunda Mandal, and Prof. Dr. Denis Andrienko. Without them this work would not have been

possible, and I am very grateful for this thriving collaboration and the outstanding input. Special thanks are due to the group of Prof. Dr. Ivan Vartaniants for the cooperation with us at the DESY beamline and for the excellent data analysis.

I would like to thank all of my fellow students and friends with whom I have had the pleasure to spend my time in Tübingen. I would especially like to thank Martin Jedele, Andreas Paul, Tobias Rösch and Steffanie Braun for their support, both at the institute and in private, whenever it was needed.

Lastly, I am profoundly grateful to my parents, Barbara and Josef Kirsch, as well as my fiancé, Anika Kaiser, for their unwavering support and for providing me with the opportunity to follow my passion in science. Their patience and encouragement have been invaluable throughout my journey.